Journal of Heat Transfer

Published Monthly by ASME

VOLUME 132 • NUMBER 4 • APRIL 2010

Special Issue on Recent Advances in Microchannels Heat Transfer

GUEST EDITORIAL

RESEARCH PAPERS

(Contents continued on inside back cover)

This journal is printed on acid-free paper, which exceeds the ANSI Z39.48-1992 specification for permanence of paper and library materials. ♾™
♲ 85% recycled content, including 10% post-consumer fibers.

Editor, **YOGESH JALURIA (2010)**
Assistant to the Editor, **S. PATEL**

Associate Editors
Yutaka Asako, Tokyo Metropolitan University, Japan (2010)
Cho Lik Chan, The University of Arizona (2010)
Louis C. Chow, University of Central Florida (2010)
Frank J. Cunha, Pratt & Whitney (2011)
Ali Ebadian, Florida International Univ. (2011)
Ofodike A. Ezekoye, Univ. of Texas-Austin (2011)
Srinivas Garimella, Georgia Institute Technology (2012)
Kenneth Goodson, Stanford University (2012)
Satish G. Kandlikar, Rochester Inst. of Tech. (2010)
Sung Jin Kim, KAIST, Korea (2010)
Giulio Lorenzini, University of Bologna (2012)
Jayathi Y. Murthy, Perdue University (2010)
Pamela M. Norris, Univ. of Virginia (2011)
Patrick H. Oosthuizen, Queens University, Canada (2012)
Patrick E. Phelan, National Science Foundation (2011)
Roger R. Schmidt, IBM Corporation (2010)
S. A. Sherif, University of Florida (2010)
Heping Tan, Harbin Institute of Technology (2011)
Wen Q. Tao, Xi'an University, China (2012)
Wei Tong, Danaher Corporation (2012)
Robert Tzou, University of Missouri-Columbia (2012)
Peter Vadasz, Northern Arizona University (2010)
Walter W. Yuen, Univ. of California–Santa Barbara (2011)

Past Editors
V. DHIR
J. R. HOWELL
R. VISKANTA
G. M. FAETH
K. T. YANG
E. M. SPARROW

HEAT TRANSFER DIVISION
Chair, **V. CAREY**
Vice Chair, **L. GRITZO**
Past Chair, **CHANG OH**

PUBLICATIONS COMMITTEE
Chair, **BAHRAM RAVANI**

OFFICERS OF THE ASME
President,
AMOS E. HOLT
Executive Director,
THOMAS G. LOUGHLIN
Treasurer,
WILBUR MARNER

PUBLISHING STAFF
Managing Director, Publishing
PHILIP DI VIETRO
Manager, Journals
COLIN McATEER
Production Coordinator
JUDITH SIERANT

Transactions of the ASME, Journal of Heat Transfer (ISSN 0022-1481) is published monthly by The American Society of Mechanical Engineers, Three Park Avenue, New York, NY 10016. Periodicals postage paid at New York, NY and additional mailing offices. POSTMASTER: Send address changes to Transactions of the ASME, Journal of Heat Transfer, c/o THE AMERICAN SOCIETY OF MECHANICAL ENGINEERS, 22 Law Drive, Box 2300, Fairfield, NJ 07007-2300. **CHANGES OF ADDRESS** must be received at Society headquarters seven weeks before they are to be effective. Please send old label and new address.

STATEMENT from By-Laws. The Society shall not be responsible for statements or opinions advanced in papers or ... printed in its publications (B7.1, Para. 3).

COPYRIGHT © 2010 by The American Society of Mechanical Engineers. For authorization to photocopy material for internal or personal use under those circumstances not falling within the fair use provisions of the Copyright Act, contact the Copyright Clearance Center (CCC), 222 Rosewood Drive, Danvers, MA 01923, tel: 978-750-8400, www.copyright.com. Request for special permission or bulk copying should be addressed to Reprints/Permission Department.

Canadian Goods & Services Tax Registration #126148048

Downloaded 05 Feb 2011 to 141.219.44.39. Redistribution subject to ASME license or copyright; see http://www.asme.org/terms/Terms_Use.cfm

The ASME Journal of Heat Transfer is abstracted and indexed in the following:

Applied Science and Technology Index, Chemical Abstracts, Chemical Engineering and Biotechnology Abstracts (Electronic equivalent of Process and Chemical Engineering), Civil Engineering Abstracts, Compendex (The electronic equivalent of Engineering Index), Corrosion Abstracts, Current Contents, E & P Health, Safety, and Environment, Ei EncompassLit, Engineered Materials Abstracts, Engineering Index, Enviroline (The electronic equivalent of Environment Abstracts), Environment Abstracts, Environmental Engineering Abstracts, Environmental Science and Pollution Management, Fluidex, Fuel and Energy Abstracts, Index to Scientific Reviews, INSPEC, International Building Services Abstracts, Mechanical & Transportation Engineering Abstracts, Mechanical Engineering Abstracts, METADEX (The electronic equivalent of Metals Abstracts and Alloys Index), Petroleum Abstracts, Process and Chemical Engineering, Referativnyi Zhurnal, Science Citation Index, SciSearch (The electronic equivalent of Science Citation Index), Theoretical Chemical Engineering

Journal of Heat Transfer

Guest Editorial

Microchannels: Rapid Growth of a Nascent Technology

It gives me great pleasure in presenting this special issue of the *ASME Journal of Heat Transfer* with focus on microchannels. Although not new in the biological field, the real impetus of their use in engineering systems was provided by the pioneering work of Tuckerman and Pease [1] in the early 1980s. Interest was renewed beginning in the late 1990s with the need to remove higher heat fluxes from electronic chips. Major efforts on microscale transport phenomena were undertaken worldwide by the advent of the twenty-first century. The birth of what is now an ASME International Conference on Nanochannels, Microchannels and Minichannels (ICNMM) in June 2003 provided a forum for interdisciplinary activities in this field. The promise of microchannels in future technologies, as highlighted in an editorial "Microchannels—Short History and Bright Future" by Kandlikar [2], is a result of the convergence of different application interests. Today, within a span of less than a decade, there are over four conferences held every year that focus on microchannels, and many sessions are devoted to this topic in any general heat transfer conference. This special issue is largely a collection of papers presented at a recent ICNMM09 conference held in Darmstadt, Germany.

From an engineering perspective, transport processes in microchannels are of importance in a number of practical applications. Single-phase flow of gases in microchannels has opened up a new dimension where rarefaction effects begin to become important at relatively high pressures. Coupling fluid flow in microchannels with heat transfer to obtain accurate solutions, while avoiding the rigor of molecular dynamic simulation poses a number of challenges. Microchannels present the first step in the journey from continuum mechanics to discrete molecular simulations.

Although liquid flows in microchannels are not affected from a continuum flow standpoint, many of the empirical correlations, such as entrance loss coefficients, need to be reevaluated. Further enhancement in heat transfer performance in single-phase liquid systems, while keeping pressure drop low, is still an active area of research [3]. As the earlier concerns on instabilities have been addressed by incorporating flow restrictors and artificial nucleation sites, flow boiling heat transfer in microchannels is facing new challenges with its lower than expected heat transfer coefficients and CHF as reported in the literature [4–8].

One of the issues still being discussed in this field relates to providing a broader definition for microchannels in engineering applications. Contrarily, defining microchannels explicitly based on the respective underlying phenomena, wherein the microscale effects start to become relevant for each process, will lead to separate classification schemes for gas flows, liquid flows and two-phase flows. Further, if we adopt such a scheme, the distinction among microchannels, minichannels and conventional channels will be dependent on the fluid, operating pressure, temperature, flow rate, etc. Two-phase flows provide additional challenges due to the presence of both gas and liquid phases, different mass fractions and void fractions, different heat fluxes and different flow patterns. One would expect a single nucleating bubble to be affected quite differently than, say, vapor under slip flow conditions in the core of a liquid annulus flowing in a channel. As an example, the confinement parameter was defined by Kew and Cornwell [9] to capture the effect of departing bubble size in relation to the channel diameter. Recently, Fogg and Goodson [10] extended this concept to include the dependence of bubble size on surface tension, buoyancy and drag forces, and the bubble growth rate expressed as a function of wall superheat. Although the confinement parameter is very valuable in understanding the bubble growth and in modeling its effect on the flow characteristics, it may not be suitable as a general channel classification scheme. A more generic classification scheme is therefore desirable to recognize a microscale system.

Among the proposed classifications, the earlier criteria in 2000 by Mehendale et al. [11] provided a simple dimension-based scheme. Mehendale et al. state in their paper that "we will arbitrarily adopt the following scheme for consistency and ease in understanding." According to their criteria, channels below 100 μm are called microchannels, channels in the 100 μm to 1 mm range are called meso-channels, in the 1–6 mm range are called compact passages, and above 6 mm are called conventional channels.

In a short span of six years, we saw an emergence of many research papers that focused on microscale effects on different transport processes. Heat exchangers with channel diameters greater than 3 mm are rarely classified as compact heat exchangers. At the same time, in addition to studying single phase and two phase flows in passages of a few hundred micrometers, manufacturing techniques and flow behavior in nanochannels were also being investigated [12]. A general classification scheme was thus warranted to address some of these emerging applications.

The classification by Kandlikar and Grande [13] is based on the microscale effects seen in several different applications. In the case of gas flow, the mean free path is used as a reference dimension, while in case of two-phase flow, the deviation from a straight-line relationship between mass fraction and void fraction for channels below 200–250 μm reported by Kawahara et al. [14] is used. The general classification scheme also provides a link to nanoscale phenomena by proposing transition boundaries between nanochannels and microchannels. In reality, the classification scheme provides mere guidelines, and is not intended to automatically define a set of analytical or empirical tools for a given problem. Under this scheme, conventional channels are greater than 3 mm diameter, minichannels cover the range 3 mm to 200 μm, microchannels cover a range from 10 μm to 200 μm, transitional microchannels cover 10 μm to 1 μm, transitional nanochannels cover 1 μm to 0.1 μm, and nanochannels cover the region below 0.1 μm. A recent evaluation of some of these criteria by Cheng et al. [15] shows that the 3 mm threshold for minichannel classification is in line with the microscale effects seen for water and some other refrigerants during flow boiling as well. The collection of papers presented in this volume mainly cover the microchannel range, from 10 μm to 200 μm, although some papers that deal with microscale effects in the minichannel range are also included.

The papers presented in this special isue provide a snapshot of the current state of microchannel research in various applications. A number of papers in this volume were presented at the Sixth International Conferences on Nanochannels, Microchannels and Minichannels held in Darmstadt, Germany in June 2008. The topics covered include single-phase gas flow, condensation, flow boiling studies in plain and enhanced microchannels, numerical and analytical modeling of single-phase gas flow and flow boiling processes, and application in high heat flux removal systems. It is also becoming clear that the interaction between microscale and nanoscale phenomena is of great importance as the local transport processes are governed by smaller scale processes. The interaction between nanoscale processes at the wall (nanostructures) as well as local modification of the transport processes (nanoparticles) are expected to yield valuable insights in developing new technologies in the future.

Special thanks to all the authors for their valuable contributions and to the reviewers who have provided in-depth reviews that helped the authors in elevating the quality of their papers. I am also very thankful to the Editor-in-Chief, Dr. Yogesh Jaluria for providing this forum to address the research issues in this emerging field. Out of the total of thirteen papers, three papers were submitted directly to the *Journal of Heat Transfer*. I am thankful to Roger Schmidt, W. Q. Tao and Jayanthi Murthi for handling the review of these three papers as Associate Editors. The assistance provided by Shefali Patel in organizing this special volume is sincerely appreciated. I would like to thank Peter Stephan at Technische Universität of Darmstadt, Darmstadt, Germany for co-chairing and hosting the ASME ICNMM08 conference.

Satish G. Kandlikar
ASME Fellow
Mechanical Engineering Department,
Rochester Institute of Technology,
Rochester, NY

References

[1] Tuckerman, D. B., and Pease, R. F. W., 1981, "High Performance Heat Sink for VLSI," IEEE Electron Device Lett., EDL-2, **5**, pp. 126–129.

[2] Kandlikar, S. G., 2002, "Microchannels—Short History and Bright Future," Heat Transfer Eng., **24**, pp. 1–2.

[3] Steinke, M. E., and Kandlikar, S. G., 2004, "Review of Single-Phase Heat Transfer Enhancement Techniques for Application in Microchannels, Minichannels and Microdevices," International Journal of Heat and Technology, **22**(2), pp. 3–11.

[4] Kandlikar, S. G., 2002, "Fundamental Issues Related to Flow Boiling in Minichannels and Microchannels," Exp. Therm. Fluid Sci., **26**(2–4), pp. 389–407.

[5] Kandlikar, S. G., Kuan, W. K., Willistein, D. A., and Borrelli, J., 2006, "Stabilization of Flow Boiling in Microchannels Using Pressure Drop Elements and Fabricated Nucleation Sites," ASME J. Heat Transfer, **128**(4), pp. 389–396.

[6] Kuo, C. J., and Peels, Y., 2008, "Flow Boiling Instabilities in Microchannels and Means for Mitigation by Reentrant Cavities," ASME J. Heat Transfer, **130**, p. 072402.

[7] Kuo, C. J., and Peels, Y., 2008, "Critical Heat Flux of Water at Subatmosheric Pressures in Microchannels," ASME J. Heat Transfer, **130**, p. 072403.

[8] Wojtan, L., Revellin, R., and Thome, J. R., 2006, "Investigation of Saturated Critical Heat Flux in a Single, Uniformly Heated Microchannel," Exp. Therm. Fluid Sci., **30**(8), pp. 765–774.

[9] Kew, P., and Cornwell, K., 1997, "Correlations for Prediction of Boiling Heat Transfer in Small Diameter Channels," Appl. Therm. Eng., **17**, pp. 705–715.

[10] Fogg, D. W., and Goodson, K. E., 2009, "Bubble-Induced Water Hammer and Cavitation in Microchannel Flow Boiling," ASME J. Heat Transfer, **131**, p. 121006.

[11] Mehendale, S. S., Jacobi, A. M., and Shah, R. K., 2000, "Fluid Flow and Heat Transfer at Micro- and Meso-Scales with Application to Heat Exchanger Design," Appl. Mech. Rev., **53**, pp. 175–193.

[12] Perry, J. L., and Kandlikar, S. G., 2005, "Review of Fabrication of Nanochannels for Single Phase Liquid Flow," Microfluid. Nanofluid., **2**(3), pp. 185–193.

[13] Kandlikar, S. G., and Grande, W. J., 2003, "Evolution of Microchannel Flow Passages—Thermohydraulic Performance and Fabrication Technology," Heat Transfer Eng., **24**(1), pp. 3–17.

[14] Kawahara, A., Sadatomi, M., Kawaji, M., Okayama, K., and Chung, P.M.-Y., 2005, "Assessment of Void Fraction Correlations for Adiabatic Two-Phase Flows in Microchannels," ASME Paper No. ICMM2005-75031.

[15] Cheng, L., Ribatski, G., and Thome, J. R., 2008, "Two-Phase Flow Patterns and Flow Pattern Maps: Fundamentals and Applications," Appl. Mech. Rev., **61**(5), p. 050802.

Effects of Axial Corrugated Roughness on Low Reynolds Number Slip Flow and Continuum Flow in Microtubes

Zhipeng Duan
Department of Mechanical and Mechatronics Engineering,
University of Waterloo,
Waterloo, ON, N2L 3G1, Canada

Y. S. Muzychka
Faculty of Engineering and Applied Science,
Memorial University of Newfoundland,
St. John's, NL, A1B 3X5, Canada

The effect of axial corrugated surface roughness on fully developed laminar flow in microtubes is investigated. The radius of a microtube varies with the axial distance due to corrugated roughness. The Stokes equation is solved using a perturbation method with slip at the boundary. Analytical models are developed to predict friction factor and pressure drop in corrugated rough microtubes for continuum flow and slip flow. The developed model proposes an explanation on the observed phenomenon that some experimental pressure drop results for microchannel flow have shown a significant increase due to roughness. The developed model for slip flow illustrates the coupled effects between velocity slip and small corrugated roughness. Compressibility effect has also been examined and simple models are proposed to predict the pressure distribution and mass flow rate for slip flow in corrugated rough microtubes. [DOI: 10.1115/1.3211854]

Keywords: corrugations, roughness, perturbation, slip flow, microtubes

1 Introduction

Fluid flow in microchannels has emerged as an important research area. This has been motivated by their various applications such as medical and biomedical use, computer chips, and chemical separations. The advent of micro-electro-mechanical systems (MEMSs) has opened up a new research area where noncontinuum and surface roughness characteristics are important.

Microchannels are a fundamental part of microfluidic systems. Understanding the flow characteristics of microchannel flows is very important in determining pressure drop, heat transfer, and transport properties of the flow. Microchannels can be defined as channels whose characteristic dimensions are from 1 μm to 1 mm. Above 1 mm the flow exhibits behavior, which is the same as continuum flows.

Some researchers have reported on deviations between microscale flow behavior and conventional macroscale flow theory. For laminar fully developed flow through microchannels, researchers have observed significant increases in the pressure drop from the macroscale flow theoretical values, as data appear up to 50% above the theoretical values [1–18]. Some publications indicate that flows on the microscale are different from that on macroscale. Several theories and models have been proposed to explain the observed deviations, but an indisputable conclusion has not yet been reached.

In macroscale flow theory, the friction factor is independent of relative roughness in the laminar region. However, some researchers proposed that the friction factor depends on the relative roughness of the walls of microchannels in the laminar region and as such the relative roughness cannot be neglected [1,10–12,15–26].

Due to limitations in current micromachining technology, the walls of microfabricated microchannels typically exhibit some degree of roughness. Roughness plays an increasingly important role in microchannel flows, but it is difficult to characterize its effects theoretically or numerically. It can be characterized using a stylus-type surface profilometer, optical measurement, scanning electron microscope (SEM), atomic force microscope (AFM), or scanning tunneling microscope (STM). Thus, there is a need for a better understanding of the effects of wall roughness on fluid characteristics in microchannels.

Mala and Li [13] measured the friction factor of water in microtubes with diameters ranging from 50 μm to 254 μm. They proposed a roughness-viscosity model to explain the increase in the friction factor.

Kleinstreuer and Koo [27] proposed a numerical model to consider the effect of wall roughness on liquid flow in microchannels. They modeled roughness by considering a porous medium layer (PML) near the wall. The porous medium layer approach is able to mimic some details of the velocity profiles and of the effect of the roughness height.

Wang et al. [28] numerically investigated the friction factors of single phase continuum flow in microchannels with various roughness elements (rectangular, triangular, and elliptical). The two-dimensional numerical solution shows significant influence of surface roughness including the height and spacing of the roughness elements on the Poiseuille number. The Poiseuille number increases with an increase in roughness height and decreases with an increase in the roughness spacing.

Bahrami et al. [12] developed a model to predict the pressure drop of fully developed laminar continuum flows in roughness microtubes. In this model, the wall roughness is assumed to possess a Gaussian isotropic distribution.

Priezjev and Troian [29] investigated the influence of periodic surface roughness on the slip behavior of a Newtonian liquid in steady planar shear. However, the physics of liquid slip is complicated and not completely understood.

Rarefaction effects must be considered in gases in which the molecular mean free path is comparable to the channel's characteristic dimension. The continuum assumption is no longer valid and the gas exhibits noncontinuum effects such as velocity slip and temperature jump at the channel walls. Traditional examples of noncontinuum gas flows in channels include low-density applications such as high-altitude aircraft or vacuum technology. The recent development of microscale fluid systems has motivated great interest in this field of study. There is strong evidence to support the use of Navier–Stokes and energy equations to model

---

Contributed by the Heat Transfer Division of ASME for publication in the JOURNAL OF HEAT TRANSFER. Manuscript received June 2, 2008; final manuscript received January 14, 2009; published online February 17, 2010. Review conducted by Satish G. Kandlikar.

the slip flow problem, while the boundary conditions are modified by including velocity slip and temperature jump at the channel walls.

The Knudsen number (Kn) relates the molecular mean free path of gas to a characteristic dimension of the duct. Knudsen numbers are very small for continuum flows. However, for microscale gas flows where the gas mean free path becomes comparable with the characteristic dimension of the duct, the Knudsen number may be greater than 10^{-3}. Microchannels with characteristic lengths on the order of 100 μm would produce flows inside the slip regime for gas with a typical mean free path of approximately 100 nm at standard conditions. The slip flow regime to be studied here is classified as $10^{-3} < \mathrm{Kn} < 10^{-1}$, and the flow is assumed to be isothermal. Since the pressure drop is a result of viscous effects and not the free expansion of the gas, the isothermal assumption should be reasonable.

Li et al. [30] studied the effects of surface roughness on the slip flow in long microtubes. The rough surface was represented as a porous film based on the Brinkman-extended Darcy model, and the core region of the flow utilized velocity slip to model the rarefaction effects. By using the appropriate matching conditions at the gas/porous interface (velocity slip and stress continuity), the governing equation of pressure distribution was derived.

Sun and Faghri [31] investigated the effects of surface roughness on nitrogen flow in a microchannel using the direct simulation Monte Carlo method. The surface roughness was modeled by an array of rectangular modules placed on two surfaces of a parallel plate channel. The effects of relative surface roughness, roughness distribution, and gas rarefaction on flow were studied. It was found that the effect of surface roughness is more pronounced at low Knudsen numbers. The roughness distribution represented by the ratio of the roughness height to spacing of the modules has a significant effect on the friction factor. The friction factor increases not only as the roughness height increases but also as the distance between the roughness modules decreases. This is consistent with the conclusions of Wang et al. [28].

The exact solutions of Hagen–Poiseuille flow can be obtained theoretically. However, when the radius of a tube varies with the axial distance, the flow cannot be characterized by Hagen–Poiseuille law. Langlois [32,33] employed the lubrication approximation to calculate the mean pressure drop. The prediction of the simple approximation method agrees well with the exact value when the tube radius varies slowly. Since Langlois' paper, some authors investigated this flow problem in tubes of slowly varying radius. Tanner and Linnett [34] extended the perturbation analysis of Blasius to predict the kinetic energy losses of viscometric capillary tubes. However, they neglected second-order viscous terms in the momentum equations. Manton [35] obtained an asymptotic series solution for the low Reynolds number flow through an axisymmetric tube whose radius varies slowly in the axial direction. However, he also neglected first and second-order viscous terms. Noticing this and the applications of this flow in biomechanics, Phan-Thien [36] developed a perturbation solution and obtained an improved solution up to the second-order $O(\varepsilon^2)$ for the mean pressure gradient. Vasudeviah and Balamurugan [37] tried to solve the corresponding problem for slip flow. However, their derivation and results are questionable, and will be discussed later in this paper. Wang [38] analyzed the Stokes flow between corrugated plates using a perturbation method. Chu [39] studied Stokes flow between corrugated plates in the slip flow regime. Later, Chu [40] investigated the small Knudsen number flow in a tube with corrugated wall by the perturbation method. In view of the importance of this flow problem, we develop a new perturbation solution for slip flow through axially corrugated rough microtubes.

The no-slip boundary conditions are not valid in the slip flow regime $(0.001 \leq \mathrm{Kn} \leq 0.1)$, and a kinetic boundary layer on the order of one mean free path [41,42], known as the ordinary Knudsen layer, starts to become dominant between the bulk of the fluid and the wall surface. The flow in the Knudsen layer cannot be analyzed using the Navier–Stokes equations, and it needs special equations of Boltzmann equation. The contributions of the Knudsen layer to the velocity field are of order Kn^2. However, for $\mathrm{Kn} \leq 0.1$, the contribution of the Knudsen layer is small since the Knudsen layer covers less than 10% of the tube diameter. Thus, the Knudsen layer can be neglected by extrapolating the bulk gas flow toward the walls [41].

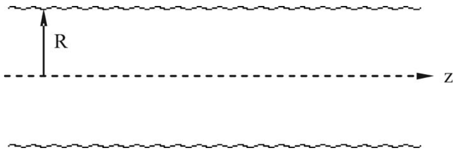

Fig. 1 An axial sinusoidal wave rough microtube

For flow past a convex body, the kinetic boundary sublayer due to curvature is present in the moments. This boundary sublayer is formed by points, which cannot be reached from the boundary along straight lines much longer than the mean free path. Sone [43] discovered that the sublayer is of order the mean free path squared divided by the radius of curvature of the boundary. Cercignani suggests there is a similar effect for concave surface. Details can be found in Refs. [43–45]. The kinetic boundary sublayer is a portion of the Knudsen layer. For $\mathrm{Kn} \leq 0.1$, the boundary sublayer covers much less than 10% of the tube diameter, and this boundary sublayer can be neglected. Using the first-order slip boundary conditions is expected to yield good approximations for $\mathrm{Kn} \leq 0.1$.

Since analytical models derived using the first-order slip boundary condition have been shown to be relatively accurate up to Knudsen numbers of approximately 0.1 [46], the first-order slip boundary condition is employed in this paper. A variety of researchers have attempted to develop second-order slip models, which can be used in the early transition regime. However, there are large variations in the second-order slip coefficient [41,46]. The lack of a universally accepted second-order slip coefficient is a major problem in extending the Navier–Stokes equations into the transition regime [46].

2 Theoretical Analysis

In this paper we examine a simple approach to modeling surface roughness in the slip flow and continuum flow $(\mathrm{Kn} \to 0)$ regime. In order to simplify the roughness problem, we can consider flow inside a microtube with a rough surface, which is approximately sinusoidal corrugation, $r' = R + R\varepsilon \sin(2\pi z'/l)$, as illustrated in Fig. 1, where R is the mean radius of the rough microtube, relative roughness $\varepsilon = b/R \ll 1$, and b and l are the amplitude and wavelength of the rough corrugated walls, respectively. It is convenient to normalize all length variables with respect to R. When the tubes are long enough $(L/D \gg 1)$ and the Reynolds number is relatively low where the inertia terms are negligible, the Stokes equation in cylindrical coordinates (r, θ, z) is [47]

$$E^4 \psi = 0 \tag{1}$$

and

$$E^2 = r \frac{\partial}{\partial r}\left(\frac{1}{r}\frac{\partial}{\partial r}\right) + \frac{\partial^2}{\partial z^2} \tag{2}$$

where ψ is the dimensionless stream function normalized by $(Q/2\pi)$.

The boundary conditions are

$$\psi = 0, \quad \frac{1}{r}\frac{\partial \psi}{\partial z} = 0 \quad \text{at} \quad r = 0 \tag{3}$$

$$\psi = 1, \quad \frac{1}{n}\frac{\partial \psi}{\partial n} = -\frac{\lambda_f}{R}\frac{2-\sigma}{\sigma}\frac{\partial}{\partial n}\left(\frac{1}{n}\frac{\partial \psi}{\partial n}\right) \quad \text{at} \quad r = 1 + \varepsilon \sin(\lambda z) \tag{4}$$

where n is the outer direction normal and λ is the wave number $(\lambda = 2\pi R/l)$. The constant σ denotes tangential momentum accommodation coefficient, which is usually between 0.87 and 1 [48]. Although the nature of the tangential momentum accommodation coefficients is still an active research problem, almost all evidence indicates that for most gas-solid interactions the coefficients are approximately 1.0. Therefore, σ may be assumed have a value of unity. It is convenient to introduce the Knudsen number

$$\text{Kn} = \frac{\lambda_f}{R} \tag{5}$$

where λ_f is the molecular mean free path. The characteristic length scale in the present analysis is defined as the microtube mean radius. The same procedure is valid even if $\sigma \neq 1$, defining a modified Knudsen number as $\text{Kn}^* = \text{Kn}(2-\sigma)/\sigma$.

Using perturbation methods, we expand ψ in terms of ε

$$\psi = \psi_0 + \varepsilon\psi_1 + \varepsilon^2\psi_2 + \cdots \tag{6}$$

for the boundary conditions (4) we can expand $\psi(1+\varepsilon \sin(\lambda z), z)$ in a Taylor series to obtain

$$\left[\psi_0 + \varepsilon\left(\psi_1 + \sin \lambda z \frac{\partial \psi_0}{\partial r}\right) + \varepsilon^2\left(\psi_2 + \sin \lambda z \frac{\partial \psi_1}{\partial r} + \frac{1}{2}\sin^2 \lambda z \frac{\partial^2 \psi_0}{\partial r^2}\right)\right]_{r=1} + O(\varepsilon^3) = 1 \tag{7}$$

and

$$\begin{aligned} \left.\frac{\partial \psi}{\partial n}\right|_{r=1+\varepsilon \sin \lambda z} &= \frac{\nabla\psi \cdot \nabla[r - 1 - \varepsilon \sin \lambda z]}{|\nabla[r - 1 - \varepsilon \sin \lambda z]|} \\ &= \left[\frac{\partial \psi}{\partial r} - \varepsilon\lambda \cos \lambda z \frac{\partial \psi}{\partial z} - \frac{\varepsilon^2\lambda^2}{2}\cos^2 \lambda z \frac{\partial \psi}{\partial r}\right]_{r=1+\varepsilon \sin \lambda z} + O(\varepsilon^3) \\ &= \left[\frac{\partial \psi_0}{\partial r} + \varepsilon\left(\frac{\partial \psi_1}{\partial r} + \sin \lambda z \frac{\partial^2 \psi_0}{\partial r^2} - \lambda \cos \lambda z \frac{\partial \psi_0}{\partial z}\right)\right. \\ &\quad + \varepsilon^2\left(\frac{\partial \psi_2}{\partial r} + \sin \lambda z \frac{\partial^2 \psi_1}{\partial r^2} - \lambda \cos \lambda z \frac{\partial \psi_1}{\partial z}\right. \\ &\quad + \frac{1}{2}\sin^2 \lambda z \frac{\partial^3 \psi_0}{\partial r^3} - \frac{\lambda}{2}\sin 2\lambda z \frac{\partial^2 \psi_0}{\partial r\, \partial z} \\ &\quad \left.\left. - \frac{\lambda^2}{2}\cos^2 \lambda z \frac{\partial \psi_0}{\partial r}\right)\right]_{r=1} + O(\varepsilon^3) \end{aligned} \tag{8}$$

and

$$\begin{aligned} \left.\frac{\partial^2 \psi}{\partial n^2}\right|_{r=1+\varepsilon \sin \lambda z} &= \left[\frac{\partial^2 \psi_0}{\partial r^2} + \varepsilon\left(\frac{\partial^2 \psi_1}{\partial r^2} + \sin \lambda z \frac{\partial^3 \psi_0}{\partial r^3}\right.\right. \\ &\quad \left. - 2\lambda \cos \lambda z \frac{\partial^2 \psi_0}{\partial r\, \partial z}\right) + \varepsilon^2\left(\frac{\partial^2 \psi_2}{\partial r^2} + \sin \lambda z \frac{\partial^3 \psi_1}{\partial r^3}\right. \\ &\quad - 2\lambda \cos \lambda z \frac{\partial^2 \psi_1}{\partial r\, \partial z} + \frac{1}{2}\sin^2 \lambda z \frac{\partial^4 \psi_0}{\partial r^4} \\ &\quad - \lambda \sin 2\lambda z \frac{\partial^3 \psi_0}{\partial r^2\, \partial z} + \lambda^2 \cos^2 \lambda z \frac{\partial^2 \psi_0}{\partial z^2} \\ &\quad \left.\left. - \lambda^2 \cos^2 \lambda z \frac{\partial^2 \psi_0}{\partial r^2} - \frac{\lambda^3}{2}\sin 2\lambda z \frac{\partial \psi_0}{\partial z}\right)\right]_{r=1} + O(\varepsilon^3) \end{aligned} \tag{9}$$

The solution of ψ_0 is governed by

$$E^4\psi_0 = 0 \tag{10}$$

$$\psi_0 = 0, \quad \frac{1}{r}\frac{\partial \psi_0}{\partial z} = 0 \quad \text{at} \quad r = 0 \tag{11}$$

$$\psi_0 = 1, \quad (1 - \text{Kn}^*)\frac{\partial \psi_0}{\partial r} + \text{Kn}^*\frac{\partial^2 \psi_0}{\partial r^2} = 0 \quad \text{at} \quad r = 1 \tag{12}$$

The zeroth-order (ε^0) solution is the usual slip Poiseuille flow

$$\psi_0 = \frac{2(1 + 2\ \text{Kn}^*)r^2 - r^4}{1 + 4\ \text{Kn}^*} \tag{13}$$

The ε^1-solution is governed by

$$E^4\psi_1 = 0 \tag{14}$$

$$\psi_1 = 0, \quad \frac{1}{r}\frac{\partial \psi_1}{\partial z} = 0 \quad \text{at} \quad r = 0 \tag{15}$$

$$\psi_1 = -\sin \lambda z \frac{\partial \psi_0}{\partial r} = -\frac{8\ \text{Kn}^*}{1 + 4\ \text{Kn}^*}\sin \lambda z \quad \text{at} \quad r = 1 \tag{16}$$

$$\begin{aligned} (1 - \text{Kn}^*)\frac{\partial \psi_1}{\partial r} + \text{Kn}^*\frac{\partial^2 \psi_1}{\partial r^2} &= -\sin \lambda z \frac{\partial^2 \psi_0}{\partial r^2} + \lambda \cos \lambda z \frac{\partial \psi_0}{\partial z} \\ &\quad - \text{Kn}^*\left(\sin \lambda z \frac{\partial^3 \psi_0}{\partial r^3} - 2\lambda \cos \lambda z \frac{\partial^2 \psi_0}{\partial r\, \partial z}\right) \\ &= \frac{8(1 + 2\ \text{Kn}^*)}{1 + 4\ \text{Kn}^*}\sin \lambda z \quad \text{at} \quad r = 1 \end{aligned} \tag{17}$$

According to the boundary conditions, the ψ_1 is in the form

$$\psi_1(r,z) = \phi_1(r)\sin \lambda z \tag{18}$$

where

$$(D^2 - \lambda^2)^2\phi_1 = 0, \quad D^2 \equiv r\frac{d}{dr}\left(\frac{1}{r}\frac{d}{dr}\right) \tag{19}$$

The solution of ϕ_1 is

$$\phi_1(r) = C_1 r I_1(\lambda r) + C_2 r^2 I_0(\lambda r) + B_1 r K_1(\lambda r) + B_2 r^2 K_0(\lambda r) \tag{20}$$

where $I_\nu(x)$ and $K_\nu(x)$ are the modified Bessel functions of the first and second kind, respectively, of order ν. Due to the boundedness of the velocity field, $B_1 = B_2 = 0$. Therefore,

$$\psi_1 = [C_1 r I_1(\lambda r) + C_2 r^2 I_0(\lambda r)]\sin \lambda z \tag{21}$$

Applying boundary conditions (16) and (17)

$$C_1 I_1(\lambda) + C_2 I_0(\lambda) = -\frac{8\ \text{Kn}^*}{1 + 4\ \text{Kn}^*} \tag{22}$$

$$\begin{aligned} C_1[\lambda I_0(\lambda) + \lambda^2\ \text{Kn}^*\ I_1(\lambda)] + C_2[(2 + \lambda^2\ \text{Kn}^*)I_0(\lambda) + \lambda(1 \\ + 2\ \text{Kn}^*)I_1(\lambda)] = \frac{8(1 + 2\ \text{Kn}^*)}{1 + 4\ \text{Kn}^*} \end{aligned} \tag{23}$$

Solving Eqs. (22) and (23), we have

$$C_1 = -\frac{8}{1+4\ \mathrm{Kn}^*} \times \frac{(1+4\ \mathrm{Kn}^* + \lambda^2\ \mathrm{Kn}^{*2})I_0(\lambda) + \lambda\ \mathrm{Kn}^*(1+2\ \mathrm{Kn}^*)I_1(\lambda)}{\lambda[I_1^2(\lambda) - I_0(\lambda)I_2(\lambda)] + 2\lambda\ \mathrm{Kn}^*\ I_1^2(\lambda)} \tag{24}$$

$$C_2 = \frac{8}{1+4\ \mathrm{Kn}^*}\frac{\lambda\ \mathrm{Kn}^* I_0(\lambda) + (1+2\ \mathrm{Kn}^* + \lambda^2\ \mathrm{Kn}^{*2})I_1(\lambda)}{\lambda[I_1^2(\lambda) - I_0(\lambda)I_2(\lambda)] + 2\lambda\ \mathrm{Kn}^*\ I_1^2(\lambda)} \tag{25}$$

It is seen that the first-order solution is periodic in z and cannot be related to a mean pressure gradient along z.

Next, the ε^2-solution is governed by

$$E^4\psi_2 = 0 \tag{26}$$

$$\psi_2 = 0, \quad \frac{1}{r}\frac{\partial\psi_2}{\partial z} = 0 \quad \text{at} \quad r=0 \tag{27}$$

$$\begin{aligned}\psi_2 &= -\sin\lambda z\frac{\partial\psi_1}{\partial r} - \frac{1}{2}\sin^2\lambda z\frac{\partial^2\psi_0}{\partial r^2}\\ &= \left[-C_1\lambda I_0(\lambda) - C_2(2I_0(\lambda) + \lambda I_1(\lambda)) + \frac{4-4\ \mathrm{Kn}^*}{1+4\ \mathrm{Kn}^*}\right]\\ &\quad\times\left(\frac{1-\cos(2\lambda z)}{2}\right) \quad \text{at} \quad r=1\end{aligned} \tag{28}$$

$$\begin{aligned}&(1-\mathrm{Kn}^*)\frac{\partial\psi_2}{\partial r} + \mathrm{Kn}^*\frac{\partial^2\psi_2}{\partial r^2}\\ &= -\sin\lambda z\frac{\partial^2\psi_1}{\partial r^2} + \lambda\cos\lambda z\frac{\partial\psi_1}{\partial z} - \frac{1}{2}\sin^2\lambda z\frac{\partial^3\psi_0}{\partial r^3}\\ &+ \frac{1}{2}\lambda\sin 2\lambda z\frac{\partial^2\psi_0}{\partial r\,\partial z} + \frac{1}{2}\lambda^2\cos^2\lambda z\frac{\partial\psi_0}{\partial r} - \mathrm{Kn}^*\left(\sin\lambda z\frac{\partial^2\psi_0}{\partial r^3}\right.\\ &- 2\lambda\cos\lambda z\frac{\partial^2\psi_1}{\partial r\,\partial z} + \frac{1}{2}\sin^2\lambda z\frac{\partial^4\psi_0}{\partial r^4} - \lambda\sin 2\lambda z\frac{\partial^3\psi_0}{\partial r^2\,\partial z}\\ &\left.+ \lambda^2\cos^2\lambda z\frac{\partial^2\psi_0}{\partial z^2} - \lambda^2\cos^2\lambda z\frac{\partial^2\psi_0}{\partial r^2} - \frac{\lambda^3}{2}\sin 2\lambda z\frac{\partial\psi_0}{\partial z}\right)\\ &= -\frac{1}{2}[(C_1\lambda + 2C_2 - C_1\lambda^3\ \mathrm{Kn}^* + C_2\lambda^2\ \mathrm{Kn}^*)I_0(\lambda) + (3C_2\lambda\\ &+ C_1\lambda^2\ \mathrm{Kn}^* + 2C_2\lambda\ \mathrm{Kn}^* - C_2\lambda^3\ \mathrm{Kn}^*)I_1(\lambda)]\\ &+ \frac{6(1+\mathrm{Kn}^*) - 2\lambda^2\ \mathrm{Kn}^* + 4\lambda^2\ \mathrm{Kn}^{*2}}{1+4\ \mathrm{Kn}^*} + \cdots\\ &\times(\cos(2\lambda z)) \quad \text{at} \quad r=1\end{aligned} \tag{29}$$

The appropriate solution is in the form

$$\psi_2(r,z) = \psi_{2a}(r) + \text{periodic solution} = \psi_{2a}(r) + \cdots \times (\cos(2\lambda z)) \tag{30}$$

It is seen that the second-order solution may cause a mean pressure gradient along z. Since periodic solution does not contribute to the mean pressure gradient, only ψ_{2a} needs to be determined. The ψ_{2a} solution is governed by

$$E^4\psi_{2a} = 0 \tag{31}$$

$$\psi_{2a} = 0, \quad \frac{1}{r}\frac{\partial\psi_{2a}}{\partial z} = 0 \quad \text{at} \quad r=0 \tag{32}$$

$$\psi_{2a} = \frac{1}{2}\left[-C_1\lambda I_0(\lambda) - C_2(2I_0(\lambda) + \lambda I_1(\lambda)) + \frac{4-4\ \mathrm{Kn}^*}{1+4\ \mathrm{Kn}^*}\right] \quad \text{at} \quad r=1 \tag{33}$$

$$\begin{aligned}&(1-\mathrm{Kn}^*)\frac{\partial\psi_{2a}}{\partial r} + \mathrm{Kn}^*\frac{\partial^2\psi_{2a}}{\partial r^2}\\ &= -\frac{1}{2}[(C_1\lambda + 2C_2 - C_1\lambda^3 Kn^* + C_2\lambda^2\ \mathrm{Kn}^*)I_0(\lambda) + (3C_2\lambda\\ &+ C_1\lambda^2\ \mathrm{Kn}^* + 2C_2\lambda\ \mathrm{Kn}^* - C_2\lambda^3\ \mathrm{Kn}^*)I_1(\lambda)]\\ &+ \frac{6(1+\mathrm{Kn}^*) - 2\lambda^2\ \mathrm{Kn}^* + 4\lambda^2\ \mathrm{Kn}^{*2}}{1+4\ \mathrm{Kn}^*} \quad \text{at} \quad r=1\end{aligned} \tag{34}$$

The solution for ψ_{2a} should be of the form

$$\psi_{2a} = C_3r^2 - C_4r^4 \tag{35}$$

In terms of boundary conditions (33) and (34), we obtain

$$C_3 = \frac{1}{2}\left[-C_1\lambda I_0(\lambda) - C_2(2I_0(\lambda) + \lambda I_1(\lambda)) + \frac{4-4\ \mathrm{Kn}^*}{1+4\ \mathrm{Kn}^*}\right] + C_4 \tag{36}$$

$$\begin{aligned}C_4 &= -\frac{1}{4(1+4\ \mathrm{Kn}^*)}[(C_1\lambda + 2C_2 + C_1\lambda^3\ \mathrm{Kn}^* - C_2\lambda^2\ \mathrm{Kn}^*)I_0(\lambda)\\ &\quad - (C_2\lambda + C_1\lambda^2\ \mathrm{Kn}^* + 2C_2\lambda\ \mathrm{Kn}^* - C_2\lambda^3\ \mathrm{Kn}^*)I_1(\lambda)]\\ &\quad - \frac{1+5\ \mathrm{Kn}^* - \lambda^2\ \mathrm{Kn}^* + 2\lambda^2\ \mathrm{Kn}^{*2}}{(1+4\ \mathrm{Kn}^*)^2}\\ &= \frac{1}{(1+4\ \mathrm{Kn}^*)^2}\left[-1 - 5\ \mathrm{Kn}^* + \lambda^2\ \mathrm{Kn}^* - 2\lambda^2\ \mathrm{Kn}^{*2}\right.\\ &\quad\left. - \frac{2[\alpha_1 I_0^2(\lambda) + \alpha_2 I_0(\lambda)I_1(\lambda) + \alpha_3 I_1^2(\lambda)]}{\lambda[I_1^2(\lambda) - I_0(\lambda)I_2(\lambda)] + 2\lambda\ \mathrm{Kn}^*\ I_1^2(\lambda)}\right]\end{aligned} \tag{37}$$

where

$$\alpha_1 = \lambda(-1 - 2\ \mathrm{Kn}^* - \lambda^2\ \mathrm{Kn}^* - 6\lambda^2\ \mathrm{Kn}^{*2} - \lambda^4\ \mathrm{Kn}^{*3}) \tag{38}$$

$$\alpha_2 = 2 + 4\ \mathrm{Kn}^* - 2\lambda^2\ \mathrm{Kn}^* - 2\lambda^4\ \mathrm{Kn}^{*3} \tag{39}$$

$$\alpha_3 = \lambda(-1 - 4\ \mathrm{Kn}^* - 4\ \mathrm{Kn}^{*2} + \lambda^2\ \mathrm{Kn}^* + 2\lambda^2\ \mathrm{Kn}^{*2} + \lambda^4\ \mathrm{Kn}^{*3}) \tag{40}$$

The total flow rate is given by

$$\begin{aligned}Q &= \frac{2\pi R^4 dp/dz'}{\mu}\frac{l}{R}\frac{1}{\int_0^{l/R}\frac{1}{r}\frac{\partial}{\partial r}(E^2\psi)dz}\\ &= -\frac{\pi R^4 dp/dz'}{8\mu}\frac{1+4\ \mathrm{Kn}^*}{1+B\varepsilon^2 + O(\varepsilon^4)}\end{aligned} \tag{41}$$

where

$$B = (1+4\ \mathrm{Kn}^*)C_4 \tag{42}$$

B is a function of wave number λ and the modified Knudsen number Kn^*. Figure 2 shows the effect of λ and Kn^* on $B(\lambda,\mathrm{Kn}^*)$. The B values increase with an increase in λ and Kn^*.

It is seen that the periodic solution cannot be related to the mean pressure gradient along z as its contribution to the integral is zero. Only ψ_0 and ψ_{2a} contribute to the mean pressure gradient

$$\frac{Q}{Q_{\mathrm{sm}}} = \frac{1+4\ \mathrm{Kn}^*}{1+B\varepsilon^2 + O(\varepsilon^4)} \tag{43}$$

where Q_{sm} is the flow rate for continuum flow in smooth microtubes. The flow rate decreases with an increase in λ. Since B is

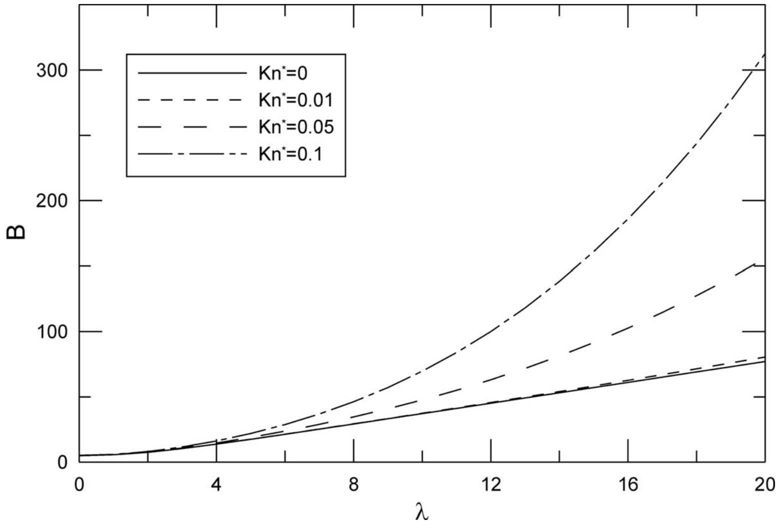

Fig. 2 $B(\lambda, \text{Kn}^*)$ **as a function of** λ **and** Kn^*

always positive indicating a decrease in the flow rate with wall roughness.

Setting $\varepsilon=0$ in Eq. (43), we obtain the corresponding expression for the flow rate in smooth microtubes as $Q/Q_{\text{sm}}=1+4\ \text{Kn}^*$. However, Vasudeviah and Balamurugan [37] gave the following misleading expression:

$$\frac{Q}{Q_{\text{sm}}}=\frac{1+5\ \text{Kn}^*}{1+\text{Kn}^*} \tag{44}$$

After integrating Eq. (41), the pressure drop along the length of the pipe (L) may be determined to be

$$\Delta p=\frac{8\mu LQ}{\pi R^4}\frac{1+B\varepsilon^2+O(\varepsilon^4)}{1+4\ \text{Kn}^*} \tag{45}$$

It can be also shown that the effect of wall roughness on the pressure drop is given by the following equation:

$$\Delta p^*=\frac{\Delta p}{\Delta p_{\text{sm}}}=\frac{1+B\varepsilon^2+O(\varepsilon^4)}{1+4\ \text{Kn}^*} \tag{46}$$

where Δp_{sm} is the pressure drop for continuum flow in smooth microtubes.

The mean fiction factor Reynolds product can be obtained simply by substituting Eq. (41) into the definition of $f\ \text{Re}$.

$$f\ \text{Re}=\frac{2\left(-\frac{A}{P}\frac{dp}{dz'}\right)D_h}{\mu\overline{u}}=\frac{2\left(-\frac{A}{P}\frac{dp}{dz'}\right)D_hA}{\mu Q}=\frac{16[1+B\varepsilon^2+O(\varepsilon^4)]}{(1+4\ \text{Kn}^*)} \tag{47}$$

Figure 3 demonstrates the effect of wave number λ, relative roughness ε, and Knudsen number Kn on pressure drop of microtubes for slip flow. Velocity slip decreases pressure drop and corrugated roughness increases pressure drop. Pressure drop depends on ε, λ, and Kn, and it can be less than, equal to, or greater than unity. The coupled effects between small corrugated roughness and velocity slip suggest a possible explanation for the observed phenomenon that Chung et al. [49] and Kohl et al. [50] found that the friction factors for gas flow in microchannels can be accurately determined from conventional theory for large channels.

2.1 Continuum Flow. The density of liquids is 100–800 times that of the typical gaseous state. The molecules are closely packed and surrounded by other molecules. Since the molecules

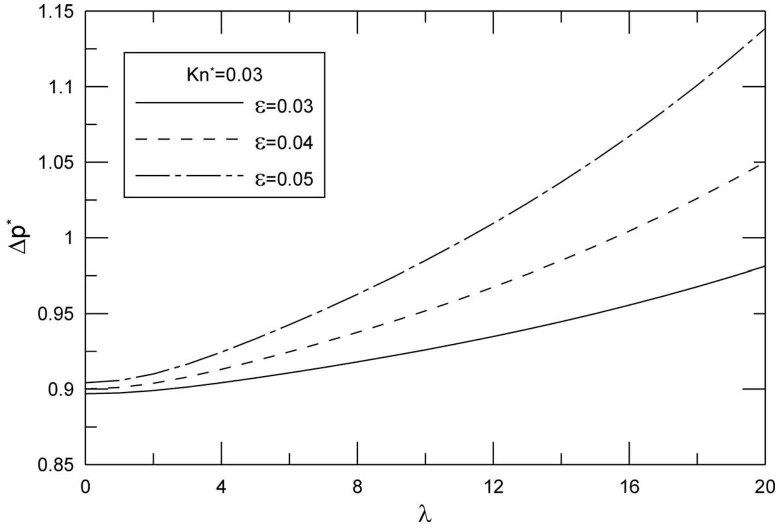

Fig. 3 Effect of relative roughness ε**, wave number** λ**, and Knudsen number Kn on pressure drop of microtubes for slip flow**

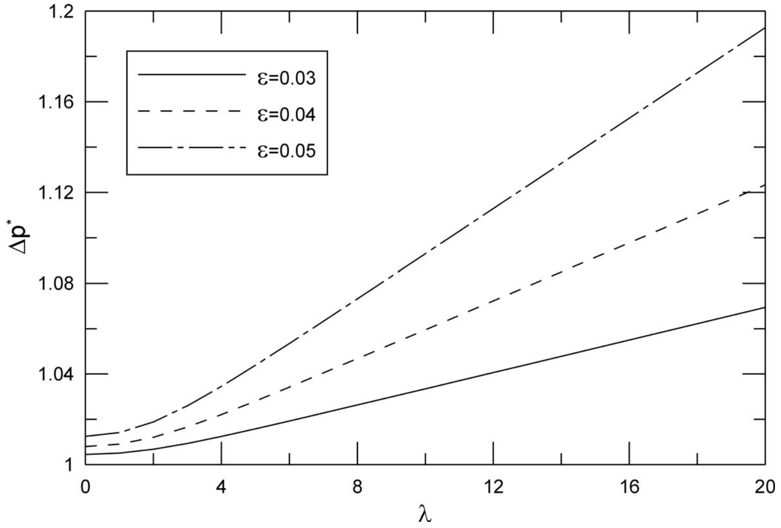

Fig. 4 Effect of relative roughness ε and wave number λ on pressure drop of microtubes for continuum flow

are continuously in collision, the concept of a mean free path is not used for liquids. The liquid particles contacting the wall must essentially be in equilibrium with the solid. For most microscale liquid flows, the Navier–Stokes equations and no-slip boundary conditions still hold. In the limit of $\mathrm{Kn}\to 0$, Eq. (42) reduces to its corresponding continuum flow solution [36]

$$B_c = -3 + \frac{4I_1^2(\lambda)}{I_1^2(\lambda) - I_0(\lambda)I_2(\lambda)} \tag{48}$$

For practical applications, a simple expression, which is valid for $\lambda \geq 3$ can be used

$$B_c = 3.92\lambda - 1.76 \tag{49}$$

The mean fiction factor Reynolds product is given by

$$f\ \mathrm{Re} = 16[1 + B_c\varepsilon^2 + O(\varepsilon^4)] \tag{50}$$

Figures 4 and 5 demonstrate the effect of wave number λ and relative roughness ε on pressure drop of microtubes for continuum flow. The pressure drop increases with an increase in λ. Since B is always positive, the pressure drop increases with wall roughness.

2.2 Compressibility Effects. Now we take account of the compressibility of the gas. The flow is assumed to be locally fully developed. The locally fully developed flow assumption means that the velocity field at any cross section is the same as that of a fully developed flow at the local density, and the wall shear stress also takes on locally fully developed values. Compressibility effects enter through the state equation and continuity equation. If the cross-sectional area slightly varies, as it is the case for a corrugated wall, the locally fully developed assumption still approximately holds since we only consider the case of $\varepsilon \ll 1$. Sun and Faghri [31] demonstrated that the locally fully developed flow model can be used to predict gas slip flow in a microchannel with low values of relative surface roughness (3–5%). For compressible flow, the mass flow rate in the microtube is given by employing the equation of state $p = \rho \Re T$

$$\dot{m} = \rho \overline{uA} = -\frac{\pi R^4}{8\mu \Re T}[1 - B\varepsilon^2 + \mathrm{O}(\varepsilon^4)]\frac{dp}{dz'}\left(p + 4\frac{2-\sigma}{\sigma}p\ \ \mathrm{Kn}\right) \tag{51}$$

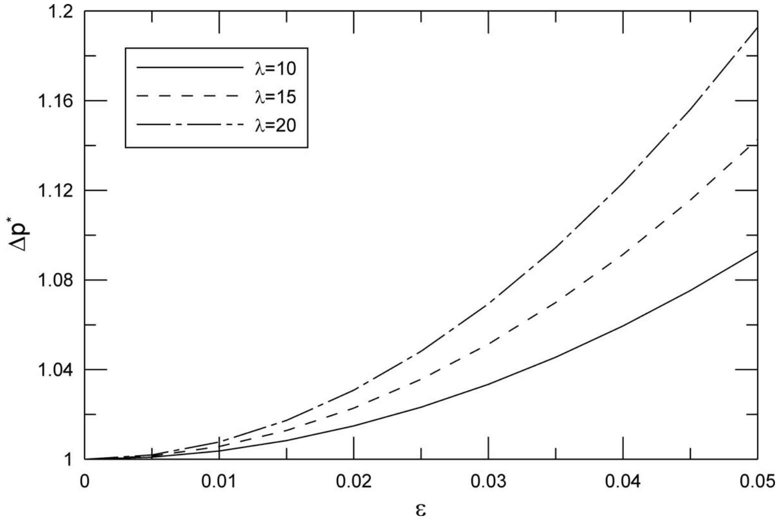

Fig. 5 Effect of relative roughness ε and wave number λ on pressure drop of microtubes for continuum flow

We can use $p\ \mathrm{Kn}=p_o\ \mathrm{Kn}_o$ since $p\ \mathrm{Kn}$ is constant for isothermal flow. Integrating Eq. (51), we obtain

$$\dot{m} = \rho\bar{u}A \cong \frac{\pi R^4 p_o^2}{16\mu\mathfrak{R}Tz'}[1-\bar{B}\varepsilon^2+\mathrm{O}(\varepsilon^4)]\left[\frac{p_i^2}{p_o^2}-\frac{p_{z'}^2}{p_o^2}+8\frac{2-\sigma}{\sigma}\mathrm{Kn}_o\left(\frac{p_i}{p_o}-\frac{p_{z'}}{p_o}\right)\right] \tag{52}$$

where $\bar{B}$ denotes the average value of $B(\lambda,\mathrm{Kn}_i^*)$ and $B(\lambda,\mathrm{Kn}_{z'}^*)$.

Letting $z'=L$ gives

$$\dot{m} = \rho\bar{u}A \cong \frac{\pi R^4 p_o^2}{16\mu\mathfrak{R}TL}[1-\bar{B}\varepsilon^2+\mathrm{O}(\varepsilon^4)]\left[\frac{p_i^2}{p_o^2}-1+8\frac{2-\sigma}{\sigma}\mathrm{Kn}_o\left(\frac{p_i}{p_o}-1\right)\right] \tag{53}$$

The continuum flow mass flow rate is given by

$$\dot{m}_c = \rho\bar{u}A = \frac{\pi R^4 p_o^2}{16\mu\mathfrak{R}TL}[1-\bar{B}\varepsilon^2+\mathrm{O}(\varepsilon^4)]\left(\frac{p_i^2}{p_o^2}-1\right) \tag{54}$$

The effect of slip may be illustrated clearly by dividing the slip flow mass flow equation (53) by the continuum mass flow equation (54)

$$\frac{\dot{m}}{\dot{m}_c} \cong 1+\frac{8\dfrac{2-\sigma}{\sigma}\mathrm{Kn}_o}{\dfrac{p_i}{p_o}+1} \tag{55}$$

It is seen that the rarefaction increases the mass flow and that the effect of rarefaction becomes more significant when the pressure ratio decreases. This could be interpreted as a decrease in the gas viscosity.

Combining Eqs. (52) and (53), we obtain the expression for pressure distribution

$$\frac{p_{z'}}{p_o} \cong -4\frac{2-\sigma}{\sigma}\mathrm{Kn}_o+\sqrt{\left(4\frac{2-\sigma}{\sigma}\mathrm{Kn}_o+\frac{p_i}{p_o}\right)^2-\left[\frac{p_i^2}{p_o^2}-1+8\frac{2-\sigma}{\sigma}\mathrm{Kn}_o\left(\frac{p_i}{p_o}-1\right)\right]\frac{z'}{L}} \tag{56}$$

The pressure distribution exhibits a nonlinear behavior due to the compressibility effect. The pressure drop required is less than that in a conventional channel. The deviations of the pressure distribution from the linear distribution decrease with an increase in Knudsen number. The nonlinearity increases as the pressure ratio increases. The effects of compressibility and rarefaction are opposite, as Karniadakis et al. [41] demonstrated. The incompressibility assumption (linear pressure distribution) is valid for a small pressure drop in the microtubes.

The deviations of the nonlinear pressure distribution from the linear distribution is given by

$$\frac{p_{z'}}{p_o}-\left[\frac{p_i}{p_o}-\left(\frac{p_i}{p_o}-1\right)\frac{z'}{L}\right] = -4\frac{2-\sigma}{\sigma}\mathrm{Kn}_o+\sqrt{\left(4\frac{2-\sigma}{\sigma}\mathrm{Kn}_o+\frac{p_i}{p_o}\right)^2-\left[\frac{p_i^2}{p_o^2}-1+8\frac{2-\sigma}{\sigma}\mathrm{Kn}_o\left(\frac{p_i}{p_o}-1\right)\right]\frac{z'}{L}}-\frac{p_i}{p_o}+\left(\frac{p_i}{p_o}-1\right)\frac{z'}{L} \tag{57}$$

Taking the derivative of Eq. (57) and setting it equal to zero, we obtain the location of maximum deviation from linearity as

$$\frac{z'}{L} = \frac{3\dfrac{p_i}{p_o}+16\dfrac{2-\sigma}{\sigma}\mathrm{Kn}_o+1}{4\left(\dfrac{p_i}{p_o}+8\dfrac{2-\sigma}{\sigma}\mathrm{Kn}_o+1\right)} \tag{58}$$

It is seen that the location of maximum deviation from linearity is between 0.5 and 0.75. The location approaches 0.5 for low pressure ratio and approaches 0.75 for high pressure ratio.

3 Summary and Conclusion

The influence of axial corrugated surface roughness on fully developed laminar flow in microtubes is studied, and models are proposed to predict friction factor and pressure drop for continuum flow and slip flow. Compressibility effect has also been examined, and simple models are proposed to predict the pressure distribution and mass flow rate for slip flow in corrugated rough microtubes.

It is observed that the normalized pressure drop, Δp^*, is a function of relative roughness ε and wave number λ for continuum flow, i.e., $\Delta p^*=F(\varepsilon,\lambda)$. The present model exhibits the influence of axial corrugated roughness. For most conventional microtubes (assuming $\varepsilon\approx 0.03-0.05$ and $\lambda=10-20$), the present model provides an explanation on the observed phenomenon that pressure drop results for continuum flow have shown an increase due to roughness.

For slip flow, Δp^* is a function of relative roughness ε, wave number λ, and Knudsen number Kn, i.e., $\Delta p^*=F_1(\varepsilon,\lambda,\mathrm{Kn})$. There exist coupled effects between velocity slip and corrugated roughness. Velocity slip decreases pressure drop and increases flow rate. Corrugated roughness increases pressure drop and decreases flow rate. These two effects can have a canceling effect in some systems.

The friction factor Reynolds product depends on the relative roughness of the walls of the microchannels also in laminar region and the relative roughness cannot be neglected for microchannels in the laminar region.

Common practice is to specify surfaces with a single parameter, average roughness as it is well established and understood. It is obvious that one parameter is not enough to describe the complete nature of a surface. The roughness spacing is another important parameter to describe surface roughness. The friction factor Reynolds product increases not only as the roughness height increases but also as the roughness spacing decreases.

The present paper extends Phan-Thien's excellent work to slip flow regime. The range of validity of the analytical models developed is $0.001\le\mathrm{Kn}\le 0.1$ (slip flow regime) and $\varepsilon\ll 1$. The developed simple models may be used by the research community to estimate roughness and velocity slip effects for the practical engineering design of microtubes.

Acknowledgment

The authors would like to express our appreciation to professors Michael Yovanovich and Richard Culham for their suggestions. The authors acknowledge the support of the Natural Sciences and Engineering Research Council of Canada (NSERC).

Nomenclature

A = flow area, m^2
b = amplitude, m
D_h = hydraulic diameter, $=4A/P$
f = Fanning friction factor, $=\tau/((1/2)\rho\overline{u}^2)$
Kn = Knudsen number, $=\lambda_f/R$
Kn* = modified Knudsen number, $=\text{Kn}(2-\sigma)/\sigma$
L = tube length, m
l = wavelength, m
$\dot{m}$ = mass flow rate, kg/s
n = outer direction normal
P = perimeter, m
p = pressure, N/m^2
Δp^* = normalized pressure drop
Q = volume flow rate, m^3/s
R = mean radius of a rough microtube, m
$\Re$ = specific gas constant, J/kg K
Re = Reynolds number, $=\overline{u}2R/\nu$
r = dimensionless radial coordinate in the cylindrical coordinate system, r'/R
r' = radial coordinate in the cylindrical coordinate system, m
T = temperature, K
u = velocity, m/s
$\overline{u}$ = average velocity, m/s
z = dimensionless coordinate in flow direction, z'/R
z' = coordinate in flow direction, m

Greek Symbols

ε = relative roughness, b/R
θ = angular coordinate in the cylindrical coordinate system, rad
λ = wave number, $=2\pi R/l$
λ_f = molecular mean free path, m
μ = dynamic viscosity, N s/m^2
ν = kinematic viscosity, m^2/s
σ = tangential momentum accommodation coefficient
τ = wall shear stress, N/m^2
ψ = dimensionless stream function, $=Q/2\pi$

Subscripts

c = continuum
i = inlet
o = outlet
sm = smooth

References

[1] Wu, P., and Little, W. A., 1983, "Measurement of Friction Factors for Flows of Gases in Very Fine Channels Used for Microminiature Joule-Thompson Refrigerators," Cryogenics, **23**, pp. 273–277.
[2] Wu, P., and Little, W. A., 1984, "Measurement of the Heat Transfer Characteristics of Gas Flow in Fine Channel Heat Exchangers Used for Microminiature Refrigerators," Cryogenics, **24**, pp. 415–420.
[3] Harley, J., Bau, H., Zemel, J. N., and Dominko, V., 1989, "Fluid Flow in Micron and Submicron Size Channels," *Proceedings of the Workshop on Micro Electro Mechanical Systems*, Salt Lake City, UT, pp. 25–28.
[4] Peng, X. F., and Peterson, G. P., 1996, "Convective Heat Transfer and Flow Friction for Water Flow in Microchannel Structures," Int. J. Heat Mass Transfer, **39**, pp. 2599–2608.
[5] Peng, X. F., Peterson, G. P., and Wang, B. X., 1994, "Frictional Flow Characteristics of Water Flowing Through Rectangular Microchannels," Exp. Heat Transfer, **7**, pp. 249–264.
[6] Wilding, P., Shoffner, M. A., and Kircka, L. J., 1994, "Manipulation and Flow of Biological Fluids in Straight Channels Micromachined in Silicon," Clin. Chem., **40**, pp. 43–47.
[7] Wu, S., Mai, J., Zohar, Y., Tai, Y. C., and Ho, C. M., 1998, "A Suspended Microchannel With Integrated Temperature Sensors for High Pressure Flow Studies," *Proceedings of the IEEE Workshop on Micro Electro Mechanical Systems*, Heidelberg, Germany, pp. 87–92.
[8] Urbanek, W., Zemel, J. N., and Bau, H., 1993, "An Investigation of the Temperature Dependence of Poiseuille Numbers in Microchannel Flow," J. Micromech. Microeng., **3**, pp. 206–209.
[9] Papautsky, I., Brazzle, J., Ameel, T. A., and Frazier, A. B., 1998, "Microchannel Fluid Behavior Using Micropolar Fluid Behavior," *Proceedings of the 1998 IEEE 11th Annual International Workshop on Micro Electro Mechanical Systems*, Heidelberg, Germany, pp. 544–549.
[10] Pfund, D., Rector, D., Shekarriz, A., Popescu, A., and Welty, J., 1998, "Pressure Drop Measurements in a Microchannel," *Proceedings of the 1998 ASME International Mechanical Engineering Congress and Exposition: DSC Micro-Electro-Mechanical Systems*, Vol. 66, pp. 193–198.
[11] Qu, W., Mala, G. M., and Li, D., 1999, "Pressure-Driven Flows in Trapezoidal Silicon Microchannels," Int. J. Heat Mass Transfer, **43**, pp. 353–364.
[12] Bahrami, M., Yovanovich, M. M., and Culham, J. R., 2006, "Pressure Drop of Fully Developed, Laminar Flow in Rough Microtubes," ASME J. Fluids Eng., **128**, pp. 632–637.
[13] Mala, G. M., and Li, D., 1999, "Flow Characteristics of Water in Microtubes," Int. J. Heat Fluid Flow, **20**, pp. 142–148.
[14] Kulinsky, L., Wang, Y., and Ferrari, M., 1999, "Electroviscous Effects in Microchannels," *SPIE Conference on Micro- and Nanofabricated Structures and Devices for Biomedical Environment Applications II*, San Jose, CA, Vol. 3606, pp. 158–168.
[15] Ding, L. S., Sun, H., Sheng, X. L., and Lee, B. D., 2000, "Measurement of Friction Factor for R134a and R12 Through Microchannels," *Proceedings of the Symposium on Energy Engineering in the 21st Century*, Vol. 2, pp. 650–657.
[16] Li, Z. X., Du, D. X., and Guo, Z. Y., 2000, "Characteristics of Frictional Resistance for Gas Flow in Microtubes," *Proceedings of the Symposium on Energy Engineering in the 21st Century*, Vol. 2, pp. 658–664.
[17] Kandlikar, S. G., Joshi, S., and Tian, S., 2001, "Effect of Channel Roughness on Heat Transfer and Fluid Flow Characteristics at Low Reynolds Numbers in Small Diameter Tubes," *Proceedings of the 35th National Heat Transfer Conference*, Anaheim, CA, Paper No. 12134.
[18] Li, Z. X., Du, D. X., and Guo, Z. Y., 2003, "Experimental Study on Flow Characteristics of Liquid in Circular Microtubes," Microscale Thermophys. Eng., **7**, pp. 253–265.
[19] Yu, D., Warrington, R., Barron, R., and Ameel, T. A., 1995, "Experimental and Theoretical Investigation of Fluid Flow and Heat Transfer in Microtubes," *Proceedings of the 1995 ASME/JSME Thermal Engineering Joint Conference*, Maui, HI, Vol. 1, pp. 523–530.
[20] Pfund, D., Shekarriz, A., Popescu, A., and Welty, J. R., 2000, "Pressure Drop Measurements in a Microchannel," AIChE J., **46**, pp. 1496–1507.
[21] Celata, G. P., Cumo, M., Guglielmi, M., and Zummo, G., 2000, "Experimental Investigation of Hydraulic and Single Phase Heat Transfer in 0.130 mm Capillary Tube," *Proceedings of the International Conference on Heat Transfer and Transport Phenomena in Microscale*, G. P. Celata, ed., Begell House, New York, pp. 108–113.
[22] Li, Z. X., Du, D. X., and Guo, Z. Y., 2000, "Experimental Study on Flow Characteristics of Liquid in Circular Microtubes," *Proceedings of the International Conference on Heat Transfer and Transport Phenomena in Microscale*, G. P. Celata, ed., Begell House, New York, pp. 162–168.
[23] Bucci, A., Celata, G. P., Cumo, M., Serra, E., and Zummo, G., 2003, "Fluid Flow and Single-Phase Flow Heat Transfer of Water in Capillary Tubes," *Proceedings of the International Conference on Minichannels and Microchannels*, Rochester, NY, Paper No. ICMM-1037.
[24] Tu, X., and Hrnjak, P., 2003, "Experimental Investigation of Single-Phase Flow Pressure Drop Through Rectangular Microchannels," *Proceedings of the International Conference on Minichannels and Microchannels*, Rochester, NY, Paper No. ICMM-1028.
[25] Baviere, R., Ayela, F., Le Person, S., and Favre-Marinet, M., 2004, "An Experimental Study of Water Flow in Smooth and Rough Rectangular Micro-Channels," *Proceedings of the Second International Conference on Minichannels and Microchannels*, Rochester, NY, Paper No. ICMM2004-2338.
[26] Tang, G. H., Li, Z., He, Y. L., and Tao, W. Q., 2007, "Experimental Study of Compressibility, Roughness and Rarefaction Influences on Microchannel Flow," Int. J. Heat Mass Transfer, **50**, pp. 2282–2295.
[27] Kleinstreuer, C., and Koo, J., 2004, "Computational Analysis of Wall Roughness Effects for Liquid Flow in Micro-Conduits," ASME J. Fluids Eng., **126**, pp. 1–9.
[28] Wang, X. Q., Yap, C., and Mujumdar, A. S., 2005, "Effects of Two-Dimensional Roughness in Flow in Microchannel," ASME J. Electron. Packag., **127**, pp. 357–361.
[29] Priezjev, N. V., and Troian, S. M., 2006, "Influence of Periodic Wall Roughness on the Slip Behaviour at Liquid/Solid Interfaces: Molecular-Scale Simulations Versus Continuum Predictions," J. Fluid Mech., **554**, pp. 25–46.
[30] Li, W. L., Lin, J. W., Lee, S. C., and Chen, M. D., 2002, "Effects of Roughness on Rarefied Gas Flow in Long Microtubes," J. Micromech. Microeng., **12**, pp. 149–156.
[31] Sun, H., and Faghri, M., 2003, "Effects of Surface Roughness on Nitrogen Flow in a Microchannel Using the Direct Simulation Monte Carlo Method," Numer. Heat Transfer, **43**, pp. 1–8.
[32] Langlois, W. E., 1958, "Creeping Viscous Flow Through a Two-Dimensional Channel of Varying Gap," *Proceedings of the Third National Congress of Applied Mechanics*, pp. 777–783.
[33] Langlois, W. E., 1958, *Slow Viscous Flow*, Macmillan, New York.
[34] Tanner, R. I., and Linnett, I. W., 1965, "Pressure Losses in Viscometric Capillary Tubes of Varying Diameter," Second Australian Conference on Hydraulics and Fluid Mechanics A, pp. 159–166.

[35] Manton, M. J., 1971, “Low Reynolds Number Flow in Slowly Varying Axisymmetric Tubes,” J. Fluid Mech., **49**, pp. 451–459.
[36] Phan-Thien, N., 1980, “On the Stokes Flow of Viscous Fluids Through Corrugated Pipes,” ASME J. Appl. Mech., **47**, pp. 961–963.
[37] Vasudeviah, M., and Balamurugan, K., 1999, “Stokes Slip Flow in a Corrugated Pipe,” Int. J. Eng. Sci., **37**, pp. 1629–1641.
[38] Wang, C. Y., 1979, “On Stokes Flow Between Corrugated Plates,” ASME J. Appl. Mech., **46**, pp. 462–464.
[39] Chu, K.-H. W., 1996, “Stokes Slip Flow Between Corrugated Walls,” Z. Angew. Math. Phys., **47**, pp. 591–599.
[40] Chu, K.-H. W., 1999, “Small-Knudsen-Number Flow in a Corrugated Tube,” Meccanica, **34**, pp. 133–137.
[41] Karniadakis, G. E., Beskok, A., and Aluru, N., 2005, *Microflows and Nanoflows*, Springer, New York.
[42] Hadjiconstantinou, N. G., 2005, “Validation of a Second-Order Slip Model for Dilute Gas Flows,” Nanoscale Microscale Thermophys. Eng., **9**, pp. 137–153.
[43] Sone, Y., 1973, “New Kind of Boundary Layer of a Convex Solid Boundary in a Rarefied Gas,” Phys. Fluids, **16**, pp. 1422–1424.
[44] Sone, Y., 2000, *Kinetic Theory and Fluid Dynamics*, Birkhauser, Boston.
[45] Cercignani, C., 1988, *The Boltzmann Equation and Its Applications*, Springer, New York.
[46] Barber, R. W., and Emerson, D. R., 2006, “Challenges in Modeling Gas-Phase Flow in Microchannels: From Slip to Transition,” Heat Transfer Eng., **27**, pp. 3–12.
[47] Goldstein, S., 1938, *Modern Developments in Fluid Dynamics*, Oxford University Press, Oxford, London.
[48] Rohsenow, W. M., and Choi, H. Y., 1961, *Heat, Mass, and Momentum Transfer*, Prentice-Hall, Englewood Cliffs, NJ.
[49] Chung, P., Kawaji, M., and Kawahara, A., 2002, “Characteristics of Single-Phase Flow in Microchannels,” *Proceedings of the ASME 2002 Fluids Engineering Division Summer Meeting*, Montreal, Canada.
[50] Kohl, M. J., Abdel-Khalik, S. I., Jeter, S. M., and Sadowski, D. I., 2005, “An Experimental Investigation of Microchannel Flow With Internal Pressure Measurements,” Int. J. Heat Mass Transfer, **48**, pp. 1518–1533.

Flow Boiling on Micropin Fins Entrenched Inside a Microchannel—Flow Patterns and Bubble Departure Diameter and Bubble Frequency

Santosh Krishnamurthy

Yoav Peles

Department of Mechanical, Aerospace, and
Nuclear Engineering,
Rensselaer Polytechnic Institute,
Troy, NY 12180

Flow boiling of HFE 7000 in five parallel microchannels of 222 μm hydraulic diameter, each containing a single row of 24 in-line 100 μm pin fins, was investigated. High speed photography revealed the dominant flow patterns, namely, the bubbly flow, the multiple flow, and the wavy-annular flow. The interaction of the bubble with the pin fins during nucleate boiling from $G=350\ \mathrm{kg/m^2\,s}$ to $G=827\ \mathrm{kg/m^2\,s}$ and wall heat fluxes from $10\ \mathrm{W/cm^2}$ to $110\ \mathrm{W/cm^2}$ is detailed. [DOI: 10.1115/1.2994718]

Keywords: flow boiling, microchannel, micro-pin fin, bubble departure frequency, bubble departure diameter, surface tension

1 Introduction

Flow boiling in microchannels has been extensively studied during the past several years because of its importance in a variety of applications, such as electronic cooling [1–13], microrockets [14], inkjet printers [15], and microchemical reactors [16]. As a direct extension of this research endeavor, new flow configurations such as micropin fins entrenched inside microchannels have also been studied for heat transfer enhancement [17–25]. Fundamental understanding of the boiling process in these microsystems is important to improve the design and to enhance their thermal-hydraulic performance.

Cross flow boiling in conventional scale has been extensively studied, and a significant scientific body of knowledge about the physical processes governing heat transfer in these systems exists [26–37]. The general consensus is that the heat transfer mechanisms are closely linked to flow morphologies and the resulting hydrodynamics. Numerous correlations and models for heat transfer coefficient have been developed by coupling the hydrodynamic and thermal characteristics. Hwang and Yao [32] studied flow pattern interaction with tubes for three different configurations, namely, single tube, single heated tube in an unheated in-line tube bundle, and heated in-line tube bundle. For each of these conditions, the onset of nucleate boiling (ONB) occurred at the cylinders rear wake, and the cylinder spacings affected the bubble interactions at high qualities. Using high speed photography, Cornwell [29] observed turbulent bubbly flow and attributed the observed heat transfer enhancement to the sliding bubbles. Fand et al. [38] stated that the maximum nucleation site density occurs at the frontal stagnation point and at the rear wake side for flow across a single cylinder.

The flow characteristics around a tube/cylinder in a tube bundle is strongly dependent on geometrical parameters such as tube configuration (in-line or staggered), longitudinal and transverse pitches, and physical parameter such as the Reynolds number [39]. In microscale, the studies pertaining to bubble dynamics have been restricted to plain microchannels [40] and channels with re-entrant cavities [41]. The growth and the dynamics of the bubbles have been observed to deviate considerably from those observed in conventional scale. The small length scale of the channel restricted the expansion of the bubble in the transverse direction and subjected it to high shear stress along the longitudinal direction, eventually causing it to depart at diameters comparable to the channel hydraulic diameter.

In the current study, flow boiling across a single row of in-line micropin fins entrenched in a microchannel is being investigated. The microdevice consists of five 200 μm wide and 243 μm deep microchannels, each equipped with an inlet orifice, consisting of 24 columns of 100 μm diameter circular pin fins, with pitch-to-diameter ratio of 4. With the aid of high speed photography, the dominant flow patterns in such flow configurations were revealed. Furthermore, the interaction of bubbles with these micropin fins was also investigated and pertinent bubble dynamics parameters such as bubble departure diameter and frequency were also measured.

2 Device Overview

A computer aided design (CAD) schematic of the microdevice, consisting of five 200 μm wide and 243 μm deep microchannels entrenched in a 1800 μm wide channel, is shown in Fig. 1. Each microchannel encompassed 24 rows of in-line 100 μm diameter micropin fins with a pitch-to-diameter ratio of 4. A micro-orifice, 400 μm long and 20 μm wide, was fabricated upstream of each microchannel. A heater was deposited on the back side of the channel-pin fin section excluding the orifice to provide the requisite heat flux. A Pyrex cover sealed the device from the top and allowed flow visualization. For additional details on the processing steps and experimental setup, the reader is referred to Ref. [18].

3 Data Reduction

The voltage, current, and pressure measurements were used to obtain the average single-phase and two-phase temperatures and mass qualities. This section gives the data reduction procedure used to obtain these parameters.

The voltage and current values were used to calculate the input power and heater resistance. The wall heat flux was calculated as

---

Contributed by the Heat Transfer Division of ASME for publication in the Journal of Heat Transfer. Manuscript received January 18, 2008; final manuscript received August 12, 2008; published online February 17, 2010. Review conducted by Satish G. Kandlikar.

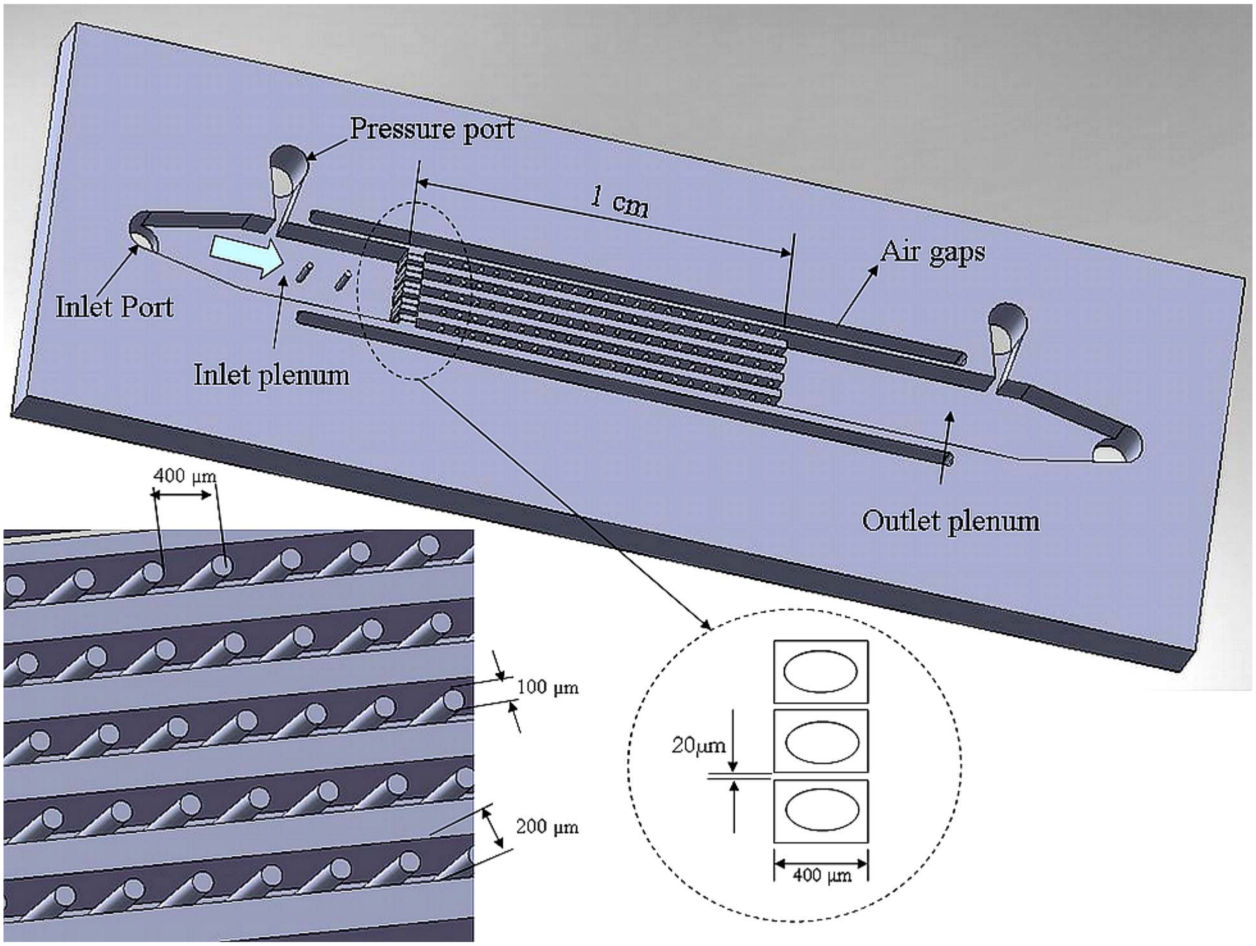

Fig. 1 Device overview showing the device dimensions

$$q''_w = \frac{P - Q_{\text{loss}}}{A_p} \tag{1}$$

The average heater temperature was obtained from the calibration curve. Assuming 1D steady state conduction through the silicon block, the average surface temperature of the device was obtained by

$$\overline{T}_{\text{sur}} = \overline{T}_{\text{heater}} - \frac{(P - Q_{\text{loss}})t_s}{k_s A_p} \tag{2}$$

The local quality was calculated from the known mass flow rate as shown below:

$$x = \frac{(P - Q_{\text{loss}})(L_x/L_o) - \dot{m}c_p(T_{\text{sat}} - T)_i}{\dot{m}h_{fg}} \tag{3}$$

The fluid temperature was measured in the inlet using a type K thermocouple. The local flow temperature was deduced indirectly from energy balances ($T_{\text{mx}} = T_{\text{mi}} + ((P - Q_{\text{loss}}/\dot{m}C_p)(L_x/L))$). Comparison of the experimental data with the existing models was done through the mean absolute error (MAE):

$$\text{MAE} = \frac{1}{M}\sum_{i=1}^{M} \frac{|\alpha_{\text{exp}} - \alpha_{\text{pred}}|}{\alpha_{\text{exp}}} \times 100 \tag{4}$$

where α is the measured physical quantity and the subscripts "exp" and "pred" refer to the experimental and predicted values, respectively. The uncertainty associated with the measured values was obtained from the manufacturers' specification sheets while the uncertainties associated with the derived quantities such as mass flux, surface temperature, and wall heat flux were obtained by using the propagation of uncertainty analysis and were 3.4%, 0.5°C, and 3.8%, respectively.

4 Results and Discussion

4.1 Flow Patterns. The flow patterns observed in the current study were classified as bubbly flow, multiple flows, and wavy-annular flow, as schematically shown in Fig. 2. Bubbly flow comprised of vapor bubbles, nucleating from the sidewalls and the micropin fins, dispersed in the liquid. As the bubbles moved downstream, they expanded and formed vapor slugs, which were sheared by the pin fins resulting in regions of vapor slugs and bubbles, termed multiple flow. Eventually, wavy-annular flow was established downstream, which was characterized by the presence of a thin wavy liquid film flowing along the sidewalls and the pin fins with a vapor core (Fig. 3). The thin liquid film on the pin fins accelerated along its frontal side and separated from the surface forming a trailing liquid drop attached to the rear side where intense mixing was observed. As the thin liquid film on the frontal section evaporated, causing local dry-out, a vapor cavity developed, which moved axially in the upstream direction and collapsed intermittently due to the drag forces exerted by the incoming fluid. With increasing heat flux, the vapor cavity stabilized,

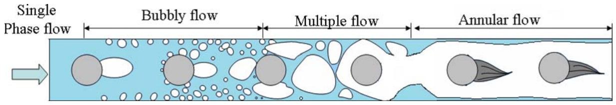

Fig. 2 Schematic of flow patterns

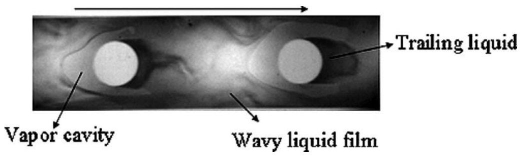

Fig. 3 Wavy-annular flow showing the trailing liquid of the pin fins and vapor cavity on the upstream side of pin fin

and the thin film completely evaporated while a liquid drop trailed on the rear side ($q''=39\ \text{W/cm}^2$ for $G=350\ \text{kg/m}^2\ \text{s}$; $q''=76\ \text{W/cm}^2$ for $G=565\ \text{kg/m}^2\ \text{s}$; $q''=98\ \text{W/cm}^2$ for $G=827\ \text{kg/m}^2\ \text{s}$). Similar flow patterns have also been observed by Cognata et al. [20] for a square micropin fin. Occasionally, the frontal region of the pin fins was wetted by a thin liquid microlayer, which evaporated rapidly resulting in a nonuniform thermal loading on the pin fin. As the heat flux was further increased, the trailing liquid drop shrunk, ultimately leading to a complete local dry-out. For the lowest mass velocity ($G=350\ \text{kg/m}^2\ \text{s}$), the single-phase liquid flow directly transitioned to multiple flow without first forming bubbly flow region. The absence of isolated bubbly flow at low mass fluxes is, to some respect, in contradiction to the trend discussed by Revellin and Thome [42]. This anomaly might be a result of the significant different flow configurations of the current study and the study of Revellin and Thome [42]. Due to the low mass velocity, the flow exhibited slight flow reversal in which a vapor bubble (cavity) initiated at the frontal stagnation point and continued to grow conically upstream, temporarily increasing the local void fraction, as shown in Fig. 4. This was accompanied by an increase in the local liquid velocity, which deformed the cavity and sheared it across the pin fins causing it to break and move downstream ($0<t<4.4$ ms). No such flow reversal was observed at higher mass velocities.

4.2 Heat Flux Versus Temperature. Figure 5 shows the average $\overline{T}_{\text{sur}}-q''_w$ curves for different mass fluxes. The heat flux as a function of the average temperature was characterized by three regions of different slopes. The first region corresponds to single-phase flow where the temperature was linearly dependent on the heat flux. The onset of boiling was accompanied by a significant drop in the surface temperature, which was observed for all mass fluxes and was attributed to boiling hysteresis. Such temperature hysteresis at the onset of boiling was caused by the good wettability of the fluid and the surface topography. The low surface tension of HFE 7000 ($\sigma=13.8\ \text{mN/m}$ at $T=22$ deg) and the surface roughness of the silicon surface ($\sim 0.3\ \mu\text{m}$) render majority of the cavities inactive even at high superheated temperatures. Ultimately, boiling was triggered and vapor bursted through the channel activating many nucleation sites and significantly reducing the surface temperature. Following the onset of boiling, the temperature continued to increase. At a certain heat flux, the temperature increased rapidly signifying the approaching critical heat flux (CHF) conditions. The hysteresis phenomenon clearly appeared when the heat flux was gradually decreased, as shown by curve *b* in Fig. 5.

4.3 Bubble Nucleation and Dynamics. At the onset of boiling, the bubbles nucleated on the microchannel sidewalls and on the pin fin surface. Flow visualization revealed that the bubbles first nucleated at the rear wake side of the first pin fin in the two-phase region, as shown in Fig. 6. The thick thermal boundary layer and the resulting high local fluid temperature initially triggered the bubble growth in this region. Figure 7 shows the distribution of the active cavities along the circumference of the pin fin for different mass velocities. The majority of the nucleation sites were distributed asymmetrically on the rear side at $90\ \text{deg}<\theta<180$ deg. It has been observed that for flow across tandem cylinders, the flow transitions from steady symmetrical flow at low Reynolds number to an oscillatory asymmetrical flow at a critical Reynolds number; for $p/d=4$, the transition corresponds to a critical Reynolds number of $\text{Re}_c=68$ [43]. It is very likely that such oscillations existed in the current study ($75<\text{Re}_d<180$) distorting the symmetry of the nucleation sites (Fig. 7). The nucleation of the bubbles on the rear side modified the hydrodynamics of the flow field, which resulted in bubbles nucleating along different locations on the downstream pin fin. Generally, bubbles from pin fins downstream the first row of the two-phase region tended to

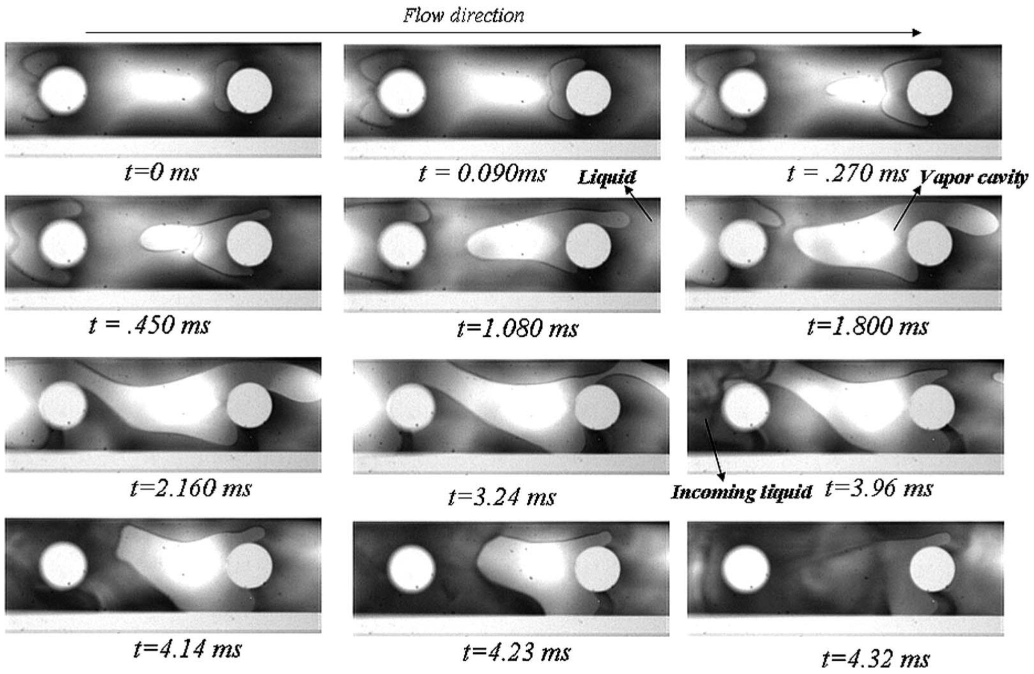

Fig. 4 Sequence of images showing the formation of vapor cavity at the stagnation point and subsequent breakage ($G=350\ \text{kg/m2s}$, $q''_w=33.2\ \text{W/cm}^2$, and $z=4$ mm)

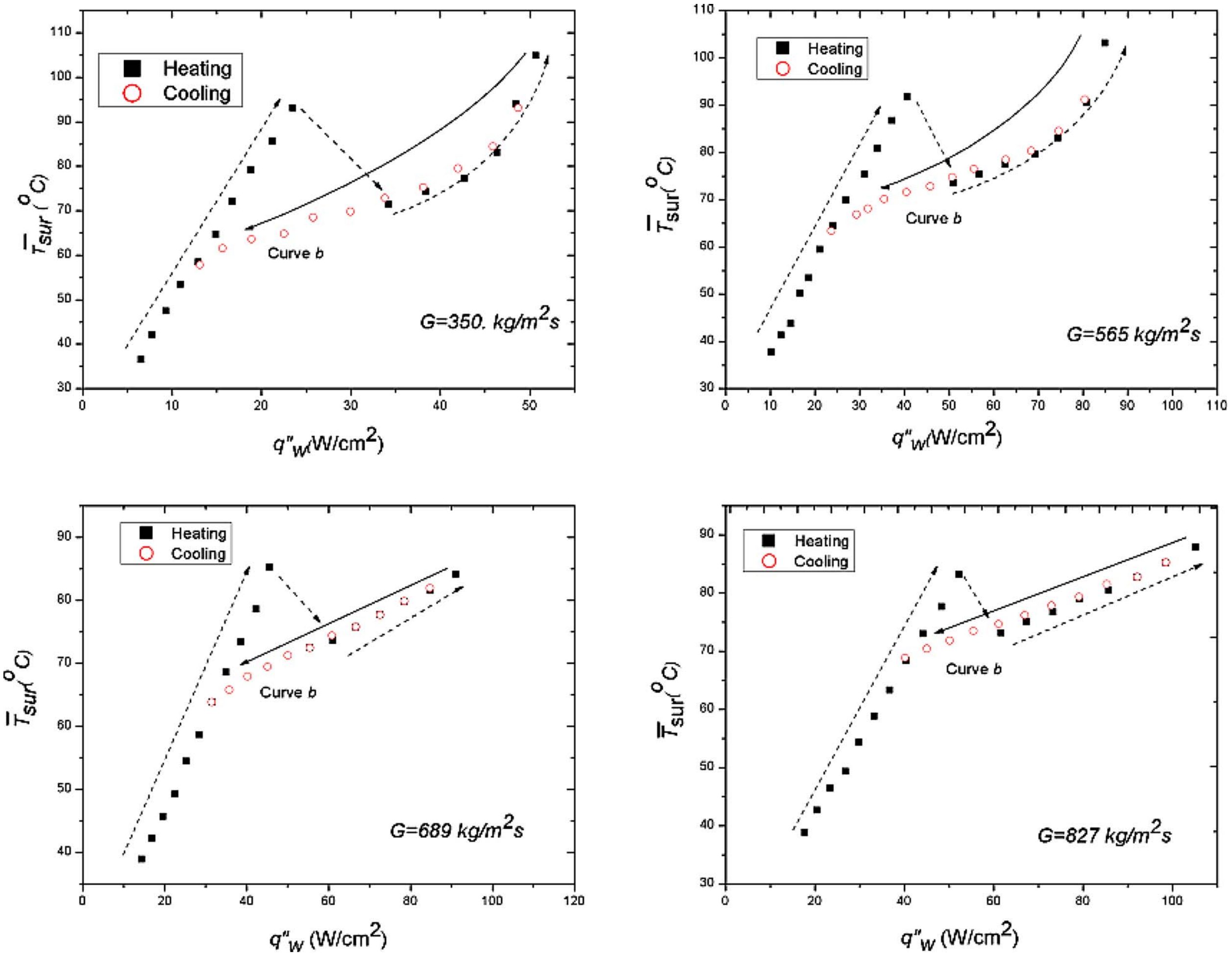

Fig. 5 Heat flux as a function of average surface temperature for various mass velocities

nucleate from the frontal stagnation point ($\theta=0$ deg). The dynamics of the bubble departing from different sites along the circumference of the pin fins also differed from each other. At $\theta=180$ deg, the bubbles grew asymmetrically due to the intensive recirculation of the flow and at some point the bubble ultimately necked close to the surface of the pin fin and eventually detached. At $\theta=0$ deg, the bubbles detached and slid along the surface while growing and ultimately lifted from the rear side of the pin fin (Fig. 8). Additionally, the bubbles departing from the upstream pin fins were often swept into the wake of the downstream pin fin causing them to circulate in the recirculation zone, expand, and coalesce with other bubbles, and in the process agitate the liquid in the recirculation zone.

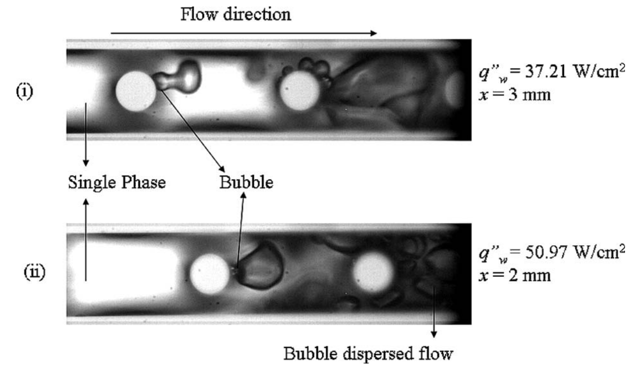

Fig. 6 Images showing the bubble nucleation on the rear side of the upstream pin fins and along the circumference on the downstream pin fins for $G=565$ kg/m^2 s under different heat fluxes

4.4 Bubble Departure Frequency and Departure Diameter. Qualitatively, the flow patterns and bubble ebullition process were similar for all channels; the quantitative results were elucidated for channel 3 (middle channel). Figure 9(*a*) shows the bubble departure diameter for $\theta=0$ deg as a function of wall heat flux for different mass velocities. The bubble departure diameter decreased with increasing heat flux and mass velocity. At high mass velocity, the increased drag force sheared the bubbles from their nucleation sites at small diameters. The departure diameter decreased with increasing heat flux at low mass velocities, but at high mass velocities, the growth of the bubble was suppressed by the impingement of the flow at the stagnation point. The bubbles departing from $\theta=180$ deg had much larger diameter than those departing from $\theta=0$ deg. However, the decreasing diameter trends were similar (Fig. 9(*b*)). The bubble departure frequency was elucidated by counting the number of bubbles departing from a nucleation site over 800 frames (fps of 12,000). Figure 10 shows the bubble departure frequency from the two most active nucleation sites on the pin fins, at $\theta=0$ deg and $\theta=180$ deg, at various mass velocities as a function of wall heat flux. The bubbles nucleated at the location of ONB for $\theta=180$ deg and at the immediate downstream pin fin for $\theta=0$ deg. The frequency and bubble departure diameter were measured in the isolated bubble region between $z=1$ mm and $z=3$ mm from the inlet of the channel where

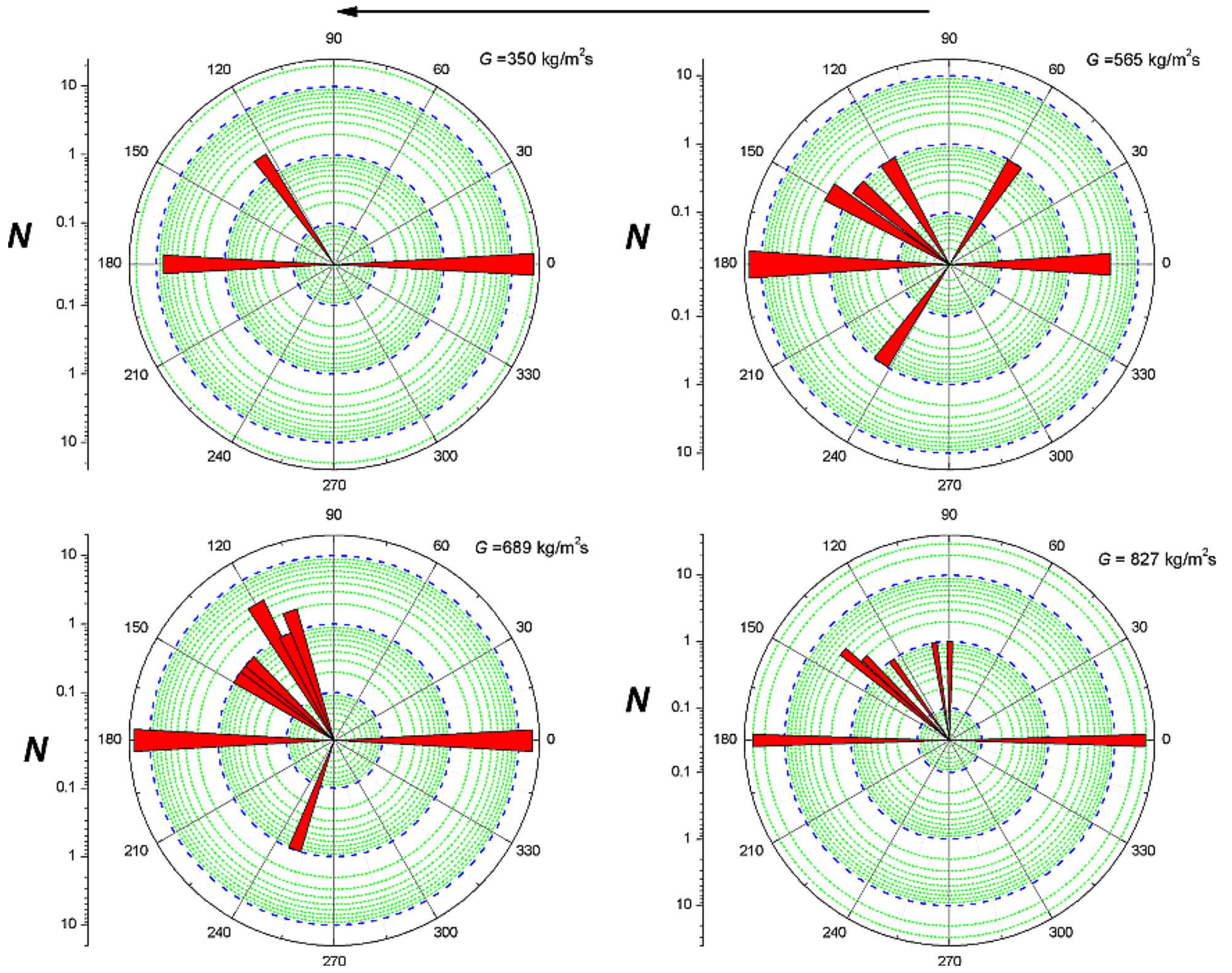

Fig. 7 Circumferential nucleation site distribution along the first pin fin to experience boiling various mass fluxes

the bubble coalescence was negligible. For $\theta=0$ deg, the bubble frequency increased linearly with the wall heat flux, although regions of two distinct slopes were observed, which was a function of the mass velocity. At low and intermediate mass velocities, the bubble frequency increased sharply with the wall heat flux, and at high mass velocities, the bubble frequency increased with a lower slope. During the bubble growth, interfacial tension acting along the contact line tended to hold the bubble in place against the inertial drag force exerted by the surrounding liquid. The bubble departed from the site when the net effect of the inertial drag exceeded the interfacial tension. At low mass velocities, due to the lower drag force exerted by the liquid on the bubble, the bubble attained a large diameter before departing, resulting in a long bubble ebullition cycle and hence low frequencies. At high mass velocities, the bubbles were subjected to higher inertial drag causing them to depart at a higher rate. Such mass flux dependency on frequency has also been observed by Lee et al. [40] for flow in a rectangular 41 μm hydraulic diameter microchannel. Vigorous boiling occurred at higher heat flux, which resulted in rapid bubble growth and thus higher frequencies. Additionally with increasing heat flux, the surface tension decreased (due to temperature increase), causing a reduction in the holding surface tension force and a reduction in the departure diameter, which in turn enhanced the bubble departure frequencies. Therefore, the bubble frequency at $\theta=0$ deg has been correlated as a function of wall heat flux by the following relations with a MAE of 18%:

$$f = 386.6q''_{\mathrm{ch}} - 4612.6 \quad (\mathrm{Re}_d < 120) \quad (\mathrm{Hz}) \tag{5}$$

and

$$f = 124.9q''_{\mathrm{ch}} - 1363.8 \quad (\mathrm{Re}_d > 120) \quad (\mathrm{Hz}) \tag{6}$$

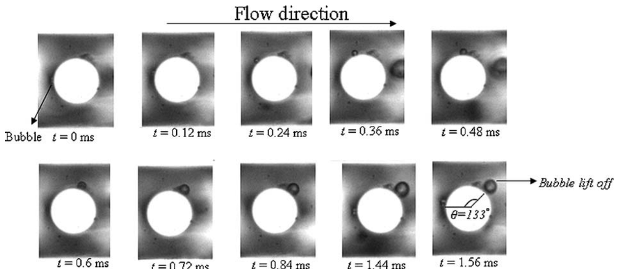

Fig. 8 Sequence of images showing the bubbles nucleating at $\theta=0$ deg and sliding along the circumference of pin fins ($q''_w=52.6$ W/cm^2 and $G=827$ kg/m^2 s)

The much larger departure diameter at $\theta=180$ deg compared with $\theta=0$ deg has important implications on the bubble frequency. As can be seen in Fig. 10(*b*) for $\theta=180$ deg, the bubble departure frequency was much smaller compared with the frequency at the frontal stagnation point. The large bubble departure diameter, caused by the low liquid velocity in the recirculation zone where the drag forces exerted on the bubble, was much weaker than for $\theta=0$ deg, increased the ebullition period. The frequency increased with mass velocity and showed a peak with respect to heat

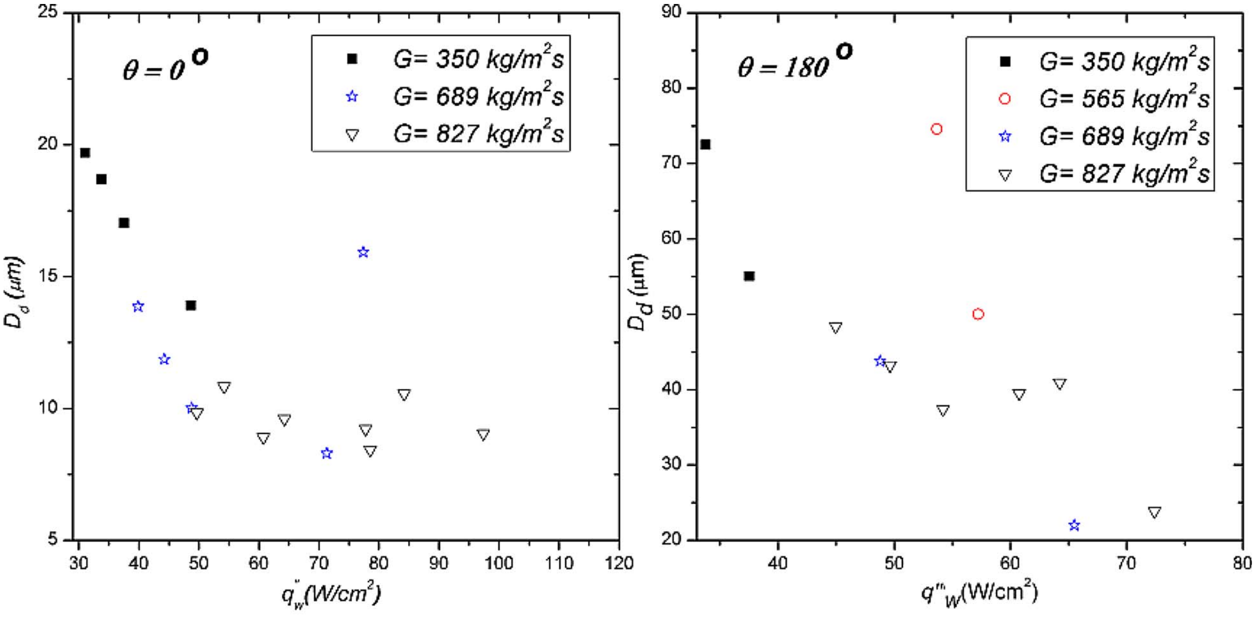

(a)

(b)

Fig. 9 Bubble departure diameter for (*a*) $\theta=0$ deg and (*b*) $\theta=180$ deg

flux, which was clearly evident for $G=827$ kg/m^2 s and $G=565$ kg/m^2 s. With increasing heat flux, the boiling front propagated upstream and the bubbles nucleating on the rear side were continuously subjected to condensation on the periphery due to an increase in the local subcooled temperature. Because of the condensation on the bubble periphery and the low velocity in the recirculation zone, the bubble, after nucleating and growing to the departure diameter, tended to be stationary before departing. This in turn extended the bubble ebullition cycle and decreased the bubble departure frequencies. Figure 11(*a*) shows the variation of the bubble departure frequency as a function of the local subcooling for bubbles departing from the rear side. Such variation with respect to local subcooling was not observed for bubbles nucleating from the frontal stagnation point of the downstream pin fins ($\theta=0$ deg), as shown in Fig. 11(*b*). Because the bubbles were very small at $\theta=0$ deg when they departed ($D_d \sim 10$ μm), their periphery was not subjected to significant condensation. Therefore, higher subcooled temperatures did not seem to slow down the bubble departure diameter. The bubble departure frequencies on the pin fins, especially at $\theta=0$ deg, are higher than those observed in other microscale studies [40,41] ($f \sim 6000$ Hz at high heat flux). For example, Kuo et al. [41] reported a maximum frequency of 600 Hz and Lee et al. [40] reported a maximum a frequency of 60 Hz for boiling in microchannel using water. The higher frequency observed in the current study is a result of the much lower surface tension of the working fluid. Since the surface tension forces are the main force resisting the bubble departure, bubbles in HFE 7000—fluid with very low surface tension—readily departed from the nucleation site. Furthermore, the lower

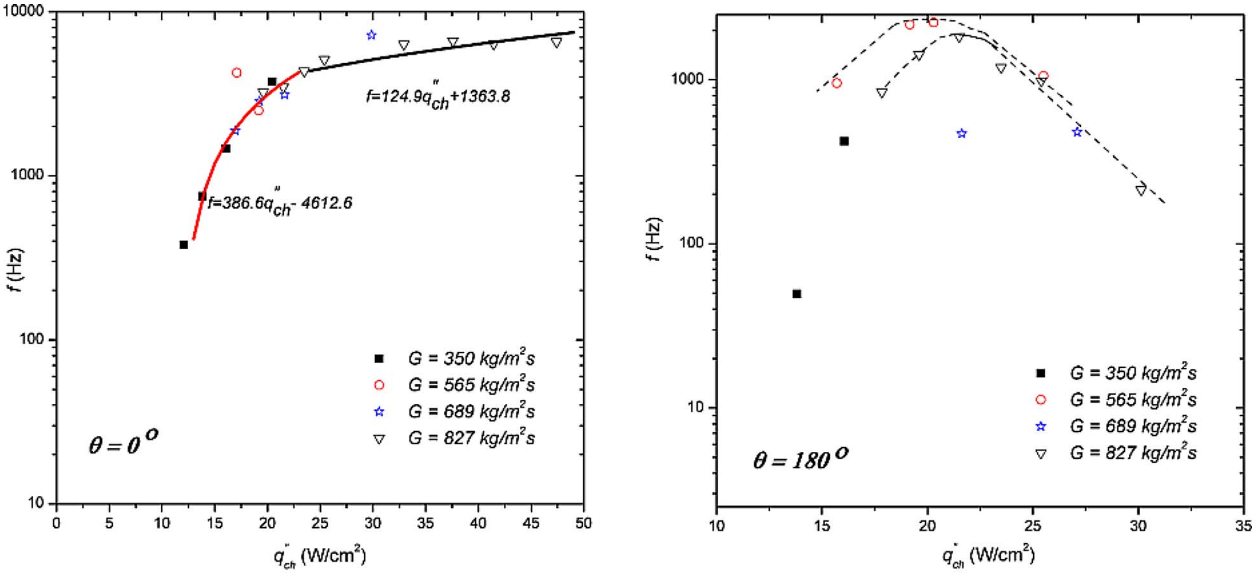

(a)

(b)

Fig. 10 Bubble departure frequency for (*a*) $\theta=0$ deg and (*b*) $\theta=180$ deg

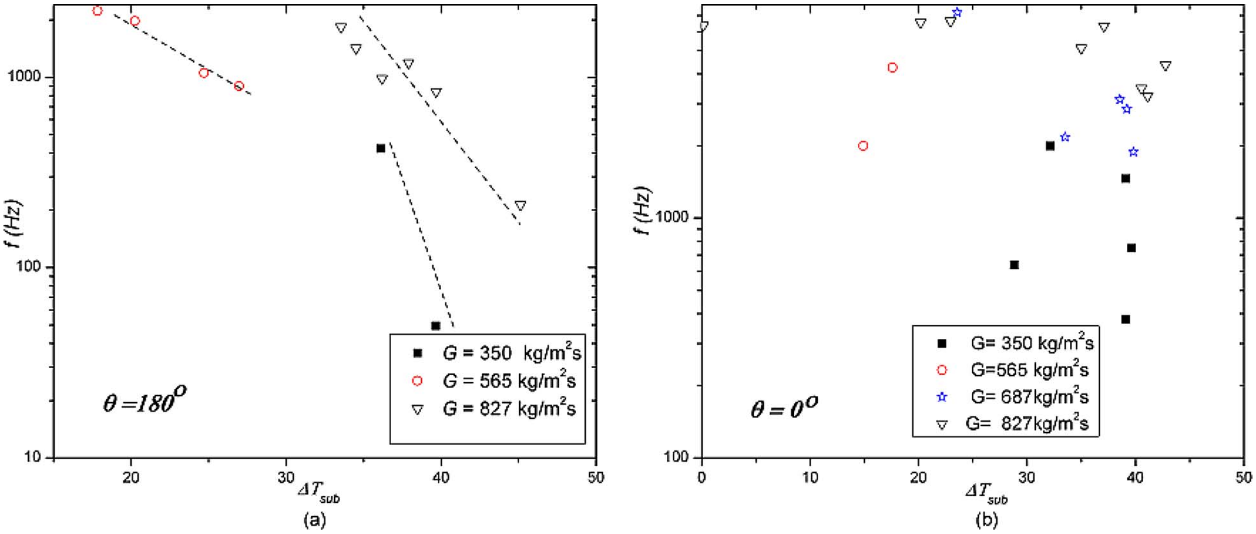

Fig. 11 The variation of departure frequency as a function of local subcool for (*a*) θ=180 deg and (*b*) θ=0 deg

latent heat of vaporization of HFE 7100 compared with water facilitated rapid growth of the bubble [44] hastening the bubble ebullition cycle.

Traditionally, the bubble frequency has been correlated through the bubble departure diameter according to $f^n D_d$=const [45–47], where n ranges from 1/2 to 2. Figure 12 compares the frequency and bubble departure diameter for θ=0 deg with conventional scale [45,48] and microchannel [41] correlations. None of the correlations agreed well with the experimental results over the entire range. Conventional scale correlations provided a better agreement with the experimental results at high heat fluxes (high frequencies), while at low heat fluxes, which was characterized by low bubble departure frequency, agreement with microchannel correlation improved. The above mentioned result indicates that there exists a partwise variation of the product fD_d in microchannels; when the bubble departure diameter is comparable to the channel hydraulic diameter, the frequency has a different functional dependency on the departure diameter than for conditions corresponding to bubbles much smaller than the channel. Kuo et al. [41] investigated bubble dynamics in water for a 222 μm hydraulic diameter rectangular microchannel with re-entrant cavities. The higher surface tension of water resulted in much larger bubble than for the current study ranging from 100 μm to 222 μm. The large bubble departure diameter-to-channel hydraulic diameter ratio modified the hydrodynamics of the flow considerably, decreasing the product (fD_d) compared with conventional scale systems. In the current study, for low mass velocities and heat fluxes, characterized by large bubble departure diameters, microchannel results for water worked well [41]. Increasing the mass velocity, resulted in bubbles considerably smaller than the channel hydraulic diameter. The channel "loses" its identity as a microscale channel and practically transitioned to hydrodynamics resembling conventional scale (or miniscale) characteristics. Therefore, under these conditions, the agreement with conventional scale models are fairly good. While the traditional form of the correlation fD_d=const has been successfully used in microscale [41], for the current flow configuration, correlation of this form cannot be used because the product (fD_d) was observed to increase with heat flux, as shown in Fig. 13(*a*). Therefore, using least squares method, the following correlation for the product of the bubble frequency and the bubble departure diameter has been developed:

$$f^n D_d = 0.000397 \tag{7}$$

where n is an empirically derived constant, which was calculated to be 0.435. 85% of the predicted data is within ±25% of the experimental data with a MAE of 14% (No. of data points=29). Unlike for θ=0 deg, for θ=180 deg, the product of the bubble departure frequency and departure diameter did not show any specific trend with respect to heat flux and mass flux, but decreased with increasing local subcooling (or the Jakob number) as shown in Fig. 13(*b*). With increased subcooling, the bubble growth was impeded by continuous condensation at the periphery, resulting in lower bubble departure frequencies and departure diameters.

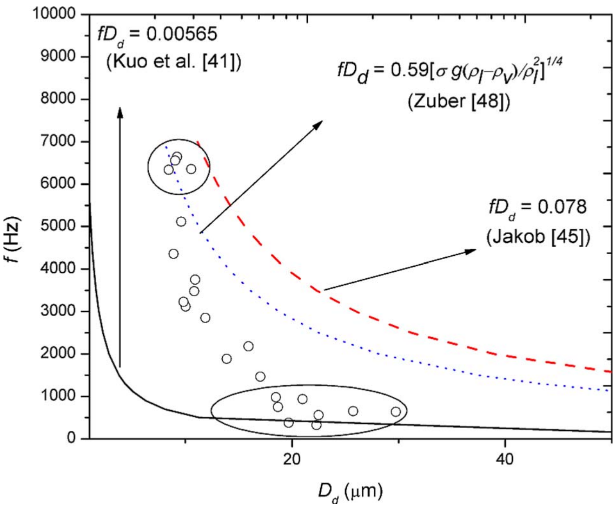

Fig. 12 Comparison of frequency and departure diameter data with different correlations

5 Conclusions

Flow visualization revealed the existence of bubbly flow, multiple flows, and wavy-annular flow.

At the onset of boiling, the bubbles nucleated on the rear side of the pin fins and with the propagation of the boiling front, bubbles started nucleating at other locations. Nucleation sites were mostly observed at θ=0 deg and θ=180 deg.

The bubble departure frequency rapidly increased with wall heat flux for θ=0 deg, but this trend gradually diminished at high heat fluxes, which has been attributed to the suppression of boiling. For θ=180 deg, the bubble departure frequency first increased and then decreased with heat flux.

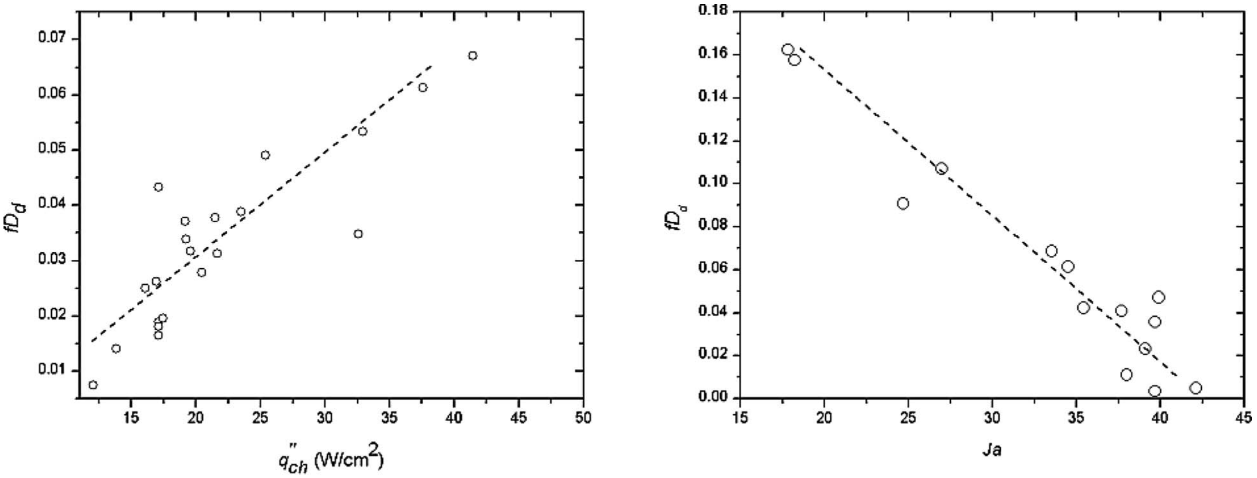

(a)

(b)

Fig. 13 Variation of fD_d product with (*a*) heat flux at $\theta = 0$ deg. (*b*) Jakob number at $\theta = 180$ deg.

The bubble departure diameter showed a decreasing trend with wall heat flux for both nucleation sites.

The product of the bubble departure frequency and bubble departure diameter follows the traditional form of the correlation used in conventional scale systems for small bubble departure diameters and tended to follow the previous studies at the microscale when the bubble was large compared with the channel hydraulic diameter. The product was observed to increase with wall heat flux.

Acknowledgment

This work was supported by the Office of Naval Research (Program Officer Mark Spector). The microfabrication was performed in part at the Cornell NanoScale Facility (a member of the National Nanotechnology Infrastructure Network) which is supported by the National Science Foundation under Grant No. ECS-0335765, its users, Cornell University, and industrial affiliates.

Nomenclature

A = dimensionless constant in Eq. (8)
A_p = planform area, m^2
b = dimensionless constant in Eq. (8)
Bo = boiling number, q''_{ch}/Gh_{fg}
c = dimensionless constant in Eq. (8)
c_p = Specific heat, kJ kg^{-1} K^{-1}
d = pin fin diameter, m
D_d = bubble departure diameter, m
f = frequency, Hz
G = mass flux, kg m^{-2} s^{-1}
H = height, m
h_{fg} = latent heat of vaporization, kJ kg^{-1}
I = current, A
Ja = Jakob number, $\rho_l c_p (T_{\text{sat}} - T_{\text{mx}}) / \rho_v h_{fg}$
k_s = thermal conductivity of silicon block, W m^{-1} K^{-1}
L = length, m
L_o = overall channel length, m^2
L_x = local channel length, m^2
$\dot{m}$ = mass flow rate, kg s^{-1}
p = pitch, m
P = power, W
q''_{ch} = heat flux based on channel surface area, W cm^{-2}
Q_{loss} = heat loss, W
q''_w = heat flux based on planform area, W cm^{-2}
Re_d = Reynolds number, Gd/μ
T_i = inlet fluid temperature, °C
T_{mx} = local mean liquid temperature, °C
T_{sat} = saturation temperature, °C
$\overline{T}_{\text{sur}}$ = average surface temperature, °C
t = time, ms
t_s = thickness of silicon block, m
x = quality
z = axial distance along the channel, m

Subscripts

l = liquid
sat = saturation
sur = surface
v = vapor
w = wall
x = local

Greek Symbols

α = measured quantity
μ = viscosity, Pa s
θ = radial angle
ρ = density, kg m^{-3}
σ = surface tension, N m^{-1}

References

[1] Garimella, S., and Singhal, V., 2004, "Single-Phase Flow and Heat Transport and Pumping Considerations in Microchannel Heat Sinks," Heat Transfer Eng., **25**(1), pp. 15–25.
[2] Muwanga, R., Hassan, I., and MacDonald, R., 2007, "Characteristics of Flow Boiling Oscillations in Silicon Microchannel Heat Sinks," ASME J. Heat Transfer, **129**, pp. 1341–1352.
[3] Saidi, M. H., and Khiabani, R. H., 2007, "Forced Convective Heat Transfer in Parallel Flow Multilayer Microchannels," ASME J. Heat Transfer, **129**, pp. 1230–1236.
[4] Coursey, J. S., Kim, J., and Kiger, K. T., 2007, "Spray Cooling of High Aspect Ratio Open Microchannels," ASME J. Heat Transfer, **129**, pp. 1052–1060.
[5] Koşar, A., and Peles, Y., 2007, "Critical Heat Flux of R-123 in Silicon-Based Microchannels," ASME J. Heat Transfer, **129**, pp. 844–851.
[6] Chen, T., and Garimella, S. V., 2006, "Effects of Dissolved Air on Subcooled Flow Boiling of a Dielectric Coolant in a Microchannel Heat Sink," ASME J. Electron. Packag., **128**, pp. 398–405.
[7] Li, J., Peterson, G., and Cheng, P., 2004, "Three-Dimensional Analysis of Heat Transfer in a Micro-Heat Sink With Single-Phase Flow," Int. J. Heat Mass Transfer, **47**, pp. 4215–4231.

[8] Koşar, A., Kuo, C.-J., and Peles, Y., 2006, “Suppression of Boiling Flow Oscillations in Parallel Microchannels With Inlet Restrictors,” ASME J. Heat Transfer, **128**(3), pp. 251–260.

[9] Koşar, A., and Peles, Y., 2006, “Thermal-Hydraulic Performance of MEMS Based Pin Fin Heat Sink,” ASME J. Heat Transfer, **128**, pp. 121–131.

[10] Koşar, A., Kuo, C.-J., and Peles, Y., 2005, “Reduced Pressure Boiling Heat Transfer in Rectangular Microchannels With Interconnected Reentrant Cavities,” ASME J. Heat Transfer, **127**(10), pp. 1106–1114.

[11] Qu, W., and Mudawar, I., 2003, “Flow Boiling Heat Transfer in Two-Phase Microchannel Heat Sink: I. Experimental Investigation and Assessment of Correlation Methods,” Int. J. Heat Mass Transfer, **46**(15), pp. 2755–2771.

[12] Qu, W., and Mudawar, I., 2003, “Flow Boiling Heat Transfer in Two-Phase Microchannel Heat Sink: II. Annular Two-Phase Flow Model,” Int. J. Heat Mass Transfer, **46**(15), pp. 2773–2784.

[13] Qu, W., and Mudawar, I., 2005, “A Systematic Methodology for Optimal Design of Two-Phase Micro-Channel Heat Sinks,” ASME J. Electron. Packag., **127**, pp. 381–390.

[14] Hitt, D. L., Zakrzwski, C. M., and Thomas, M. A., 2001, “Mems-Based Satellite Micropropulsion Via Catalyzed Hydrogen Peroxide Decomposition,” Smart Mater. Struct., **10**, pp. 1163–1175.

[15] Allen, R., Meyer, J. D., and Knight, W. R., 1985, “Thermodynamics and Hydrodynamics of Thermal Ink Jets,” Hewlett-Packard J., **36**, pp. 21–27.

[16] Losey, M. W., Jackman, J., Firebaugh, S. L., Schmidt, M. A., and Jensen, K., 2002, “Design and Fabrication of Microfluidic Devices for Multiphase Mixing and Reaction,” J. Microelectromech. Syst., **11**, pp. 709–717.

[17] Prasher, R. S., Dirner, J., Chang, J.-Y., Myers, A., Chau, D., He, D., and Prstic, S., 2007, “Nusselt Number and Friction Factor of Staggered Arrays of Low Aspect Ratio Micropin-Fins Under Cross Flow for Water as Fluid,” ASME J. Heat Transfer, **129**(2), pp. 141–153.

[18] Krishnamurthy, S., and Peles, Y., 2008, “Flow Boiling of Water in a Circular Staggered Micropin Fin Heat Sink,” Int. J. Heat Mass Transfer, **51**(5–6), pp. 1349–1364.

[19] Siu-Ho, A., Qu, W., and Pfefferkorn, F. E., 2007, “Experimental Study of Pressure Drop and Heat Transfer in a Single-Phase Micropin-Fin Heat Sink,” ASME J. Electron. Packag., **129**(4), pp. 479–487.

[20] Cognata, T. J., Hollingsworth, K. D., and Witte, L. C., 2007, “High-Speed Visualization of Two-Phase Flow in a Micro-Scale Pin-Fin Heat Exchanger,” Heat Transfer Eng., **28**(10), pp. 861–869.

[21] Koşar, A., and Peles, Y., 2006, “Convective Flow of Refrigerant (R-123) Across a Bank of Micro Pin Fins,” Int. J. Heat Mass Transfer, **49**, pp. 3142–3155.

[22] Krishnamurthy, S., and Peles, Y., 2007, “Gas-Liquid Two-Phase Flow Across a Bank of Micro Pillars,” Phys. Fluids, **19**(4), p. 043302.

[23] Koşar, A., and Peles, Y., 2007, “Boiling Heat Transfer in a Hydrofoil-Based Micro Pin Fin Heat Sink,” Int. J. Heat Mass Transfer, **50**(5-6), pp. 1018–1034.

[24] Koşar, A., and Peles, Y., 2007, “Micro Scale Pin Fin Heat Sinks—Parametric Performance Evaluation Study,” IEEE Trans. Compon. Packag. Technol., **30**(4), pp. 855–865.

[25] Siu-Ho, A. M., Qu, W., and Pfefferkorn, F. E., 2006, “Pressure Drop and Heat Transfer in a Single-Phase Micro-Pin-Fin Heat Sink, ASME Paper No. IMECE2006-14777.

[26] Schrage, D. S., Hsu, J.-T., and Jensen, M. K., 1988, “Two-Phase Pressure Drop in Vertical Cross-Flow Across a Horizontal Tube Bundle,” AIChE J., **34**, pp. 107–115.

[27] Xu, G. P., Tou, K. W., and Tso, C. P., 1998, “Two-Phase Void Fraction and Pressure Drop in Horizontal Crossflow Across a Tube Bundle,” ASME J. Fluids Eng., **120**, pp. 140–145.

[28] Jensen, M. K., and Hsu, J.-T., 1988, “A Parametric Study of Boiling Heat Transfer in Horizontal Tube Bundle,” ASME J. Heat Transfer., **110**, pp. 976–981.

[29] Cornwell, K., 1990, “The Influence of Bubbly Flow on Boiling From a Tube in a Bundle,” Int. J. Heat Mass Transfer, **33**(12), pp. 2579–2584.

[30] Polley, G. T., Ralston, T., and Grant, I. D. R., “Forced Crossflow Boiling in an Ideal In-Line Tube Bundle,” ASME Paper No. 80-HT-46.

[31] Leong, L. S., and Cornwell, K., 1979, “Heat Transfer Coefficient in a Reboiler Tube Bundle,” Chemical Engineering, **343**, pp. 219–221.

[32] Hwang, T. H., and Yao, S. C., 1986, “Cross Flow Heat Transfer in Tube Bundles at Low Reynolds Numbers,” ASME J. Heat Transfer, **108**, pp. 697–700.

[33] Leroux, K., and Jensen, M., 1992, “Critical Heat Flux in Horizontal Tube Bundles in Vertical Crossflow of r-113,” ASME J. Heat Transfer, **114**, pp. 179–184.

[34] Jensen, M., and Tang, H., 1994, “Correlations for the CHF Condition in Two-Phase Crossflow Through Multitube Bundles,” ASME J. Heat Transfer, **116**, pp. 780–783.

[35] Mandrusiak, G., and Carey, V., 1989, “Convective Boiling in Vertical Channels With Different Offset Strip Fin Geometries,” ASME J. Heat Transfer, **111**, pp. 697–700.

[36] McGillis, G., and Carey, V., 1993, “Subcooled Convective Boiling of Binary Mixtures Over an Array of Heated Elements,” J. Thermophys. Heat Transfer, **7**(2), pp. 346–351.

[37] Roser, R., Thonon, B., and Mercier, P., 1999, “Experimental Investigations on Boiling of N-Pentane Across a Horizontal Tube Bundle: Two-Phase Flow and Heat Characteristics,” International Journal of Refrigeration, **22**, pp. 536–547.

[38] Fand, R. M., Keswani, K. K., Jotwani, M. M., and Ho, R. C. C., 1976, “Simultaneous Boiling and Forced Convection Heat Transfer From a Horizontal Cylinder to Water,” ASME J. Heat Transfer, **98**, pp. 395–400.

[39] Zdravkovich, M. M., 1987, “The Effect of Interference Between Circular Cylinders in Crossflow,” J. Fluids Struct., **1**, pp. 239–261.

[40] Lee, P. C., Tseng, F. G., and Pan, C., 2004, “Bubble Dynamics in Micro Channels. Part I: Single Microchannel,” Int. J. Heat Mass Transfer, **47**, pp. 5575–5589.

[41] Kuo, C.-J., Koşar, A., Peles, Y., Virost, S., Mishra, C., and Jensen, M., 2006, “Bubble Dynamics During Boiling in Enhanced Surface Microchannels,” J. Microelectromech. Syst., **15**(6), pp. 1514–1527.

[42] Revellin, R., and Thome, J. R., 2007, “A New Type of Diabatic Flow Pattern Map For Boiling Heat Transfer in Microchannels,” J. Micromech. Microeng., **17**(4), pp. 788–796.

[43] Mizushima, J., and Suehiro, N., 2005, “Instability and Transition of Flow Past Two Tandem Circular Cylinders,” Phys. Fluids, **17**, p. 104107.

[44] Carey, V. P., 1992, *Liquid-Vapor Phase-Change Phenomena*, Taylor & Francis, London.

[45] Jakob, M., and Fritz, W., 1931, “Versuche über den Verdampfungsvorgang,” Forschung im Ingenieurwesen **2**, pp. 435–447.

[46] Ivey, H. J., 1967, “Relationship Between Bubble Frequency, Departure Diameter and Rise Velocity in Nucleate Boiling,” Int. J. Heat Mass Transfer, **10**, pp. 1023–1040.

[47] Cole, R., 1967, “Frequency and Departure Diameter at Sub-Atmospheric Pressures,” AIChE J., **13**, pp. 779–783.

[48] Zuber, N., 1963, “Nucleate Boiling-the Region of Isolated Bubbles-Similarity With Natural Convection,” Int. J. Heat Mass Transfer, **6**, pp. 53–65.

Heat Transfer in Microchannels With Suspended Solid Particles: Lattice-Boltzmann Based Computations

Reza H. Khiabani

Yogendra Joshi

Cyrus K. Aidun[1]
e-mail: cyrus.aidun@me.gatech.edu

G. W. Woodruff School of Mechanical Engineering,
Georgia Institute of Technology,
Atlanta, GA 30332

This paper presents computational results on the effect of fixed or suspended cylindrical solid particles on heat transfer in a channel flow. The computational method is based on the solution of the lattice-Boltzmann equation for the fluid flow, coupled with the energy equation for thermal transport and the Newtonian dynamic equations for direct simulation of suspended particle transport. The effects of Reynolds number, particle-to-channel size ratio, and the eccentricity of the particle on heat transfer from the channel walls for single and multi-particles are presented. The multi-particle flow condition represents a case with solid particles suspended in the cooling medium, such as in micro/nanofluids, to augment heat transfer. The results provide insight into the mechanism by which suspended particles can change the rate of heat transfer in a microchannel.

[DOI: 10.1115/1.4000860]

Keywords: nanofluid heat transfer, suspended particles, lattice-Boltzmann method for heat transfer, numerical simulation

1 Introduction

There are several applications in thermal systems such as heat exchangers, turbine blade cooling, and electronics thermal management, in which forced convective heat transfer in microchannels is important. The increasing use of microchannel heat exchangers in high performance thermal systems motivates exploration of techniques to further improve the channel heat transfer rate. The possibility to enhance the rate of heat transfer through interaction between a stationary or moving solid particle and the fluid flow confined within a channel is of significant interest. These interactions cause variations in the flow field and temperature distribution and consequently change the thermal performance of the system.

Analytical solutions for laminar forced convection heat transfer in ducts are summarized by Shah and London [1]. Furthermore, many numerical and experimental studies consider different channel flow geometries [2–6]. Khan et al. [7] reported an integral approach to study the heat transfer from a cylinder confined between parallel plates. Mettu et al. [8] and Dennis et al. [9] reported numerical results for heat transfer from an isothermal cylinder in a channel flow. An experimental investigation was done by Nakagawa et al. [10] for the heat transfer in a channel flow around a rectangular cylinder. They have shown that the heat transfer is enhanced compared with a channel with no blockage. Sharma and Eswaran [11] studied the effect of channel confinement on the natural convection from a rectangular body using a finite volume method. Wu et al. [12] studied numerically the transient mixed heat convection around three heated cylinders in a horizontal channel and the effect of cylinder spacing on it.

Several studies consider the effect of a moving solid particle in a channel. Fu and co-workers [13,14] adopted an arbitrary Lagrangian–Eulerian method to simulate the heat transfer induced by an isothermal rectangular body, moving in the streamwise direction in an adiabatic channel. The heat transfer around a heated oscillating cylinder is studied experimentally by Gau et al. [15]. Patnaik et al. [16] did finite element simulations of heat transfer in internal flows employing a velocity correction algorithm, with a Galerkin weighted residual formulation. Most of the previous works outlined above are focused on heat transfer from the solid particle. The fluid flow and heat transfer due to a moving body is studied in some special conditions by finite element methods. These methods consider a moving boundary problem and require remeshing in each (few) time step(s). An alternative method is based on the solution of the discrete Boltzmann equation over a lattice space for the fluid phase. This is a robust and efficient computational method for the analysis of solid particles suspended in fluid [17]. An advantage of the lattice-Boltzmann method is that the code can be easily implemented on parallel processors because of the local nature of the time evolution operator. Another advantage of this method is that the computational time is independent of the Reynolds number and weakly dependent on the number of solid particles, although it is dependent on the size of the computational domain.

In this study, the lattice-Boltzmann method is used together with the energy equation to investigate the effect of solid particles on the fluid flow and heat transfer in a two-dimensional channel. It was shown that the lattice-Boltzmann equation with an appropriate equilibrium distribution function reduces to the full Navier–Stokes equations [18–20]. The method presented here is based on the method developed by Aidun, Lu and Ding (ALD) [17,21], which solves the lattice-Boltzmann equation for the fluid phase, as it is coupled to the movement of the solid particles suspended in the flow. The temperature distribution is found by solving the energy equation using a hybrid differencing scheme. The effects of the Reynolds number, the blockage ratio, and the vertical location of the particle on the heat transfer from the channel walls are considered for the cases of single and multiparticles at rest, moving with a constant velocity, and freely suspended in fluid. The results show that the existence of particles can significantly change the heat transfer characteristics in the channel. This approach can be applied to estimate the effectiveness of employing solid particles within a channel to improve the heat transfer rate.

---

[1] Corresponding author.

Contributed by the Heat Transfer Division of ASME for publication in the JOURNAL OF HEAT TRANSFER. Manuscript received July 23, 2007; final manuscript received February 19, 2009; published online February 17, 2010. Assoc. Editor: Satish G. Kandlikar.

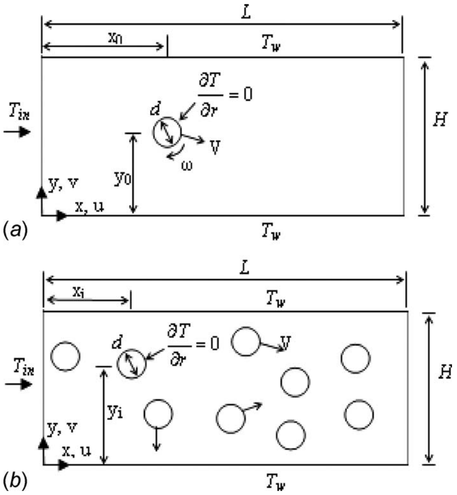

Fig. 1 Schematic of the physical domain

2 Problem Description

The physical domain with the coordinate system and the relevant parameters are presented in Fig. 1. The focus of this study is on the effect of solid particles on the flow and heat transfer in a microchannel flow. Cylindrical solid particles with diameter d are considered for the cases of (i) fixed, (ii) moving with constant velocity, and (iii) freely suspended inside a microchannel with dimensions $L \times H$. The channel walls (top and bottom surfaces) are considered at constant temperature T_w. The particle is assumed to be adiabatic. Periodic boundary conditions for the forced flow are used at the inlet and outlet boundaries at $x=0$ and $x=L$, respectively. The inlet temperature T_{in} of the fluid is assumed constant and the temperature gradient normal to the outlet boundary $(x=L)$ is set to zero.

3 Governing Equations

The lattice-Boltzmann method is used for the flow field simulations. In this method, the physical domain is discretized as a lattice and the flow field is described defining the distribution function $f_{\sigma i}(x,t)$ in each lattice node. The distribution function is the population of fluid particles at location x and time t that move in the discrete directions σi with discrete velocities $e_{\sigma i}$. In the two-dimensional case, the D2Q9 model is used, in which the fluid particle may be at rest or move to the nearest lattice point in the horizontal, vertical, or diagonal directions [22]. The velocity vectors are denoted as e_{01} for the fluid particles at rest, e_{1i} for the fluid particles moving in the horizontal or vertical directions, and e_{2i} for the fluid particles moving in the diagonal directions. The discrete velocity vectors are defined as

$$e_{01} = (0,0)$$

$$e_{1i} = \left(\cos\frac{i-1}{2}\pi, \sin\frac{i-1}{2}\pi\right), \quad i = 1, \ldots, 4 \tag{1}$$

$$e_{2i} = \sqrt{2}\left(\cos\left(\frac{i-1}{2}\pi + \frac{\pi}{4}\right), \sin\left(\frac{i-1}{2}\pi + \frac{\pi}{4}\right)\right), \quad i = 1, \ldots, 4$$

The density $\rho(x,t)$ and the macroscopic velocity vector $\boldsymbol{u}(x,t)$ of the continuum fluid are defined in terms of the fluid distribution function as

$$\rho(x,t) = \sum_{\sigma,i} f_{\sigma i}(x,t) \tag{2}$$

$$\rho(x,t)\boldsymbol{u}(x,t) = \sum_{\sigma,i} f_{\sigma i}(x,t) e_{\sigma i} \tag{3}$$

The discrete Boltzmann equation is used to update the distribution function $f_{\sigma i}(x,t)$ with the Bhatangar–Gross–Krook (BGK) collision term, given by [22]

$$f_{\sigma i}(x + e_{\sigma i}, t+1) - f_{\sigma i}(x,t) = -\frac{1}{\tau}\left[f_{\sigma i}(x,t) - f_{\sigma i}^{\mathrm{eq}}(x,t)\right] \tag{4}$$

where $f_{\sigma i}^{\mathrm{eq}}(x,t)$ is the equilibrium distribution function at x and t, and τ is the relaxation time, which controls the rate of approach to the equilibrium.

The equilibrium distribution function $f_{\sigma i}^{\mathrm{eq}}(x,t)$ is defined as [17]

$$f_{\sigma i}^{\mathrm{eq}}(x,t) = \rho(x,t)\left[A_\sigma + B_\sigma(e_{\sigma i} \cdot \boldsymbol{u}) + C_\sigma(e_{\sigma i} \cdot \boldsymbol{u})^2 + D_\sigma(\boldsymbol{u} \cdot \boldsymbol{u})\right] \tag{5}$$

Considering the conservation laws for mass, momentum, and kinetic energy, the coefficients can be determined as [22]

$$A_0 = \frac{4}{9}, \quad B_0 = 0, \quad C_0 = 0, \quad D_0 = -\frac{2}{3}$$

$$A_1 = \frac{1}{9}, \quad B_1 = \frac{1}{3}, \quad C_1 = \frac{1}{2}, \quad D_1 = -\frac{1}{6} \tag{6}$$

$$A_2 = \frac{1}{36}, \quad B_2 = \frac{1}{12}, \quad C_2 = \frac{1}{8}, \quad D_2 = -\frac{1}{24}$$

The relaxation time is related to the kinematic viscosity by

$$\upsilon = \frac{2\tau - 1}{6} \tag{7}$$

The results presented here for simulating the movement of suspended solid particles are based on the ALD method [21]. In this method, by combining Newtonian dynamics of the solid particles with a lattice-Boltzmann model of the fluid, the movement of the solid particles can be simulated. Furthermore, the interaction between the particles is calculated using the near contact lubrication forces. The no slip boundary conditions are applied at the solid surfaces. The Knudsen number for liquid flow in microchannels is much less than 0.01, so the no slip boundary condition applies. The lattice-Boltzmann operators should be modified at the boundaries to incorporate the boundary conditions. Here, the bounce-back boundary condition is used to calculate the momentum transfer between the fluid and the solid surface, where the boundary is always assumed to be located at the middle of the boundary links [17].

The temperature field is obtained by solving the energy equation

$$\rho c_p\left(\frac{\partial T}{\partial t} + \boldsymbol{u} \cdot \nabla T\right) = k\nabla^2 T \tag{8}$$

The dimensionless temperature is defined as

$$\theta = \frac{T - T_{\mathrm{in}}}{T_w - T_{\mathrm{in}}} \tag{9}$$

Using the lattice units for time, location, and velocity, the dimensionless energy equation and the thermal boundary conditions can be written as

$$\frac{\partial \theta}{\partial t} + \boldsymbol{u} \cdot \nabla \theta = \frac{1}{\mathrm{Re\ Pr}}\nabla^2 \theta \tag{10}$$

$$
\begin{aligned}
&\theta = 0 \quad \text{at} \quad x = 0\\
&\theta = 1 \quad \text{at} \quad y = 0, H\\
&\frac{\partial \theta}{\partial x} = 0 \quad \text{at} \quad x = L\\
&\frac{\partial \theta}{\partial r} = 0 \quad \text{at particle surface}
\end{aligned}
\tag{11}
$$

The Reynolds number $\mathrm{Re}=u_m H/\upsilon$, is defined based on the channel width and the mean inlet velocity u_m. In order to compare the thermal performance, the local Nusselt number is defined as

$$
\mathrm{Nu}_x = \frac{2H}{\theta_w - \theta_{mx}}\left(-\left.\frac{\partial \theta}{\partial y}\right|_{y=0,H}\right) \tag{12}
$$

where θ_w is the nondimensional temperature at the wall and θ_{mx} is the nondimensional form of the mean fluid temperature at location x, defined as

$$
T_{mx} = \frac{1}{u_m H}\int_0^H uTdy \tag{13}
$$

where the mean velocity is given by

$$
u_m = \frac{1}{H}\int_0^H udy \tag{14}
$$

The average Nusselt number between two locations x_1 and x_2 is defined as

$$
\overline{\mathrm{Nu}} = \frac{1}{x_2 - x_1}\int_{x_1}^{x_2} \mathrm{Nu}_x dx \tag{15}
$$

where x_1 can be selected anywhere in the channel. In the following results, the average Nu has been computed between $x_1=25$ and x_2 located at the end of the channel. Eccentricity is defined as a measure of the distance between the vertical positions of the particle with respect to the centerline of the channel, given by

$$
e = \frac{|2y_0 - H|}{H} \tag{16}
$$

Blockage ratio b is defined as a measure of the size of the particle

$$
b = \frac{d}{H} \tag{17}
$$

The computational approach presented here solves the fully coupled transient equation for direct simulation of fluid flow, particle dynamics, and heat transfer [23].

4 Numerical Method Validation

The appropriate grid size for a grid-independent solution is determined first. The numerical results are then validated by comparison with prior results available in the literature for heat transfer from a hot particle in cross flow in a channel. To find the appropriate grid size, the effect of a stationary solid particle on heat transfer in the channel flow is considered. Three mesh sizes of 256×64, 128×32, and 64×16, corresponding to 16065, 3937, and 945 lattice units, are considered. Figure 2 compares the effect of lattice units on the horizontal and vertical velocity, and the temperature distribution along a line parallel to the y axis and through the center of the solid particle. The difference between the results for grid sizes of 256×64 and 128×32 is less than 5% in the worse case. Therefore, the lattice size of 256×64 is selected.

To validate the results, heat transfer from a circular cylinder confined in a channel is selected. In this problem, heat is removed from a two-dimensional cylinder with a constant surface temperature confined in a channel. The flow is from left to right. Here, Re is calculated based on the cylinder diameter and the channel flow rate over the cylinder, defined as

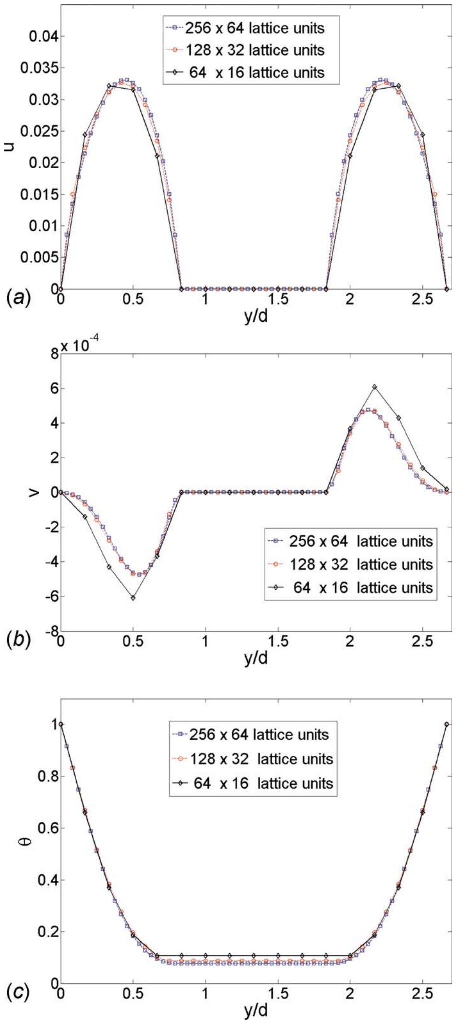

Fig. 2 Comparing (*a*) horizontal velocity, (*b*) vertical velocity, and (*c*) temperature profile for different lattice units

$$
u_c = \frac{1}{d}\int_{y_0-d/2}^{y_0+d/2} u(0,y)dy \tag{18}
$$

Figure 3 shows the streamlines and isotherms for a flow with Pr=0.74 and Re=5 and 50. For Re=5, the streamlines and isotherms are attached and symmetric. At Re=50, a pair of symmetric and counter-rotating vortices appear. Figure 4 shows the snapshots of the streamlines and isotherms at Re=110, where periodic vortex shedding occurs in the cylinder wake. The snapshots are at four equally spaced time intervals through the periodic vortex shedding cycle.

The variation in average cylinder Nu with Re from the present computations are compared with the experimental results of Hilpert [24], numerical results of Mettu et al. [8], and the analytical results of Khan et al. [7] for $b=0.2$ in Fig. 5. The current results are in close agreement with the previous experimental and computational results.

5 Results and Discussions

In this section, the effect of solid cylindrical particles within the channel on the heat transfer from the channel walls is studied. Three cases are considered: (i) stationary, (ii) moving with a con-

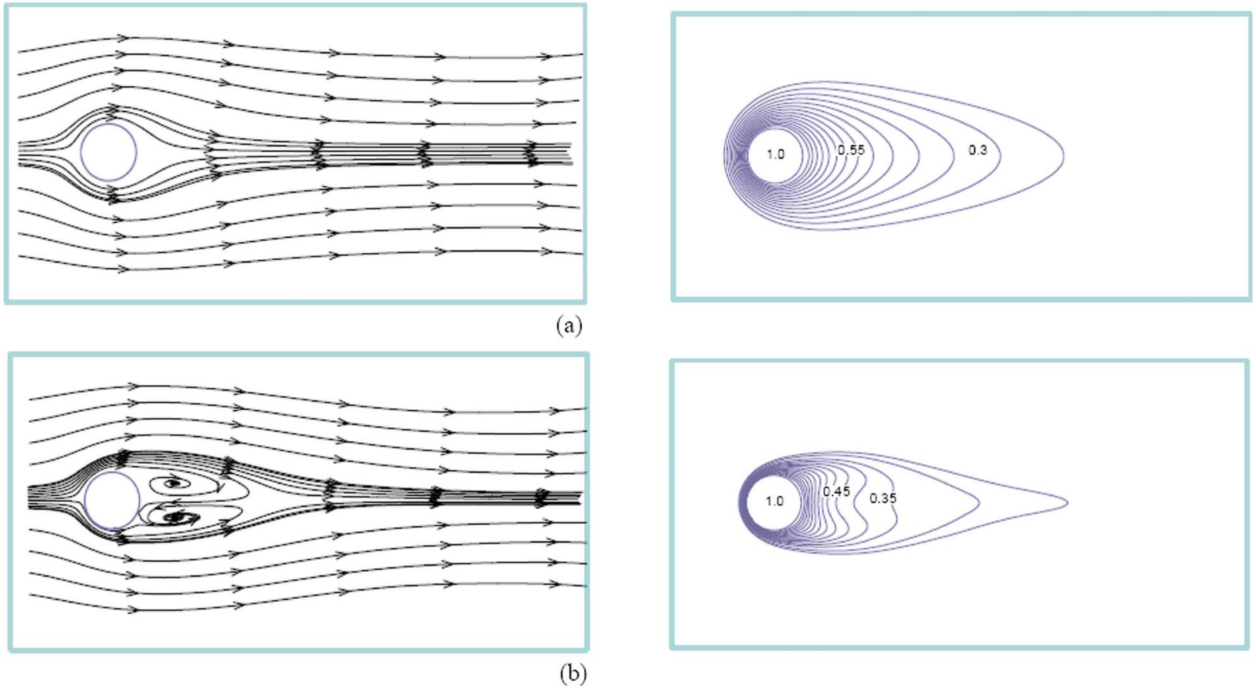

Fig. 3 Streamlines and isotherms around a hot particle for (*a*) Re=5 and (*b*) Re=50

stant velocity, and (iii) freely suspended in the flow. The fluid is water at Pr=6.0. Thorough validation for simulation of freely moving particles suspended in flow is provided in the previous publications by Aidun et al. [17,21].

5.1 Effect of a Single Particle. Figure 6 shows the streamlines and isotherms in a channel with and without a solid particle with different conditions. Comparing Figs. 6(*a*) and 6(*b*), it is seen that the interaction of the fluid with the particle results in deviations in the streamlines. This effect results in a faster fluid motion and larger heat transfer rate near the wall. The constant velocity particle (5*c*), and freely suspended particle (5*d*) cases will be discussed in the following sections.

Figure 7 shows the Nu distribution along the channel walls for pure fluid, as well as a case with a stationary solid particle. Prior analytical [1] and numerical [14] results are also presented in this figure, showing good agreement with the current results. It is seen that the wall Nusselt number is larger near the particle with a local peak in Nu, due to the higher fluid speed in this region. In this case, the local Nu is 90% higher near the particle, and the average Nu for the channel containing a solid particle is 7.6% higher than the average Nu for an unblocked channel. Results show that heat transfer can be enhanced with solid particles inside the channel, suggesting a method to provide cooling in the presence of nonuniform heat dissipation, for example, when there are hot spots in the channel walls that require locally more effective heat transfer. In that case, an obstacle could be placed in the channel behind the hot spot to locally increase the heat transfer rate.

Figure 8 shows the Nu distribution along the channel wall containing a solid particle for different Re. It is seen that with increasing Re, the local peak in Nu increases. The local Nu at the location of the particle for Re=70 and 30 is 67% and 50% higher, compared with the local Nu for Re=15, resulting in a relatively higher average Nu. Therefore, the average Nu for Re=70 and 30 is 55% and 23%, respectively, higher than the average Nu for Re=15.

The size of the particle can affect the flow field, and therefore, thermal performance. Figure 9 shows the distribution of Nu for particles with different sizes. As the size of the particle increases, the streamlines become denser near the wall above and under the particle, causing a higher fluid velocity in the vicinity of the hot walls, and therefore, a better heat transfer rate. For $b=0.35$ and 0.25, the average Nu numbers are 7% and 3% higher than $b=0.15$ at Re=40.

The effect of the vertical position or eccentricity of the solid particle on the Nu variation is shown in Fig. 10. When the particle is located closer to the lower wall, there is a higher peak in the Nu distribution at the lower wall compared with the upper wall. For example, for 22% eccentricity, the local peak in the lower wall is 14% higher than the local peak when the particle is at the center. In this case, the streamlines are denser near the lower wall, and the fluid velocity is higher, resulting in a better heat removal and a higher Nu. Therefore, the local peak in Nu increases, as the eccentricity increases. On the other hand, the fluid velocity is slower near the upper wall. Therefore, the local peak at the upper wall is smaller, relative to the local peak at the lower wall. It is also smaller than the local peak when the particle is located at the center of the channel. The fluid tends to move toward the center of the channel after the particle. The movement is more effective near the lower wall because of the higher fluid velocity. It causes Nu to decline more at the lower wall, compared with the upper wall. Therefore, the overall heat transfer enhancement is more effective in the upper wall and the average Nu is 8% larger in this case. Thus, moving the particle toward a wall in the channel locally enhances the heat transfer at that wall, but the overall heat transfer becomes worse at that wall.

5.2 Effects of Multiple Particles. When there is more than one particle inside the channel, the Nu variation along the channel walls is more complex. Figure 11 presents the Nu distribution for a channel containing one, two, or three stationary solid particles at different locations at Re=40. The disturbance in the flow field is more, while there are multiple particles inside the channel. Therefore, the heat transfer is enhanced more, and the average Nu is higher. In fact, each particle can locally increase the heat transfer rate due to the flow modification near the wall. If the particles are close to each other, the upstream particle affects the flow downstream. If the particles are far enough, for example, at $x=70$ and

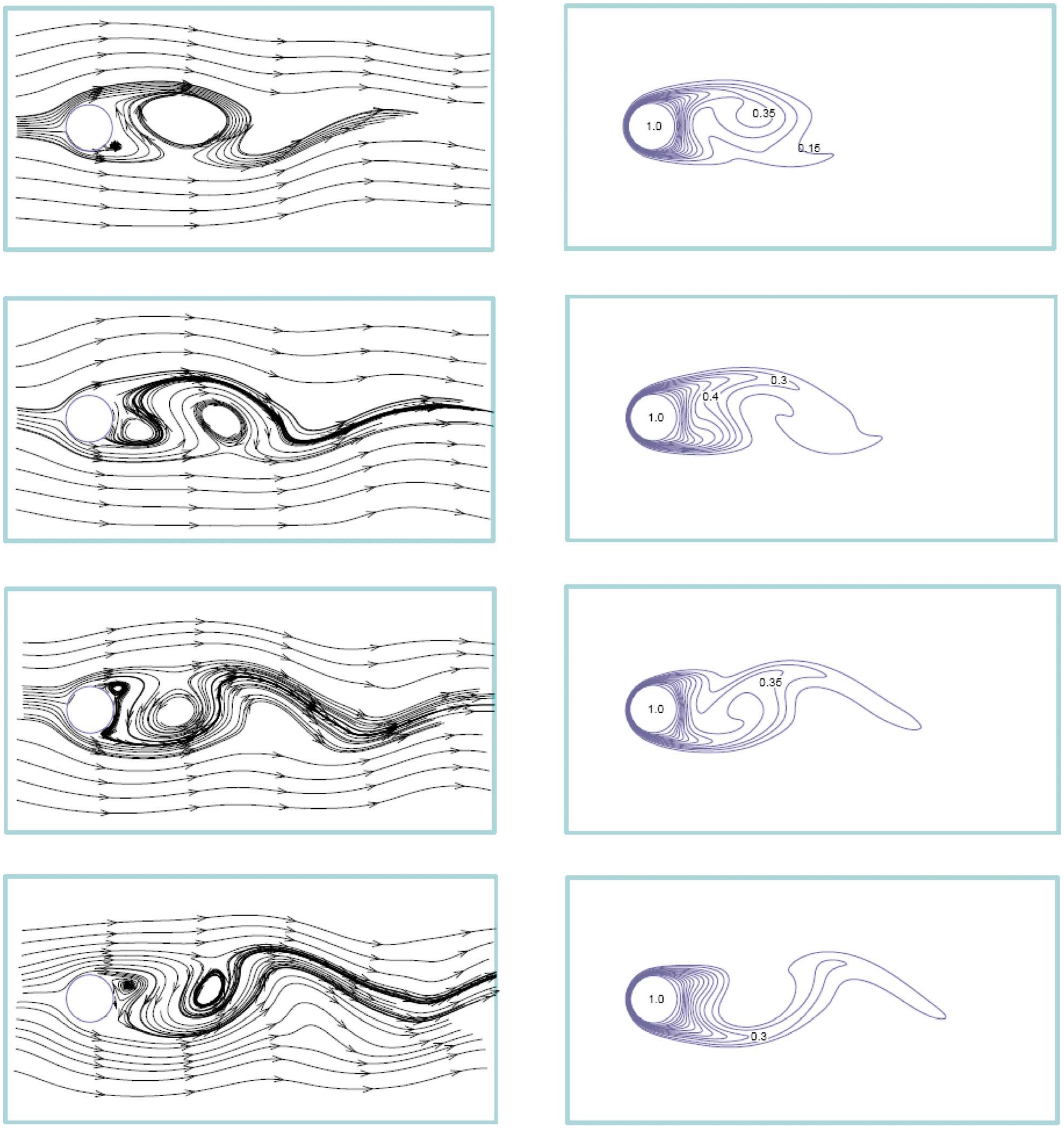

Fig. 4 Snapshots of streamlines and isotherms around a hot particle for Re=110

150, the shape and the magnitude of Nu around the particle may be approximated from the results for a channel containing one particle at that location.

5.3 Effect of a Particle Moving With a Constant Velocity. Figure 6(*c*) shows the streamline and isotherms for a particle, which is moving to the right with a constant velocity equal to 0.03 for Re=50. Compared with a stationary particle, when a particle moves with a constant velocity, there is a sudden vacant space behind it, which is occupied by the surrounding fluid. It causes the fluid to move toward the center right before the particle. This results in a drop in Nu. The flow then passes the particle, and therefore, the streamlines become somehow deflected toward the wall. In front of the particle, there is no obstacle in the flow, so the fluid tends to move toward the center of the channel. The isotherms also behave in a similar manner. Therefore, it is expected that Nu will decease in front of the particle. Figure 12 shows the Nu distribution at different Re. The sudden drop right before the particle is because of the earlier mentioned movement of the adjacent fluid to the vacant space before the particle. At higher Re, the mean fluid velocity is higher than the particle velocity; therefore, it is observed that as the Re increases, the local Nu increases as well.

5.4 Effect of Freely Suspended Particles. When a particle is freely suspended in the main flow, as in Fig. 6, the flow conditions are different, relative to when a particle moves with constant velocity: For this case, the streamlines and isotherms are shown in Fig. 6(*d*) for Re=50. The streamlines behind the particle are deflected to the wall. On the other hand, the streamlines smoothly go toward the center of the channel in front of the particle. These effects are also observed in the isotherms, which are denser and

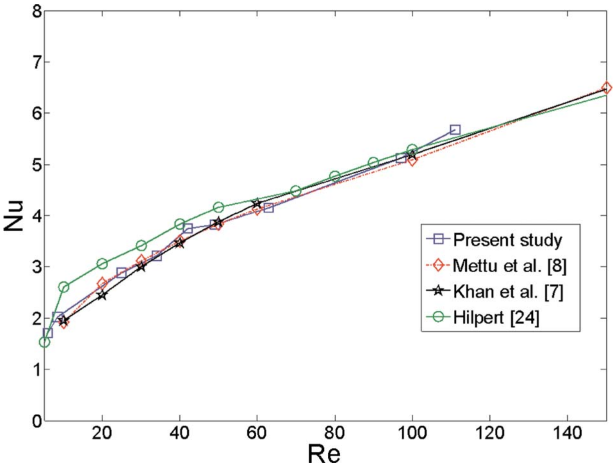

Fig. 5 Variation in average Nu with Re

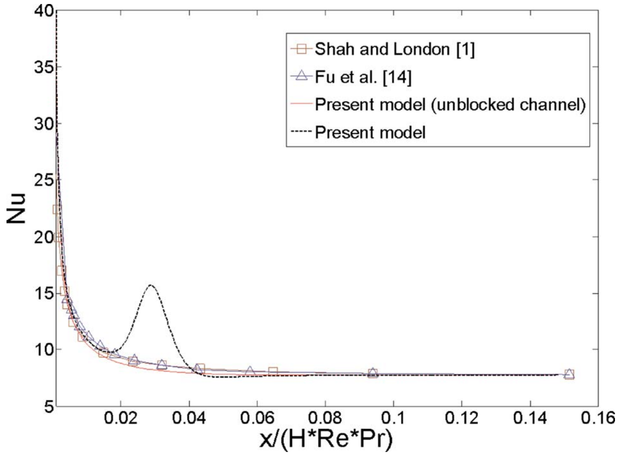

Fig. 7 Local Nu distribution along the channel wall; *b*=35%

smoother behind the particle, causing the local Nu to be relatively constant in the region at the upstream proximity of the particle. Furthermore, a sudden drop of Nu, such as in Fig. 12, is not observed in this case. The isotherms decline toward the center in front of the particle, and finally approach those in a channel containing no particles. Therefore, Nu decreases in front of the particle. Figure 13 shows the Nu distribution at different times during the flow.

Nu distribution along the channel wall, containing a feely suspended solid particle for different Re, is shown in Fig. 14. For the same number of time steps, the displacement of a particle suspended in a flow with lower Re is smaller. It is seen that with increasing Re, the local Nu in the entry region increases. The effect of the suspended particle on the Nu distribution is similar for different Re. Nu is nearly constant behind the particle and there is a sudden drop in Nu in front of the particle.

Figure 15 shows the distribution of Nu for suspended particles with different sizes. It is seen that the blockage ratio does not have an important effect on the Nu distribution.

There are several applications in which there are multiple solid particles freely suspended in the cooling medium (Fig. 1, b) such as in micro/nanofluids. Figure 16 presents the Nu distributions for channel flow, in which 48 solid particles are suspended in the fluid. The suspension flow is nonhomogeneous, so the Nu distribution in the upper and the lower channel walls are not similar. It is observed that the Nu distribution is similar to that in a channel containing no particles with some local fluctuations. The location and the amount of variation in the Nu depend on many factors such as the position of the particle and the Re. The heat transfer is enhanced when the particles are closer to the wall, or when a particle is located close to another particle. Furthermore, when there is more than one particle inside the channel, the Nu variation along the channel walls is more complex. Therefore, different thermal effects are expected when the particles are in different locations. These results are especially interesting for studying heat transfer in a nanofluid. In that case, many particles are homogeneously distributed in the fluid, and we expect to observe similar effects on heat transfer. Simulations with larger domains considering nanofluids are required to confirm these influences.

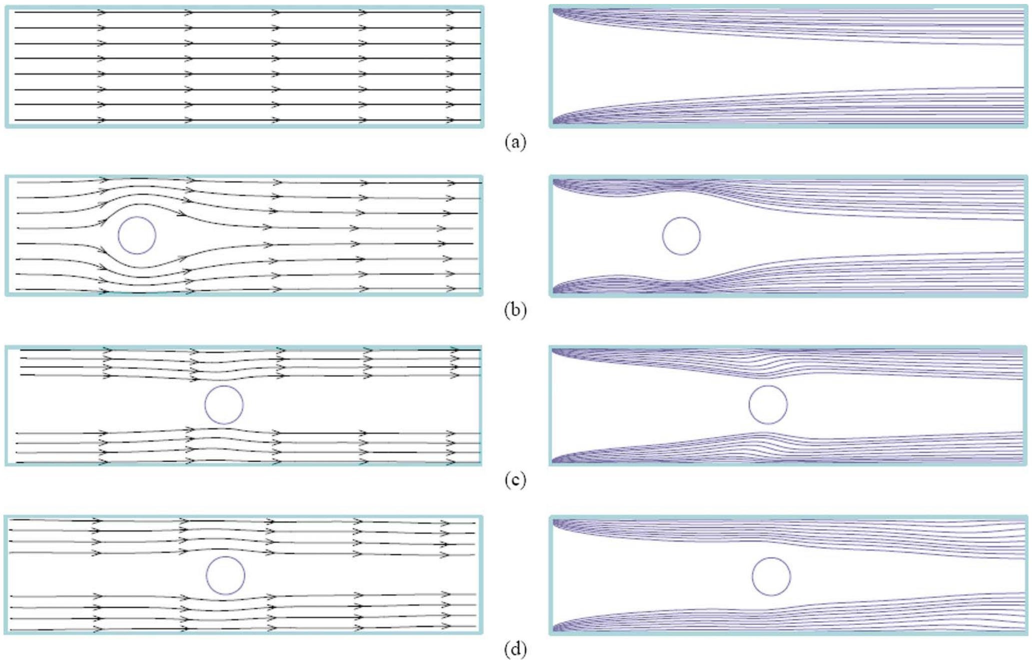
(a)
(b)
(c)
(d)

Fig. 6 Streamlines and isotherms for (*a*) unblocked channel, a channel containing a (*b*) stationary, (*c*) moving with constant velocity, and (*d*) freely suspended particle

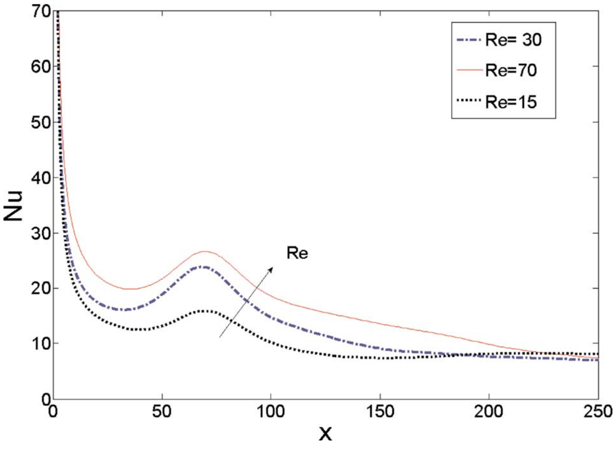

Fig. 8 Effect of Re on Nu (stationary particle); *b*=35%

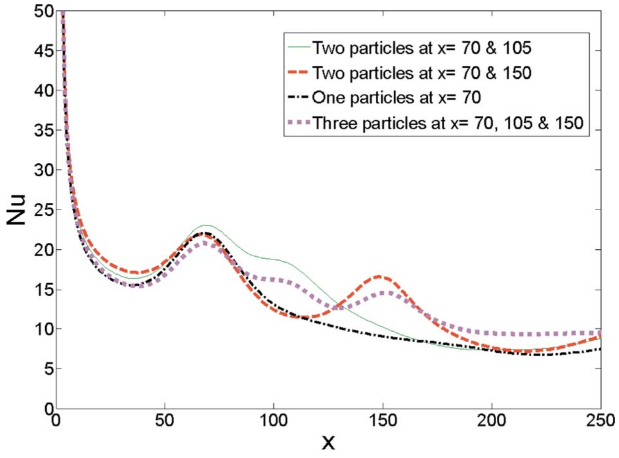

Fig. 11 Nu distribution (multiple stationary particles); Re=40

6 Conclusions

The effect of existence of cylindrical solid particles on the heat transfer in a microchannel is studied, based on the lattice-Boltzmann method for the fluid flow and the energy equation. The results show that each particle can locally enhance the heat transfer, and therefore, the average heat transfer can be enhanced. These local effects can be used to provide an efficient cooling for a system with nonuniform heat generation, or for a substrate with hot spots. The average Nu increases with increasing Re and blockage ratio for a particle, which is stationary or is moving with constant speed. When a particle is moving with a constant velocity, the streamlines and isotherms have somewhat different shapes,

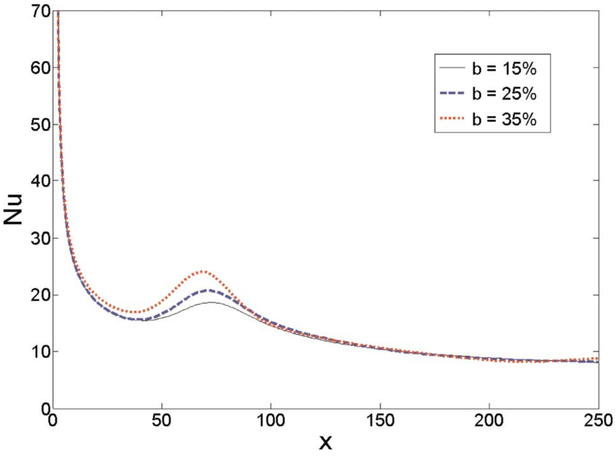

Fig. 9 Effect of blockage ratio on Nu (stationary particle); Re =40

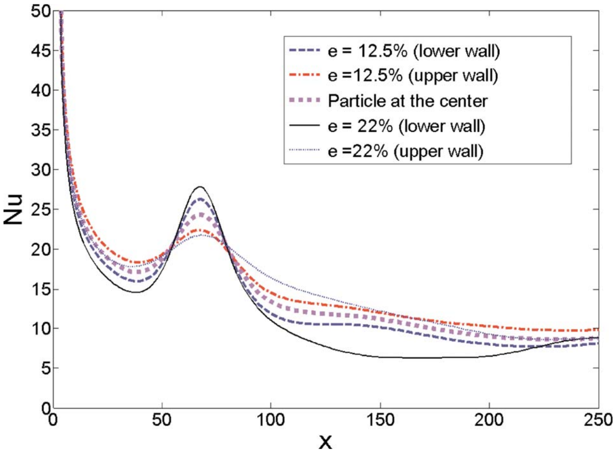

Fig. 10 Effect of Eccentricity on Nu (stationary particle); Re =40 and *b*=35%

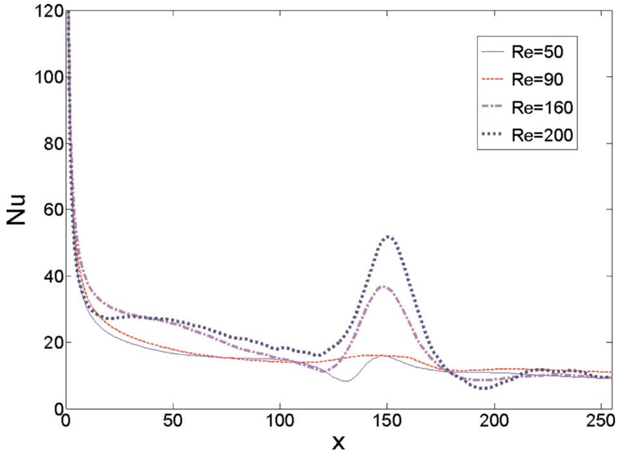

Fig. 12 Nu distribution for particle moving with const. velocity; *b*=35%

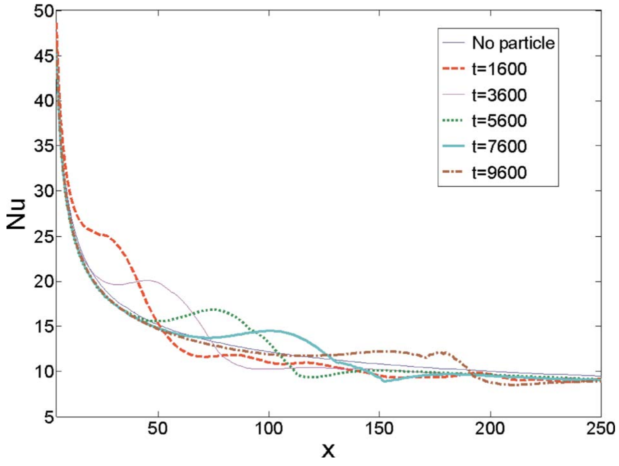

Fig. 13 Nu distribution at different times (freely suspended particle); Re=45 and *b*=35%

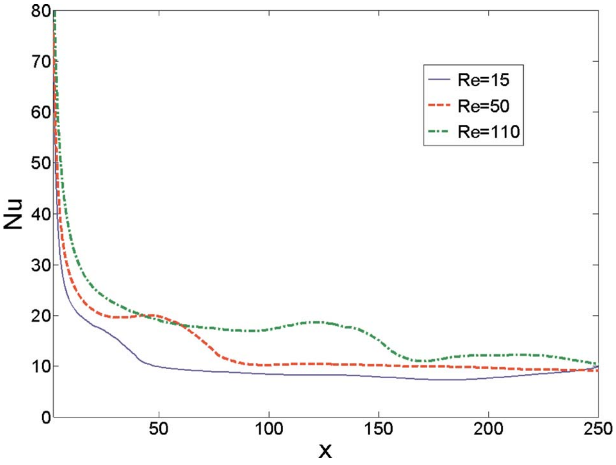

Fig. 14 Effect of Re on Nu distribution; $b=35\%$

compared with when there is a freely suspended particle inside the channel. The spatial distribution of the particles can also affect the heat transfer. This effect may be neglected when there is large number of particles homogeneously distributed within the fluid. These results may be used to estimate the effectiveness of applying solid particles within the flow to improve the rate of heat transfer.

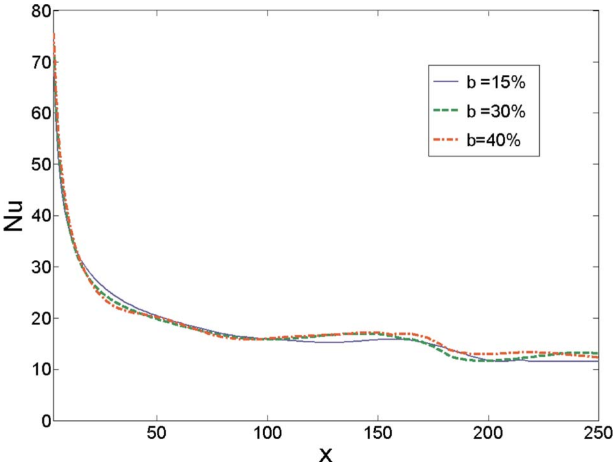

Fig. 15 Effect of blockage ratio on Nu (suspended particle); Re=110

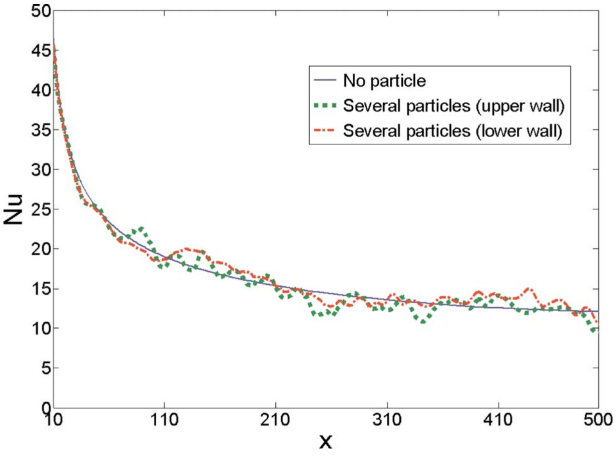

Fig. 16 Nu distributions for a fluid containing several suspended particles; Re=220 and $b=6\%$

Nomenclature

b = blockage ratio
c_p = specific heat (J/kg K)
d = diameter (m)
e = velocity vector, eccentricity
f = distribution function
h = convective heat transfer coefficient ($\mathrm{W/m^2\,K}$)
H = channel height (m)
k = conductivity (W/m K)
L = channel length (m)
Nu = Nusselt number
Pr = Prandtl number
r = radius (m)
Re = Reynolds number
t = time (s)
T = temperature (K)
u = velocity
x = location, horizontal axis
y = vertical location

Greek Symbols

ν = kinematic viscosity ($\mathrm{m^2/s}$)
θ = dimensionless temperature
ρ = density ($\mathrm{kg/m^3}$)
τ = relaxation time
ω = angular velocity

Subscripts

in = inlet
m = mean
w = wall

References

[1] Shah, R. K., and London, A. L., 1978, *Laminar Flow Forced Convection in Ducts*, Academic, New York.

[2] Hung, T. C., and Fu, C. S., 1999, “Conjugate Heat Transfer Analysis for the Passive Enhancement of Electronic Cooling Through Geometric Modification in a Mixed Convection Domain,” Numer. Heat Transfer, Part A, **35**(5), pp. 519–535.

[3] Wang, Y., and Ghajar, A. J., 1991, “Effect of Component Geometry and Layout on Flow Distribution for Surface Mounted Electronic Components: A Smoke Flow Visualization Study,” *Heat Transfer Enhancements in Electronics Cooling*, ASME, New York, Vol. 183, pp. 25–31.

[4] Saidi, M. H., and Khiabani, R. H., 2007, “Forced Convective Heat Transfer in Parallel Flow Multilayer Microchannels,” ASME J. Heat Transfer, **129**(9), pp. 1230–1236.

[5] Aidun, C. K., and Lin, S. P., 1987, “Large Amplitude Modulation of Heat Transfer From a Circular Cylinder,” Int. J. Heat Mass Transfer, **30**(2), pp. 408–411.

[6] Aidun, C. K., and Lin, S. P., 1986, “Conjugate Heat Transfer From a Hollow Cylinder,” *Proceedings of the Eighth International Heat Transfere Conference*, San Francisco, CA, Vol. 2, pp. 373–378.

[7] Khan, W. A., Culham, J. R., and Yovanovich, M. M., 2004, “Fluid Flow and Heat Transfer From a Cylinder Between Parallel Planes,” J. Thermophys. Heat Transfer, **18**(3), pp. 395–403.

[8] Mettu, S., Verma, N., and Chhabra, R. P., 2006, “Momentum and Heat Transfer From an Asymmetrically Confined Circular Cylinder in a Plane Channel,” Heat Mass Transfer, **42**(11), pp. 1037–1048.

[9] Dennis, S. C. R., Hudson, J. D., and Smith, N., 1968, “Steady Laminar Forced Convection From a Circular Cylinder at Low Reynolds Numbers,” Phys. Fluids, **11**(5), pp. 933–934.

[10] Nakagawa, S., Senda, M., Kikkawa, S., Wakasugi, H., and Hiraide, A., 1998, “Heat Transfer in Channel Flow Around a Rectangular Cylinder,” Heat Transfer-Jpn. Res., **27**(1), pp. 84–97.

[11] Sharma, A., and Eswaran, V., 2005, “Effect of Channel-Confinement and Aiding/Opposing Buoyancy on the Two-Dimensional Laminar Flow and Heat Transfer Across a Square Cylinder,” Int. J. Heat Mass Transfer, **48**(25–26), pp. 5310–5322.

[12] Wu, H.-W., Perng, S.-W., Huang, S.-Y., and Jue, T.-C., 2006, “Transient Mixed Convective Heat Transfer Predictions Around Three Heated Cylinders in a Horizontal Channel,” Int. J. Numer. Methods Heat Fluid Flow, **16**(6), pp. 674–692.

[13] Fu, W. S., and Yang, S. J., 2000, "Numerical Simulation of Heat Transfer Induced by a Body Moving in the Same Direction as Flowing Fluids," Heat Mass Transfer, **36**(3), pp. 257–264.
[14] Fu, W. S., and Tong, B. H., 2003, "Numerical Investigation of Heat Transfer of a Heated Channel With an Oscillating Cylinder," Numer. Heat Transfer, Part A, **43**(6), pp. 639–658.
[15] Gau, C., Wu, J. M., and Liang, C. Y., 1999, "Heat Transfer Enhancement and Vortex Flow Structure Over a Heated Cylinder Oscillating in the Crossflow Direction," ASME Trans. J. Heat Transfer, **121**(4), pp. 789–795.
[16] Patnaik, B. S. V., Gowda, Y. T. K., Ravisankar, M. S., Narayana, P. A. A., and Seetharamu, K. N., 2001, "Finite Element Simulation of Internal Flows With Heat Transfer Using a Velocity Correction Approach," Sadhana: Proc., Indian Acad. Sci., **26**(3), pp. 251–283.
[17] Aidun, C. K., Lu, Y., and Ding, E. J., 1998, "Direct Analysis of Particulate Suspensions With Inertia Using the Discrete Boltzmann Equation," J. Fluid Mech., **373**, pp. 287–311.
[18] Hu, H. H., Joseph, D. D., and Crochet, M. J., 1992, "Direct Simulation of Fluid Particle Motions," Theor. Comput. Fluid Dyn., **3**(5), pp. 285–306.
[19] Chen, H., Chen, S., and Matthaeus, W. H., 1992, "Recovery of Navier-Stokes Equations Using a Lattice-Gas Boltzmann Method," Phys. Rev. A, **45**(8), pp. 5339–5342.
[20] McNamara, G. R., and Zanetti, G., 1988, "Use of the Boltzmann Equation to Simulate Lattice-Gas Automata," Phys. Rev. Lett., **61**(20), pp. 2332–2335.
[21] Ding, E.-J., and Aidun, C. K., 2003, "Extension of the Lattice-Boltzmann Method for Direct Simulation of Suspended Particles Near Contact," J. Stat. Phys., **112**(3–4), pp. 685–708.
[22] Hou, S., Zou, Q., Chen, S., and Doolen, G., 1995, "Simulation of Cavity Flow by the Lattice Boltzmann Method," J. Comput. Phys., **118**(2), pp. 329–347.
[23] Versteeg, H. K., and Malalasekera, W., 1995, *An Introduction to Computational Fluid Dynamics: The Finite Volume Method*, Wiley, New York.
[24] Hilpert, R., 1933, "Waermeabgabe Von Geheizten Draehten Und Rohren Im Luftstrom," Forsch. Geb. Ingenieurwes., **4**(5), pp. 215–224.

Hee Joon Lee
Department of Mechanical Engineering,
Carnegie Mellon University,
Pittsburgh, PA 15213

Dong Yao Liu
College of Power Engineering,
Nanjing University of Science and Technology,
Jiangsu 210094, P. R. China

Y. Alyousef
KACST Energy Research Institute,
Riyadh 11442, Saudi Arabia

Shi-chune Yao
Fellow ASME
Department of Mechanical Engineering,
Carnegie Mellon University,
Pittsburgh, PA 15213
e-mail: scyao@cmu.edu

Generalized Two-Phase Pressure Drop and Heat Transfer Correlations in Evaporative Micro/Minichannels

Existing databases and correlations in literature on the microchannel pressure drop and heat transfer are reviewed in this paper. From this review, it is found that none of the existing correlations can cover the wide ranges of working fluids, operational conditions, and different microchannel dimensions. In addition, the importance of the Bond number, which relates the nominal bubble dimension or capillary parameter with the channel size, is revealed in this paper. Using the Bond number, improved correlations of pressure drop and heat transfer are established, which predict the existing data well over a wide range of channel sizes, fluids, and operational conditions. [DOI: 10.1115/1.4000861]

Keywords: two-phase, correlation, pressure drop, heat transfer, evaporation, microchannel

1 Introduction

Evaporative microchannel heat transfer is attractive due to the large surface area and the utilization of latent heat of vaporization; however, severe pressure drop occurs, wherein relatively large pumping power is required. At the initial planning stage of designing an evaporative microchannel system for a given application, it is important to select the working fluids and the optimal channel dimensions for the application in concern. However, it is difficult to identify a good correlation for the two-phase pressure drop because most of the published correlations covers mainly the author's own or a restricted set of experimental data. For example, Ribatski et al. [1] concluded that the correlation of Muller-Steinhagen and Heck [2] gave the best prediction for the macrochannel data. The homogeneous flow model and the Mishima–Hibiki [3] model were ranked together as the second best. However, none of the present methods can be a general design tool for microchannels [1]. In a later section of this paper, the limitations of the existing correlations are further revealed in detail. Generally speaking, most of the reported correlations do not have the capability to predict two-phase pressure drop with a wide range of working fluids and channel sizes.

In considering the two-phase heat transfer of micro/minichannels, it is found that different correlations may give drastically different predictions even for a same data set. For example, Thome et al. [4] suggested a flow regime based model to predict the two-phase heat transfer in minichannels of a refrigerant. As will be detailed in a later section of this paper, it appears that Thome's model works satisfactorily on others' refrigerant data, but cannot predict either water in a microchannel or refrigerant data in a macrochannel. On the other hand, Lee–Mudawar [5] proposed the two-phase heat transfer correlation, which satisfactory predicts water data in a microchannel, but not for a refrigerant experimental data. Therefore, many of the well-recognized heat transfer correlations also cannot be used over wide ranges of working fluids and operational conditions for general design.

On the other hand, there has been an issue on the classification of evaporative microchannels. Kandlikar–Grande [6] set the classification in terms of the absolute diameter of channels. However, it is important to question whether this criterion should be varied when different working fluids and operational pressures are applied.

Theoretically, the criterion of being a microchannel should be based upon the comparison of the channel dimension with the nominal size of the bubbles. When the bubbles are squeezed in the flow channel, the pressure drop and heat transfer phenomena will deviate from those of conventional channels. As a result, the microchannel behavior shall occur. Since the nominal bubble size is closely related to the capillary parameter, the comparison of the nominal bubble size and the channel diameter can be expressed in terms of the confinement number, which is in inverse relation to the Bond number, Bo. Here, the Bond number is used

$$\mathrm{Bo} = \frac{g(\rho_l - \rho_g)d_h^2}{\sigma} = \frac{d_h^2}{d_b^2} \tag{1}$$

where

$$d_b = \sqrt{\frac{\sigma}{g(\rho_l - \rho_g)}}$$

In general, surface tension is an important parameter for a two-phase flow in a microchannel. Except for the Bond number, the Weber and capillary numbers include surface tension. However, the capillary number does not contain the channel dimension. The Weber number involves flow inertia, which may not be significant in a microchannel. Therefore, the Bond number is selected here. On the other hand, the Bond number is only dependent on properties. To include the fluid dynamics, the thermodynamic quality is considered important because it is related with the velocity ratio between phases, which means interfacial drag. Therefore, it is anticipated that the Bond number and thermodynamic quality may have the potential of relating the existing data in literature together into a general correlation.

In this paper, we analyzed a large number of experimental data of different fluids for the two-phase pressure drop and heat transfer coefficient in micro/minichannels with various existing correlations to verify their respective accuracies. The significance of the Bond number in predicting the two-phase pressure drop and heat transfer coefficient in micro/minichannels was investigated. In order to accommodate for simple correlations to support a broad scope of initial design of evaporative microchannel sys-

---

Manuscript received January 31, 2008; final manuscript received February 19, 2009; published online February 18, 2010. Assoc. Editor: Satish G. Kandlikar.

Table 1 Average error (%) of two-phase pressure drop experimental data set when compared with the existing correlations (all data are diabatic experiments; unit: percentage)

		Exp. data									
	Correlation	Qu and Mudawar [8] (water)	Lee et al. [16] (water)	Brutin and Tadrist [17] (*n*-pentane)	Ungar and Cornwell [15] (ammonia)	Pettersen [14] (CO_2)	Yun et al. [10] (R410A)	Yan and Lin [18] (R134A)	Tran et al. [13] (R134A)	Tran et al. [13] (R12)	Quibén and Thome [11] (R134A, R22, R410A)
Parameters	Data	19	20	69	40	20	39	61	94	122	1745
	Bo	0.02	0.02	0.33	0.5	1.1~1.7	2.5~3	4.6~5.1	9.5~9.6	9.7~9.9	71~253
	$\mathrm{Re}_{lo}(\times 10^3)$	0.32	0.05~0.11	1.21~5.6	0.22~1.03	1.5~3.1	1.5~3.1	0.46~1.82	0.72~6.6	0.92~10.1	
	$\mathrm{Re}_{go}(\times 10^3)$	7.2	1.2~2.5	33.4~155	3~13.8	10.4~21	18.6~37.2	8.86~35.5	10.7~97.2	13~144.2	
	d_h (mm)	0.35	0.35	0.89	1.46	0.81	1.44	2	2.46	2.46	8, 13.8
	ρ_f/ρ_g	1400	1400	208	75~83	6.4~9.6	26~39	53	28~30	27~29	31~75
	x	0~0.2	0~0.24	0~0.3	0.09~0.98	0.3~0.98	0.28~0.85	0.09~0.93	0.24~0.9	0.21~0.94	0~1.0
	G ($\mathrm{kg/m^2/s}$)	255	41.8~65.2	228~2267	20.3~92.6	190~380	200~400	50~200	52~475	69~704	70~700
Existing corr.	Homogeneous	252	66	414	25	64	56	68	40	37	
	Lockhart–Mar. (LL)	46	49	77	69	79	78	95	69	64	
	Lockhart–Mar. (LT)	71	33	68	28	24	48	57	19	33	
	Mishima–Hibiki	15	38	18	63	79	74	91	55	48	
	Lee–Lee	25	58	54	58	27	59	61	24	36	
	Lee–Mudawar	1	18	199	76	55	53	92	51	51	
	Muller–Steinhagen	132	32	138	22	50	45	51	26	28	30[a]
	English–Kandlikar	8	15	8	76	88	85	97	76	72	
	Quibén–Thome	801	388	387	616						30[b]
New corr.	Bo and exit quality	13	9	6	28	31	51	79	24	27	

[a] 82% of experimental data of Quibén [11].

[b] 76% of experimental data of Quibén [11].

tems, the sophisticated two-phase flow regime approach of correlation was not selected in this paper, due to the multiple step of the process for design application and the lack of regime maps in some cases. Instead, the modification of simple commonly used correlations was studied. Finally, generalized correlations utilizing the Bond number and other relevant parameters were developed for various working fluids, channel sizes, and working conditions.

2 Review of Existing Data and Correlations

2.1 Two-Phase Pressure Drop

2.1.1 Literature Reviews and Data Selection. Recently, there have been a number of papers that discuss two-phase pressure drop in microchannels. Most of the studies built their own new correlations based on mainly the respective author's own experiments. Mishima and Hibiki [3] reported that the Chisholm parameter of the Lockhart–Martinelli correlation should include the tube diameter to correlate air and water data. Lee and Lee [7] studied the two-phase pressure drop of air-water in rectangular microchannels. They found that the Mishima–Hibiki model is not accurate in its data predictions. They suggested a new correlation that accounts for the effect of mass flux and gap size. Qu and Mudawar [8] reviewed existing correlations and compared them to their water data in microchannels of size $231\times 713\ \mu\mathrm{m}^2$. They reported that two of the microchannel correlations (Mishima–Hibiki, Lee–Lee) predicted their experiment data reasonably well. They developed a correlation with variable channel size and mass velocity. Lee and Mudawar [9] explored the two-phase pressure drop of R134A in a microchannel. They reported that conventional macrochannel correlations predicted their refrigerant data better than microchannel correlations. Their conclusions were consistent with the R410A experiment of Yun et al. [10], which reported that the two-phase pressure drops followed general trends observed in large diameter tubes. Lee and Mudawar [9] developed new correlations in a similar manner as Lee and Lee [7], based on both their R134A data and water data of Qu and Mudawar [8]. Quibén and Thome [11,12] developed a new macrochannel pressure drop model at each two-phase flow regime. Although the comparisons were reasonably agreeable, their correlations only covered CO_2 data in a microchannel. Tran et al. [13] studied the flow boiling pressure drop of refrigerants (R134A, R12, and R113) and developed a correlation. Pettersen [14] studied CO_2 in tubes with a 0.8 mm inner diameter and a length of 0.5 m. Ungar and Cornwell [15] studied ammonia flows in small diameter horizontal tubes and indicated that the homogeneous flow model with the McAdams equation predicts the two-phase pressure drop for ammonia. Most of these correlations were compared with the author's own data, but were not compared with wide ranges of published data of different microchannel dimensions and different working fluids.

In the present study, nine sets of experimental two-phase pressure drop data were collected for micro/minichannels of diameters below 3 mm, as shown in Table 1, in which the working fluids are water [8,16], *n*-pentane [17], ammonia [15], CO_2 [14], R410A [10], R134A [13,18], and R12 [13]. The reason that adiabatic experimental data were not collected in these data sets is because the nature of the bubble nucleation of diabatic microchannels could be different from adiabatic experiments, and the general correlation will be mainly applied to the design of evaporative microchannel systems with heat transfer. Therefore, all collected data sets are for diabatic experiments. In reviewing the working fluids, it is found that there are only limited data sets of diabatic water experiments in microchannels with the complete experimental conditions reported. Furthermore, R410A is a mixture of two refrigerants (R32/R125). Since R410A is a nearly azeotropic mixture, which behaves as pure substances at phase change [19], the R410A is not regarded as a problem and is included in the data sets.

In the case in which the Bond number is less than 1, flow instabilities were reported in the water (Bo=0.02) data of Qu and Mudawar [8] and the *n*-pentane (Bo=0.33) data of Brutin and Tadrist [17], because a growing bubble was squeezed by narrow channel surfaces. A throttling valve at the inlet was adopted by Qu and Mudawar [8] to reduce flow instabilities. They estimated the uncertainties as 4% and 3.5% for the flow rate and pressure measurement, respectively, and the uncertainty of heat loss as 4%. Brutin and Tadrist [17] used a buffer tank to reduce flow instabilities, and collected 69 stable data points. Heat loss was 5% in Brutin's experiment. In the case in which the Bond number was larger than 1, no flow instabilities were reported.

Overall, 484 data points were considered in this paper. Except for the CO_2 data of Pettersen [14], the maximum uncertainties of experiments were ±2 kPa [13] and ±0.25% of the full scale [16] for pressure measurements and ±0.3°C [8] for temperature measurements.

2.1.2 Basic Equations. Two-phase pressure drop consists of frictional, accelerational, and gravitational pressure drop

$$\Delta p_{\text{tp}} = \Delta p_{\text{fric}} + \Delta p_{\text{acc}} + \Delta p_{\text{gr}} \tag{2}$$

All of the selected data were obtained in horizontal channels, with the gravitational pressure drop considered as neglected. There are two general approaches in predicting the pressure drop of two-phase flows [20]: the homogeneous flow model and the separated flow model. The homogeneous flow model assumes that two-phase flows have equal vapor and liquid velocities. On the other hand, the separated flow model assumes different velocities for each phase, and correlations are established empirically with a two-phase multiplier and void fraction. The differential forms of frictional and accelerational pressure drop for the separated flow model are [20]

$$-\left.\frac{dp}{dz}\right|_{\text{fric}} = -\left(\left.\frac{dp}{dz}\right|_{\text{fric}}\right)_l \phi_l^2 \tag{3}$$

$$-\left.\frac{dp}{dz}\right|_{\text{acc}} = G^2 \frac{d}{dz}\left[\frac{x^2 v_g}{\alpha} + \frac{(1-x)^2 v_l}{(1-\alpha)}\right] \tag{4}$$

The single phase friction factor for laminar flows is

$$f_{\text{sp}}\,\text{Re} = 24[1 - 1.3553\beta + 1.9467\beta^2 - 1.7012\beta^3 + 0.9564\beta^4 - 0.2537\beta^5] \tag{5}$$

Lee and Lee [7] reported that the origin of this polynomial equation was obtained by Hartnett and Kostic [21]. The Blasius equation [20] is adopted for the turbulent friction factor.

A typical two-phase multiplier is the Lockhart–Martinelli model [20] using the Chisholm parameter C

$$\phi_l^2 = 1 + \frac{C}{X} + \frac{1}{X^2} \tag{6}$$

where

$$X^2 = \left(\left.\frac{dp}{dz}\right|_{\text{fric}}\right)_l \Big/ \left(\left.\frac{dp}{dz}\right|_{\text{fric}}\right)_g$$

Several authors have modified the Chisholm parameter, based on their experimental data. For example, the Mishima–Hibiki model [3] considered the channel diameter effect

$$C_{\text{MH}} = 21(1 - e^{-0.319 d_h}) \tag{7}$$

to correlate air and water data. Zivi's void fraction [22]

$$\alpha_{\text{zivi}} = \left[1 + \frac{1-x}{x}\left(\frac{\rho_g}{\rho_l}\right)^{2/3}\right]^{-1} \tag{8}$$

was commonly adopted for separated flow models of annular flows in micro/minichannels.

To compare existing correlations against the nine complete databases of the two-phase pressure drop in micro/minichannels, calculations were made to the channel divided into 100 segments along the flow to integrate Eqs. (3) and (4). The properties were recalculated along the saturation pressure in each segment. The properties of working fluids come from the NIST database [23].

2.1.3 Data Comparison. Qu and Mudawar [8] reported comparisons of many existing correlations with their microchannel water data. Those correlations are either based upon the homogeneous flow model or the separated flow model, where modifications are made on the Chisholm parameter. Only the correlations of Mishima–Hibiki [3] and Lee–Lee [7] are acceptable. Yun et al. [10] and Lee and Mudawar [9] reported that conventional macrochannel correlations predicted their refrigerant data in microchannels well, as opposed to microchannel correlations. This is due to the comparison of relative channel sizes. In the case of water, a nominal bubble is squeezed due to a low Bond number. However, the nominal bubble size is less than the channel diameter for a high Bond number fluid such as a refrigerant. Therefore, a macrochannel correlation may work with refrigerants in a microchannel.

Table 1 shows the average absolute error of two-phase pressure drop predictions when compared with experimental data sets. The average error is defined as

$$\text{Average error} = \frac{1}{N}\sum_{i=1}^{N} \frac{|\Delta p_{\text{exp},i} - \Delta p_{\text{cal},i}|}{\Delta p_{\text{exp},i}} \times 100(\%) \tag{9}$$

In Table 1, the predictions of Mishma–Hibiki [3] and English–Kandlikar [24], which are the best ones for water and *n*-pentane among all correlations, are provided. English and Kandlikar [24] modified the Chisholm factor in the Mishima–Hibiki model as 5 for the laminar-laminar flows on adiabatic experimental conditions. In Table 1, the modifying correlation of English–Kandlikar predicted the collected water and *n*-pentane data well, but not for the refrigerant data. The predictions of classical homogeneous and separated flow models are also provided as reference. The homogeneous flow model is typically used for bubbly flow, where the Bond number is large. This is typical for the refrigerant, but not for water. It can be observed that when the Bond number increases, the average error of the homogeneous model decreases. This is evident from the data in Table 1, which shows that the error decreases from 252% for water (Bo=0.02), 414% for *n*-pentane (Bo=0.33), to 37% for R12, which has a Bond number of 9.89. It is obvious that a homogeneous flow model cannot predict the data when the Bond number is less than 1.

Separated flow models are suitable to the annular flow regime where the nominal size of the bubble is much greater than the channel size, and the Bond number is small. As shown in Table 1, the Lockhart–Martinelli models have a much improved error for water when compared with the homogeneous model. This model is also generally good for refrigerants because, although their Bond numbers are high, the exit quality may not be as small as the flows like that of the frequently annular type. The Mishima–Hibiki model predicted the two-phase pressure drop best as Qu and Mudawar [8] reported, especially with the error of 15% with water and 18% with *n*-pentane at a low Bond number. In general, a separated flow model is favored more than the homogenous model for flows with a small Bond number.

Ribatski et al. [1] reported that the Muller-Steinhagen and Heck correlation [2] was the best prediction with the refrigerant data for the macrochannel. Quibén and Thome [12] reported that the Muller-Steinhagen and Heck correlation provided a reasonable agreement with their data. This correlation was validated, as shown in Table 1. However, the Muller-Steinhagen and Heck correlation shows large errors of 132% with water and 138% with *n*-pentane; meaning, it is not good for a microchannel and working fluid at a small Bond number.

Although Quibén and Thome [11,12] provided a reasonable argument on the importance of the two-phase flow regime in the correlation of the two-phase pressure drop, their flow correlation

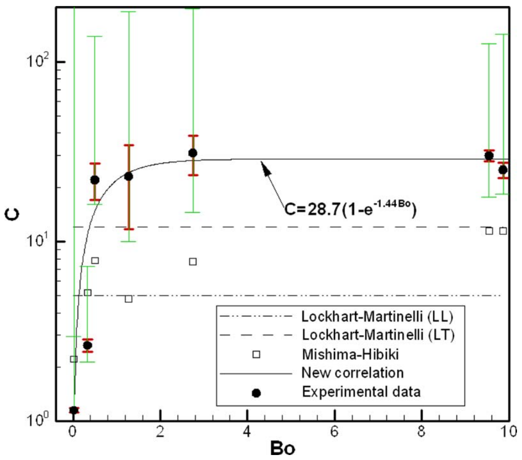

Fig. 1 Chisholm parameter versus Bond number

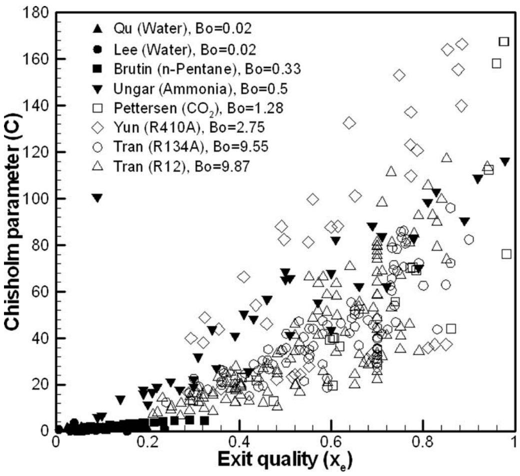

Fig. 2 Chisholm parameter versus exit quality

is difficult to apply to a wide range of pressure drop calculations. This is because the flow regime is dependent upon many factors, which include the flow rate and working fluid. In spite of this, the correlation of Quibén and Thome was applied to water and *n*-pentane data in a microchannel, assuming that the water is in an annular flow pattern and the *n*-pentane is in a slug and intermittent pattern, based on the reported flow pattern image. This correlation shows a huge discrepancy for water and *n*-pentane with the error range between 387 and 800% in Table 1.

For the separated flow model, the relation of the Chisholm parameter and the Bond number is revealed in Fig. 1. From each of the nine experimental data sets, the Chisholm parameter, which gives a minimum error with all experimental data, was calculated and plotted as data points. Moreover, the error bars indicating the standard deviation and the whole range of the data were plotted in Fig. 1. At a large Bond number, many bubbles exist that the interfacial interaction between the phases is stronger than that of one elongated bubble at a low Bond number. As a result, as shown in Fig. 1, the Chisholm parameter, which indicates the interaction of phases, increases as the Bond number increases. In comparison, the Chisholm parameter of the Lockhart–Martinelli model is a fixed value. As shown in Fig. 1, the Mishima–Hibiki model cannot fit the experimental data because the Chisholm parameter is only a function of the channel diameter.

In the present study, instead of using the flow regime like that of Quibén and Thome [11,12], the dynamic behavior of the two-phase flow is characterized in terms of the exit quality. The exit quality was estimated by thermodynamic energy balance in a microchannel. The ratio of the flow velocity of each phase can be estimated at the exit by mass conservation, and is related to the interfacial interaction between the phases. Therefore, as shown in Fig. 2, the Chisholm parameter increases as the exit quality increases. At high quality conditions (mostly Pettersen's CO_2 data), the Chisholm parameter reaches to about 100, which is much higher than the traditional value of 20 in the Lockhart–Martinelli model, or 21 in the Mishima–Hibiki model at large diameter tubes. This is possibly because the interaction among nucleating bubbles and liquid at diabatic flow in the confined microchannels would be much stronger than the two-phase flow in macrochannels.

It can thus be seen that both the Bond number and the exit quality should be considered as important variables to correlate the Chisholm parameter.

2.2 Two-Phase Heat Transfer Coefficient

2.2.1 Literature Reviews and Data Selection. Kandlikar [25] developed a correlation, which combines nucleate boiling and convective mechanisms; however, it was based on the conventional channel size. Moreover, it includes a fluid-dependent parameter F_{fl} in the nucleate boiling term to accommodate different fluids. This is limited to specific working fluids. Kandlikar and Balasubramanian [26] modified this correlation of Kandlikar [25] for minichannels by using the laminar single phase correlation for the heat transfer coefficient and correcting with the Froude number in horizontal micro/minichannels. However, this modified correlation was only validated in the refrigerant data, which are of very large Bond numbers. As shown in Fig. 3, this correlation cannot predict their own water data [27] $(\mathrm{Bo}=0.007)$ and for Qu and Mudawar [28] $(\mathrm{Bo}=0.02)$ in microchannels. Furthermore, due to the use of F_{fl}, which is not known for many fluids, this correlation is not adopted for the present general correlation.

Thome et al. [4] proposed a correlation, based on the assumption that transient evaporation of the liquid film dominates the boiling heat transfer in microchannels. Dupont et al. [29] optimized the parameters in the correlation. The data that they have selected are channels with hydraulic diameters larger than 1.0 mm, and with the working fluids limited to refrigerants. Although this correlation has been validated for the minichannel refrigerant data, it incorporates a significant number of empirical factors such as initial film thickness, minimum film thickness, and bubble pair frequency. The need to include each of the required factors makes this correlation difficult to apply to general applications.

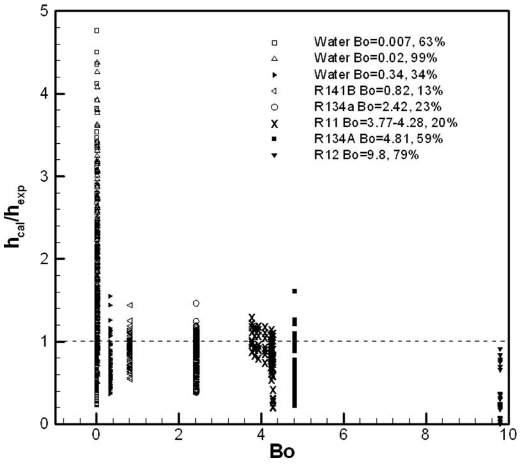

Fig. 3 The prediction of the correlation of Kandlikar compared with the experimental data in micro/minichannels with average % errors shown in legend

Table 2 Average error (%) of flow boiling heat transfer experimental data set when compared with the existing correlations (all data are diabatic experiments; unit: percentage)

Author	Fluids	Bo	Data	d_h (mm)	x_{out}	G (kg/m^2/s)	Error (%)		
							Thome [4]	Lee–Mudawar [5]	New corr.
Steinke and Kandlikar [27]	H_2O	0.007	170	0.207	1.0	157 ~ 1782	283	50	64
Qu and Mudawar [8]	H_2O	0.02	201	0.349	0.2	135 ~ 402	802	12	13
Yen et al. [32]	R123	0.25	70	0.51	1.0	50 ~ 300	81	64	63
Sumith et al. [33]	H_2O	0.34	84	1.45	0.8	23.4 ~ 152.7	251	69	63
Lin et al. [34]	R141B	0.82	94	1.1	0.8	510	34	47	35
Wang et al. [35]	R134A	2.42	189	1.3	0.8	310 ~ 860	23	87	60
Yun et al. [36]	CO_2	2.74	26	1.14	0.9	200 ~ 400	68	87	59
Bao et al. [37]	R11	3.77 ~ 4.28	82	1.95	0.9	50 ~ 1800	13	71	34
Bao et al. [37]	R123	4.8 ~ 5.4	80	1.95	0.9	50 ~ 1800	8	75	38
Agostini and Bontemps [38]	R134A	4.81	120	2.01	0.9	090 ~ 295	31	71	39
Jeong et al. [39]	CO_2	7.1 ~ 10.3	109	2	1.0	150 ~ 750	29	92	66
Tran et al. [40]	R12	9.8	58	2.40,2.46	0.8	45 ~ 505, 63 ~ 832	4	76	31
Pamitran and Choi [41]	R410A	12.7	69	3	1.0	300 ~ 600	119	90	59
Zucher et al. [42]	Ammonia	38.3	271	14	0.9	10 ~ 140	1434	89	58

Lee and Mudawar [5] divided the flow boiling mechanism into three stages, divided by qualities at 0.05 and 0.55. They compared the prediction with the data of water under $x < 0.2$, and with R134A at $0.25 < x < 0.9$ in channels of 0.231 mm by 0.713 mm. However, they did not cite any other published data for comparison. For example, Steinke and Kandlikar [27] published similar water data, except at a much large vapor quality ($x \sim 0.9$).

Kosar et al. [30] and Kuo and Peles [31] investigated water flow boiling in parallel microchannels with structured reentrant cavities. The structured surface significantly reduced the boiling inception superheat. Hence, it substantially increases the heat transfer coefficient and critical heat flux by promoting bubble ebullitions. Therefore, it is inadequate to compare with the existing correlations, which have developed for regular surfaces, not for enhanced nucleation cavities.

Table 2 lists the experimental data of the two-phase heat transfer in micro/minichannels, which covers the fluids of ammonia, CO_2, R11, R12, R22, R123, R134A, R141B, R410A, and water. Hydraulic diameters of the channels are between 0.2 mm to 14 mm. The corresponding Bond number is from 0.007 to 38.3. Overall, 1623 data points were collected in this paper. Except for the R11 and R123 data of Bao [37], the CO_2 data of Jeong et al. [39], and the R410A data of Pamitran and Choi [41], the range of uncertainty of the temperature measurements was between $\pm 0.1°\text{C}$ [27,33,36] and $\pm 0.5°\text{C}$ [34]. Most data do not include the uncertainty of the heat transfer coefficient, but Steinke and Kandlikar [27] and Wang et al. [35] reported 8.61% and ±10.3 ~12.05% for $\pm 0.1°\text{C}$ and $\pm 0.2°\text{C}$ of the uncertainty of temperature, respectively.

2.2.2 Basic Equations. Although many correlations have been proposed for the two-phase heat transfer in micro/minichannels, few of them have been verified with large sets of data. The most popular existing correlations, which include Tran et al. [40], etc, were already compared with the experimental data by Lee and Mudawar [5] and Thome and Ribatski [43]. They [5,43] reported that many of the existing heat transfer correlations cannot predict most of the general microchannel experiment data well. Hence, they developed new correlations recently.

The correlations of Thome et al. [4] and Lee and Mudawar [5] were selected in this paper for consideration. The first reason behind the selection of these two heat transfer correlations is that they are the latest ones developed for a micro/minichannel. The second reason for their selection is that the correlations of Thome et al. and Lee and Mudawar are currently better for refrigerants and water, respectively, than many others.

The correlation of Thome et al. [4] considered a three-zone model (liquid slug, film boiling, dry-out) when a liquid is evaporating in channels. h_l, h_{film}, and h_{dry} are heat transfer coefficients in each zone. The local time-averaged heat transfer coefficient can be presented as follows:

$$h_{\text{tp}} = \frac{1}{\tau}(t_l h_l + t_{\text{film}} h_{\text{film}} + t_{\text{dry}} h_{\text{dry}}) \tag{10}$$

where $1/\tau$ is the bubble formation and departure frequency, and t_l, t_{film}, and t_{dry} are the passing time of liquid slug, film boiling and dry-out zone.

The correlation of Thome et al. [4] gave a clear description of the evaporating process, and the Bond number was introduced to calculate the initial film thickness in the beginning of the bubble slug regime. Unfortunately, the elaborate correlation also introduced five experimentally dependent parameters. Dupont et al. [29] selected a published data set and deduced generalized parameters by the least-squared error method.

Lee and Mudawar [5] divided the flow boiling mechanism into three stages, divided by qualities at 0.05 and 0.55. At lower quality ($x < 0.05$), the heat transfer coefficient is determined by the Martinelli parameter X because nucleate boiling dominates. In the medium quality stage ($0.05 < x < 0.55$), the heat transfer coefficient not only depends on the Martinelli parameter, but also on the boiling and Weber numbers. Meanwhile, in the high quality stage ($x > 0.55$), the heat transfer coefficient is decided by a traditional film boiling correlation. The correlation of Lee and Mudawar [5] is

$$h_{\text{tp}} = 3.856 X^{0.267} h_{\text{sp},l}; \quad 0 \le x < 0.05$$

$$h_{\text{tp}} = 436.48 \text{Bo}^{0.522} \text{We}_{\text{lo}}^{0.351} X^{0.665} h_{\text{sp},l}; \quad 0.05 \le x < 0.55 \tag{11}$$

$$h_{\text{tp}} = \max\{(108.6 X^{1.665} h_{\text{sp},g}), h_{\text{sp},g}\}; \quad 0.55 \le x < 1$$

In the correlation of Lee and Mudawar, the Weber number is introduced to express the influence of the channel diameter to liquid properties.

2.2.3 Data Comparison. As shown in Table 2, the correlation of Thome et al. [4] can only predict refrigerant data satisfactorily in minichannels. However, the correlation of Lee and Mudawar [5] can only work well for water data in microchannels. The average absolute errors are defined similar to Eq. (9).

Figure 4 is the detailed comparison of the correlation of Thome with the refrigerant data in micro/minichannels. It appears that this correlation can predict the heat transfer of refrigerant in microchannels adequately. However, as shown in Fig. 5, it did not compare satisfactorily with the experimental data of water in a

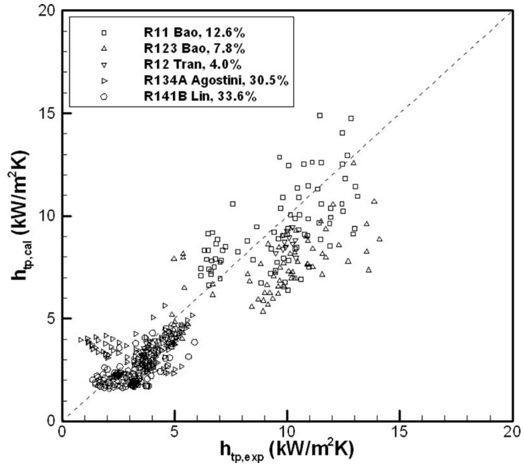

Fig. 4 The prediction of the correlation of Thome compared with the experimental data of refrigerants in micro/minichannels with average % errors shown in legend

microchannel and of ammonia in a macrochannel. As a result, the correlation of Thome et al. [4] only works well for the refrigerant in a minichannel.

Lee and Mudawar [5] used the water data of Qu and Mudawar [28] in their correlation. The detailed comparison of the Lee and Mudawar correlation with the water data of Steinke and Kandlikar [27] are shown in Fig. 6. The experimental conditions of Steinke and Kandlikar are very similar to those of Qu and Mudawar, except the former has a much large vapor quality ($x \sim 0.9$). Interestingly, it is observed that the prediction of the correlation of Lee and Mudawar is inconsistent with the water data of Steinke and Kandlikar [27]. A similar discrepancy also occurs when the correlation of Steinke and Kandlikar is applied to the water data of Qu and Mudawar. Such a data inconsistency may come from flow instability because both Qu and Mudawar [28] and Steinke and Kandlikar [27] reported that flow instabilities existed in their experiment.

Tadrist [44] and Kuan and Kandlikar [45] carefully reviewed publications about flow instabilities in microchannels or narrow spaces. They indicated that flow restriction of microchannels induced two-phase flow instability. Recently, Lee and Yao [46] studied flow instability in microchannels. They suggested that inlet orifices and expanding channels are effective to reduce flow instability. The collected water data sets, Steinke and Kandlikar [27] and Sumith et al. [33], did not suppress flow instability. Even though Qu and Mudawar [28] suppressed pressure drop oscillation using the throttling valve, density wave oscillation still remains in microchannels. It is therefore difficult to expect good data at the condition, which flow instability occurs in a microchannel of water.

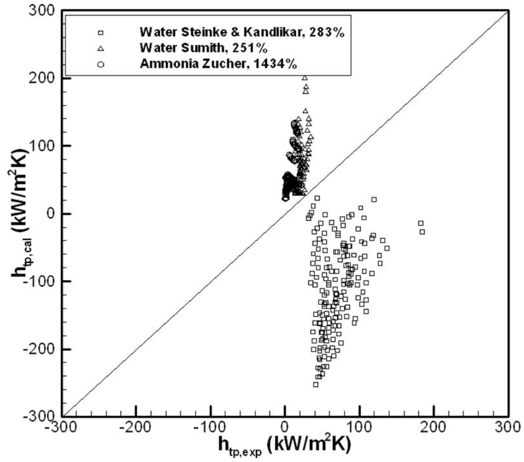

Fig. 5 The prediction of the correlation of Thome compared with the experimental data of water in a microchannel and ammonia in a macrochannel with average % errors shown in legend

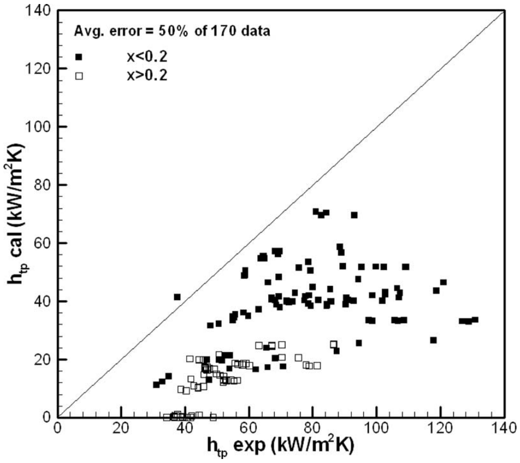

Fig. 6 The prediction of the correlation of Lee and Mudawar compared with the water data of Steinke and Kandlikar

The correlation of Lee and Mudawar [5] also cannot predict the refrigerant data in a micro/minichannel and ammonia data in a macrochannel, as shown in Table 2.

From the above examination, it appears that the recent developed two-phase heat transfer correlations in a micro/minichannel are not generally applicable for a wide range of working fluids.

3 New Correlations

3.1 Two-Phase Pressure Drop. From the above reviews, it is clear that the two-phase pressure drop correlation should include the effects of both Bond number and exit quality. Through the least-squares fitting of the data in Figs. 1 and 2, a new correlation is therefore established in terms of both the Bond number and the exit quality as

$$C_{\text{new}} = 121.6(1 - e^{-22.7\text{Bo}})x_e^{1.85} \tag{12}$$

This new correlation is compared with various data sets at the bottom of Table 1. It appears better than all the existing correlations for the whole range of cases. In particular, this new correlation predicts especially well for water and *n*-pentane with an average error of 13% and 6%, respectively, and about the same average error as the Lockhart–Martinelli laminar-turbulent for the refrigerant. The new correlation is better than the Mishima–Hibiki model for a wide range of working fluids and channel dimensions.

Moreover, traditionally, the Chisholm parameter of the Lockhart–Martinelli model is a fixed value as 5 (laminar-laminar, LL), 10 (turbulent-laminar, TL), 12 (laminar-turbulent, LT), and 20 (turbulent-turbulent, TT). This is a primitive approach to predict pressure drop because the Chisholm parameter is supposed to be a continuous function to describe the interfacial drag between phases. The new correlation is a continuous function. As a reference, when the Bond number is very large (extreme condition of the conventional channel), the Chisholm parameter will be 5, 10, 12, and 20 at the corresponding quality of 0.18, 0.26, 0.29, and 0.39 by the new correlation, respectively. Therefore, the new correlation at the condition of an extremely large channel dimension does not conflict with our traditional understanding of the Chisholm parameter in a macrochannel.

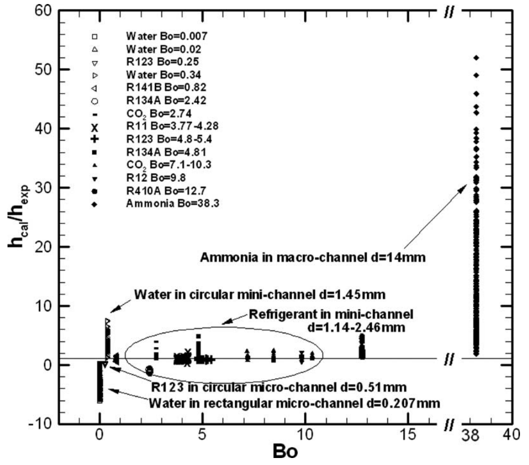

Fig. 7 The correlation of Thome compared with data of a different Bond number

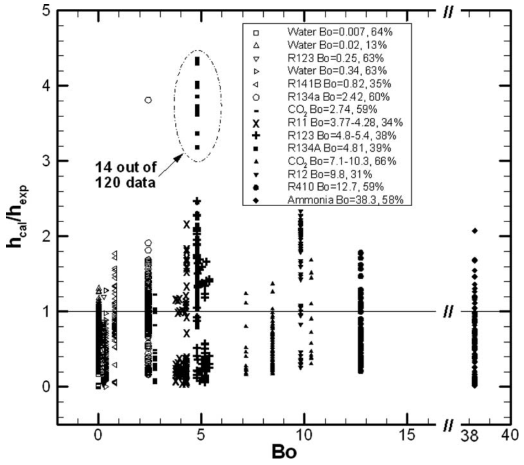

Fig. 9 The modified correlation of Lee and Mudawar with the present correlation factor compared with data of a different Bond number with average % errors shown in legend

3.2 Two-Phase Heat Transfer Coefficient. The Bond number is expected to also have a similarly important effect to the heat transfer in evaporative microchannels. To establish a new correlation, the two most potential correlations, Thome et al. [4] and Lee–Mudawar [5], are considered.

The comparison of the correlation of Thome et al. with the experiment data at a different Bond number is shown in Fig. 7. The ratio of prediction to the experiment of each data point was provided without averaging. It can be seen that this correlation fits the experiment data well when the Bond number is between 2 and 10, which is a typical range for the refrigerant in minichannels [29]. When the Bond number is smaller than 1, such as water in a micro/minichannel or refrigerant in a microchannel, the correlation increases the maximum error by a factor of 5 or more. For the larger Bond number data of ammonia in a macrochannel, the correlation underpredicts the data by the maximum factor of 20 ~30. In other words, Thome's model gives a satisfactory prediction in a minichannel, but for the microchannel flow (Bo<1) or macrochannels (Bo>10), the predictions are off.

Figure 8 shows the comparison of the correlation of Lee and Mudawar [5] with data at various Bond numbers over the range from a microchannel (Bo=0.007) to a macrochannel (Bo=38.3). This correlation, as shown in Eq. (11), contains flow quality and other fluid dynamic effects, but not the Bond number. The correlation of Lee and Mudawar [5] is consistent with their own water data in a microchannel at a low Bond number. As the Bond number increases, the microchannel effect is reduced and the predictions show errors. As shown in Fig. 8, the discrepancy of the prediction and data shows a clear exponential trend as the Bond number increases. An adjustment factor f, which shows the exponential decay effect with the Bond number, is derived by the least-squares fitting method

$$f = 0.958\,\exp(-\,\mathrm{Bo}/1.537) + 0.126 \tag{13}$$

The correlation of Lee–Mudawar [5], given in Eq. (11), should be multiplied by the factor of the reciprocal of f. That means

$$h_{\mathrm{new,Bo}} = \frac{h_{\mathrm{tp,LM}}}{f} = \frac{h_{\mathrm{tp,LM}}}{0.958\,\exp(-\,\mathrm{Bo}/1.537) + 0.126} \tag{14}$$

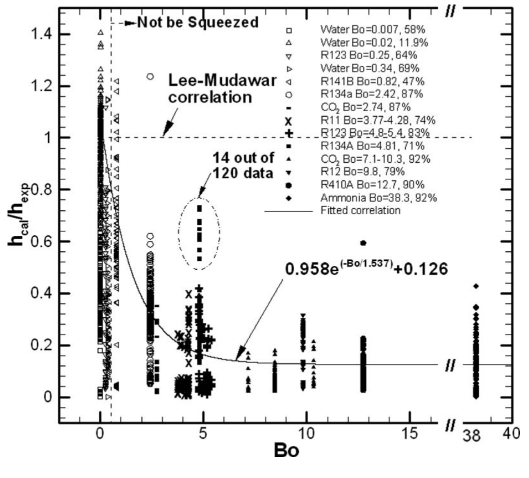

Fig. 8 The correlation of Lee and Mudawar compared with data of a different Bond number with average % errors shown in legend

The predicted results using the improved correlation are compared with the data in Fig. 9. The improved correlation (solid line) fits the trend of data better than the original one (dash line) in Fig. 8, while the discrepancy between the data of Lee–Mudawar [5] and Steinke–Kandlikar [27], possibly related with the flow instability, still exists. Steinke–Kandlikar [27] and Sumith et al. [33] reported severe channel two-phase flow instability and local dry-out in their water boiling experiments. At this condition, it is difficult to decide the local heat transfer coefficient.

Moreover, some R134A data (Bo=4.81) of Agostini and Bontemps [38] are dispersed much in Fig. 9. The dispersed data is only 14 out of 120 points. Most data points are in better agreement with the modified correlation. Nevertheless, as separately shown in Fig. 10, this new correlation reasonably predicted refrigerant data in minichannels. As shown in Table 2, although the modified correlation does not predict the data of refrigerants, as well as the correlation of Thome et al. [4], it has resolved the large errors at very small or very large Bond numbers. As a result, this modified correlation effectively reduces the error of the predicted heat transfer coefficient of micro/minichannels over a wide range of operational conditions and different working fluids for general initial design purposes of evaporative microchannel systems.

4 Conclusion

1. A large amount of two-phase pressure drop and boiling heat transfer data of microchannels are reviewed. It is seen that the existing correlations fail to predict the data over a wide range of working fluids, operational conditions, and channel dimensions.
2. The importance of the Bond number, which relates the capillary parameter (or nominal bubble size) and the channel

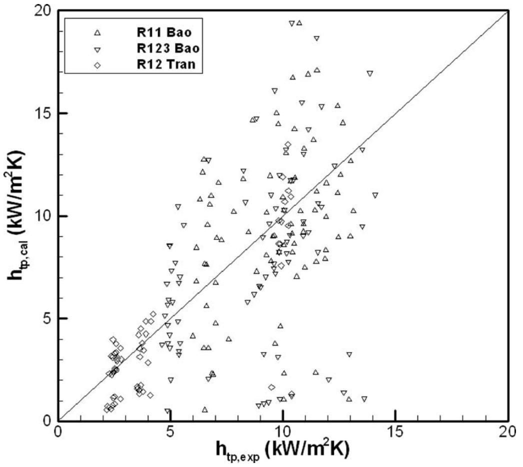

Fig. 10 The prediction of the new improved correlation compared with the experimental data of refrigerants in micro/minichannels

size, has been revealed for correlating data of pressure drop and heat transfer. The Bond number could also be considered as a general parameter to classify a channel as micro, mini, or macrochannel.

3. The Chisholm parameter in the separated flow model of the two-phase pressure drop is modified with both the Bond number and the exit quality in Eq. (12). This new correlation shows much improved results for a wide range of working fluids, operational conditions, and channel dimensions.
4. The Bond number is also used to establish a correction factor, Eq. (14), to the Lee–Mudawar correlation of heat transfer. The results also show much improved predictions of heat transfer in different working fluids at wide ranges of operational conditions and channel sizes. Should any new correlation be developed by researchers in the future, it is important to include the Bond number effect in the correlation.

Acknowledgment

This work was supported in part by the Pennsylvania Infrastructure Technology Alliance, a partnership of Carnegie Mellon, Lehigh University, and the Commonwealth of Pennsylvania's Department of Community and Economic Development (DCED).

Nomenclature

B = boiling number
Bo = Bond number
C = Chisholm parameter
d_h = hydraulic diameter (mm)
f = adjustment factor for new heat transfer coefficient
g = the acceleration of gravity (m/s^2)
h = heat transfer coefficient (kW/m^2 K)
LL = laminar-laminar
LT = laminar-turbulent
Re = Reynolds number
TL = turbulent-laminar
TT = turbulent-turbulent
We = Weber number
X = Lockhart–Martinelli parameter
x = quality
z = channel length

Greek Symbols

α = void fraction
β = aspect ratio of rectangular channel
Δ = difference
ϕ = two-phase multipliers
ρ = density
σ = surface tension
τ = bubble formation and departure time

Subscripts

acc = accelerational
b = bubble
Bo = Bond number
dry = dry-out
e = exit
film = film boiling
fric = frictional
g = vapor
go = vapor only
gr = gravitational
LM = Lee–Mudawar
l = liquid
lo = liquid only
MH = Mishima–Hibiki
new = new correlation
sp = single phase
tp = two-phase

References

[1] Ribatski, G., Wojtana, L., and Thome, J. R., 2006, "An Analysis of Experimental Data and Prediction Methods for Two-Phase Frictional Pressure Drop and Flow Boiling Heat Transfer in Micro-Scale Channels," Exp. Therm. Fluid Sci., **31**(1), pp. 1–19.
[2] Muller-Steinhagen, H., and Heck, K., 1986, "A Simple Friction Pressure Drop Correlation for Two-Phase Flow in Pipes," Chem. Eng. Process., **20**(6), pp. 297–308.
[3] Mishima, K., and Hibiki, T., 1996, "Some Characteristics of Air-Water Two-Phase Flow in Small Diameter Vertical Tubes," Int. J. Multiphase Flow, **22**(4), pp. 703–712.
[4] Thome, J. R., Dupont, V., and Jacobi, A. M., 2004, "Heat Transfer Model for Evaporation in Microchannels. Part I: Presentation of the Model," Int. J. Heat Mass Transfer, **47**(14–16), pp. 3375–3385.
[5] Lee, J., and Mudawar, I., 2005, "Two-Phase Flow in High-Heat-Flux Micro-Channel Heat Sink for Refrigeration Cooling Applications: Part II—Heat Transfer Characteristics," Int. J. Heat Mass Transfer, **48**(5), pp. 941–955.
[6] Kandlikar, S. G., and Grande, W. J., 2003, "Evolution of Microchannel Flow Passages—Thermohydraulic Performance and Fabrication Technology," Heat Transfer Eng., **24**(1), pp. 3–17.
[7] Lee, H. J., and Lee, S. Y., 2001, "Pressure Drop Correlations for Two-Phase Flow Within Horizontal Rectangular Channels With Small Height," Int. J. Multiphase Flow, **27**(5), pp. 783–796.
[8] Qu, W., and Mudawar, I., 2003, "Measurement and Prediction of Pressure Drop in Two-Phase Micro-Channel Heat Sinks," Int. J. Heat Mass Transfer, **46**(15), pp. 2737–2753.
[9] Lee, J., and Mudawar, I., 2005, "Two-Phase Flow in High-Heat-Flux Micro-Channel Heat Sink for Refrigeration Cooling Applications: Part I—Pressure Drop Characteristics," Int. J. Heat Mass Transfer, **48**(5), pp. 928–940.
[10] Yun, R., Heo, J. H., and Kim, Y., 2006, "Evaporative Heat Transfer and Pressure Drop of R410A in Microchannels," Int. J. Refrig., **29**(1), pp. 92–100.
[11] Quibén, J. M., and Thome, J. R., 2007, "Flow Pattern Based Two-Phase Frictional Pressure Drop Model for Horizontal Tubes. Part I: Diabatic and Adiabatic Experimental Study," Int. J. Heat Fluid Flow, **28**(5), pp. 1049–1059.
[12] Quibén, J. M., and Thome, J. R., 2007, "Flow Pattern Based Two-Phase Frictional Pressure Drop Model for Horizontal Tubes. Part II: New Phenomenological Model," Int. J. Heat Fluid Flow, **28**(5), pp. 1060–1072.
[13] Tran, T. N., Chyu, M.-C., Wambsganss, M. W., and France, D. M., 2000, "Two-Phase Pressure Drop of Refrigerants During Flow Boiling in Small Channels: An Experimental Investigation and Correlation Development," Int. J. Multiphase Flow, **26**(11), pp. 1739–1754.
[14] Pettersen, J., 2004, "Flow Vaporization of CO_2 in Microchannel Tubes," Exp. Therm. Fluid Sci., **28**(2–3), pp. 111–121.
[15] Ungar, E. K., and Cornwell, J. D., 1992, "Two-Phase Pressure Drop of Ammonia in Small Diameter Horizontal Tubes," AIAA Paper No. 92-3891.
[16] Lee, H. J., Liu, D., and Yao, S. C., 2008, "Experimental Study of Pressure Drop and Flow Instability in Evaporative Micro-Channels," *Proceedings of the ASME Heat Transfer, Fluids, Energy, Solar and Nano Conference*, Jacksonville, FL.
[17] Brutin, D., and Tadrist, L., 2004, "Pressure Drop and Heat Transfer Analysis of Flow Boiling in a Minichannel: Influence of the Inlet Condition on Two-Phase Flow Stability," Int. J. Heat Mass Transfer, **47**(10–11), pp. 2365–2377.
[18] Yan, Y.-Y., and Lin, T.-F., 1998, "Evaporation Heat Transfer and Pressure Drop of Refrigerant R134a in a Small Pipe," Int. J. Heat Mass Transfer, **41**(24), pp. 4183–4194.
[19] Cheng, L., and Mewes, D., 2006, "Review of Two-Phase Flow and Flow

Boiling of Mixtures in Small and Mini Channels," Int. J. Multiphase Flow, **32**(2), pp. 183–207.
[20] Collier, J. G., and Thome, J. R., 1994, *Convective Boiling and Condensation*, Oxford University Press, New York, Chap. 2.
[21] Hartnett, J. P., and Kostic, M., 1989, "Heat Transfer to Newtonian and Non-Newtonian Fluids in Rectangular Ducts," Adv. Heat Transfer, **19**, pp. 247–356.
[22] Zivi, S. M., 1964, "Estimation of Steady-State Steam Void-Fraction by Means of the Principle of Minimum Entropy Production," ASME J. Heat Transfer, **86**, pp. 247–252.
[23] http://webbook.nist.gov/chemistry/fluid/
[24] English, N. J., and Kandlikar, S. G., 2005, "An Experimental Investigation Into the Effect of Surfactants on Air-Water Two-Phase Flow in Minichannels," *Proceedings of the Third International Conference on Microchannels and Minichannels*, Toronto, Ontario, Canada.
[25] Kandlikar, S. G., 1990, "A General Correlation for Two Phase Flow Boiling Heat Transfer Coefficient inside Horizontal and Vertical Tubes," ASME J. Heat Transfer, **112**(1), pp. 219–228.
[26] Kandlikar, S. G., and Balasubramanian, P., 2004, "An Extension of the Flow Boiling Correlation to Transition, Laminar, and Deep Laminar Flows in Minichannels and Microchannels," Heat Transfer Eng., **25**(3), pp. 86–93.
[27] Steinke, M. E., and Kandlikar, S. G., 2004, "An Experimental Investigation of Flow Boiling Characteristics of Water in Parallel Microchannels," ASME J. Heat Transfer, **126**(4), pp. 518–526.
[28] Qu, W., and Mudawar, I., 2003, "Flow Boiling Heat Transfer in Two-Phase Micro-Channel Heat Sinks—I. Experimental Investigation and Assessment of Correlation Methods," Int. J. Heat Mass Transfer, **46**(15), pp. 2755–2771.
[29] Dupont, V., Thome, J. R., and Jacobi, A. M., 2004, "Heat Transfer Model for Evaporation in Microchannels. Part II: Comparison With the Database," Int. J. Heat Mass Transfer, **47**(14–16), pp. 3387–3401.
[30] Kosar, A., Kuo, C.-J., and Peles, Y., 2005, "Boiling Heat Transfer in Rectangular Microchannels With Reentrant Cavities," Int. J. Heat Mass Transfer, **48**(23–24), pp. 4867–4886.
[31] Kuo, C.-J., and Peles, Y., 2007, "Local Measurement of Flow Boiling in Structured Surface Microchannels," Int. J. Heat Mass Transfer, **50**(23–24), pp. 4513–4526.
[32] Yen, T. H., Kasagi, N., and Suzuki, Y., 2002, "Forced Convective Boiling Heat Transfer in Microtubes at Low Mass and Heat Fluxes," *Proceedings of the Symposium on Compact Heat Exchangers, A Festschrift on the 60th Birthday of Ramesh K. Shah*, Grenoble, France, pp. 401–406.
[33] Sumith, B., Kaminaga, F., and Matsumura, K., 2003, "Saturated Flow Boiling of Water in a Vertical Small Diameter Tube," Exp. Therm. Fluid Sci., **27**(7), pp. 789–801.
[34] Lin, S., Kew, P. A., and Cornwell, K., 2001, "Two-Phase Heat Transfer to a Refrigerant in a 1 mm Diameter Tube," Int. J. Refrig., **24**(1), pp. 51–56.
[35] Wang, L.-H., Chen, M., and Croll, M., 2005, "Experimental Study of Flow Boiling Heat Transfer in Mini-Tube," *Proceedings of the Third International Conference on Microchannels and Minichannels*, Toronto, Ontario, Canada.
[36] Yun, R., Kim, Y., and Kim, M. S., 2005, "Convective Boiling Heat Transfer Characteristics of CO_2 in Microchannels," Int. J. Heat Mass Transfer, **48**(2), pp. 235–242.
[37] Bao, Z. Y., Fletcher, D. F., and Haynes, B. S., 2000, "Flow Boiling Heat Transfer of Freon R11 and HCFC123 in Narrow Passages," Int. J. Heat Mass Transfer, **43**(18), pp. 3347–3358.
[38] Agostini, B., and Bontemps, A., 2005, "Vertical Flow Boiling of Refrigerant R134a in Small Channels," Int. J. Heat Fluid Flow, **26**(2), pp. 296–306.
[39] Jeong, S., Cho, E., and Kim, H., "Evaporative Heat Transfer and Pressure Drop of CO_2 in a Microchannel Tubes," *Proceedings of the Third International Conference on Microchannels and Minichannels*, Toronto, Ontario, Canada.
[40] Tran, T. N., Wambsganss, M. W., and France, D. M., 1996, "Small Circular- and Rectangular-Channel Boiling With Two Refrigerants," Int. J. Multiphase Flow, **22**(3), pp. 485–498.
[41] Pamitran, A. S., and Choi, K. I., 2003, "Effect on Boiling Heat Transfer of Horizontal Smooth Microchannel for R410A and R407C," *Proceedings of the 21st IIR International Congress of Refrigeration*, Washington, DC.
[42] Zürcher, O., Favrat, D., and Thome, J. R., 2002, "Evaporation of Refrigerants in a Horizontal Tube: An Improved Flow Pattern Dependent Heat Transfer Model Compared to Ammonia Data," Int. J. Heat Mass Transfer, **45**(2), pp. 303–317.
[43] Thome, J. R., and Ribatski, G., 2005, "State-of-the-Art of Two-Phase Flow and Flow Boiling Heat Transfer and Pressure Drop of CO_2 in Macro- and Micro-Channels," Int. J. Refrig., **28**(8), pp. 1149–1168.
[44] Tadrist, L., 2007, "Review on Two-Phase Flow Instabilities in Narrow Spaces," Int. J. Heat Mass Transfer, **28**(1), pp. 54–62.
[45] Kuan, W. K., and Kandlikar, S. G., 2007, "Experimental Study on the Effect of Stabilization on Flow Boiling Heat Transfer in Microchannels," Heat Transfer Eng., **28**(8–9), pp. 746–752.
[46] Lee, H. J., and Yao, S. C., 2008, "Stability Analysis and Network Design of Evaporative Micro-Channels," *Proceedings of the ASME Heat Transfer, Fluids, Energy, Solar and Nano Conferences*, Aug. 10–14, Jacksonville, FL.

Numerical Investigation of Heat Transfer Enhancement in a Microchannel With Grooved Surfaces

O. Abouali
e-mail: abouali@shirazu.ac.ir

N. Baghernezhad

Department of Mechanical Engineering,
School of Engineering,
Shiraz University,
Shiraz, Fars 71348-51154, Iran

This paper presents a numerical investigation for two types of grooves (rectangular and arc shapes) fabricated in the microchannel surfaces, which leads to enhancement in single-phase cooling. The pressure drop and heat transfer characteristics of the single-phase microchannel heat sink were investigated numerically for laminar flow. For this purpose, the conjugate heat transfer problem involving simultaneous determination of temperature fields in both solid and liquid regions was solved numerically. The numerical model was validated with comparison to experimental data, in which good agreement was seen. A simple microchannel with available experimental data was selected, and it was shown that using grooved surfaces on this microchannel has a noticeable effect and heat removal rate can be increased using this technique. The results depict that the arc grooves have a higher heat removal flux compared with rectangular grooves but the latter have a higher coefficient of performance for the case in which grooves are made in the floor and both side walls. Also, it was shown that a grooved microchannel with higher wall thickness and lower mass flow rate of cooling water has a higher heat removal flux and coefficient of performance compared with a simple microchannel with minimum wall thickness. Effect of various sizes and distances of the floor grooves was determined, and the cases for maximum heat removal rate and coefficient of performance for both rectangular and arc grooves were obtained. [DOI: 10.1115/1.4000862]

Keywords: microchannel, groove, heat transfer enhancement, COP

1 Introduction

The circuit temperature is one of the most important parameters affecting the performance of silicon integrated circuits. Maintaining the circuit temperature below certain limit of about 85°C is very important. Air cooling has been the most commonly used cooling method for majority of chips used in computer applications but it is not effective for large amount of heat removal rates.

Microchannel heat sinks are an innovative cooling technology for the removal of a large amount of heat from a small area. The heat sink is usually made from a solid with high thermal conductivity such as silicon or copper. Microchannels fabricated into the surface of this solid part by microfabrication technology. Microchannel heat sinks combine the attributes of very high surface area to volume ratio, large convective heat transfer coefficient, small mass and volume, and small coolant inventory. These heat sinks are very suitable for cooling devices such as high performance microprocessors.

The microchannel heat sink cooling concept was first introduced by Tuckerman and Pease [1]. They fabricated a rectangular microchannel heat sink in a 1×1 cm^2 silicon wafer. The channels had a width of 50 μm and a depth of 302 μm, and were separated by 50 μm thick walls. Using water as cooling fluid, the microchannel heat sink was capable of dissipating 790 W/cm^2 with a maximum substrate temperature raise of 71°C above the water inlet temperature and a pressure drop of 2.2 bar.

Heat transfer augmentation has been the subject of many researches. In the 1980s the benefits of this field began to emerge in industry and also in open literature [2]. There are several thousand papers that have been published on the subject of heat transfer enhancement (HTE) or augmentation. Bergles et al. [3] compiled the available literature on convective heat transfer. They sampled several journals, conferences, and patents to generate a database of over 5000 papers and classified the augmentation techniques into two categories: passive and active. Balaras [4] reviewed augmentation techniques and classified them as surface, fluid, and combined and compound methods. The surface methods included modifications to the heated surface such as extended surfaces, roughened surfaces, swirl-flow devices, and surface vibration. The fluids methods involved external fluid vibration, additives, and electrostatic forces. The combined and compound methods use suction, injection, and a combination of the other methods.

Tao et al. [5] presented three possible mechanisms for the single-phase heat transfer enhancement. These mechanisms are as follows: (1) decreasing the thermal boundary layer; (2) increasing flow interruptions; and (3) increasing the velocity gradient near the heated surface. It is the manipulation of these three mechanisms that results in heat transfer augmentation.

Wei et al. [6] presented an experimental and numerical study for a stacked microchannel heat sink. Effects of coolant flow direction, flow rate allocation among layers, and nonuniform heating were studied. They showed that stacked microchannels compared with single-layered microchannels provide larger flow passages, so that for a fixed heat load, the required pressure drop is significantly reduced. They have also identified that over the tested flow rate range, counterflow arrangement provides better temperature uniformity, while parallel flow has the best performance in reducing the peak temperature.

Morini and Spiga [7] investigated the role of viscous dissipation in liquid flowing through heated microchannels. The main aim of their work was to demonstrate that the problem of heat

---

Contributed by the Heat Transfer Division of ASME for publication in the JOURNAL OF HEAT TRANSFER. Manuscript received September 30, 2008; final manuscript received April 11, 2009; published online February 18, 2010. Assoc. Editor: Satish G. Kandlikar.

transfer enhancement in the microdevices cannot be solved by indefinitely reducing the microchannel dimensions because of the viscous dissipation effect.

Steinke and Kandlikar [8] reviewed conventional heat transfer enhancement techniques. They identified several ideas for the techniques that can be used in minichannels and microchannels to improve the heat transfer. Grande and Kandlikar [9] evaluated the use of engineered structures within microchannels and fabrication methodologies for two specific classes of devices, microchannels containing structures within the channel and microchannels with grooves etched into the channel walls. Colgan et al. [10] presented an enhanced microchannel heat exchanger with a similar structure. Their main focus was on developing a microchannel heat exchanger that could be directly attached to an existing microprocessor. Once fabricated, the enhanced microchannels were tested using an experimental facility developed by Steinke et al. [11]. The authors reviewed several experimental microchannel papers to develop an experimental test bed for investigation of microchannel pressure drop and heat transfer for a wide range of parameters. The facility could accurately measure flow rates, pressure drops, and heat transfer for the enhanced microchannel heat exchanger. Steinke and Kandlikar [12] experimentally showed that an offset strip fin enhanced microchannel heat exchanger had a thermal resistance lower than plain microchannel, and they defined a new parameter called pumping power flux to aid in evaluation and comparison of enhanced microchannel heat exchangers.

Presence of irregularity or grooved structures on the microchannel walls may lead to hydrophobic interactions. This feature has been studied by Chakraborty [13,14]. He showed that the confining rough surfaces made of water-disliking materials may trigger the formation of tiny bubbles adhering to the walls in tiny channels. This incipient vapor layer acts as an effective smoothening blanket, and for these cases, the liquid is not likely to feel the presence of the wall directly and may smoothly sail over the intervening vapor layer shield. Capillary-driven filling of microchannels has found important applications in the lab-on-a-chip-based microdevices. Chakraborty and Mittal [15] presented a theoretical approach to analyze the droplet dynamics in a microchannel subjected to electrocapillary actuation mechanisms. Also Chakraborty [16] showed the effect of various non-Newtonian parameters on the electroosmotically driven capillary dynamics of liquids in microfluidic channels. Certain critical features of electrokinetics and contact angle characteristics were considered.

The focus of the present work is the incorporation of arc and rectangular grooves in the floor and sidewalls of a microchannel to achieve heat transfer enhancement, and also presenting an optimum groove size on the bottom surface of microchannel for maximum heat transfer and coefficient of performance. Capillary transport or possible hydrophobic interactions are not studied.

2 Model Description

The microchannels heat sink tested in the experimental work of Qu and Mudawar [17] was selected for numerical study in present numerical work. The heat sink was 1 cm wide and 4.4 cm long. Twenty-one channels were fixed in the given width. The channels were equidistantly spaced within the 1 cm heat sink width and had the cross-sectional dimensions of 231 μm width and 713 μm height. The microchannel length to the hydraulic diameter ratio (L/D_h) is 126.

In this paper we examine the use of structures formed in the sidewalls and floor of the microchannel. Figure 1 illustrates two types of the grooves in the floor and sidewalls of the microchannel perpendicular to the direction of flow. Table 1 summarizes the specification of these grooves.

3 Computational Modeling

A unit cell containing a single microchannel is chosen to perform the numerical analysis. Symmetry allows these results to be easily extended to the entire heat sink. Figure 2 illustrates the unit cell, corresponding coordinate system, and key notations. Dimensions of unit cell are given in Table 2.

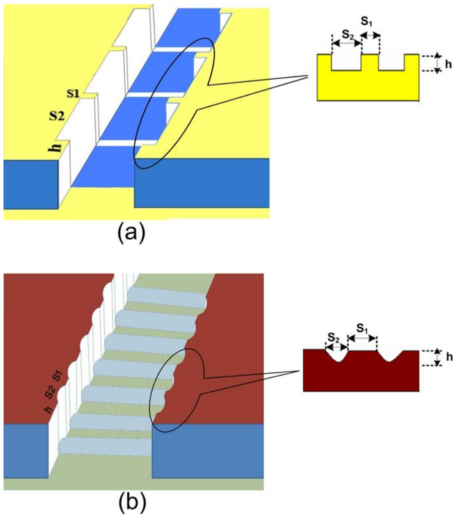

Fig. 1 Microchannel with structures formed in the sidewalls and floor of the channel: (*a*) rectangular groove; (*b*) arc groove

Considering the geometry of the microchannel, the following assumptions are made:

1. Flow is steady, laminar, and incompressible.
2. Radiation heat loss is negligible.
3. Properties are constant for fluid and solid materials.
4. Body force was neglected.

Table 1 Numbers and sizes of grooves

Number of grooves (n)	Length of grooves s_2 (μm)	Depth of grooves h (μm)	Distance of the two grooves s_1 (μm)
29	1000	100	500

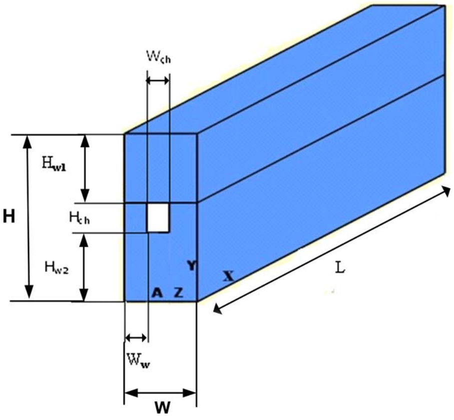

Fig. 2 Schematic of the heat sink unit cell for the numerical simulation

Table 2 Dimensions of the microchannel heat sink

W_w (μm)	W_{ch} (μm)	H_{w1} (μm)	H_{ch} (μm)	H_{w2} (μm)	L (mm)
118	231	12700	713	5637	44

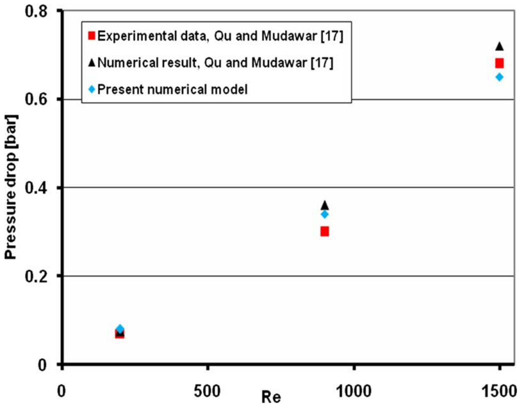

Fig. 3 Comparison of the present numerical result and experimental data of Qu and Mudawar [17] for the pressure drop in a simple microchannel

3.1 Governing Equations for Fluid.

Based on the above assumptions, the governing differential equations used to describe the fluid flow and heat transfer in the unit cell are as follows. For the cooling water, the continuity, momentum, and energy equations are expressed respectively as

$$\nabla \cdot \boldsymbol{V} = 0 \tag{1}$$

$$\rho_f(\boldsymbol{V} \cdot \nabla \boldsymbol{V}) = -\nabla P + \nabla(\mu_f \nabla \boldsymbol{V}) \tag{2}$$

$$\rho_f C_p(\boldsymbol{V} \cdot \nabla T) = k_f \nabla^2 T \tag{3}$$

3.2 Governing Equation for Solid.

For the solid region, the energy equation is

$$k_s \nabla^2 T = 0 \tag{4}$$

3.3 Boundary Condition.

For flow boundary conditions, a uniform velocity was applied at the channel inlet. This velocity is computed based on the Reynolds number of the flow. The flow is assumed fully developed at the channel outlet, and the velocity is zero along all other solid boundaries.

For thermal boundary conditions in the solid region, a constant temperature is applied at the unit cell bottom ($T_s = 85°\text{C}$), and a constant temperature T_{in} was set at the inlet of the channel. Other surfaces are considered adiabatic or symmetric.

Numerical simulation is based on a finite volume formulation. The discretized governing equations were solved by employing SIMPLE algorithm for the pressure correction processes, and convective and diffusive terms are discretized by upwind and central difference schemes, respectively. A computational fluid dynamics (CFD) code was used for this aim. The grid independent study was done, and a structured grid with total number of about 700,000 elements was selected for numerical model.

4 Validation of Numerical Model

At first the presented numerical model was validated for a simple and grooved microchannel with comparison to available experimental data.

4.1 Simple Microchannel.

Figure 3 shows a good agreement between experimental data of Qu and Mudawar [17] and predicted pressure drop for simple microchannel. For a fluid with constant properties flowing through a rectangular channel, one would expect a linear relationship between pressure drop and Reynolds number. The small difference between the present numerical results and numerical data of Qu and Mudawar [17] might be because of the different numerical approaches. Also variation in viscosity with temperature considered in their work was neglected in the present numerical simulation. Although a Reynolds number as high as 1500 is not commonly obtained in microchannel liquid flows but the data for this high Reynolds number are available in the experimental work of Qu and Mudawar [17], and in present numerical work, this case is also considered. The possibility of the chaotic transport as a consequence of this high Reynolds number needs more research.

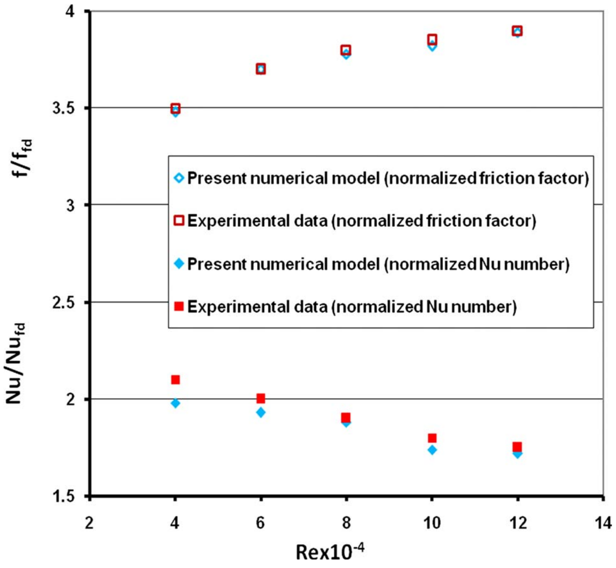

Fig. 4 Comparison of the present numerical result and experimental data of Hong and Hsieh [18] for the normalized Nusselt number and friction factor

4.2 Grooved Microchannel.

The major difficulty of model validation in the present simulation was the lack of the experimental data for the microchannels with arc and rectangular grooved surfaces. So the experimental data of Hong and Hsieh [18] for a channel with in-line ribs were used for validation of present numerical model. The ribs are in rectangular shape and put with a similar structure in the bottom of the channel. Figure 4 compares the Nusselt number and friction factor of the present numerical solution with the experimental data, which shows a reasonable agreement. Here, the Nusselt number and friction factor are normalized with those of a simple channel.

5 Result and Discussion

5.1 Microchannel With Rectangular Grooves.

The effect of these grooves was studied for three cases. The first case includes 29 rectangular grooves with $S_2/S_1 = 2$ fabricated on the floor of microchannel. For the second case, one of the side surfaces was grooved too. At the third case, the floor and both sides were grooved. In all three cases, the grooves have similar structures.

Figure 5 compares the maximum heat removal for simple and grooved microchannels at constant substrate temperature and Re = 900. The microchannels with rectangular grooves are dissipating more heat compared with a simple microchannel. In the microchannel with grooves on the floor and both side walls, 65% enhancement in heat transfer can be obtained.

The physical reason of this enhancement in heat transfer for the microchannel with grooved surface is the developing flow type conditions created by the grooves on the flow field. A periodically developing flow occurs in streamwise direction of the channel and a completely fully developed condition never could be reached in the microchannel. This point was illustrated in Fig. 6, which shows the axial velocity component of the flow in the centerline of a simple and a grooved microchannel.

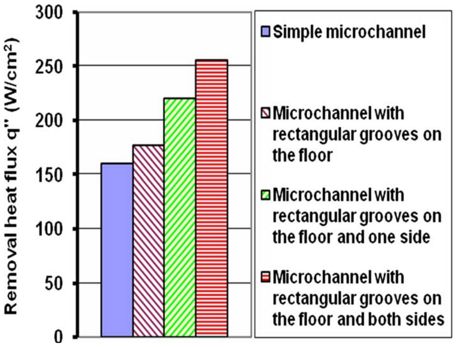

Fig. 5 Comparison between the simple microchannel and microchannel with rectangular groove surfaces for maximum heat removal flux ($T_s=85°C$, Re=900)

As Fig. 7 shows, this heat transfer enhancement will come at the price of added pressure drop and friction factor. The friction factor is defined as follows:

$$f = \frac{\Delta P}{4(l/D_h)(1/2)\rho_f U_{\text{in}}^2} \tag{5}$$

The friction factor for grooved surfaces microchannel is higher compared with simple microchannel. The fabricated grooves on the side surfaces of the microchannel has a major effect on increasing in the pressure drop in channel. The enhancement heat transfer must be carefully weighed with the added pressure penalty. It is critical to measure the overall pressure drop in order to properly size a fluid pump.

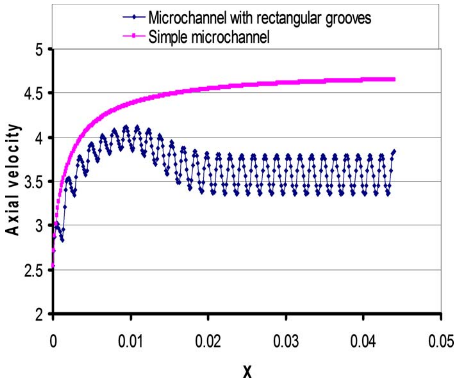

Fig. 6 Comparison between the simple and rectangular grooved microchannels for axial velocity in the centerline of the channel (Re=900)

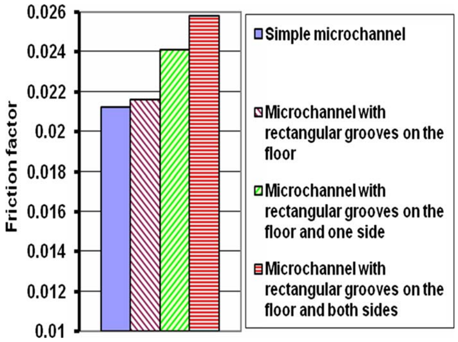

Fig. 7 Comparison between the simple microchannel and microchannels with rectangular groove surfaces for the friction factor ($T_s=85°C$, Re=900)

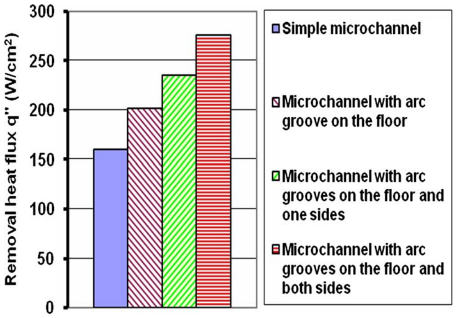

Fig. 8 Comparison between the simple microchannel and microchannel with arc groove surfaces for the maximum heat removal flux ($T_s=85°C$, Re=900)

5.2 Microchannel With Arc Grooves. These grooves were examined for three cases. The first case includes 29 arc shape grooves fabricated on floor of microchannels with $S_2/S_1=2$. For the second case, one of the side surfaces was grooved too. The last case has grooves on the floor and both sides. In all three cases, the grooves have similar structures.

The amount of removal heat flux for simple microchannel and that with arc grooves is compared in Fig. 8. The microchannels with arc grooves are dissipating more heat compared with a simple microchannel. The simple microchannel needs to operate at much higher flow rates to remove heat compared with the grooved microchannel. However, the grooved microchannel comes only with added pressure drop of a few kilopascals in comparison with the simple microchannel.

Figure 9 shows the friction factor for microchannels with arc grooves. The fabricated grooves on the bottom surface of the microchannel have a major effect on the increase in the pressure drop in the channel. The friction factor of microchannels with arc grooves is higher than that of microchannels with rectangular grooves.

5.3 COP. To compare properly the different microchannel heat exchanger geometries, a parameter including both dissipated heat flux and the pressure drop should be defined. Therefore, a novel parameter called the pumping power flux developed by Steinke and Kandlikar [12] was used in present study for comparison of grooved microchannels.

This pumping power parameter was defined as follows:

$$P = \frac{\dot{m}\Delta p}{\rho} \tag{6}$$

Dividing by the free flow area, the pumping power can be manipulated to a flux term. Equation (7) shows the formula for the pumping power flux, or the pumping flux

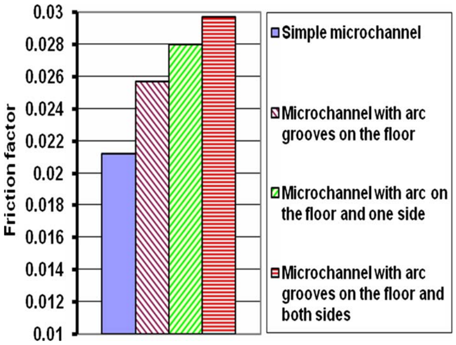

Fig. 9 Comparison between the simple microchannel and microchannels with arc groove surfaces for the friction factor ($T_s=85°C$, Re=900)

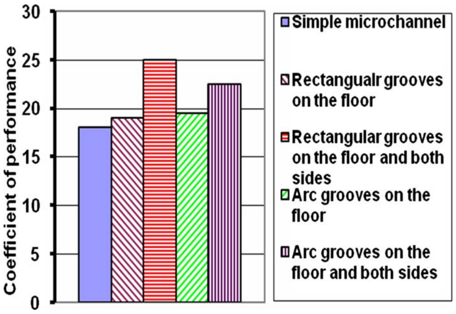

Fig. 10 Comparison of COP for microchannels with rectangular and arc grooves (Re=900, T_s=85°C)

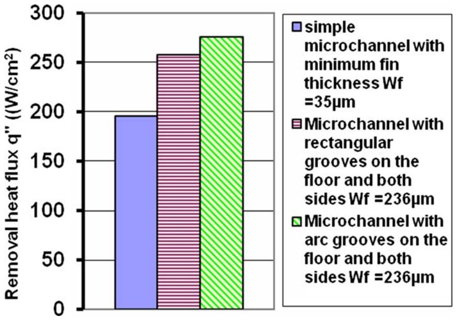

Fig. 11 Comparison between microchannel with rectangular and arc grooves and simple microchannel with minimum fin thickness for removal heat flux (T_s=85°C, Re=900)

$$P'' = \frac{\dot{m}\Delta p}{\rho A_{\text{free}}} \tag{7}$$

where A_{free} is the free flow area. The heat and pumping power fluxes can be related in a simple manner in a coefficient of performance (COP).

For the present work, the COP will be the desired dissipated heat flux divided by the required pumping power flux

$$COP = \frac{q''}{P''} \tag{8}$$

Substituting Eq. (7) in Eq. (8) leads to

$$COP = \frac{\rho q''}{\dot{m}\Delta p} A_{\text{free}} \tag{9}$$

The COP for simple microchannels and those with rectangular and arc grooves are shown in Fig. 10. The COP of microchannels with grooves is greater than that of a simple microchannel. Although microchannels with arc grooves on the floor and side walls present more heat transfer enhancement compared with those with rectangular grooves on the same walls, they have a smaller COP because of their higher pressure drop. The microchannel with rectangular grooves on the floor and both sides has the highest coefficient of performance ($COP=25$) compared with others. Comparison of heat transfer and COP enhancement for all the above discussed cases is given in Table 3. As the table shows the microchannels with arc grooves present 72% heat transfer enhancement compared with simple microchannels.

5.4 Comparison Between a Grooved Microchannel and a Simple Microchannel With Minimum Fin Thickness. The optimum size of the fin thickness for maximum heat removal flux in a simple microchannel is the minimum possible size, because in this case, the number of channel is maximum for a fixed width of the substrate. The minimum wall thickness is assumed to be 35 μm, which is the minimum easily manufactured thickness with current fabrication technology. A possible concern about a microchannel with grooves on the side walls is the needed higher fin thickness. Using the minimum size of the fin thickness (35 μm) for the studied simple microchannel compared with that used in grooved microchannel (236 μm) increases the number of the channels from 21 to 37. So for a fixed Reynolds number, the mass flow rate of cooling water is higher in this simple microchannel. In this section the grooved microchannels are compared with the simple microchannel, which has a minimum fin thickness. Figures 11 and 12 show these comparisons. As the results show, grooved microchannels with a less number of channels and lower flow rate have a higher removal heat flux and COP compared with the simple microchannel with minimum fin thickness.

Table 3 Removal heat flux, percent of HTE, COP, and percent of COP enhancement for the studied microchannels (Re=900, T_s=85°C)

Cases	q'' (W/cm^2)	HTE (%)	COP	% COP enhancement
Simple	160	-	18.02	-
Rectangular grooves on the floor	178	11	19.28	6.9
Rectangular grooves on the floor and both sides	258	61	25	38
Arc grooves on the floor	201	26	19.61	8.8
Arc grooves on the floor and both sides	278	72	22.5	24

6 Study of Various Distances and Sizes of the Grooves

In this section an optimization study was done to find the distance and size of the grooves on the floor of the channel for the highest heat removal flux and COP. The microchannels with two groove shapes (rectangular and arc) were investigated. Various studied cases in this section are given in Table 4. For these cases, the depth of the grooves were set constant (100 μm). Higher depth for the grooves did not have a noticeable effect on heat transfer performance (details not shown here). Four different aspect ratios and three different distances for the grooves were studied.

6.1 Comparison of Heat Removal Flux. Figure 13 shows the maximum heat removal flux of microchannel with rectangular grooves for three Reynolds numbers. The results show that the grooves with $S_2/S_1=4$ and $S_1/h=4$ have the maximum heat removal flux. For the microchannel with arc grooves as Fig. 14 shows, the case with $S_2/S_1=2$ and $S_1/h=4$ has highest removal heat flux. As Figs. 13 and 14 show, the optimum size of the

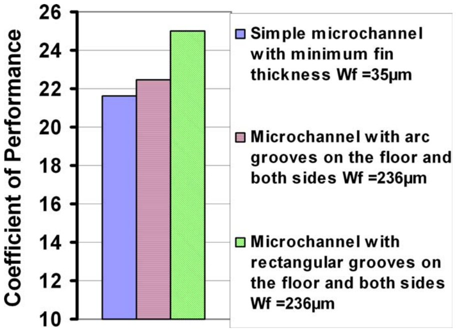

Fig. 12 Comparison between microchannel with rectangular and arc grooves and simple microchannel with minimum fin thickness for COP (T_s=85°C, Re=900)

Table 4 The different cases of the groove sizes and spacings considered to find the optimum case

Case No.	S_1/h	S_2/S_1	h (μm)
1	4	1	100
2	4	2	100
3	4	3	100
4	4	4	100
5	5	1	100
6	5	2	100
7	5	3	100
8	5	4	100
9	6	1	100
10	6	2	100
11	6	3	100
12	6	4	100

grooves and their distances are independent from the Reynolds number. Also the results show that the removal heat flux is more dependent on S_2/S_1 compared with S_1/h. Comparison of these optimum cases for removal heat flux with those studied in the last section shows that studied cases as a first try were near to optimum condition.

6.2 Comparison of the Friction Factor. Figures 15 and 16 compare the friction factor of the microchannels with rectangular and arc grooves for various sizes and spacings of the grooves. As was expected, the friction factor for all cases decreases with an increase in Reynolds number. The results show that the arc grooves make a higher pressure drop in the microchannel compared with rectangular grooves. The maximum pressure drop is for the case with $S_2/S_1=2$ and $S_1/h=6$. Friction factor has a small variation with sizes and spacings of the rectangular grooves. For arc grooves the maximum pressure drop is for the case with $S_2/S_1=2$ and $S_1/h=4$. The variation in the friction factor for various sizes and spacings are more noticeable for arc grooves. The minimum pressure drop for both rectangular and arc grooves is for the case with $S_2/S_1=4$ and $S_1/h=6$, which has minimum number of grooves and maximum groove spacings. The results of this

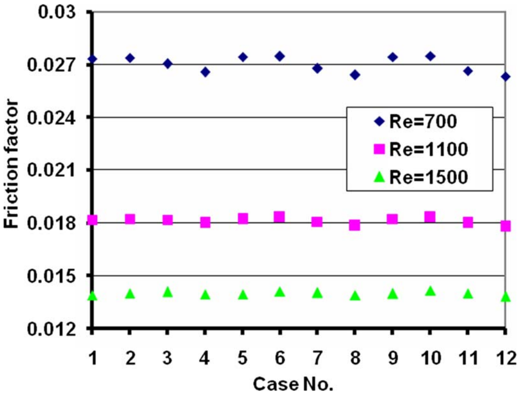

Fig. 15 Friction factor of microchannel with various sizes and spacings of rectangular grooves ($T_s=85°C$)

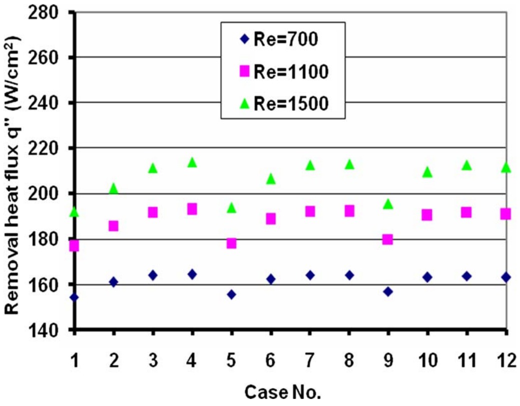

Fig. 13 Removal heat flux for the microchannel with various sizes and spacings of rectangular grooves ($T_s=85°C$)

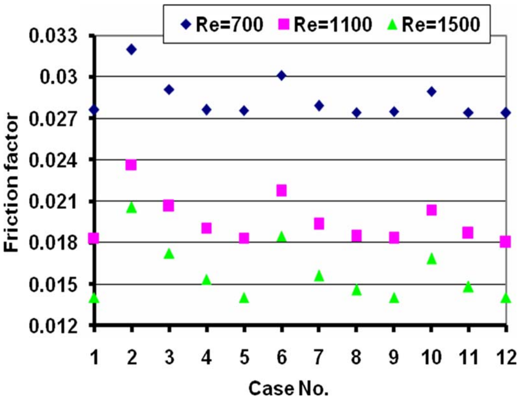

Fig. 16 Friction factor of microchannel with various sizes and spacings of arc grooves ($T_s=85°C$)

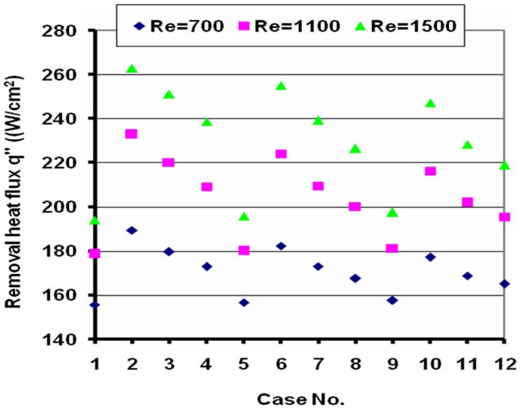

Fig. 14 Removal heat flux for microchannel with various sizes and spacings of arc grooves ($T_s=85°C$)

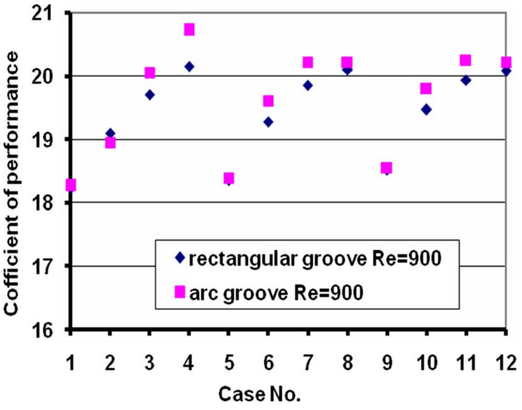

Fig. 17 COP for microchannel with various sizes of rectangular and arc grooves (Re=900, $T_s=85°C$)

Table 5 The cases of maximum HTE and COP for microchannel with rectangular and arc grooves ($\mathrm{Re}=900$, $T_s=85°\mathrm{C}$)

Case of microchannel	q'' ($\mathrm{w/cm^2}$)	HTE (%)	Case of microchannel	COP	% COP increase
Simple	160	-	Simple	18.02	-
Rectangular groove ($S_2/S_1=4$, $S_1/h=4$)	179.3	12	Rectangular groove ($S_2/S_1=4$, $S_1/h=4$)	20.15	11
Arc groove ($S_2/S_1=2$, $S_1/h=4$)	211.9	32	Arc groove ($S_2/S_1=4$ $S_1/h=4$)	20.72	15

section also show that the optimum and worst cases among all studied cases for pressure drop are independent of the Reynolds number.

6.3 Comparison of COP. Comparison of coefficient of performance for microchannels with various sizes of rectangular and arc grooves at $\mathrm{Re}=900$ are shown in Fig. 17. Because of independency of the optimum cases from Reynolds number only result of one Reynolds number is shown hear. The maximum COP for both types of grooved microchannel is for the case with $S_2/S_1=4$ and $S_1/h=4$. The results show that when only the floor of the microchannel are grooved, the case of the arc grooves has a higher COP compared with that of the rectangular grooves. Table 5 summarizes the groove sizes and spacings for maximum enhancement in HTE and COP. It should be noted these enhancements are for the cases, which only the floor of the channel are being grooved and as the results of the last two section showed, the case with grooves on the floor and side walls has much higher removal heat flux and COP.

7 Conclusion

The effect of two types of the grooves on the heat transfer and friction factor of the microchannels was determined numerically and the following results were obtained:

1. Fabricating the grooves on the surfaces of a microchannel increases the heat removal flux and COP.
2. The grooves with an arc shape have a better effect on the heat removal performance of the microchannels compared with the rectangular grooves, although the pressure drop for the former is higher.
3. For the studied microchannel, using the rectangular grooves on the floor and side walls, heat removal flux can be increased by about 61%. The friction factor increases 25% for this case. The percent of increase in heat removal and friction factor flux using arc grooves on the floor and both sides of the channel is about 72% and 42%, respectively.
4. A grooved microchannel even performs a better performance compared with a simple microchannel, which has the minimum fin thickness. It was shown that a grooved microchannel removes 23% heat more from the substrate even with a lower total mass flow rate. For microchannel with arc grooves, the situation is better and the removal heat flux is 30% more. COP of the microchannels with rectangular and arc grooves is 4.4% and 14% higher than that of a simple microchannel with minimum fin thickness, respectively.
5. For maximum heat removal and COP, the optimum size and spacings for the grooves on the floor of the channel were obtained. For maximum removal heat flux, the optimum case for rectangular grooves is the case with $S_2/S_1=4$ and $S_1/h=4$, and for arc grooves, the case with $S_2/S_1=2$ and $S_1/h=4$ presents the optimum case. For maximum COP, the optimum case of both rectangular and arc grooves is the case with $S_2/S_1=4$ and $S_1/h=4$.

Nomenclatures

A_{ch} = cross-sectional of channel
A_{free} = free flow area
C_p = specific heat capacity
H = height of unit channel
H_{ch} = height of channel
H_{w1} = cover plate thickness
H_{w2} = thickness from the unit cell bottom to the channel bottom
K = thermal conductivity
L = length of unit cell
b = width of the substrate
P = pressure
ΔP = pressure drop
q'' = heat flux
Re = Reynolds number
S_1 = groove spacing
S_2 = length of groove
T = temperature
T_{in} = fluid inlet temperature
W_f = fin thickness ($W_f=2W_w$)
W = width of unit cell
W_{ch} = channel width
W_w = half-width of the fin thickness
U_{in} = inlet velocity
Nu = Nusselt number
$\mathbf{V}$ = velocity vector
f = friction factor
h = groove depth
n = number of channel

Greek Symbols

μ = dynamic viscosity
ρ = density

Subscripts

f = fluid
s = solid
in = inlet
out = outlet
fd = fully developed

References

[1] Tuckerman, D. B., and Pease, R. F. W., 1981, "High-Performance Heat Sinking for VLSI," IEEE Electron Device Lett., **2**, pp. 126–129.
[2] Bergles, A. E., 1997, "Heat Transfer Enhancement—The Encouragement and Accommodation of High Heat Flux," ASME J. Heat Transfer, **119**, pp. 8–19.
[3] Bergles, A. E., Jensen, M. K., and Shome, B., 1996, "The Literature on Enhancement of Convective Heat and Mass Transfer," J. Enhanced Heat Transfer, **4**, pp. 1–6.
[4] Balaras, C. A., 1990, "A Review of Augmentation Techniques for Heat Transfer Surfaces in Single-Phase Heat Exchangers," Energy, **15**(10), pp. 899–906.
[5] Tao, W. Q., He, Y. L., Wang, Q. W., Qu, Z. G., and Song, F. Q., 2002, "A Unified Analysis on Enhancing Single Phase Convective Heat Transfer With Field Synergy Principle," Int. J. Heat Mass Transfer, **45**(24), pp. 4871–4879.
[6] Wei, X., Joshi, Y., and Patterson, M., 2007, "Experimental and Numerical

Study of a Stacked Microchannel Heat Sink for Liquid Cooling of Microelectronic Devices," ASME J. Heat Transfer, **129**, pp. 1432–1445.

[7] Morini, G., and Spiga, M., 2007, "The Role of the Viscous Dissipation in Heated Microchannels," ASME J. Heat Transfer, **129**, pp. 308–318.

[8] Steinke, M. E., and Kandlikar, S. G., 2004, "Review of Single Phase Heat Transfer Enhancement Techniques for Application in Microchannels, Minichannels and Microdevices," International Journal of Heat & Technology, **22**(2), pp. 3–11.

[9] Kandlikar, S. G., and Grande, W. J., 2004, "Evaluation of Single Phase Flow in Microchannels for High Flux Chip Cooling-Thermohydraulic Performance Enhancement and Fabrication Technology," *Proceedings of the International Conference on Microchannels and Minichannels*, Rochester, NY, Paper No. ICNMM04-2321.

[10] Colgan, E. G., Furman, B., Gaynes, M., Graham, W., Labianca, N., Magerlein, J. H., Polastre, R. J., Toy, H., Wakil, J., Zitz, J., and Schmidt, R., 2005, "A Practical Implementation of Silicon Microchannel Coolers for High Power Chips," *Proceedings of the Semiconductor Thermal Measurement, Modeling, and Management Symposium*.

[11] Steinke, M. E., Kandlikar, S. G., Magerlein, J. H., Colgan, E., and Raisanen, A. D., 2006, "Development of an Experimental Facility for Investigation Single-Phase Liquid Flow in Microchannels," Heat Transfer Eng., **27**(4), pp. 41–52.

[12] Steinke, M. E., and Kandlikar, S. G., 2006, "Single Phase Liquid Heat Transfer in Plain and Enhanced Microchannels," *Proceedings of the International Conference on Nanochannels, Microchannels and Minichannels*, Limerick, Ireland, Paper No. ICNMM06-96227.

[13] Chakraborty, S., 2007, "Order Parameter Modeling of Fluid Dynamics in Narrow Confinements Subjected to Hydrophobic Interactions," Phys. Rev. Lett., **99**, p. 094504.

[14] Chakraborty, S., 2007, "Towards a Generalized Representation of Surface Effects on Pressure-Driven Liquid Flow in Microchannels," Appl. Phys. Lett., **90**, p. 034108.

[15] Chakraborty, S., and Mittal, R., 2007, "Droplet Dynamics in a Microchannel Subjected to Electrocapillary Actuation," J. Appl. Phys., **101**, p. 104901.

[16] Chakraborty, S., 2007, "Electroosmotically Driven Capillary Transport of Typical Non-Newtonian Biofluids in Rectangular Microchannels," Anal. Chim. Acta, **605**, pp. 175–184.

[17] Qu, W., and Mudawar, I., 2002, "Experimental and Numerical Study of Pressure Drop and Heat Transfer in a Single Phase Microchannel Heat Sink," Int. J. Heat Mass Transfer, **45**, pp. 2549–2565.

[18] Hong, J., and Hsieh, S., 1993, "Heat Transfer and Friction Factor Measurements in Ducts With Staggered and In-Line Ribs," Int. J. Heat Mass Transfer, **115**, pp. 58–65.

An Extension to the Navier–Stokes Equations to Incorporate Gas Molecular Collisions With Boundaries

Erik J. Arlemark[1]
e-mail: erik.arlemark@strath.ac.uk

S. Kokou Dadzie

Jason M. Reese

Department of Mechanical Engineering,
University of Strathclyde,
Glasgow G1 1XJ, UK

We investigate a model for microgas-flows consisting of the Navier–Stokes equations extended to include a description of molecular collisions with solid-boundaries together with first- and second-order velocity-slip boundary conditions. By considering molecular collisions affected by boundaries in gas flows, we capture some of the near-wall effects that the conventional Navier–Stokes equations with a linear stress-/strain-rate relationship are unable to describe. Our model is expressed through a geometry-dependent mean-free-path yielding a new viscosity expression, which makes the stress-/strain-rate constitutive relationship nonlinear. Test cases consisting of Couette and Poiseuille flows are solved using these extended Navier–Stokes equations and we compare the resulting velocity profiles with conventional Navier–Stokes solutions and those from the BGK kinetic model. The Poiseuille mass flow rate results are compared with results from the BGK-model and experimental data for various degrees of rarefaction. We assess the range of applicability of our model and show that it can extend the applicability of conventional fluid dynamic techniques into the early continuum-transition regime. We also discuss the limitations of our model due to its various physical assumptions and we outline ideas for further development. [DOI: 10.1115/1.4000877]

Keywords: microgas-flows, Navier–Stokes equations, mean-free-path, nonlinear constitutive relationships, velocity-slip, Knudsen-layer

1 Introduction

As interest in microgas-flow applications is growing with improved manufacturing capabilities, it is also becoming more widely appreciated that the conventional incompressible Navier–Stokes (NS) equations with no-velocity-slip boundary conditions (BCs) fail to predict many of these flows properly. This is because microgas-flows differ from macrogas-flows due to the relatively large ratio of the confining boundary surface area to the volume of the confined gas, which means that certain surface effects must be taken into account. These surface effects considerably influence the flow in the near-wall region (the Knudsen-layer), which because of the small scale of the system, comprises a substantial volume of many microgas-flows. The width of this Knudsen-layer is usually expressed in terms of the average traveling distance of molecules between intermolecular collisions—the mean-free-path, λ. The Knudsen-layer is about one to two mean-free-paths wide.

To indicate the degree of rarefaction, or state of nonequilibrium, of gas flows, the key parameter is the Knudsen number

$$\mathrm{Kn} = \frac{\lambda}{H} \tag{1}$$

where for example, for a microchannel the full height H of the channel is the measure of the system length scale. Microgas-flows often have relatively large Kn due to the small length scales and certain rarefaction effects then become apparent. Experiments, such as those performed by Arkilic et al. [1] and Colin [2], showed that the NS equations cannot capture the correct mass flow rates along a microchannel without requiring a velocity-slip boundary condition to be applied. The conventional no-slip boundary condition commonly used with NS is valid only for cases where the gas is in a state of near-equilibrium. Microgas-flows of relatively large Kn require different boundary conditions [3]. The lower threshold value for applying a slip boundary condition is generally $\mathrm{Kn}=0.001$, which therefore is referred to as the lower limit of the “slip regime.” For gas-flows at larger Kn, further modeling modifications are needed because the linear constitutive NS relationships break down. This happens at about $\mathrm{Kn}=0.1$, which is known as the lower limit of the “continuum-transition” regime: the gas-flow is not modeled well either by a conventional continuum description nor by a free molecular description. This is the regime that we mostly focus on in this paper.

The modeling of surface effects in the Knudsen-layer should ideally be performed using kinetic theory. However an approximate extension to the NS-model would be less demanding in terms of computational capacity and the simplicity and practicality of NS make it desirable to solve flow cases using this model for as high-Kn flows as possible. As suggested by Guo et al. [4], NS may be extended to larger Kn by incorporating the gas molecular interactions with unyielding boundary walls through modification of the conventional expression of the molecular mean-free-path. In this paper, by considering the molecular interactions with the walls, we obtain an “effective” geometry-dependent mean-free-path λ_{eff}, which is in turn used to obtain an effective fluid viscosity, which follows through into a nonlinear stress-/strain-rate relationship.

We solve our new NS-model for isothermal cases using velocity-slip boundary conditions of first-order as well as of second-order and focus on the predictions of Couette and Poiseuille velocity flow profiles and the Poiseuille mass flow rate (all in planar-wall channel geometries).

---

[1] Corresponding author.

Manuscript received October 2, 2008; final manuscript received March 5, 2009; published online February 18, 2010. Assoc. Editor: Satish G. Kandlikar.

2 Velocity-Slip

The commonly used velocity-slip boundary condition proposed by Maxwell [5] has the following form for isothermal cases:

$$\boldsymbol{U}_{\text{slip}} = -\frac{2-\sigma}{\sigma}\frac{\lambda}{\mu}\boldsymbol{\tau}_w \tag{2}$$

where $\boldsymbol{U}$ is the mass average velocity vector, $\boldsymbol{\tau}$ is the viscous stress vector,[2] tangential to the surface and μ is the gas dynamic viscosity [6]. The tangential momentum accommodation coefficient σ describes the proportion of molecules being reflected diffusively ($\sigma=1$) from the wall as opposed to those that experience specular reflections ($\sigma=0$). If the reflections of the molecules are diffusive their tangential momentum is, on average, lost relative to the wall, as opposed to specular reflections where the tangential momentum is retained. In Eq. (2), the "slip" denotes the velocity difference between the wall and the gas next to the wall for which the notation "w" is used.

We obtain a first-order velocity-slip by inserting the tangential viscous stress vector of the NS equations into Eq. (2). The velocity-slip for planar walls can then be expressed as

$$\boldsymbol{U}_{\text{slip}} = -\frac{2-\sigma}{\sigma}\lambda\left(\frac{\partial \boldsymbol{U}}{\partial y}\right)_w = -C_1\lambda\left(\frac{\partial \boldsymbol{U}}{\partial y}\right)_w \tag{3}$$

where y is the coordinate perpendicular to the wall and in this case $y=0$ is the middle of the channel.[3] As listed by Karniadakis et al. [7], while the coefficient C_1 is set to 1 by many investigators, Cercignani [8] uses $C_1=1.1466$. Following the latter, we set the coefficient $C_1=1.1466$ when using the conventional NS with first-order slip.

Some investigators of microgas-flows argue that second-order velocity-slip boundary conditions should be used when modeling gas flows in the transition regime [3,7,9]. There are several suggested formulations for second-order velocity-slip; for planar walls and for our coordinate system most have the following form:

$$\boldsymbol{U}_{\text{slip}} = -C_1\lambda\left(\frac{\partial \boldsymbol{U}}{\partial y}\right)_w - C_2\lambda^2\left(\frac{\partial^2 \boldsymbol{U}}{\partial y^2}\right)_w \tag{4}$$

and there are various proposals for the modeling parameters C_1 and C_2. Some are purely theoretically derived, whereas others have been obtained through comparisons with experimental results [9]. The commonly used value for C_1 in the second-order slip is the same as for the first-order slip and the C_2 parameter varies in a wide range from -0.5 to $5\pi/12$. We choose to use, for NS using second-order slip, Cercignani's proposed slip boundary coefficients $C_1=1.1466$ and $C_2=0.647$ [7].

Generally, the kinetic derivations of the velocity-slip such as the one performed by Cercignani [8] are based on a diffuse reflection approximation for the gas/surface interaction. An alternative approach to this is to use a correction for the gas/surface interaction using the coefficient $(2-\sigma)/\sigma$ in Eq. (2). We are interested in the way the surface not only modifies the slip coefficients but also affects the mean-free-path locally. Therefore, we start with the formal first- and second-order velocity-slip expressions, Eqs. (3) and (4), respectively, and use instead a mean-free-path modified to incorporate the effect of a surface λ_{eff}, i.e.,

$$\boldsymbol{U}_{\text{slip}} = -A_1\lambda_{\text{eff}}\left(\frac{\partial \boldsymbol{U}}{\partial y}\right)_w \tag{5}$$

and

$$\boldsymbol{U}_{\text{slip}} = -A_2\lambda_{\text{eff}}\left(\frac{\partial \boldsymbol{U}}{\partial y}\right)_w - A_3\lambda_{\text{eff}}^2\left(\frac{\partial^2 \boldsymbol{U}}{\partial y^2}\right)_w \tag{6}$$

These expressions have coefficients A_1, A_2, and A_3 different from the conventional coefficients using C_1 and C_2. This is because λ_{eff} is expected to incorporate some surface effects, most likely requiring a change in the slip coefficient values. The conventional velocity-slip definitions represent surface effects through their slip coefficients rather than through the mean-free-path model.

In what follows, we present a model for the mean-free-path that takes into account the bounding solid surfaces.

3 Navier–Stokes Equations and Geometry-Dependent Viscosity

Since microgas-flows have a large ratio of their confining boundary areas to their volumes in the fluid mechanical model, we should account for gas molecular collisions with the solid-boundaries in addition to accounting for intermolecular collisions. This modeling modification is expected to have a significant effect only for confined microgas-flows with negligible effect for larger scale gas-flows.

Here we use the relationship

$$\mu = \rho\frac{\lambda}{\sqrt{\pi/2RT}} \tag{7}$$

which is discussed in further depth by Cercignani [8], relating the dynamic viscosity μ to the mean-free-path λ with ρ as the gas density, R as the specific gas constant, and T as the gas temperature. We assume that Eq. (7), which is normally valid only for gases in local equilibrium far from surfaces, remains formally valid at the surface even after taking into account that the mean-free-path is affected by gas molecular collisions with surfaces. If the "unconfined" expression for the mean-free-path λ is replaced by an effective and geometry-dependent mean-free-path λ_{eff} we obtain a nonconstant, geometry-dependent, effective viscosity μ_{eff} that can be used in the momentum conservation equation.

$$\boldsymbol{\Pi} = \mu_{\text{eff}}[\nabla\boldsymbol{U} + (\nabla\boldsymbol{U})^t] + \left(\frac{2}{3}\mu_{\text{eff}} - \kappa\right)(\nabla\boldsymbol{U})I \tag{8}$$

where κ is the bulk viscosity, I is the identity tensor, and t is the transpose operator. Our modification in Eq. (8) is analogous to replacing the NS stress expression with the Burnett (or other high-order) stress expression in the general momentum conservation equation.

For many steady-state microgas-flow situations the flow is extremely slow. This means that the inertia term $\rho(\boldsymbol{U}\cdot\nabla)\boldsymbol{U}$ can be discarded. The conventional NS equations then reduce to the Stokes equation [7], which for our new approach would have the following form:

$$\nabla\mu_{\text{eff}}[\nabla\boldsymbol{U} + (\nabla\boldsymbol{U})^t] = \nabla p \tag{9}$$

where p is the gas pressure. We now need to derive a new expression for the mean-free-path λ_{eff} and hence obtain μ_{eff}.

4 Previous Effective Mean-Free-Path Models

The idea of using transport parameters that are influenced by an effective mean-free-path can be traced back to Stops [10]. Stops investigated the probability density

$$p_d(r) = \frac{1}{\lambda}\exp\left(-\frac{r}{\lambda}\right) \tag{10}$$

describing the distribution of the molecular free path in terms of the molecular traveling distance r. The value of the unconfined, conventional mean-free-path, when no solid-boundaries are present, can then be obtained by integrating $rp_d(r)$ with respect to r from zero to infinity.

---

[2] The viscous tangential stress vector, $\boldsymbol{\tau}$, relates to the viscous stress tensor, $\boldsymbol{\Pi}$, through the expression $\boldsymbol{\tau}=(\hat{n}\cdot\boldsymbol{\Pi})\cdot(I-\hat{n}\hat{n})$, where $\hat{n}$ is the unit vector normal to a surface and I is the identity tensor [6].

[3] In Eqs. (3) and (4) the "−" sign is applied to the first-order velocity gradient if y is oriented in the opposite direction to the wall normal, otherwise "−" is replaced with "+" in these equations.

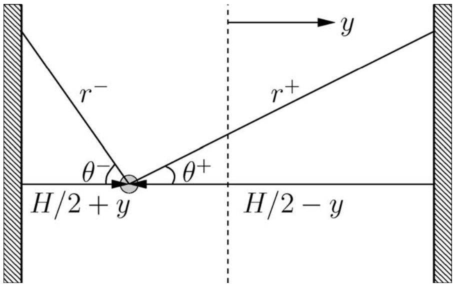

Fig. 1 A molecule confined between two-planar walls with spacing *H*. The molecule has an equal probability to travel in any zenith angle θ^- or θ^+ or to travel in either the positive or negative *y*-direction. The molecule under consideration is assumed to have just experienced an intermolecular collision at its current position $H/2-y$.

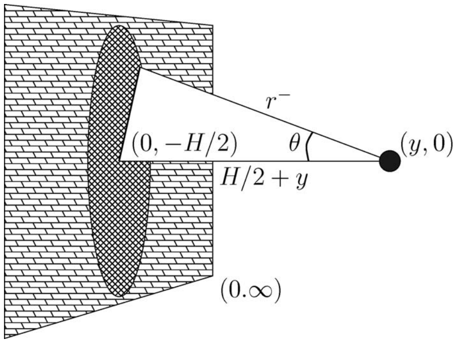

Fig. 2 A molecule at a distance $H/2+y$ from a planar wall; possible trajectories for a molecule traveling in the negative *y*-direction in cylindrical coordinates $(H/2+y,(H/2+y)\tan\theta)$, where ∞ denotes infinity.

The effective mean-free-path expression developed by Stops $\lambda_{\mathrm{eff}(S)}$ is derived by using solid-angle-analysis and by shortening the upper integrational limit of r from infinity to the distance to the confining wall. The integration of $rp(r)$ then yield $\lambda_{\mathrm{eff}(S)}=\lambda K_{(S)}(y,\lambda,H)$ for molecules in a two parallel planar-wall confinement, where H is the wall spacing and

$$K_{(S)}(y,\lambda,H)=\frac{1}{2}\left\{2+\left(\frac{H/2+y}{\lambda}-1\right)\exp\left(-\frac{H/2+y}{\lambda}\right)-\left(\frac{H/2+y}{\lambda}\right)^2 Ei\left(\frac{H/2+y}{\lambda}\right)+\left(\frac{H/2-y}{\lambda}-1\right)\exp\left(\frac{H/2-y}{\lambda}\right)-\left(\frac{H/2-y}{\lambda}\right)^2 Ei\left(\frac{H/2-y}{\lambda}\right)\right\} \tag{11}$$

This expression is used by Guo et al. [4] in solving their microgas-flows. The function Ei in Eq. (11) is the exponential integral function defined as

$$Ei(z)=\int_1^{\infty} t^{-1}\exp(-zt)dt \tag{12}$$

In the next section we derive a model similar to $\lambda_{\mathrm{eff}(S)}$ but without the dependence on the $Ei(z)$-function, which may therefore be easier to implement and more computationally efficient for microgas-flow calculations.

5 A Probability Function-Based Effective Mean-Free-Path Model

We use instead the integrated form of the density function $p_d(r)$, defined in Eq. (10), referred to as the probability function, i.e.,

$$P(r)=\int p_d(r)dr=D-\exp\left(-\frac{r}{\lambda}\right) \tag{13}$$

This function describes the probability a molecule travels a distance $r+dr$ without experiencing a collision. The integration constant D is set to one so that the probability ranges from zero to one.

Our model is derived for the two-planar-wall configuration shown in Fig. 1. We use the notation r^- if the molecule is traveling in the negative y-direction and r^+ if the molecule is traveling in the positive y-direction. We also use the notations θ^- and θ^+ for the equally probable zenith angle traveling direction of the molecule. These quantities are related through $r^-=(H/2+y)/\cos(\theta^-)$ and $r^+=(H/2-y)/\cos(\theta^+)$.

The molecular free path l is retrieved by weighting the unconfined molecular mean-free-path, λ, with P as follows:

$$l=\lambda\frac{1}{2}[P(r^-)+P(r^+)]=\lambda\left\{1-\frac{1}{2}\left[\exp\left(-\frac{r^-}{\lambda}\right)+\exp\left(-\frac{r^+}{\lambda}\right)\right]\right\} \tag{14}$$

A three-dimensional mean-free-path depending on the molecule's distance to a wall is then obtained by averaging the free path with respect to θ^- and θ^+ in the range $[0,\pi/2]$ using the mean integral theorem

$$\langle X(\theta)\rangle=\frac{2}{\pi}\int_0^{\pi/2} X(\theta)d\theta \tag{15}$$

where the integrational domain is illustrated in Fig. 2 for a molecule traveling in the negative y-direction. Averaging over the free paths in Eq. (14) may be done using Simpson's numerical integration involving 14 subintervals[4] results in $\lambda_{\mathrm{eff}}=\lambda K(y,\lambda,H)$, where

$$K(y,\lambda,H)=1-\frac{1}{82}\left[\exp\left(-\frac{H/2+y}{\lambda}\right)+\exp\left(-\frac{H/2-y}{\lambda}\right)+4\sum_{i=1}^{7}\exp\left(-\frac{H/2+y}{\lambda\cos[(2i-1)\pi/28]}\right)+4\sum_{i=1}^{7}\exp\left(-\frac{H/2-y}{\lambda\cos[(2i-1)\pi/28]}\right)+2\sum_{i=1}^{6}\exp\left(-\frac{H/2+y}{\lambda\cos[\pi i/14]}\right)+2\sum_{i=1}^{6}\exp\left(-\frac{H/2-y}{\lambda\cos[\pi i/14]}\right)\right] \tag{16}$$

In the remainder of this paper we will focus on the y-dependence of K, as λ and H are determined through the rarefaction parameter Kn and the microchannel geometry, respectively. The different K-functions, Eqs. (11) and (16) are compared in Fig. 3 for four Kn: $\mathrm{Kn}_A=0.04$, $\mathrm{Kn}_B=0.25$, $\mathrm{Kn}_C=1$, and $\mathrm{Kn}_D=20$. It is seen that both models show similar results for all Kn-cases, with the largest

---

[4] The difference in our mass flow results, see below, for 14 and 16 integration intervals is 1.54% for Kn=1, indicating that further increase of the number of integration intervals will only marginally affect the results.

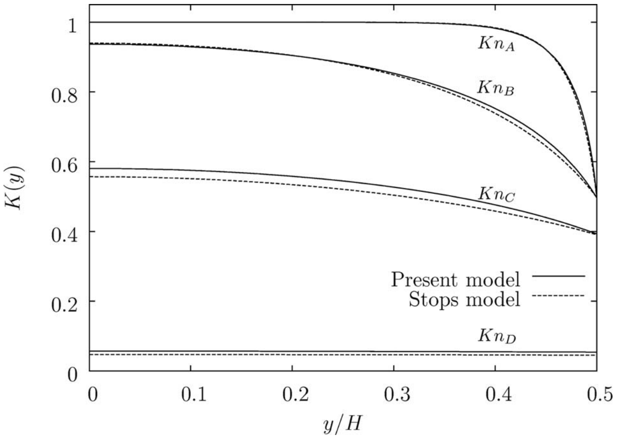

Fig. 3 Comparison of different λ_{eff}-models in a half-channel for different Knudsen numbers, where $\lambda_{\mathrm{eff}}=\lambda K(y)$ and $\mathrm{Kn}_A=0.04$, $\mathrm{Kn}_B=0.25$, $\mathrm{Kn}_C=1$, and $\mathrm{Kn}_D=20$

difference at Kn_C. By inspection of the Kn_A-case, both models fulfill the physically intuitive requirements that

$$K(0)\approx 1 \quad \text{and} \quad K(H/2)\approx \frac{1}{2} \tag{17}$$

The requirement at the wall can be realized by considering the average of the equal probabilities of a molecule traveling in the direction toward the confining wall (not yielding any traveling length contribution) and the probability of it traveling into the bulk of the flow (yielding a contribution of the length λ). The requirement for molecules far away from the wall is that the effective mean-free-path should approach its conventional unconfined value. For $\mathrm{Kn}_B=0.25$, the channel is four unconfined mean-free-paths wide; since the effective mean-free-path almost achieves the conventional unconfined value at $y=0$, the Knudsen-layer can be said to be approximately two unconfined mean-free-paths wide.

For higher Kn, the entire $K(y)$ profile is lowered due to Knudsen-layer overlap and thereby an increasing likelihood of wall collisions. The basic physical requirement of decreasing $K(y)$ with increasing Kn can be seen by inspection of the considerably lower profile of the Kn_D-case compared with the other cases. The Kn_B and Kn_C cases represent intermediate states between the Kn_A and Kn_D cases, where the profile near the wall is lower than the near-wall requirement in Eq. (17) because a molecule close to one of the walls has a significant probability of traveling directly to the other side of the channel and colliding with that wall, which results in a contribution of less than a mean-free-path for this traveling direction.

In the next section we present simple flow test cases using our λ_{eff}-dependent parameter μ_{eff} within the Navier–Stokes equations.

6 Test Case Results

Isothermal, fully developed velocity profiles in planar Couette and Poiseuille flow are calculated from our modified Stokes equation.

$$\frac{\partial}{\partial y}\left[\mu_{\mathrm{eff}}\frac{\partial U_x}{\partial y}\right]=\frac{\partial p}{\partial x} \tag{18}$$

which uses an effective viscosity derived by using λ_{eff} in Eq. (7). The velocity U_x is in the axial direction (x-direction) of the channel and it is assumed to vary only in the direction normal to the wall, the y-direction. This model is applied in turn with the first-order velocity-slip of Eq. (5) and then with the second-order velocity-slip of Eq. (6) in which λ is again replaced by its near-wall value, at $y=H/2$, of λ_{eff}. As this is now a different slip model than the conventional one, we choose to set the coefficients $A_1=1$ for our first-order velocity-slip and $A_2=0.05$ and $A_3=0.63$ for our second-order velocity-slip. These values for our present model are chosen purely based on which produce the best velocity profile results in the Couette and Poiseuille flows, and the mass flow rate in the Poiseuille flow. Since our present model uses a slip definition that has a different velocity gradient at the wall compared with NS and we apply a wall value of λ_{eff} instead of the unconfined value, it is not expected that the slip coefficients should have their conventional values.

It is shown by experimental investigators, such as Turner et al. [11], that microgas-flows have compressible characteristics even when the flow velocities are less than Mach 0.3. Due to this, we use the same solution method to solve for this compressible flow as in Kandlikar et al. [12], i.e., the normalized velocity profile in the channel cross section of the flow is obtained by assuming fully developed incompressible flow but the density can be recalculated using the ideal gas law. The mass flow rate in the Poiseuille flow case is calculated through cross-channel integration of the velocity profiles.

6.1 Couette Flow.

In Couette flow the pressure gradient of Eq. (18) is assumed negligible, yielding the governing equation

$$\frac{\partial}{\partial y}\left(\mu_{\mathrm{eff}}\frac{\partial U_x}{\partial y}\right)=0 \tag{19}$$

where $\mu_{\mathrm{eff}}=\mu K(y,\lambda,H)$. The solution to this equation, which we refer to as the "$\mathrm{NS}_{\mathrm{eff}}$-solution," using the first-order λ_{eff}-dependent velocity-slip, is

$$\frac{U_x}{U_w}=\frac{F(y)-F(y=0)}{F(y=H/2)+A_1\lambda-F(y=0)} \tag{20}$$

where

$$F(y)=\int\frac{1}{K(y)}dy \tag{21}$$

and U_w is the velocity of the wall. The $\mathrm{NS}_{\mathrm{eff}}$-solution using the second-order velocity-slip is

$$\frac{U_x}{U_w}=\frac{F(y)-F(y=0)}{F(y=H/2)+A_2\lambda-A_3\lambda^2K'(y=H/2)-F(y=0)} \tag{22}$$

where

$$K'(y)=\frac{dK(y)}{dy} \tag{23}$$

The conventional solution to Eq. (19), with constant viscosity and boundary conditions applied using the conventional λ, is as follows:[5]

$$\frac{U_x}{U_w}=\frac{y}{H/2+C_1\lambda} \tag{24}$$

The $\mathrm{NS}_{\mathrm{eff}}$-solutions, Eqs. (20) and (22), and the NS-solution Eq. (24) are compared in Figs. 4 and 5 for five different Kn of 0.01, 0.04, 0.08, 0.113, and 0.339 alongside the kinetic BGK-model solution obtained by Sharipov [13].

Figure 4 shows that for $\mathrm{Kn}_E=0.01$ all of the fluid model solutions have a sufficiently linear profile to match the BGK-result; the $\mathrm{NS}_{\mathrm{eff}}$ model with second-order velocity-slip best captures the amount of slip. For the Kn_B and the Kn_F cases, the nonlinear velocity profile at the wall is evident and is captured by both our $\mathrm{NS}_{\mathrm{eff}}$ models. The bulk of the flow is also considered to be well described by our models, although there is a slight deviation for all models for the Kn_F-case.

Figure 5 shows the Kn_E-case again for reference. In the

---

[5] The second-order velocity-slip solution is the same as the first-order slip solution because the second gradient of the velocity does not exist in this test case.

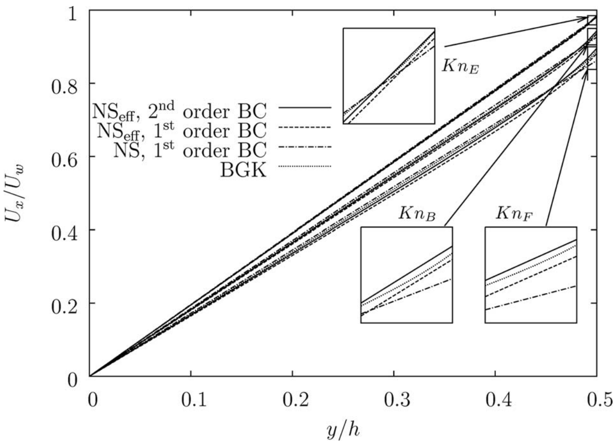

Fig. 4 Half-channel Couette flow velocity profiles using conventional NS and our effective viscosity model (NS$_{\text{eff}}$), using first- and second-order BCs, compared with the BGK-results of Sharipov [13]. The velocity profiles are for Kn$_E$=0.01, Kn$_B$=0.04 and Kn$_F$=0.08, and y=0 is the channel center. The slip coefficients for our second-order model are A_2=0.05 and A_3=0.63 and for our first-order model A_1=1.

Kn$_G$-case the slip amount and the near-wall curvature is captured by our models while the conventional NS-model captures the bulk velocity profile best, in comparison to the BGK-results. In the Kn$_H$-case, the conventional NS-model deviates quite severely from the BGK-results through the channel; our first-order slip model captures the amount of slip best while our second-order slip model captures the bulk velocity profile the best.

6.2 Poiseuille Flow. We now calculate the velocity profiles and the mass flow rate for isothermal, fully developed Poiseuille flow in a planar-wall channel.

6.2.1 Velocity Profile Results. In this case, the solution to Eq. (18) using our NS$_{\text{eff}}$ model with first-order λ$_{\text{eff}}$-dependent velocity-slip is as follows:

$$\frac{U_x}{U_0}=\frac{8}{H^2}\left[G(H/2)+A_1\lambda\frac{H}{2}-G(y)\right] \tag{25}$$

where

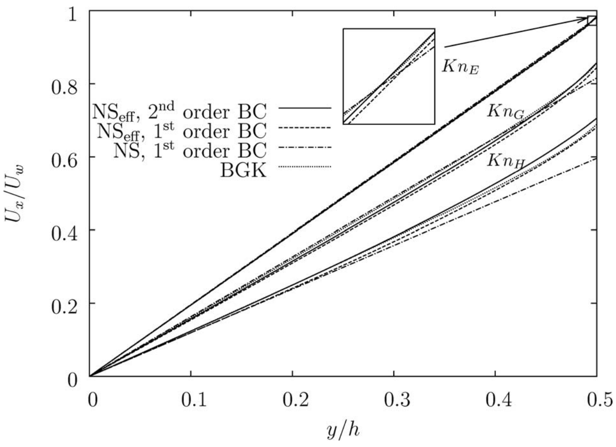

Fig. 5 Couette flow velocity profiles using conventional NS and our effective viscosity model (NS$_{\text{eff}}$) with first- and second-order BCs, compared with the BGK-results of Sharipov [13]; Kn$_E$=0.01, Kn$_G$=0.113 and Kn$_H$=0.339, and y=0 is the channel center. The coefficients for our second-order slip model are A_2=0.05 and A_3=0.63 and for our first-order model A_1=1.

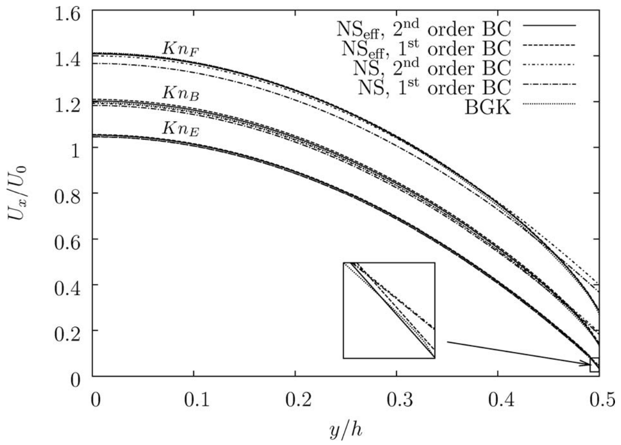

Fig. 6 Half-channel Poiseuille flow velocity profiles using conventional NS and our effective viscosity model NS$_{\text{eff}}$, using first- and second-order BCs compared with the BGK-results of Sharipov [13]. The velocity profiles are for Kn$_E$=0.01, Kn$_B$=0.04 and Kn$_F$=0.08, and y=0 is the channel center. The slip coefficients for our second-order model are A_2=0.05 and A_3=0.63 and for our first-order model A_1=1.

$$G(y)=\int\frac{y}{K(y)}dy \quad \text{and} \quad U_0=-\frac{H^2}{8\mu}\frac{dp}{dx} \tag{26}$$

The NS$_{\text{eff}}$-solution with second-order λ$_{\text{eff}}$-dependent velocity-slip is

$$\frac{U_x}{U_0}=\frac{8}{H^2}\left[G(H/2)+A_2\lambda\frac{H}{2}+A_3\lambda^2\left[K(H/2)-\frac{H}{2}K'(H/2)\right]-G(y)\right] \tag{27}$$

where

$$K'(y)=\frac{dK(y)}{dy} \tag{28}$$

The solution of the conventional NS equation, with constant viscosity and first-order velocity-slip using the unconfined λ, is

$$\frac{U_x}{U_0}=1-4\left(\frac{y}{H}\right)^2+4C_1\frac{\lambda}{H} \tag{29}$$

and the NS-solution with second-order velocity-slip using the unconfined λ is

$$\frac{U_x}{U_0}=1-4\left(\frac{y}{H}\right)^2+4C_1\frac{\lambda}{H}+8C_2\left(\frac{\lambda}{H}\right)^2 \tag{30}$$

In Figs. 6 and 7, the results of these various NS-based models are shown together with results from the BGK-model presented by Sharipov [13], for various Kn as listed in the captions.

In Fig. 6, it is seen for all Kn-cases that both our present models describe the bulk velocity profiles and the near-wall region quite well. For the Kn$_B$ and Kn$_F$ cases the conventional NS equations with second-order slip describe the bulk velocity profile well but do not capture the same curvature as the BGK-model at the wall. The conventional NS with first-order slip deviates significantly in the Kn$_B$ case and even more in the Kn$_F$, case as expected.

In Fig. 7, in the Kn$_G$ case it is seen that only our two present models manage to match the velocity profile of the BGK-model. In the Kn$_H$ case it is only our present model using second-order slip that captures the same slip amount as the BGK-model. While none of the NS-based models capture the same velocity profile as the BGK-model, our present models have a higher amplitude of the profile relative to the conventional NS-models, which suggests that our present models are in closer agreement with the BGK-model for the Kn$_H$-case. In the Kn$_I$-case only the result of our

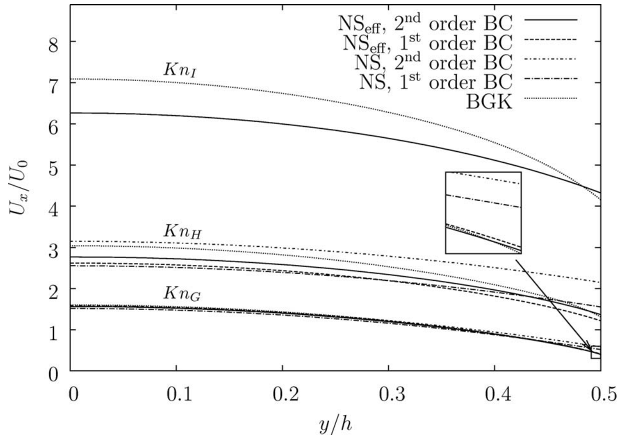

Fig. 7 Half-channel Poiseuille flow velocity profiles using conventional NS and our effective viscosity model NS$_{\text{eff}}$ with first- and second-order BCs, compared with the BGK-results of Sharipov [13]; Kn$_G$=0.113, Kn$_H$=0.339 and Kn$_I$=0.903, and y=0 is the channel center. The coefficients for our second-order slip model are A_2=0.05 and A_3=0.63 and for our first-order model A_1=1.

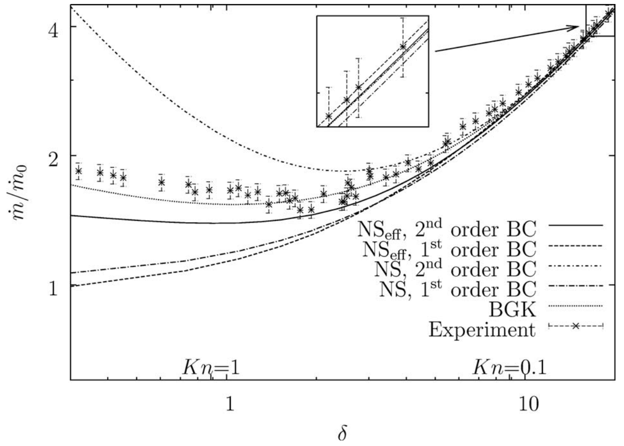

Fig. 8 Mass flow results from conventional NS and our effective viscosity model NS$_{\text{eff}}$, using first- and second-order BCs. The results are compared with BGK solutions by Sharipov [13] and experimental results by Ewart et al. [9]. The height of the error bars of the experimental data is set to 4.5% of the normalized mass flow rate values, consistent with the data in Ref. [9]. The coefficients for our second-order slip model are A_2=0.05 and A_3=0.63 and for our firs-order slip model A_1=1.

present model with second-order slip is compared with the BGK-model because the other models deviate to a too great extent. As can be seen, our model captures a reasonable average velocity across the channel, although we still cannot capture flow predictions correctly in the high Knudsen number range from about 0.903.

6.2.2 Mass Flow Results. We now compare the mass flow rates predicted by the present models with experimental results by Ewart et al. [9] for various degrees of rarefaction. The experimental measurements of Ewart et al. are made for helium gas, driven by a pressure ratio of 5 between the inlet and the outlet of the channel. Mass flow rates are obtained in the Kn-range of 0.03 to 50. The experimental channel dimensions are: height H =9.38 μm, width W=492 μm, and length L=9.39 μm. Since this channel is wide compared with its height it is assumed that a comparison with our model for just two-planar walls is valid. However, according to Sharipov [13] there is still an influence of the lateral walls, here separated by W; the error due to this influence can be taken into account by multiplying the mass predicted flow rate by $1-0.63H/W\approx 0.99$.

In order to compare our results with experiment, the velocity-dependent mass flow rate is calculated using the following relation:

$$\dot{m} = \rho\langle U_x\rangle A_{\text{CS}} = \frac{p\langle U_x\rangle A_{\text{CS}}}{RT} \tag{31}$$

where A_{CS} is the area of the cross section of the channel and

$$\tilde{U}_x = \frac{\langle U_x\rangle}{U_0} = \frac{2}{H}\int_0^{H/2}\frac{U_x}{U_0}dy \tag{32}$$

is the normalized average velocity across the channel width. We will here use the mass flow definition of Eq. (31) with the averaged velocities of the four NS-based velocity expressions given in Eqs. (25), (27), (29), and (30) and normalize by the quantity

$$\dot{m}_0 = -\frac{A_{\text{CS}}H}{\sqrt{2RT}}\frac{dp}{dx} \tag{33}$$

We then obtain the normalized expression for the mass flow rate

$$\frac{\dot{m}}{\dot{m}_0} = \frac{U_0}{\dot{m}_0}\frac{pA_{\text{CS}}}{RT}\tilde{U}_x = \frac{\sqrt{\pi}}{8}\frac{H}{\lambda}\tilde{U}_x = \frac{\delta}{4}\tilde{U}_x(\delta) \tag{34}$$

where the inverse rarefaction parameter is

$$\delta = \frac{\sqrt{\pi}}{2}\frac{H}{\lambda} \tag{35}$$

The results of the mass flow rates of the NS and NS$_{\text{eff}}$ models are shown in Fig. 8 together with the BGK-results reported by Sharipov [13] and the experimental results of Ewart et al. [9]. In Table 1, we also list an approximate range of applicability within the δ-inspection range of 0.3–20, for the NS-based models and the BGK-model. These applicability ranges are estimated by the ability of the different models to reproduce mass flow rates similar to the experimental data within a reasonable range of the stated error bars.

Figure 8 shows that all of the models are asymptotic to the experimental data for low Kn (i.e., high δ), which strengthens our presumption that the influence of the effective viscosity and the effective mean-free-path should decay with decreasing degree of rarefaction. Our NS$_{\text{eff}}$-model using second-order velocity-slip has a slightly low mass flow rate at about δ=2, compared with the validation data of the BGK-method [13] and experimental data [9]. This result can also be seen by inspection of the velocity profile for the Kn$_I$-case of Fig. 7, where the velocity profile is low

Table 1 Applicability ranges of the tested NS-based models estimated by comparing the model predictions of mass flow rates with the experimental data of Ewart et al. [9]

	Approximate range of applicability	
Model	In terms of δ	In terms of Kn
NS$_{\text{eff}}$, second-order BC	2–20	0.04–0.44
NS$_{\text{eff}}$, first-order BC	4–20	0.04–0.22
NS, second-order BC[a]	3–20	0.04–0.30
NS, first-order BC	4–15	0.04–0.06
BGK	0.3–2.95	0.04–2.95

[a] It should be noted that the investigators Colin et al. [14] and Maurer et al. [15] found that for special cases the applicability range of NS with second-order boundary condition reached up to Kn=0.25 and Kn=0.3, respectively.

in comparison to the BGK-model. In Fig. 8 it is only the second-order slip models of the NS-based models that capture the mass flow minimum, which occurs for the conventional model at about $\delta=2$ and for the present model at $\delta=1$. The comparison data of the BGK-model and the experimental data have a minimum at $\delta=1.2$. The conventional NS-model with second-order slip has a mass flow rate that is unbounded and therefore unphysical for low δ-values.

7 Discussion and Conclusions

A velocity-slip boundary condition is required in the application of the continuum Navier–Stokes equations to microgas-flows in the slip regime in order to achieve better predictions. In this paper we have presented a continuum fluid model for microgas-flows in the lower transition-continuum regime by incorporating a molecular collision length description into the Navier–Stokes equations, as well as using first- and second-order velocity-slip boundary conditions. Our molecular description takes into account gas molecular collisions with boundaries in the conventional definition of the mean-free-path, which therefore becomes a geometry-dependent and effective parameter varying with distance from a solid surface. This new definition of the effective mean-free-path yields an effective viscosity, and hence a nonlinear stress-/strain-rate constitutive relationship in the Navier–Stokes framework. The velocity boundary conditions applied with our models then also become dependent on the mean-free-path near the wall.

Although a simple model is preferred to describe flow characteristics for a wide range of Kn, it was found by inspection of Couette flow and Poiseuille flow results that the conventional Navier–Stokes equations are able to predict mass flows correctly up to about $\mathrm{Kn}=0.30$. However, our effective mean-free-path-based model using first- and second-order velocity-slip showed reasonably good results for velocity profiles and mass flow up to slightly higher Kn than for the conventional methods.

It should be noted that the conventional Navier–Stokes equations can produce results, which fit the validation data better for higher Kn in the Poiseuille mass flow case. For example, Maurer et al. [14] present results where the conventional NS with second-order velocity-slip captures the mass flow correctly up to about $\mathrm{Kn}=1$, for helium and nitrogen gas using slip coefficients $C_1=1.2, 1.3$, respectively, and $C_2=0.91, 0.87$, respectively. In this paper, we use the coefficients of Cercignani $C_1=1.4466$ and $C_2=0.647$ [7] for the conventional Navier–Stokes equations since these coefficients present good velocity profile results to about $\mathrm{Kn}=0.01$ but above this fail to capture the near-wall velocity profiles reported by the BGK-model of Sharipov [13].

For our new model we have applied coefficients that produce the best results for the velocity profiles in Couette and Poiseuille flow, as well as the mass flow rates of Poiseuille flow. For second-order velocity-slip, with our mean-free-path model, these coefficients are found to be $A_2=0.05$ and $A_3=0.63$; for our first-order boundary condition the best coefficient is found to be $A_1=1$. Generally, our model of a modified Navier–Stokes equation with second-order velocity-slip produces better results than our model with only first-order velocity-slip. The low value of A_2 in our velocity-slip formulations may be explained by the fact that our model incorporates some surface effects through the mean-free-path, not entirely through the slip coefficient as in Cercignani's coefficients.

The Poiseuille mass flow rate results show that only by using second-order boundary conditions can the mass flow minimum be captured. However, our model did not fully capture the velocity profile produced by the BGK-model of Sharipov [13] at $\mathrm{Kn}=0.339$, and we still cannot capture the mass flow prediction correctly in the high Knudsen number range from about 0.903. Corrections to our description of an effective mean-free-path may, however, increase the range of applicability of our approach further into the continuum-transition regime. For example, the present description of the effective mean-free-path requires that intermolecular collisions should be accounted for in the same way as molecular collisions with the boundaries. However, intermolecular collisions cause a shortening of the free paths of both of the involved molecules, which is why we will investigate further the relationship between the unconfined mean-free-path and our geometry-dependent mean-free-path to take these differences into account. In future work we also aim to validate the geometry-dependence of the molecular mean-free-path in the presence of solid-boundaries by using molecular dynamics simulations.

Acknowledgment

The authors would like to thank Simon Mizzi for helpful discussions and Timothée Ewart for providing experimental data, and the referees of this paper for their useful comments. This research is funded in the UK by the Engineering and Physical Sciences Research Council under Grant No. EP/D007488/1.

Nomenclature

A = slip coefficient for models in this paper
A_{CS} = cross-sectional area
C = conventional slip coefficient
H = channel height
I = identity tensor
Kn = Knudsen number
l = molecular-free-path
L = length of a channel
$\dot{m}$ = mass flow rate
$\hat{n}$ = unit vector normal to a surface
p = gas pressure
p_d = molecular collision probability density
P = molecular collision probability function
r = molecular traveling length
R = specific gas constant
T = gas temperature
$\boldsymbol{U}$ = mass average velocity
$\boldsymbol{U}_{\mathrm{slip}}$ = velocity-slip
$\widetilde{U}_x$ = normalized average velocity across the channel width
W = width of a channel
y = coordinate perpendicular to a wall or surface
δ = inverse rarefaction parameter
θ = zenith angle of molecular traveling direction
κ = bulk viscosity.
λ = unconfined and conventional molecular mean-free-path.
μ = dynamic viscosity
ρ = gas density
$\mathbf{\Pi}$ = viscous stress tensor
σ = tangential momentum accommodation coefficient
$\boldsymbol{\tau}$ = viscous stress vector
X^t = transpose operator
X_{eff} = an "effective quantity" that is geometry-dependent
X_w = a quantity determined the wall or surface
X_x = the x-component of a vector quantity

References

[1] Arkilic, E., Schmidt, M., and Breuer, K., 1997, "Gaseous Slip Flow in Long Microchannels," J. Microelectromech. Syst., **6**(2), pp. 167–178.
[2] Colin, S., 2005, "Rarefaction and Compressibility Effects on Steady and Transient Gas Flows in Microchannels," Microfluid. Nanofluid., **1**(3), pp. 268–279.
[3] Gad-el-Hak, M., 1999, "Fluid Mechanics of Microdevices—The Freeman Scholar Lecture," ASME J. Fluids Eng., **121**(1), pp. 5–33.
[4] Guo, Z. L., Shi, B. C., and Zheng, C. G., 2007, "An Extended Navier–Stokes Formulation for Gas Flows in the Knudsen Layer Near a Wall," Europhys. Lett., **80**(2), pp. 24001–24006.
[5] Maxwell, J., 1879, "On Stresses in Rarefied Gases Arising From Inequalities

of Temperature," Philos. Trans. R. Soc. London, **170**, pp. 231–256.
[6] Lockerby, D. A., Reese, J. M., Emerson, D. R., and Barber, R. W., 2004, "Velocity Boundary Condition at Solid Walls in Rarefied Gas Calculations," Phys. Rev. E, **70**(1), p. 017303.
[7] Karniadakis, G., Beskok, A., and Aluru, N., 2005, *Microflows and Nanoflows: Fundamentals and Simulation*, Springer, New York.
[8] Cercignani, C., 2000, *Rarefied Gas Dynamics: From Basic Concepts to Actual Calculations*, Cambridge University Press, Cambridge, UK.
[9] Ewart, T., Perrier, P., Graur, I. A., and Meolans, J. G., 2007, "Mass Flow Rate Measurements in a Microchannel, From Hydrodynamic to Near Free Molecular Regimes," J. Fluid Mech., **584**, pp. 337–356.
[10] Stops, D. W., 1970, "The Mean Free Path of Gas Molecules in the Transition Regime," J. Phys. D, **3**(5), pp. 685–696.
[11] Turner, S. E., Lam, L. C., Faghri, M., and Gregory, O. J., 2004, "Experimental Investigation of Gas Flow in Microchannels," ASME J. Heat Transfer, **126**(5), pp. 753–763.
[12] Kandlikar, S., Garimella, S., Li, D., Colin, S., and King, M. R., 2005, *Heat Transfer and Fluid Flow in Minichannels and Microchannels*, Elsevier, Oxford, UK.
[13] Sharipov, F., 1999, "Rarefied Gas Flow Through a Long Rectangular Channel," J. Vac. Sci. Technol. A, **17**(5), pp. 3062–3066.
[14] Colin, S., Lalonde, P., and Caen, R., 2004, "Validation of a Second-Order Slip Flow Model in Rectangular Microchannels," Heat Transfer Eng., **25**(3), pp. 23–30.
[15] Maurer, J., Tabeling, P., Joseph, P., and Willaime, H., 2003, "Second-Order Slip Laws in Microchannels for Helium and Nitrogen," Phys. Fluids, **15**(9), pp. 2613–2621.

Flow Boiling Heat Transfer on Micro Pin Fins Entrenched in a Microchannel

Santosh Krishnamurthy

Yoav Peles

Department of Mechanical, Aerospace, and
Nuclear Engineering,
Rensselaer Polytechnic Institute,
Troy, NY 12180

Flow boiling of 1-methoxyheptafluoropropane (HFE 7000) in 222 μm hydraulic diameter channels containing a single row of 24 inline 100 μm pin fins was studied for mass fluxes from 350 kg/m^2 s to 827 kg/m^2 s and wall heat fluxes from 10 W/cm^2 to 110 W/cm^2. Flow visualization revealed the existence of isolated bubbles, bubbles interacting, multiple flow, and annular flow. The observed flow patterns were mapped as a function of the boiling number and the normalized axial distance. The local heat transfer coefficient during subcooled boiling was measured and found to be considerably higher than the corresponding single-phase flow. Furthermore, a thermal performance evaluation comparison with a plain microchannel revealed that the presence of pin fins considerably enhanced the heat transfer coefficient. [DOI: 10.1115/1.4000878]

Keywords: micro pin fins, heat transfer coefficient, flow maps

1 Introduction

The level of device integration and the clock speed of microelectronic devices have been steadily increasing over the last several decades. This has resulted in a continuous increase in the power density of electronic devices, giving rise to the need for aggressive and effective cooling solutions. The recent development in microfabrication technology has enabled a new class of heat sinks for high heat flux applications made of microelectromechanical system (MEMS) based microchannel. Microchannels with micro pin fins have been receiving attention because they can significantly enhance the performance of heat sinks compared with plain microchannels. As a result, a research on flow boiling and single-phase flow in micro-pin fin heat sinks has been carried out by several groups [1–12]. It is well known that heat transfer during subcooled flow boiling can be significantly enhanced compared with single-phase liquid flow. However, very limited studies have been performed to elucidate the heat transfer characteristics of subcooled boiling in micro pin fin configurations.

In conventional scale, subcooled flow boiling has been extensively studied for in-tube systems and various models have been developed to predict the heat transfer rates. These methods can be broadly classified into three categories, namely: empirical correlations to predict the wall heat flux [13–17], empirical correlations to predict the partitioning of wall heat flux [14,18,19], and mechanistic correlations for the total heat flux and their partitioning [20–22]. Warrier and Dhir [23] provided a detailed review on these various methods and concluded that mechanistic correlations give a better physical insight into subcooled boiling phenomenon and proposed the use of submodels to define the bubble dynamics. Literature review reveals that boiling in crossflow systems has been extensively studied, but very limited studies have been reported in subcooled boiling regime for these configurations. Huang and Witte [24,25] studied the effect of liquid flow and high subcooling across a bank of horizontal tube bundles and developed a correlation for the heat transfer coefficient using the methodology by Chen [26] developed for saturated nucleate boiling. Shah [27] compared his correlation for heat transfer coefficient around a single-tube, developed for highly subcooled liquid, with various correlations developed for low subcooled liquid and found good agreement. Cornwell [28] studied saturated nucleate flow boiling in tube bundles and attributed the enhancement in heat transfer rates to sliding bubbles. Gupta [29] attributed the enhancement in the heat transfer coefficient during nucleate boiling to the turbulence caused by the presence of bubbles on the surface.

It has been shown that reduction in length scale has a considerable affect on the bubble dynamics and flow characteristics during flow boiling. For subcooled flow boiling this is especially important since the heat transfer mechanism is very dependent on the bubble nucleation process. For example, Lee et al. [30] and Kuo et al. [31] examined the bubble dynamics for water in a microchannel and observed considerable differences compared with conventional scale systems. Cognata et al. [5] performed a visual study on flow pattern in staggered square micro pin fins and observed bubbly, slug, and annular flows. Krishnamurthy and Peles [3] investigated flow boiling heat transfer of water across densely packed staggered micro pin fins—primarily focusing on saturated flow boiling—and found that convective boiling was the dominant heat transfer mechanism.

Based on previous studies, it can be concluded that knowledge about bubble characteristics in diminishing length scales is important to elucidate heat transfer mechanisms. In the current manuscript, flow boiling across a single row of inline micro pin fins entrenched in a microchannel is presented. The microdevice consists of five 200 μm wide and 243 μm deep microchannels, each equipped with an inlet orifice, consisting of 24 columns of 100 μm diameter circular pin fins, with pitch-to-diameter ratio of 4. This study aims to elucidate the local heat transfer coefficient, to identify flow patterns, and to decipher the heat transfer mechanisms. Additionally, the performance of the pin fin device was compared with a plain microchannel device.

2 Device Design

A computer aided design (CAD) schematic of the microdevice, consisting of five 200 μm wide and 243 μm deep microchannels entrenched in a 1800 μm wide channel, is shown in Fig. 1. Each microchannel encompassed 24 inline 100 μm diameter micro pin fins with a pitch-to-diameter ratio of 4. Pressure taps were placed at the inlet and the exit of the microchannel array to enable pressure measurements. A micro-orifice, 400 μm long and 20 μm wide, was fabricated upstream of each microchannel to suppress

---

Contributed by the Heat Transfer Division of ASME for publication in the Journal of Heat Transfer. Manuscript received November 24, 2008; final manuscript received September 30, 2009; published online February 19, 2010. Assoc. Editor: Satish G. Kandlikar.

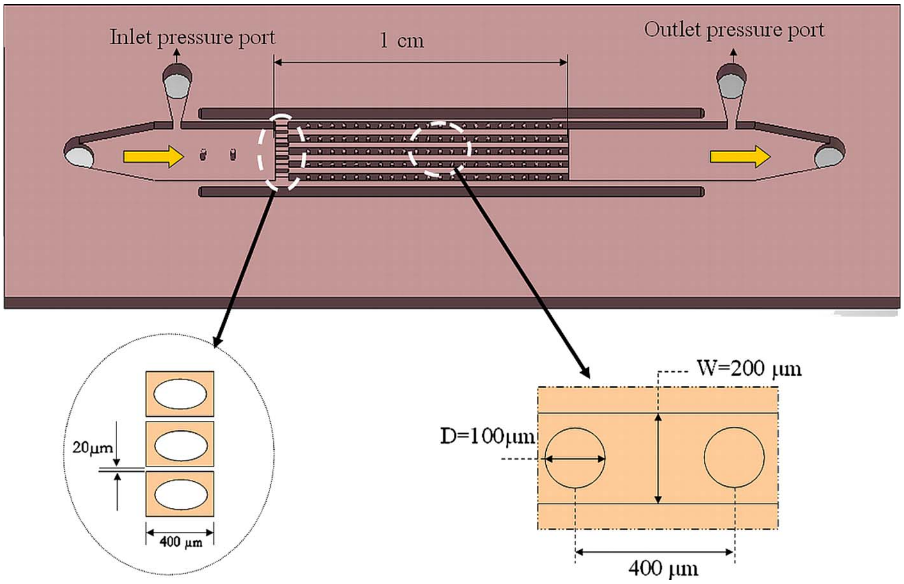

Fig. 1 Device overview showing the device dimensions

flow oscillations. A heater was deposited on the backside of the channel-pin fin section excluding the orifice to provide the requisite heat flux. A thermistor 10 μm wide and 300 μm long was placed 3.33 mm from the channel inlet. A Pyrex cover sealed the device from the top and allowed flow visualization. For details regarding the experimental set up and microfabrication process flow, please refer to Ref. [3].

3 Data Reduction

The voltage and current were used to calculate the input power, while the local temperature from the thermistor was obtained from the calibration curve. Assuming 1D steady state conduction through the silicon block, the local surface temperature of the device was obtained by

$$T_{x,s} = T_{\text{thermistor}} - \frac{(P - Q_{\text{loss}})t_s}{k_s A_p} \tag{1}$$

The local quality was calculated from the known mass flow rate according to

Table 1 Uncertainty of variables

Uncertainty variable	Measurement range	Error
Flow rate, Q [a]	0–18 ml/min	2%
Voltage, V	0–40 V	0.5%
Current, I	0–5 A	0.5%
Ambient temperature, T_{amb}	NA	±1°C
Channel width, w	NA	1%
Channel height, H	NA	0.67%
Density of liquid, ρ_l	NA	0.5%
Mass flux, G	NA	3.4%
Average surface temperature, T_r	NA	±0.5°C
Pressure, p	0–1379 kPa	3.5 kPa
Heat flux, q''_w	NA	3%
Local thermal resistance R_{conv}	NA	12–16%
Local heat transfer coefficient, h_x	NA	12–16%
Average heat transfer coefficient, h	NA	10–15%
Average Nusselt number, Nu	NA	10–15%
Reynolds number, Re_D	NA	3.4%
Boiling number, Bo	NA	11%

[a] The manufacturer provided the flow rate range for water, while experiments were performed with HFE-7000. The flow meter was calibrated prior to experiments.

$$x = \frac{(P - Q_{\text{loss}})(L_x/L_o) - \dot{m}c_p(T_{\text{sat}} - T_i)}{\dot{m}h_{fg}} \tag{2}$$

The local heat transfer coefficient for the microchannel with pin fins was calculated according to

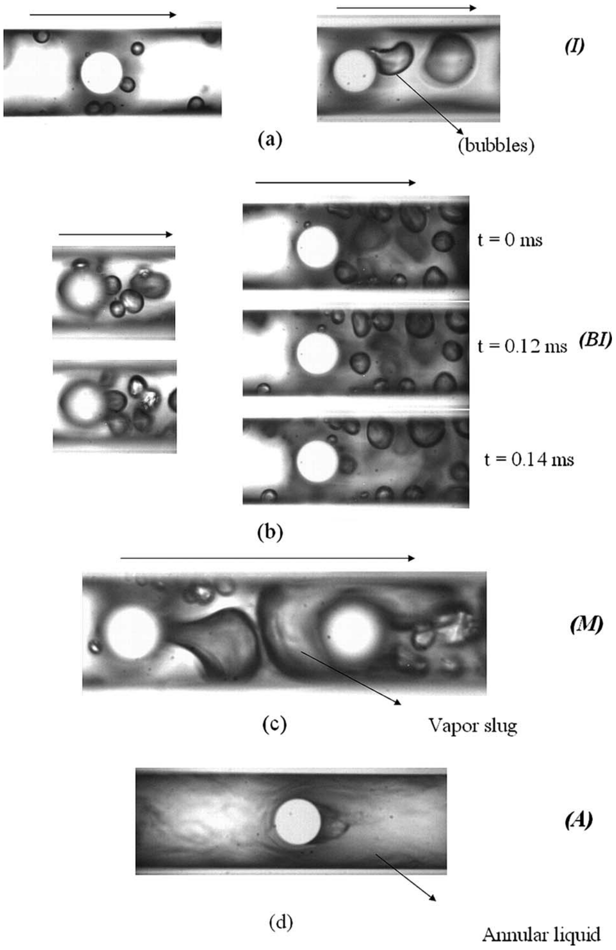

Fig. 2 Images showing: (*a*) isolated bubble region (*I*), (*b*) bubble interacting (*BI*), (*c*) multiple flow region (*M*), and (*d*) annular flow (*A*)

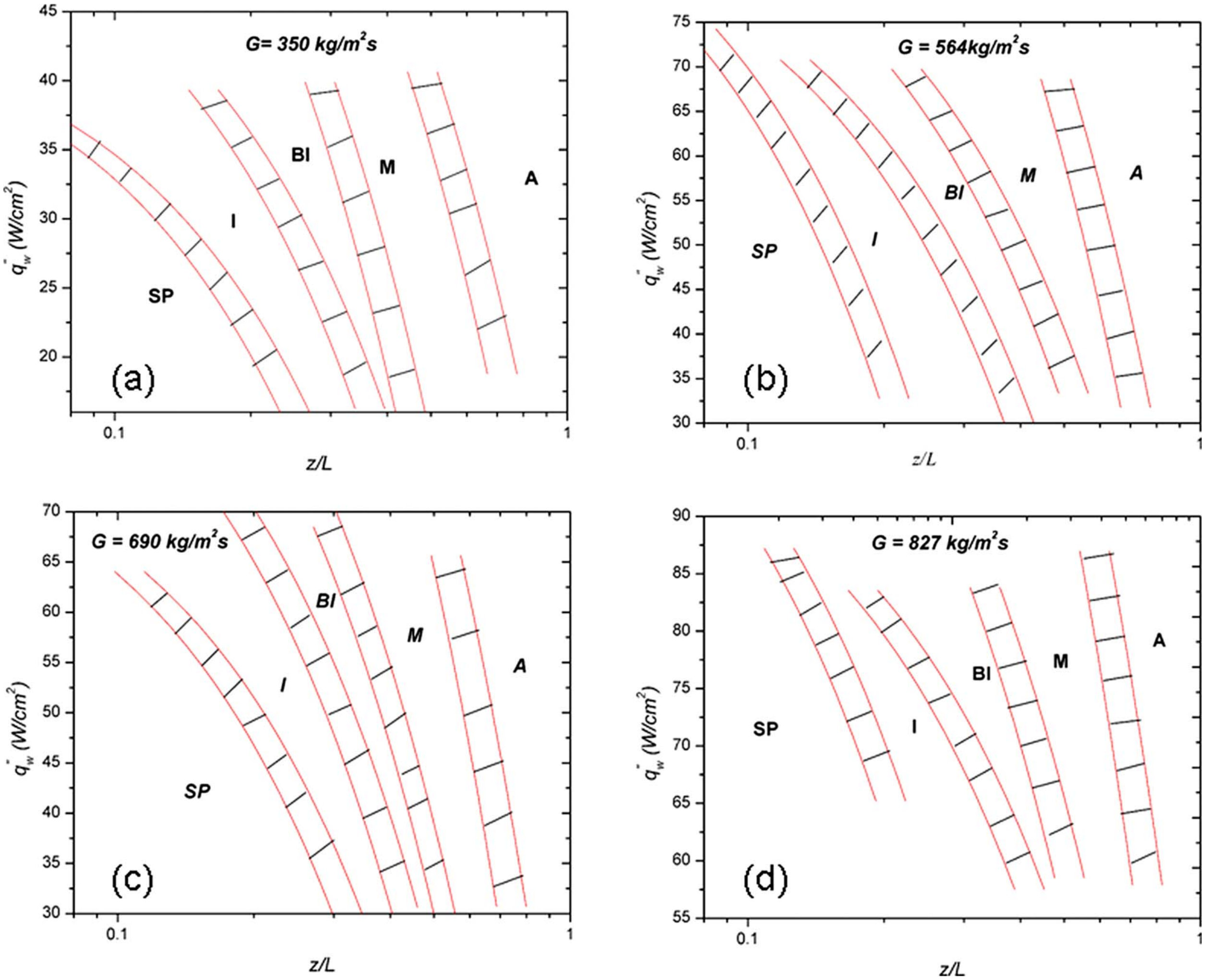

Fig. 3 Flow maps based on wall heat flux for all the mass fluxes: (*a*) $G=350\ \mathrm{kg/m^2\,s}$, (*b*) $G=564\ \mathrm{kg/m^2\,s}$, (*c*) $G=689\ \mathrm{kg/m^2\,s}$, and (*d*) $G=827\ \mathrm{kg/m^2\,s}$

$$h_x = \frac{P - Q_{\text{loss}}}{A_t(T_{x,s} - T_1)} \tag{3}$$

where $T_1 = T_{mx}$ if $x < 0$ and $T_1 = T_{\text{sat}}$ if $x > 0$. The mean local fluid temperature (T_{mx}) was obtained through an energy balance

$$T_{mx} = T_{mi} + \left(\frac{P - Q_{\text{loss}}}{\dot{m}C_p}\frac{L_x}{L}\right) \tag{4}$$

The total surface area of the channel is given by

$$A_t = N_f \eta_f A_{s,f} + A_b + N_p \eta_p A_{s,p} \tag{5}$$

where

$$\eta_f = \frac{\tanh(m_f H)}{m_f H}, \quad m_f = \sqrt{\frac{h_x(2(W+L))}{k_s W L}},$$

$$\eta_p = \frac{\tanh(m_p H)}{m_p H}, \quad m_f = \sqrt{\frac{h_x(\pi D H)}{k_s\left(\frac{\pi D^2}{4}\right)}}$$

The above equations (Eqs. (3) and (5)) were solved iteratively to obtain the local heat transfer coefficient. Similar methodology was adopted to obtain the heat transfer coefficient for the plain channel, but the total surface area was calculated as

$$A_{t,\text{plain}} = N_f \eta_f A_{s,f} + A_t - N_f A_{s,f} \tag{6}$$

The convective resistance used to evaluate the thermal performance is

$$R_{\text{conv}} = \frac{1}{h_x A_t} \tag{7}$$

The statistical average value of the heat transfer coefficients h_x and the corresponding Nusselt numbers over all heat fluxes for a fixed Reynolds number in the single-phase region was obtained by

$$\overline{h_x} = \frac{1}{M}\sum_{i=1}^{M} h_{x,i} \tag{8}$$

$$\overline{\mathrm{Nu}}_x = \frac{1}{M}\sum_{i=1}^{M} \overline{\mathrm{Nu}}_{x,i} \tag{9}$$

The uncertainties associated with the measured values were obtained from the manufacturers' specification sheets (Table 1) while the uncertainties associated with the derived quantities were obtained by using the propagation of uncertainty analysis, and are also given in Table 1.

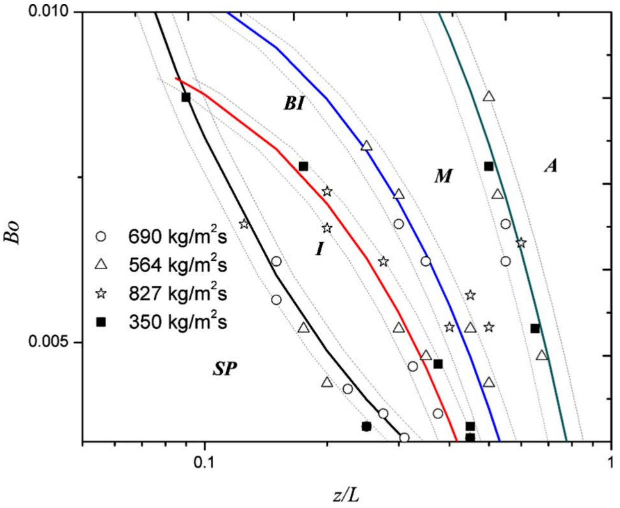

Fig. 4 Flow map showing the different flow patterns along the channel

4 Results and Discussion

4.1 Flow Pattern. In order to determine the dominant flow patterns in the device, images were taken at 10 different locations along the length of the channel. The flow patterns were then manually classified into bubbly flow, multiple flow (*M*), and annular flow (*A*). The bubbly flow was further categorized into two regions: isolated bubbles (*I*) and bubbles interacting (*BI*). The isolated bubble region extends over a relatively small section of the channel, where bubbles nucleated and departed without coalescing with bubbles from neighboring sites (Fig. 2(*a*)). With increasing nucleation site density, bubbles began to coalesce (Fig. 2(*b*)), and formed larger bubbles with diameter smaller than the pin in diameter. Further downstream, these bubbles grew and developed into vapor slugs, which were intermittently sheared by the pin fins and broken into bubbles again. This region where bubbles and vapor slugs coexisted was termed multiple flow (Fig. 2(*c*)). Eventually, the vapor slugs merged and the flow transitioned to annular flow, where liquid traversed through the channel walls, while vapor propagated through the core—nucleation was suppressed (Fig. 2(*d*)). In the channel inlet, only liquid single-phase was present. As expected, for a given mass flux, all flow patterns shifted upstream with increasing heat flux. Figures 3(*a*)–3(*d*) show a flow maps for all mass fluxes as a function of wall heat flux and normalized axial distance. The hatch regions on the flow map indicate flow transition regions. Visualization measurements were repeated three times to obtain a meaningful statistical average transition zone. In order to obtain a more general flow map using all mass fluxes and heat fluxes, an attempt to collapse the four flow maps into a single map using the boiling number was carried out. This was done by first plotting the above flow maps in terms of the boiling number and normalized axial distance, followed by fitting the data points with a best curve fit, as shown in Fig. 4. 90% of the transition data points fell within ±12% of the transition lines, as shown by the dotted lines in the figure.

4.2 Heat Transfer Coefficient. The local single-phase heat transfer coefficient is shown as a function of the wall heat flux for different mass fluxes in Fig. 5(*a*). The heat transfer coefficient characteristics followed similar trend to those observed in conventional scale tube bundle systems, i.e., independent of wall heat flux and increasing with mass fluxes. Figure 5(*b*) also shows the variation in the Nusselt number (Nu_h)—defined based on channel hydraulic diameter—as a function of the Reynolds number (Re_D). The local heat transfer coefficients during boiling as a function of wall heat flux are shown for different mass fluxes in Figs. 6(*a*)–6(*d*) (the exit pressure was maintained at 260 kPa). For $G = 350\ \mathrm{kg/m^2\,s}$, the heat transfer coefficient increased linearly with wall heat flux for $q''_w < 45\ \mathrm{W/cm^2}$, and subsequently decreased. Similar decrease in the heat transfer coefficient was also observed for $G = 564\ \mathrm{kg/m^2\,s}$ at $q''_w = 80\ \mathrm{W/cm^2}$. For mass fluxes of $689\ \mathrm{kg/m^2\,s}$ and $827\ \mathrm{kg/m^2\,s}$, the heat transfer coefficient increased linearly with wall heat flux. Figure 7 shows the variation in the heat transfer coefficient as a function of the local quality for the four mass fluxes. The majority of the datum points corresponding to two-phase flow are in the subcooled boiling regime. Figure 7 also shows that the heat transfer coefficient during subcooled boiling is considerably higher compared with the single-phase heat transfer coefficient. Such an enhancement during heat transfer coefficient in nucleate boiling has been observed in both conventional scale channels and minichannels [32,33] and has been attributed to various mechanisms, such as the evaporation of the microlayer beneath a growing bubble, transient conduction through the cold liquid layer replacing the superheated liquid layer carried away by the departing bubble [21], and sliding bubbles [28]. The contribution of these mechanisms are added linearly to account for the total heat flux according to [21]

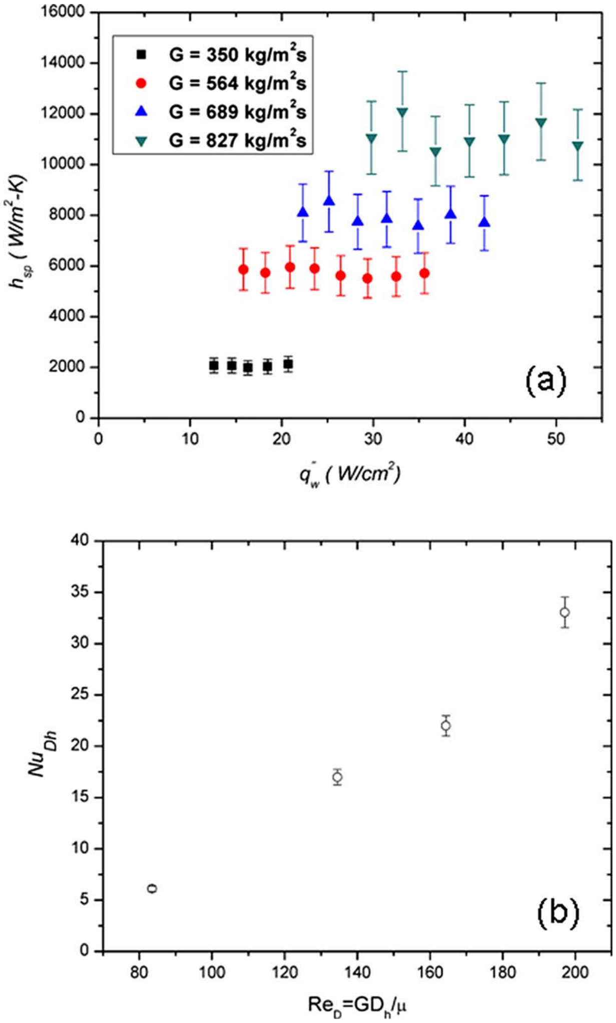

Fig. 5 (*a*) The variation in single-phase heat transfer coefficient as a function of wall heat flux and (*b*) variation in Nusselt number as a function of the Reynolds number

$$q''_t = q''_{\mathrm{ev}} + q''_{\mathrm{tr}} + q''_{\mathrm{sp}} \tag{10}$$

where q''_t, q''_{ev}, q''_{tr}, and q''_{sp} are the total heat flux, evaporative heat flux, quenching heat flux, and single-phase heat flux, respectively.

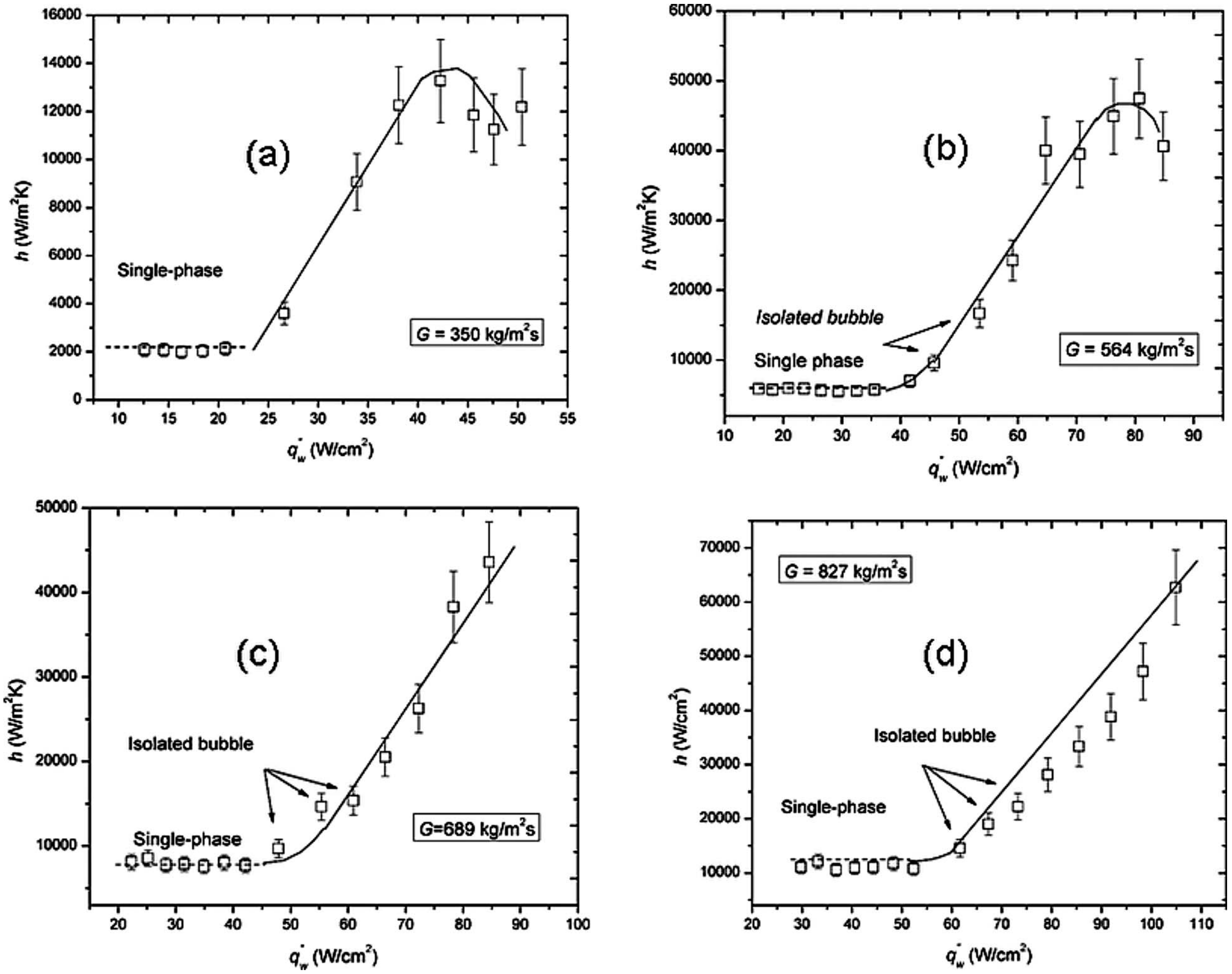

Fig. 6 Heat transfer coefficients as a function of wall heat flux: (*a*) $G=350\ \mathrm{kg/m^2\,s}$, (*b*) $G=564\ \mathrm{kg/m^2\,s}$, (*c*) $G=689\ \mathrm{kg/m^2\,s}$, and (*d*) $G=827\ \mathrm{kg/m^2\,s}$

The contribution of the above mentioned mechanisms toward the observed enhancement in the heat transfer is assessed below.

5 Heat Transfer Enhancement Mechanisms

Evaporative heat flux. The evaporative heat flux is defined as the latent energy carried away by the bubbles per unit area and consists of two terms arising from the stationary and sliding bubbles

$$q''_{\mathrm{ev}} = q''_{\mathrm{ev,st}} + q''_{\mathrm{ev,sl}} = fV_d\rho_v N_a h_{fg} + f(V_l - V_d)\rho_v N_a h_{fg} \qquad (11)$$

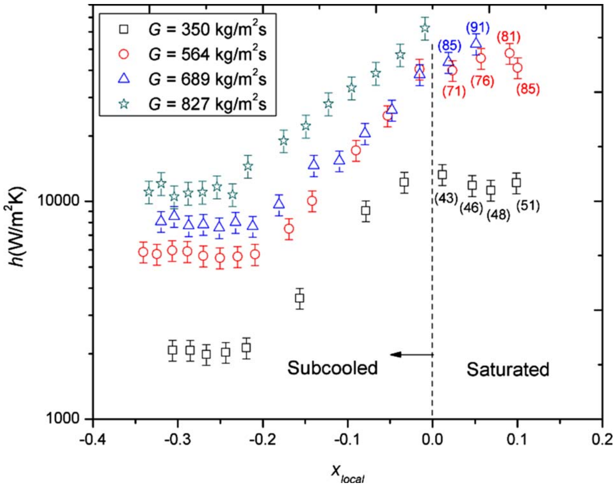

Fig. 7 The variation in heat transfer coefficient as a function of local quality (heat flux in $\mathrm{W/cm^2}$ in parenthesis)

The stationary bubble heat flux is associated with the growth of the bubble nucleating on the surface, and the sliding bubble is associated with the heat transfer during bubble growth while moving along the surface. In Eq. (11), the bubble departure frequency was assumed to be equal to the bubble lift off frequency—an assumption that is based on observation of many bubbles. Assuming the departing bubble to be spherical, the volume of the departing and lifting bubbles can be calculated as

$$V_d = \frac{\pi D_d^3}{6}, \quad V_l = \frac{\pi D_l^3}{6} \qquad (12)$$

Quenching heat flux. As a bubble departs from a nucleation site, it displaces superheated liquid adjacent to the wall by cold liquid from the bulk flow. Han and Griffith [34] postulated that the departing bubble carries away with it liquid from an area—termed area of influence—that is four times the projected area of the departing bubble. The quenching heat flux was obtained by following the approach adopted by Mikic and Rohsenow [35] assuming pure conduction through the liquid in the area of influence. For any stationary bubble departing from the site, the total average heat flux over the area of influence is given by

Table 2 Bubble dynamics in the isolated bubble region ($z=2.5-3.5$ mm)

G	q_{ch}	N_{wall}	$N_{\theta=0}$	$N_{\theta=180}$	f_{wall}	$f_{\theta=0}$	$f_{\theta=180}$	$D_{d,wall}$	$D_{d,\theta=180}$	$D_{d,\theta=0}$	q_{ev} (%)	q_{tr} (%)
350	13	2	2	3	3511	413	50	32	18	72	0.62	8.12
350	16.05	5	2	4	4300	1592	445	34	14	55	1.77	7.38
565	19.2	5	2	3	4712	2799	2175	32.5	18.5	74.6	2.6	8.9
565	20.3	10	3	5	3472	3235	2233	40.3	13	70.6	4.8	12.1
689	27.1	16	3	4	2550	4749	481	37.7	10.02	43	2.5	5.2
689	29.9	20	6	4	2819	5095	468	33.6	10.02	30	2.3	5.9
827	36.2	20	4	7	2260	5885	250	41.9	9.22	42	2.8	7.5
827	39.5	25	5	12	3805	6297	110	38	8.9	25	3.96	8.9

$$q''_{\mathrm{tr,st}} = 2\sqrt{\pi(k\rho c_p)_l f}D_d^2 N_a (T_w - T_l) \tag{13}$$

In addition to the stationary bubbles, the bubbles sliding along the surface also displaced the liquid from the surface. Assuming transient conduction through the displaced liquid layer, the total average heat flux over the area swept by the bubble is given by

$$q''_{\mathrm{tr,st}} = f\int_0^t \left(\frac{k(T_w - T_l)}{\sqrt{\pi\alpha t}}A_{\mathrm{sl}}N_a\right)dt \tag{14}$$

$$= \frac{2}{\sqrt{\pi}}\sqrt{(k\rho c_p)_l f}A_{\mathrm{sl}}N_a(T_w - T_l) \tag{15}$$

The sliding area for the bubbles was obtained as follows:

$$A_{\mathrm{sl}} = D_{\mathrm{av}}l = \frac{D_d + D_l}{2}l \tag{16}$$

l is the sliding distance, which was obtained through flow visualization. The bubble lift off diameter was found to be approximately four times the bubble departure diameter for bubbles nucleating from the frontal stagnation point ($\theta=0$ deg) and twice the bubble departure diameter for bubbles departing from the sidewalls.

It should be noted that the use of Han and Griffith's quenching term might not be entirely adequate to sliding bubbles since a sliding bubble is merely moving the superheat liquid layer along the wall rather than displacing it from the surface. However, it can be argued that because of this the model should overpredict the contribution of a sliding bubble. The analysis about the heat transfer mechanisms discussed in the paper will later show that the contribution of the quenching to the total heat flux is insignificant and therefore, that quenching is not an important heat transfer mechanism in this study. In other words, the use of the quenching model by Han and Griffith [34] serves in this study to demonstrate that it is not an important mechanism rather than to obtain accurate measure of the quenching effect.

The total heat transfer through transient conduction can be added linearly as

$$q''_{\mathrm{tr}} = q''_{\mathrm{tr,st}} + q''_{\mathrm{tr,sl}} \tag{17}$$

In order to determine the above heat fluxes, the bubble dynamics on the heated wall, such as bubble departure frequency, nucleation site density, and bubble departure diameter are necessary, and were obtained through flow visualization technique discussed in Ref. [36]. Since clear bubble images were required to obtain the parameters defining the bubble dynamics, all images were taken in the isolated bubble region. Figures 6(*a*)–6(*d*) also show the conditions under which the isolated bubbles were observed (shown by arrows). Table 2 gives values of various parameters defining the bubble dynamics between $z=2.5$ mm and $z=3.5$ mm. Table 2 also shows the contribution of the evaporative and transient conduction heat fluxes to the total heat flux. Since the bubbles emanated from two angular positions ($\theta=0$ deg, $\theta=180$ deg) [36], the bubble dynamics parameters for these locations were included in the calculation of the evaporative and transient heat fluxes. The contributions of both the evaporative and the transient conduction heat fluxes toward the total heat flux were insignificant. This shows that another significant mechanism in the form of bulk fluid agitation is a more potent heat transfer mode than the local heat removal (or just the motion) of the superheated layer adjacent to the wall. Basu et al. [21] stated that for regions between the onset of nucleate boiling and onset of significant void—the region where the bubble interaction begin to dominate—the enhancement in the heat transfer coefficient was mainly due to single-phase convection, which was enhanced (by up to 30%) as a result of the presence of bubbles on the surface. The enhancement in the heat transfer coefficient in the current study ranges between 50–90% in the isolated bubble region, which was larger than those observed in conventional scale systems. Based on the values obtained for the evaporative and transient conduction heat fluxes in the current study, it can be concluded that in the isolated bubble region, the observed enhancement in the heat transfer coefficient is neither due to microlayer evaporation nor due to the transient conduction through the liquid layer. It appears that the presence of bubble in the flow has a more pronounced influence on the heat transfer characteristics in the current microscale study than in large scale systems. The relatively large bubble diameter-to-channel hydraulic diameter ratio, compared with conventional scale systems, can significantly alter the flow characteristics in the channel, and thus, the heat transfer mechanisms. For example, the Reynolds number calculated for a bubble of largest diameter (approximately 75 μm) and the highest mean flow velocity in this study (827 $\mathrm{kg/m^2\,s}$) is 124, which corresponds to laminar flow. It can thus be postulated that the bubbles growing on the sidewalls and the pin fins induce wakes downstream the channel (very much similar to the vortex shedding observed in classical fluid dynamics such as flow across cylinders and spheres), which disrupts the boundary layer significantly beyond the region immediately adjacent to the bubble resulting in higher heat transfer coefficient. The small length scale of the channel can significantly amplify the bubble agitation effect. Additionally, the presence of recirculation zone upstream and downstream the pin fin can also contribute significantly toward enhanced mixing, and thus, enhanced heat transfer. Therefore, at low qualities, the observed enhancement can be attributed to bubble agitation and perturbation of the boundary layer. Similar argument was recently made by Donnelly et al. [37] who studied flow across a sliding bubble on an inclined surface and concluded that bubble induced wakes contribute significantly toward heat transfer enhancement. At high qualities, the nucleation site density increased and bubbles began to merge. This in turn increased the evaporation and transient conduction contributions to the total heat flux. At higher qualities (multiple bubble interaction region), the heat transfer enhancement might be due to similar mechanisms observed in a conventional scale.

5.1 Comparison With a Plain Microchannel.

To study the effect of the pin fins on the heat transfer coefficient, experiments with plain microchannels were also conducted under similar thermal hydraulic conditions and the thermal resistances of the two devices were compared. The total thermal resistance consists of

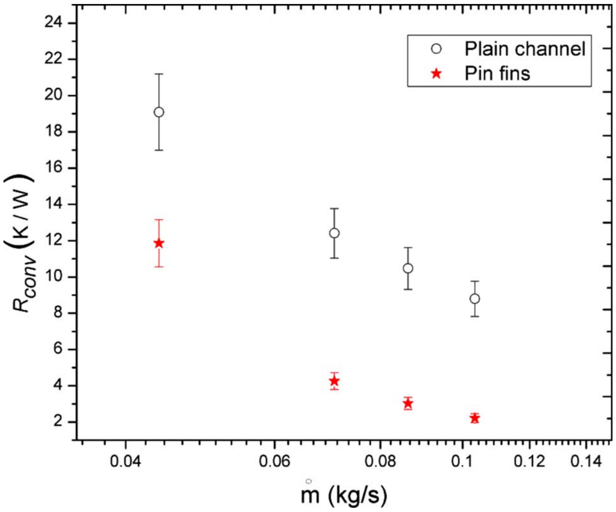

Fig. 8 Comparison of convective resistance as a function of mass flow rate for both devices

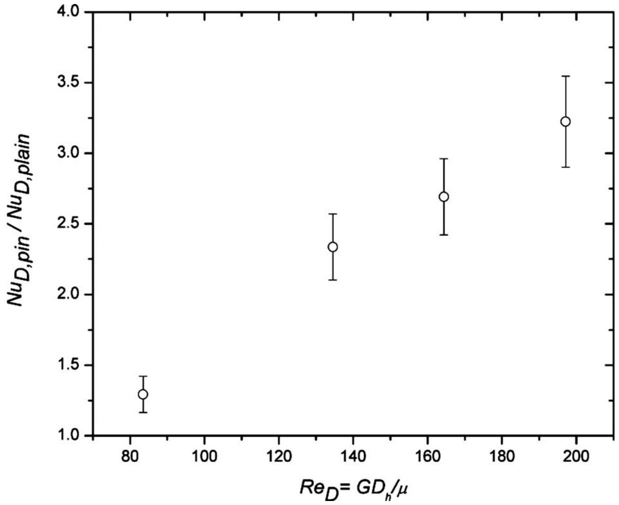

Fig. 9 Enhancement in the single-phase Nusselt number for different Reynolds numbers

conductive resistance (R_{cond}) resulting from heat conduction from the base of the silicon block to the channel surface; sensible heat resistance due to heating of the liquid (R_{heat}); and convective resistance (R_{conv}) resulting from convection from the channel walls to the fluid. Since the experiments were conducted at similar mass flow rates for both devices, the resistances due to sensible heating were the same. Likewise, the conductive resistance was the same for the two devices. Thus, only the convective resistance was

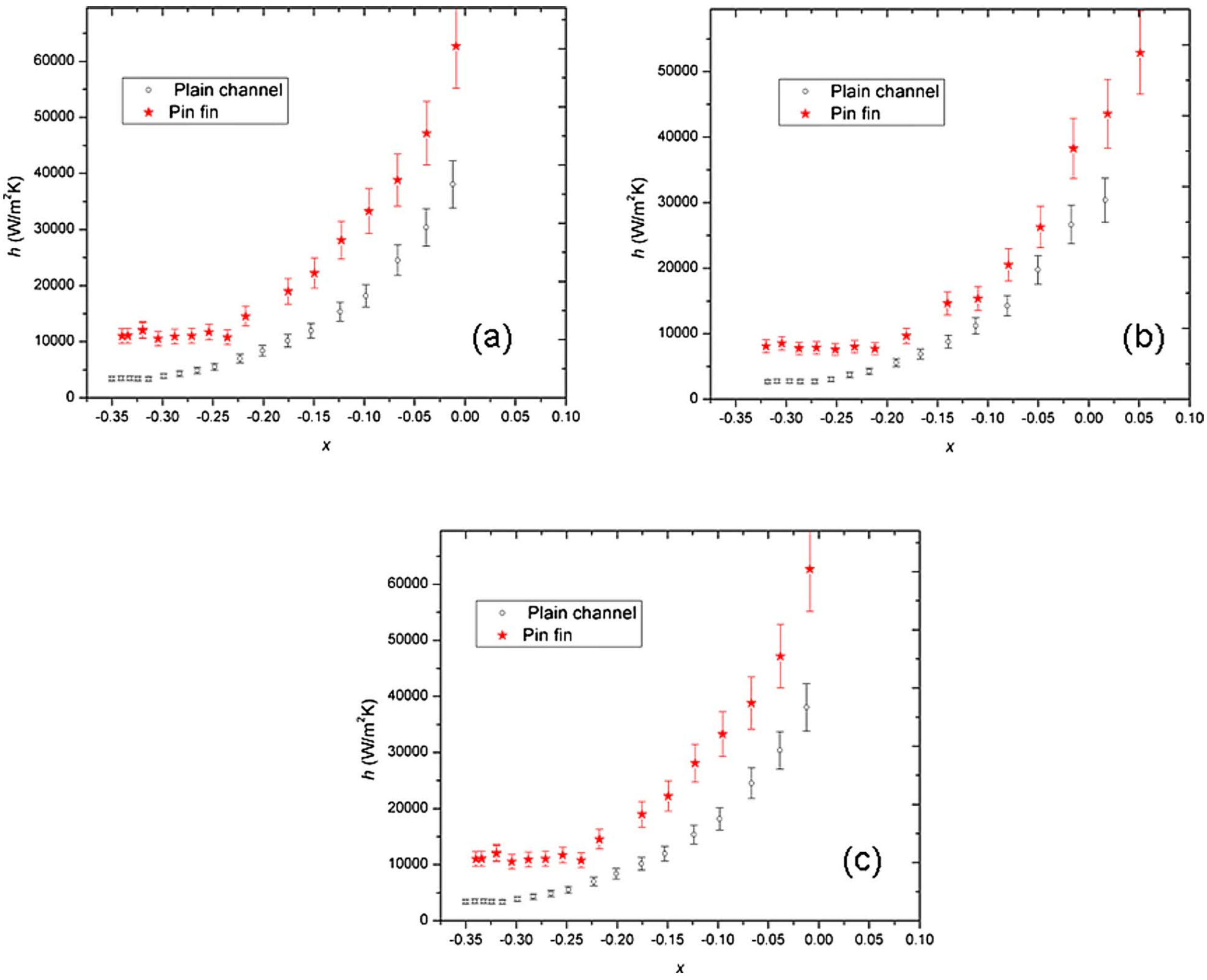

Fig. 10 Comparison of heat transfer coefficients for a microchannel with pin fins and a plain microchannel for different mass fluxes: (*a*) $G_{\text{ch}} = 282$ kg/m^2 s, (*b*) $G_{\text{ch}} = 345$ kg/m^2 s, and (*c*) $G_{\text{ch}} = 413$ kg/m^2 s

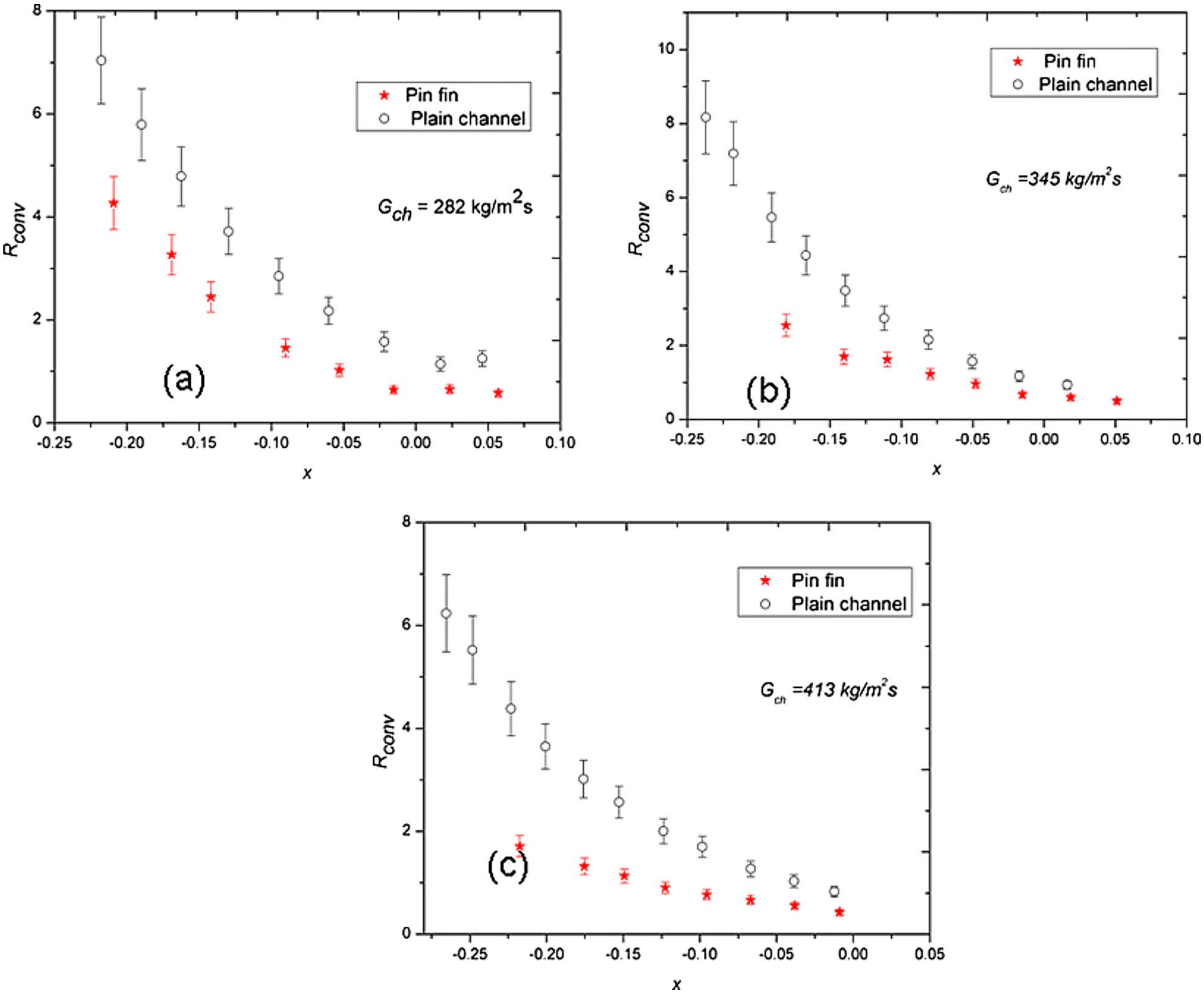

Fig. 11 Comparison of thermal convective resistances for both devices: (*a*) $G_{ch}=282$ kg/m^2 s, (*b*) $G_{ch}=345$ kg/m^2 s, and (*c*) $G_{ch}=413$ kg/m^2 s

evaluated and compared. Figure 8 compares the single-phase convective resistance (Eq. (7)) as a function of mass flow rate for both microchannel systems. The convective resistance decreases with increasing mass flow rate for both devices. The lower thermal resistance of the microchannels with pin fins compared with the plain microchannel is a result of the higher heat transfer coefficient and larger surface area. Figure 9 compares the ratio of the Nusselt number—based on the channel hydraulic diameter—for both devices as a function of Reynolds number (Re_D defined based on hydraulic diameter of the channel). The enhancement of the heat transfer coefficient increased from 1.3 to 3 when the Reynolds number increased from 84 to 197. Therefore, in addition to the surface area enhancement ($A_{\mathrm{pin}}=1.25\ A_{\mathrm{plain}}$), the presence of pin fins significantly affects the hydrodynamic characteristics of the flow resulting in increased heat transfer coefficient. The enhancement increase with the Reynolds number can be attributed to the wake interaction between the pin fins. At low Reynolds number, the wake interaction is less rigorous, and thus, a lower enhancement in the heat transfer coefficient was observed. But at higher Reynolds number, the interaction between the wakes increased, promoting advection (mixing), and thus, reducing the thermal resistance. Figures 10(*a*)–10(*c*) show the heat transfer coefficient as a function of mass quality for both devices. The heat transfer coefficient followed similar trend with respect to quality, but was quantitatively lower for the plain microchannel for all mass fluxes. The comparison of the convective resistance as a function of local quality (Figs. 11(*a*)–11(*c*)) also shows that the resistance is lower for the microchannel with pin fins. It is also evident that the rate at which the convective resistance decreases for the plain microchannel is higher compared with that observed in the microchannel with pin fins. This can partly be attributed to the more rapid decrease in the fin efficiency of the micro pin fins compared with that of channel sidewalls. Thus, with increasing heat flux, the effective surface area of the microchannel with pin fins decreased more rapidly compared with that of plain microchannel. As a result, the resistance of the microchannel with pin fins decreases more moderately. Nevertheless, the heat transfer is still enhanced by convective mixing of the pin fins, which lowers the convective resistances compared with plain microchannel. The enhancement in heat transfer coefficient is quantified by an enhancement factor E_p defined as

$$E_p = \frac{h_{\mathrm{pin\ fin}}}{h_{\mathrm{plain}}} \tag{18}$$

Figure 12 shows the variation in the enhancement factor for different qualities. The enhancement in the two-phase heat transfer coefficient is smaller when compared with the enhancement observed during single-phase. As discussed previously, the enhancement in the two-phase heat transfer coefficient in the isolated bubble region is due to bubble agitation and the perturbation of the boundary layer by the bubbles. Unlike in channel with micro-

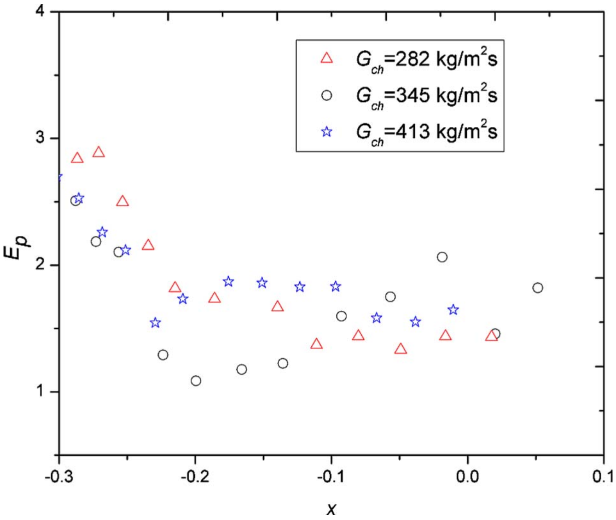

Fig. 12 Enhancement in the heat transfer coefficient for a microchannel with pin fins as a function of mass quality

pin fins, where the presence of pin fins shadows the agitation affect, in plain microchannel, such agitation can affect extended regions of the channel. As a result, the heat transfer coefficient for the plain channel increases at a higher rate compared with microchannel with pin fins in the isolated bubble region. But with increasing heat flux, for the microchannel with pin fins in the multiple bubble interaction region, the heat transfer coefficient increases significantly due to convective mixing aided by the presence of the pin fins. It follows that the enhancement increases after reaching a minimum, which was observed for both $G_{\text{ch}} = 282\ \text{kg/m}^2\ \text{s}$ and $G_{\text{ch}} = 417\ \text{kg/m}^2\ \text{s}$.

6 Summary

Subcooled and low quality saturated flow boiling across micro pin fins entrenched in a microchannel was studied for various mass fluxes and heat fluxes. The following summarizes the main findings of this study.

- Flow visualization revealed the existence of isolated bubbles, bubbles interacting, multiple flow pattern, and annular regions along the channel length. The observed flow patterns were mapped as a function of the boiling number along the channel length.
- Single-phase heat transfer coefficient for the microchannels with pin fins was found to be considerably higher compared with the plain wall channels. This was attributed to a combination of enhanced area and mixing.
- Considerable enhancement in the heat transfer coefficient during subcooled boiling over the corresponding single-phase heat transfer coefficient was observed. In the isolated bubbles region, this enhancement was attributed to the agitation of the liquid due to bubble protrusion and disruption of the boundary layer.
- The heat transfer coefficient during subcooled boiling for the microchannel with pin fins was higher than the corresponding value for plain microchannel. But the enhancement in the heat transfer coefficient was smaller in comparison to that observed during single-phase flow, especially in the isolated bubble region. This was attributed to the reduction in fin efficiency.

Acknowledgment

This work is supported by the Office of Naval Research (ONR) under the Multidisciplinary University Research Initiative (MURI) Award No. GG10919 entitled “System-Level Approach for Multi-Phase, Nanotechnology-Enhanced Cooling of High Power Microelectronic Systems.” The microfabrication was performed in part at the Cornell NanoScale Facility (a member of the National Nanotechnology Infrastructure Network), which is supported by the National Science Foundation under Grant No. ECS-0335765, its users, Cornell University, and industrial affiliates.

Nomenclature

A_p = platform area (m^2)
A_t = total surface area (m^2)
A_{sl} = sliding area swept by bubbles (m^2)
Bo = boiling number (q''_{ch}/Gh_{fg})
c_p = specific heat capacity (kJ/kg K)
D = diameter of pin fin (m)
D_h = hydraulic channel diameter (m)
D_d = bubble departure diameter (m)
D_l = bubble lift off departure diameter (m)
E_p = enhancement factor
f = bubble departure frequency (Hz)
G = mass flux (kg/m^2 s)
h_{fg} = latent heat of vaporization (kJ/kg)
h_x = local heat transfer coefficient (W/m^2 K)
H = height of microchannel (m)
I = current (A)
k_s = substrate thermal conductivity (W/m K)
L = length of the channel (m)
$\dot{m}$ = mass flow rate (kg/s)
N_a = nucleation site density
N_f = number of fins
N_p = number of pin fins
Nu$_x$ = local Nusselt number based on characteristic length scale (hD/k_f;hD_h/k_f)
P = power (W)
q''_{ev} = evaporative heat flux (W/m^2)
$q''_{\text{ev,st}}$ = stationary bubble evaporative heat flux (W/m^2)
$q''_{\text{ev,sl}}$ = sliding bubble evaporative heat flux (W/m^2)
$q''_{\text{tr,st}}$ = stationary bubble quenching heat flux (W/m^2)
$q''_{\text{tr,sl}}$ = sliding bubble quenching heat flux (W/m^2)
Q_{loss} = heat loss (W)
Re$_D$ = Reynolds number based on channel hydraulic diameter (GD_h/μ)
R_{conv} = thermal convective resistance (K/W)
R_{cond} = thermal conductive resistance (K/W)
R_{heat} = resistance due to sensible heating of fluid (K/W)
T_l = liquid temperature (K)
T_{mx} = local fluid temperature (K)
T_{mi} = inlet fluid temperature (K)
T_{sat} = saturation temperature (K)
$T_{x,s}$ = local surface temperature (K)
$T_{\text{thermistor}}$ = temperature of thermistor (K)
t_s = substrate thickness (m)
V = voltage (V)
W = width of rectangular pin fin (m)
x = vapor quality

Symbol

η_f = fin efficiency
η_p = pin fin efficiency
ρ_v = vapor density
θ = radial angle

References

[1] Qu, W., and Siu-Ho, A., 2008, “Liquid Single-Phase in an Array of Micro-Pin-Fin—Part I: Heat Transfer Characteristics,” ASME J. Heat Transfer, **130**(12),

p. 122402.

[2] Qu, W., and Siu-Ho, A., 2008, “Liquid Single-Phase in an Array of Micro-Pin-Fin—Part II: Pressure Drop Characteristics,” ASME J. Heat Transfer, **130**(12), p. 124501.

[3] Krishnamurthy, S., and Peles, Y., 2008, “Flow Boiling of Water in a Circular Staggered Micro-Pin Fin Heat Sink,” Int. J. Heat Mass Transfer, **51**(5–6), pp. 1349–1364.

[4] Siu-Ho, A., Qu, W., and Pfefferkorn, F., 2007, “Experimental Study of Pressure Drop and Heat Transfer in a Single-Phase Micropin-Fin Heat Sink,” ASME J. Electron. Packag., **129**(4), pp. 479–487.

[5] Cognata, T. J., Hollingsworth, K. D., and Witte, L. C., 2007, “High-Speed Visualization of Two-Phase Flow in a Micro-Scale Pin-Fin Heat Exchanger,” Heat Transfer Eng., **28**(10), pp. 861–869.

[6] Prasher, R. S., Dirner, J., Chang, J.-Y., Myers, A., Chau, D., He, D., and Prstic, S., 2007, “Nusselt Number and Friction Factor of Staggered Arrays of Low Aspect Ratio Micropin-Fins Under Cross Flow for Water as Fluid,” ASME J. Heat Transfer, **129**(2), pp. 141–153.

[7] Koşar, A., and Peles, Y., 2006, “Convective Flow of Refrigerant (R-123) Across a Bank of Micro Pin Fins,” Int. J. Heat Mass Transfer, **49**, pp. 3142–3155.

[8] Krishnamurthy, S., and Peles, Y., 2007, “Gas-Liquid Two-Phase Flow Across a Bank of Micro Pillars,” Phys. Fluids, **19**(4), p. 043302.

[9] Koşar, A., and Peles, Y., 2007, “Boiling Heat Transfer in a Hydrofoil-Based Micro Pin Fin Heat Sink,” Int. J. Heat Mass Transfer, **50**(5–6), pp. 1018–1034.

[10] Koşar, A., and Peles, Y., 2007, “Micro Scale Pin Fin Heat Sinks Parametric Performance Evaluation Study,” IEEE Trans. Compon. Packag. Technol., **30**(4), pp. 855–865.

[11] Siu-Ho, A. M., Qu, W., and Pfefferkorn, F. E., 2006, “Pressure Drop and Heat Transfer in a Single-Phase Micro-Pin-Fin Heat Sink,” ASME Paper No. IMECE2006 14777.

[12] Krishnamurthy, S., and Peles, Y., 2008, “Two-Phase Flow Pattern Transition Across Micropillars Size Scale Effect at the Micro Scale,” Phys. Fluids, **2**, p. 023602.

[13] Bjorg, R. W., Hall, G. R., and Rohsenow, W. M., 1982, “Correlation of Forced Convection Boiling Heat Transfer Data,” Int. J. Heat Mass Transfer, **25**, pp. 753–757.

[14] Bowring, R. W., 1962, “Physical Model Based on Bubble Detachment and Calculation of Steam Voidage in the Subcooled Region of a Heated Channel,” Institutt for Atomenergi, Halden, Norway, Paper No. Hpr-10.

[15] Bergles, A. E., and Rohsenow, W. M., 1964, “The Determination of Forced Convection, Surface Boiling Heat Transfer,” ASME J. Heat Transfer, **86**, pp. 365–372.

[16] Kutateladze, S. S., 1961, “Boiling Heat Transfer,” Int. J. Heat Mass Transfer, **4**, pp. 31–45.

[17] Kandlikar, S. G., 1998, “Heat Transfer and Flow Characteristics in Partial Boiling, Fully Developed Boiling, and Significant Void Flow Regions of Subcooled Flow Boiling,” ASME J. Heat Transfer, **120**, pp. 395–401.

[18] Rouhani, S. Z., and Axelsson, E., 1970, “Calculation of Void Volume Fraction in the Subcooled and Quality Boiling Regions,” Int. J. Heat Mass Transfer, **13**, pp. 383–393.

[19] Lahey, R. T., 1978, “A Mechanistic Subcooled Boiling Model,” *Proceedings of the Sixth International Heat Transfer Conference*, Vol. 1, Toronto, Canada, pp. 292–297.

[20] Del Valle, V. H. M., and Kenning, D. B. R., 1985, “Subcooled Flow Boiling at High Heat Flux,” Int. J. Heat Mass Transfer, **28**, pp. 1907–1920.

[21] Basu, N., Warrier, G. R., and Dhir, V. K., 2005, “Wall Heat Flux Partitioning During Subcooled Flow Boiling—Part I: Model Development,” ASME J. Heat Transfer, **127**, pp. 131–140.

[22] Basu, N., Warrier, G. R., and Dhir, V. K., 2005, “Wall Heat Flux Partitioning During Subcooled Flow Boiling—Part II: Model Validation,” ASME J. Heat Transfer, **127**, pp. 141–148.

[23] Warrier, G. R., and Dhir, V. K., 2006, “Heat Transfer and Wall Heat Flux Partitioning During Subcooled Flow Nucleate Boiling, A Review,” ASME J. Heat Transfer, **128**, pp. 1243–1256.

[24] Huang, L.-D., and Witte, L., 2001, “Highly Subcooled Boiling in Crossflow,” ASME J. Heat Transfer, **123**, pp. 1080–1085.

[25] Huang, H. L., and Witte, L. C., 1996, “An Experimental Investigation of the Effects of Subcooling and Velocity on Boiling of Freon-113,” ASME J. Heat Transfer, **118**, pp. 436–441.

[26] Chen, J. C., 1966, “Correlation for Boiling Heat Transfer to Saturated Fluids in Convective Flow,” I&EC Process Des. Dev., **5**(3), pp. 322–329.

[27] Shah, M. M., 2005, “Improved General Correlation for Subcooled Boiling Heat Transfer During Flow Across Tubes and Tube Bundles,” HVAC&R Res., **11**(2), pp. 285–303.

[28] Cornwell, K., 1990, “The Influence of Bubbly Flow on Boiling From a Tube in a Bundle,” Int. J. Heat Mass Transfer, **33**(12), pp. 2579–2584.

[29] Gupta, A., 2005, “Enhancement of Boiling Heat Transfer in a 5×3 Tube Bundle,” Int. J. Heat Mass Transfer, **48**, pp. 3763–3772.

[30] Lee, P. C., Tseng, F. G., and Pan, C., 2004, “Bubble Dynamics in Micro Channels. Part I: Single Microchannel,” Int. J. Heat Mass Transfer, **47**, pp. 5575–5589.

[31] Kuo, C.-J., Koşar, A., Peles, Y., Virost, S., Mishra, C., and Jensen, M., 2006, “Bubble Dynamics During Boiling in Enhanced Surface Microchannels,” J. Microelectromech. Syst., **15**(6), pp. 1514–1527.

[32] Lie, Y., and Lin, T., 2006, “Subcooled Flow Boiling Heat Transfer and Associated Bubble Characteristics of R-134a in a Narrow Annular Duct,” Int. J. Heat Mass Transfer, **49**, pp. 2077–2089.

[33] Martín-Callizo, C., Palm, B., and Owhaib, W., 2007, “Subcooled Flow Boiling of R-134a in Vertical Channels of Small Diameter,” Int. J. Multiphase Flow, **33**, pp. 822–832.

[34] Han, C., and Griffith, P., 1965, “The Mechanism of Heat Transfer in Nucleate Pool Boiling, Bubble Initiation, Growth and Departure,” Int. J. Heat Mass Transfer, **8**, p. 887904.

[35] Mikic, B. B., and Rohsenow, W. M., 1969, “A New Correlation of Pool-Boiling Data Including the Effect of Heating Surface Characteristics,” ASME J. Heat Transfer, **44**(14), pp. 245–250.

[36] Krishnamurthy, S., and Peles, Y., 2010, “Flow Boiling on Micropin Fins Entrenched Inside a Microchannel—Flow Patterns and Bubble Departure Diameter and Bubble Frequency,” ASME J. Heat Transfer, **132**(4), p. 041002.

[37] Donnelly, B., O’Donovan, T. S., and Murray, D. B., 2009, “Surface Heat Transfer Due to Sliding Bubble Motion,” Appl. Therm. Eng., **29**(7), pp. 1319–1326.

J. Yang

J. J. Ye[1]
e-mail: zdhjkz@zju.edu.cn

J. Y. Zheng

P. Tang Institute of Chemical Engineering Process
and Machinery,
Zhejiang University,
Hangzhou 310027, China

I. Wong
Department of Mechanical and Aerospace
Engineering,
University of California, Los Angeles,
Los Angeles, CA 90095

C. K. Lam
Department of Mechanical Engineering,
University of California, Berkeley,
Berkeley, CA 94704

P. Xu
School of Aeronautics and Astronautics,
Zhejang University,
Hangzhou 310027, China

R. X. Chen

Z. H. Zhu

Zhejang Chengxin Pharm&Chem Equipment Co.
Ltd.,
Taizhou 318012, China

Using Direct Simulation Monte Carlo With Improved Boundary Conditions for Heat and Mass Transfer in Microchannels

Micro-electromechanical systems and nano-electromechanical systems have attracted a great deal of attention in recent years. The flow and heat transfer behaviors of micromachines for separation applications are usually different from that of macro counterparts. In this paper, heat and mass transfer characteristics of rarefied nitrogen gas flows in microchannels are investigated using direct simulation Monte Carlo with improved pressure boundary conditions. The influence of aspect ratio and wall temperature on mass flowrate and wall heat flux in microchannels are studied parametrically. In order to examine the aspect ratio effect on heat and mass transfer behaviors, the wall temperature is set constant at 350 K and the aspect ratio of the microchannel varies from 5 to 20. The results show that as the aspect ratio increases, the velocity of the flow decreases, so does the mass flowrate. In a small aspect ratio channel, the heat transfer occurs throughout the microchannel; as the aspect ratio of the microchannel increases, the region of thermal equilibrium extends. To investigate the effects of wall temperature (T_w) on the mass flowrate and wall heat flux in a microchannel, the temperature of the incoming gas flow (T_{in}) is set constant at 300 K and the wall temperature varies from 200 K to 800 K while the aspect ratio is remained unchanged. Results show that majority of the wall heat flux stays within the channel entrance region and drops to nearly zero at the halfway in the channel. When $T_w < T_{in}$, under the restriction of pressure-driven condition and continuity of pressure, the molecular number density of the flow decreases along the flow direction after a short increase at the entrance region. When $T_w > T_{in}$, the molecular number density of the flow drops rapidly near the inlet and the temperature of the gas flow increases along the channel. As T_w increases, the flow becomes more rarefied, the mass flowrate decreases, and the resistance at the entrance region increases. Furthermore, when $T_w > T_{in}$, a sudden jump of heat transfer flux and temperature are observed at the exit region of the channel. [DOI: 10.1115/1.4000880]

Keywords: direct simulation Monte Carlo, heat flux, mass flowrate, microfluidics, pressure boundary conditions

1 Introduction

Micro-electromechanical systems (MEMS) and nano-electromechanical systems (NEMS) have received great interest in recent years. These highly integrated systems have been widely applied to various applications. One major application is in the field of microfluidics such as micropumps, microfilters, microjet impingement cooling, microheat pipe, and microsimulated moving beds [1–3]. The success of designing and fabricating these devices depends on the operation of a number of components. The most fundamental of which are flows through narrow microchannels with dimensions ranging from tenths to hundreds of micrometers. For examples, a commercial Whatman alumina filters (anodisc 13) with a thickness of 60 μm has a density and pore size of $5-8\times10^{12}$ m^{-2} and 212 nm, respectively, as measured by scanning electron microscope (SEM) [4]. The SEM image of the surface of these filters is shown in Fig. 1(*a*). Similar microfluidic filters were developed to capture airborne particles for detailed chemical analysis [5]. As shown in Fig. 1(*b*), the filters are fabricated by opening an array of holes in thin silicon membranes. The membrane thickness was 1 μm and has a typical pore or hole size, determined by the minimum size of the particles to be filtered, ranged from 5 μm to 10 μm. For these exciting applications, a better understanding of the fundamentals of fluid mechanics and its heat and mass transfer behaviors at the microscale or nanoscale is crucial for a better design and thermal management of the MEMS/NEMS devices. On one hand, instrumentation for microscale/nanoscale measurements has been very difficult to use and, sometimes, imprecise, resulting in a very scarce database on the microfluid/nanofluid flow properties. On the other hand, due to the small characteristic scale of the MEMS/NEMS devices, the performance of MEMS/NEMS devices often defies predictions made using scaling laws developed for large systems. Therefore, there is a pressing need for reliable computational capabilities for accurate predictions of these devices

In microfluidic systems, the mean free path of fluid molecules is on the order of the system size. The Knudsen number Kn $=\lambda/H$, where λ is the mean free path of gas molecules and H is the characteristic length of flow gradient in the system in a rarefied gas flow regime ranges from 0.01 to 10. In this regime, the fluid can no longer be regarded as a continuum and its motion has to be described from a molecular point of view. The continuum-based approach may lead to large errors in predicting fluid flows in MEMS devices. Previous researches have shown that there are

---

[1] Corresponding author.

Contributed by the Heat Transfer Division of ASME for publication in the JOURNAL OF HEAT TRANSFER. Manuscript received January 1, 2009; final manuscript received June 24, 2009; published online February 19, 2010. Assoc. Editor: Satish G. Kandlikar.

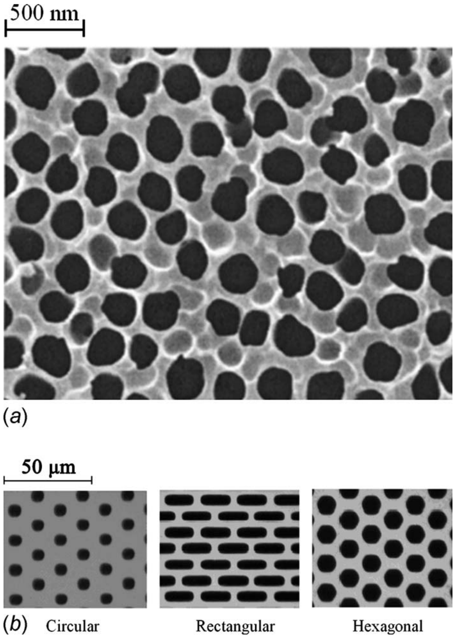

Fig. 1 Scanning electron microscope images of filters: (*a*) Whatman alumina filter (anodisc) and (*b*) microfabricated membrane filters

definite differences between continuum predictions and actual experiments [6–9]. Arkilic and co-workers [10,11] developed an analytical solution for microchannel flows based on slip boundary conditions. Their results showed that the pressure distribution in the microchannels is nonlinear. They also studied the effect of tangential momentum accommodation coefficients for the slip-flow conditions. Pong et al. [12] experimentally investigated the pressure distribution along a microchannel. Their results proved experimentally, for the first time, nonlinearity in the pressure distribution along a microchannel. On the other hand, the direct simulation Monte Carlo (DSMC) method, proposed by Bird [13,14], can be an appropriate solution in the microregime/nanoregime. The DSMC method is based on the decoupling of the molecular motions and intermolecular collisions by choosing a time step smaller than the mean collision time, and tracking the evolution of these molecular processes in space and time. It has gained a great success in predicting rarefied gaseous flows at high Knudsen numbers and is traditionally applied in modeling hypersonic rarefied gaseous flows [15,16]. It has also been proven as a valid prediction technique for microflow behaviors. Recently, this method has also been extended to low velocity flows in microchannels [17,18]. The DSMC method is considered to be one of the most successful particle simulation methods for computing flow and heat transfer behaviors of rarefied flows.

Some works have been studied on the flow and heat transfer characteristics in microchannels using the DSMC method. Mavriplis et al. [19] investigated the applicability of the DSMC method to the fluid and thermal analysis of a two-dimensional supersonic and subsonic gas flow. Liou and Fang [20] studied the heat transfer characteristics of supersonic flows in microchannels where possible causes of the increase in wall heat transfer were discussed. Using the DSMC method with pressure boundary conditions applied at the I/O boundary, Le et al. [21] investigated the flow and heat transfer behaviors under different Knudsen numbers for subsonic flows in parallel and series microchannels. Moreover, Kursun and Kapat [22] studied the microscale flow behavior over backward facing steps where flow field, temperature, and wall heat flux at various Kn numbers were compared.

In previous studies, the channel length, pressure ratio, and Kn number were varied to investigate the effects of these factors on the flow and heat transfer characteristics. Yet, there are only few works documented on the effect of wall temperature to the heat and flow behaviors in microchannels. In this paper, an improved pressure-driven boundary condition for DSMC is used to study the nitrogen gas flow in microchannels. The effects of the aspect ratio and the wall temperature on heat and mass transfer behaviors in microchannels are examined. In particular, the effect of the wall temperature on mass flowrate is also studied here, which has never been discussed in previous literatures.

2 The DSMC Method and Its Improvement

2.1 DSMC Method. The DSMC method is a probabilistic simulation method that employs a large number of statistically selected simulated particles of appropriate physical size. It is a numerical effective method to solve the dynamic equations for real gases. Each simulated molecule represents a large number of real molecules. The positions, velocities, and motion states of these simulated molecules are stored and updated in every time step. During the movement of molecules, the interactions with boundaries and with other molecules are characterized with momentum and energy conservation. During each time interval, which is much smaller than the mean collision time, molecular motion and intermolecular collisions are uncoupled. In the DSMC method, the calculation zone is divided into many computational cells, and each cell is further divided into subcells. The macroscopic flow characteristics, such as pressure, density, and temperature, are obtained statistically by sampling the simulated molecules' properties in each cell. The variable hard sphere model and the no time counter method are often used to simulate the molecular collision kinetics. The time step is set so that each simulated molecule moves about one-fifth of the cell dimension at the most probable molecular speed.

2.2 Improvement of the Pressure Boundary Conditions. The approach to boundary conditions is very important when using DSMC to predict gaseous flows in microchannels. Traditional DSMC method normally uses the Dirichlet type of velocity boundary conditions for hypersonic flows. This approach is generally applied in the simulations of external flows where downstream conditions are required to be far away from the base region. However, in microscale experiments, boundary conditions that can be directly obtained are usually pressure and temperature values whereas velocity is generally difficult to be measured accurately. Therefore, the pressure boundary conditions are much closer to the experimental conditions than the velocity boundary conditions for microchannel flow [23].

Previous works have been proposed on some methods treated with pressure boundary condition. The attempts to model pressure boundary condition for the DSMC method based on the particle flux method were introduced by Piekos and Breuer [24], Nance et al. [25], and Wu et al. [26]. According to the number of particles passing through the boundary in both positive and negative flow directions in one time step, the average inlet velocity for the whole boundary or the boundary cells can be calculated. However, due to the nature of the particle flux method, scattering can be rather large at low-speed flow conditions, leading to a poor computational stability in the numerical solution. Based on this issue, Liou and Fang [27] proposed an alternative method. By updating the boundary information obtained from the previous iteration, they significantly improved the stability issue. Nevertheless, since no pressure information is taken into consideration, this method still suffered from a relatively slow convergence in obtaining steady inlet velocities. Wang implemented the theory of characteristics for both upstream and downstream boundaries to the DSMC method [28]. The molecular number density at the inlet was calculated by the specified inlet pressure and temperature using ideal gas law. The downstream boundary was treated using the same method as Liou while the acceptance-rejection method and Maxwellian distribution were employed to determine molecular velocities and the number flux at the boundaries. This approach has been proved to enhance the convergence efficiency compared with Liou's method. In this paper, an improved pressure boundary treatment based on our previous study is re-employed in the DSMC calculation [29]. This iteration process not only introduces the pressure information into the velocity calculation but also brings the iteration step length into consideration. Compared with the methods developed by Liou and Wang, our method demonstrates major improvements in terms of convergence and applicability.

2.3 Upstream Boundary. At the upstream boundary, the inlet pressure p_{in} and temperature T_{in} are given parameters. The molecular number density n_{in} can be obtained from the state equation of ideal gas

$$n_{\text{in}} = \frac{p_{\text{in}}}{kT_{\text{in}}} \tag{1}$$

The transverse mean velocity $(v_{\text{in}})_m$ is set at zero. First-order extrapolation is used to determine the inlet mean velocity, $(u_{\text{in}})_m$ from the computed velocity for cell m as following:

$$(u_{\text{in}})_m = u_m + 2\frac{p_{\text{in}} - p_m}{\rho_m c_w}\Delta t \tag{2}$$

$$(v_{\text{in}})_m = v_m \tag{3}$$

$$(w_{\text{in}})_m = w_m \tag{4}$$

where the subscript m denotes average cell values and in denotes the inlet boundary. ρ is the density and c_w is the cell length.

2.4 Downstream Boundary. At the downstream boundary, the only given parameter is the exit pressure p_e. The other mean properties of the flow will be determined as the calculation proceeds. In the present method, the flow variables are first computed by the following equations:

$$(\rho_e)_m = \rho_m + \frac{p_e - p_m}{(a_m)^2} \tag{5}$$

$$(u_e)_m = u_m + 2\frac{p_m - p_e}{\rho_m c_w}\Delta t \tag{6}$$

$$(v_e)_m = v_m \tag{7}$$

$$(w_e)_m = w_m \tag{8}$$

$$(T_e)_m = \frac{p_e}{(\rho_e)_m R} \tag{9}$$

3 Temperature and Heat Transfer

Neglecting the vibrational energy of the diatomic nitrogen gas molecules at equilibrium, the temperature T is the weight average of the translational temperature T_{tr} and the rotational temperature T_{rot}.

$$T = (3T_{\text{tr}} + \zeta_r T_{\text{rot}})/(3 + \zeta_r) \tag{10}$$

$$\frac{3}{2}kT_{\text{tr}} = \overline{m_d c^2} - \overline{m_d} c_0^2 \tag{11}$$

$$T_{\text{rot}} = (2/k)(\overline{\varepsilon_{\text{rot}}}/\zeta_r) \tag{12}$$

where ζ_r denotes the number of rotational degrees-of-freedom (for nitrogen, ζ_r=2), k denotes the Boltzmann constant (k=1.3806 $\times 10^{-23}$ J/K), m_d denotes the mass of the molecule, c denotes the velocity of a molecule, c_0 denotes the mean velocity of simulated molecules, and $\overline{\varepsilon_{\text{rot}}}$ denotes the sample average of molecular rotational energy. In this nitrogen gas flows, rotational energy of molecules is included and the Larsen–Borgnakke model is applied in this simulation. Based on the Larsen–Borgnakke model, in order to approach physical reality, collisions are regarded as inelastic and the total energy is reassigned between the translational and internal modes. In literature [13], the process of solving the Larsen–Borgnakke model was described in detail by Bird. The wall heat flux can be evaluated from

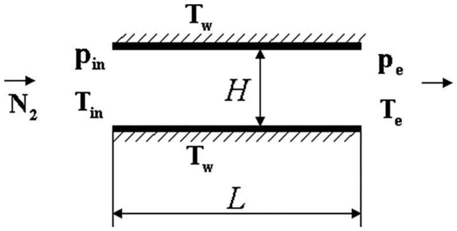

Fig. 2 Sketch of the microchannel with two parallel plates

$$q = \frac{\left[\left(\sum_{i=1}^{n_p}\varepsilon_{\text{tr}} + \sum_{i=1}^{n_p}\varepsilon_{\text{rot}}\right)_{\text{inc}} - \left(\sum_{i=1}^{n_p}\varepsilon_{\text{tr}} + \sum_{i=1}^{n_p}\varepsilon_{\text{rot}}\right)_{\text{ref}}\right]\cdot F_{n_p}}{\Delta t_s(l\cdot\Delta x)} \tag{13}$$

where n_p is the total number of simulated molecules that strike the wall element during sampling, F_{n_p} is the number of gaseous molecules associated with a simulated molecule, and Δt_s is the sampling time period.

4 Physical Modeling

The improved pressure boundary treatment is implemented into the DSMC code originally developed by Bird. The improved DSMC code, programmed in FORTRAN, is employed to simulate a micro-Poiseuille nitrogen gas flow as shown in Fig. 2. In the present work, channel aspect ratio (AR) and wall temperature (T_w) are varied, respectively, to investigate their effects on the heat transfer and mass transfer characteristics. The numerical details of all cases are listed in Tables 1 and 2, for the cases with constant T_w and the cases with constant AR, respectively. As shown in Table 1 for the constant T_w cases, channel length is set at 10 μm and pressure ratio is set at 2 by fixing the inlet pressure and the outlet pressure at 1.0×10^5 Pa and 0.5×10^5 Pa, respectively. AR

Table 1 Numerical detail of the cases with different channel AR

Quantity	Case 1	Case 2	Case 3	Case 4
H (μm)	2	1.5	1	0.5
L (μm)	10	10	10	10
AR (L/H)	5	6.67	10	20
P_{in} (Pa)	1.0×10^5			
P_e (Pa)	0.5×10^5			
T_{in} (K)	300			
T_w (K)	350			

Table 2 Numerical detail of the cases of different wall temperatures (T_w)

Quantity	Case 5	Case 6	Case 7	Case 8	Case 9	Case 10
H (μm)	1					
L (μm)	10					
AR (L/H)	10					
P_{in} (Pa)	1.5×10^5					
P_e (Pa)	0.5×10^5					
T_{in} (K)	300					
T_w (K)	200	250	300	350	500	800

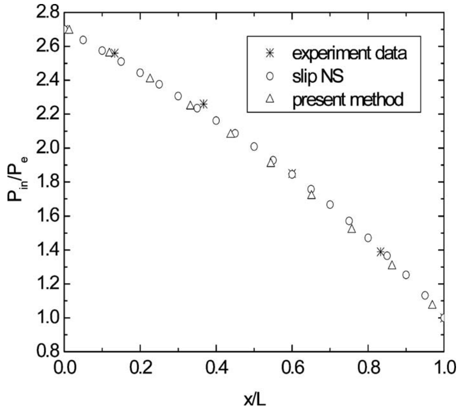

Fig. 3 Result comparison between our new method and Pong's experimental data

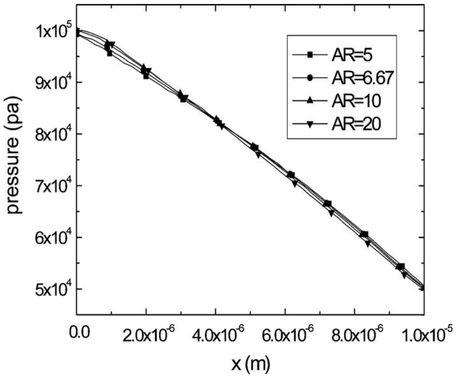

Fig. 4 Pressure distributions along the centerline of the microchannel at different AR

is varied from 5 to 20 by changing the height of the microchannel to preserve the pressure gradient in the streamwise direction for all cases. For the constant AR cases listed in Table 2, the wall temperature T_w is independently varied from 200 K to 800 K, which covers the temperature range from cooling conditions to heating conditions while the temperature of the incoming gas flow T_{in} is set constant at 300 K. The channel height is set at 1 μm and the length is 10 μm. The channel length is shortened reasonably compared with real experiments due to limitations in computational capability [30]. The pressure ratio is set at a constant of 3 by fixing the inlet pressure and the outlet pressure at 1.5×10^5 Pa and 0.5×10^5 Pa, respectively. Each computation grid contains 400×50 rectangular cells, and the number of simulated particles is about 8×10^5. The calculations are implemented on a high-performance computer and the main configurations are: Intel Xeon CPU with eight processors (the main frequency of each processor is 2.33 GHz) and 12 GB memory. Each calculation takes about 150 h of CPU time.

5 Results and Discussions

5.1 Verification of the New Pressure Boundary Treatment. To verify the validity of the new pressure boundary treatment on the DSMC method, result of the new method for a micro-Poiseuille flow is compared with experimental data from previous work by Pong et al. [12] in 1994. In their experiment, four pressure sensors were integrated along the flow direction of the microchannel with a dimension of 3000 μm in length, 40 μm in width, and 1.2 μm in height. According to literature [31], as the aspect ratio of the cross-section of the microchannel exceeds 5, the flow field of the microchannel can be simplified to a two-dimensional flow. This simplification has been applied to the analytical solutions as well as calculations in Pong's work. The analytical solution is based on the slip-flow solution of Navier–Stokes equations, which was proposed by Arkilic and Breuer [10]. As for our simulation, a total of 200,000 (50×4000) cells are used for the microchannel of the same dimensions as the above work. There are about 30 particles in each cell. Figure 3 shows the comparisons of the results of our proposed method with Pong's experimental data and slip-flow solution. It clearly shows that the pressure distribution along the channel is nonlinear. The excellent agreement between our simulation results and their experimental data confirms that our new method is valid in simulating microchannel flow.

5.2 Effect of the AR on the Heat and Mass Transfer in Microchannels. In order to investigate the flow behaviors in microchannels as shown in Fig. 1(*b*) with different AR, wall temperature is set constant at 350 K, whereas AR is changed from 5 to 20 from case 1 to case 4, as listed in Table 1. Figure 4 shows the pressure distributions along the centerline of the channels with four different ARs. It shows that the distribution of pressure is not sensitive to the changes in AR. Figure 5 shows that the Kn increases as AR increases. Local Kn increases from 0.028 at the inlet and 0.06 at the exit at AR=5 to 0.12 at the inlet and 0.25 at the exit at AR=20. This increase in Kn with AR is mainly due to the decrease in height of the microchannels, which leads to a much more rarefied state (higher Kn) in microchannels. Moreover, when AR=10, the local Kn varies from below 0.1 to above 0.1, indicating that it is possible to have flow conditions with mixed Kn regimes. The result proves that the DSMC method is a valid tool to predict this behavior.

Figure 6(*a*) shows the contours of the streamwise mean velocity at different AR and Fig. 6(*b*) plots the centerline velocity along the microchannels at different AR. In all these cases, flow velocity increases as it develops downstream and as AR increases, all local velocity decreases. When AR=5, the centerline velocity is 73 m/s at the inlet and 182 m/s at the exit. When AR=20, the centerline velocity is 12 m/s at the inlet and 27 m/s at the exit. The decrease in centerline velocity is because as AR increases, microchannel becomes narrower and increases the rarefaction of the flow. Accordingly, gas molecules are more prone to collide with channel wall and increase the local resistance of the flow field, which in turn, lead to reduction in flow velocity, even though the pressure gradient along the channel remains the same. Similar results can be found at T_w=500 K (not presented here). Figure 7 shows the effect of AR (cases 1–4) on the mass transfer characteristics. When AR=5 (case 1), the mass flowrate of the channel is 1.45×10^{-4} kg/s. But the mass flowrate sharply decreases to 7.31×10^{-5} kg/s when AR=6.67 (case 2) and 5.36×10^{-6} kg/s when AR=20 (case 4). These results again show that the mass flowrate

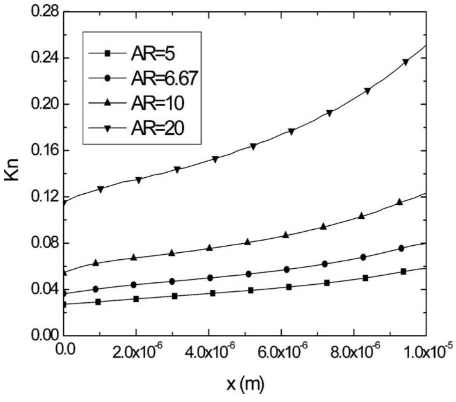

Fig. 5 Kn number distributions along the microchannel at different AR

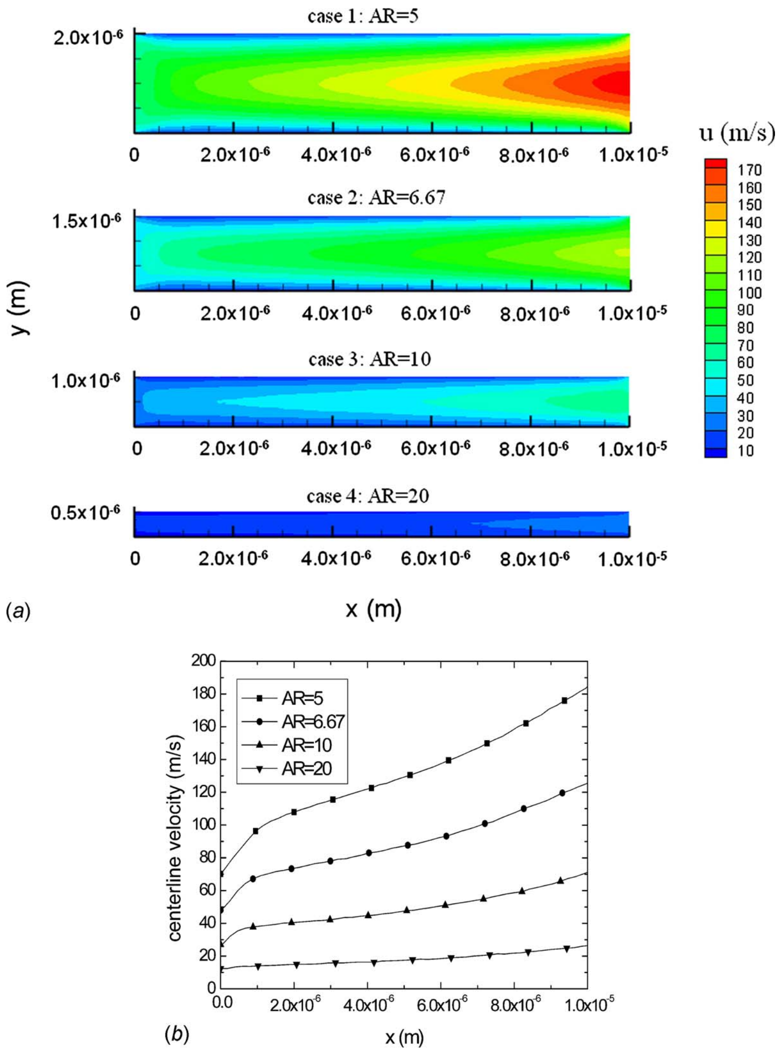

Fig. 6 Effect of AR on the velocity distributions in the microchannel: (*a*) streamwise velocity magnitude contours and (*b*) velocity distributions along the centerline

decreases as AR increases. Since the channel length is set constant in cases 1–4, any change in AR means change in the cross-sectional area of the channel. Therefore the mass flowrate also depends on the cross-sectional area. The result also indicates that a channel with high AR or small cross-sectional area is disadvantageous to the mass transfer process.

Figure 8 shows the distributions of centerline temperature at different AR values with $T_w = 350$ K (cases 1–4). For case 1 with $\mathrm{AR} = 5$, the temperature of the gas initially rises at the inlet, peaks at about $x/L = 0.6$ and drops notably near the exit of the channel.

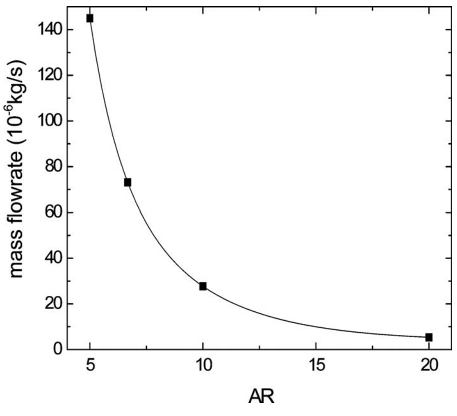

Fig. 7 Effects of the AR on mass flowrate

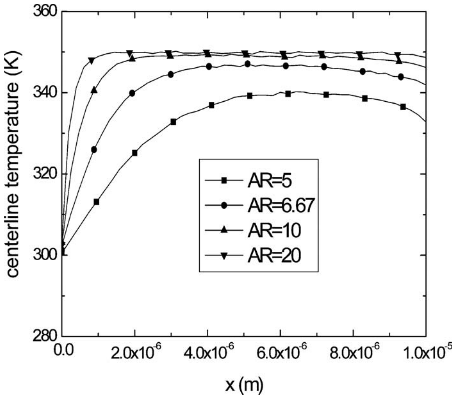

Fig. 8 Temperature distributions along the centerline of the microchannel at different AR

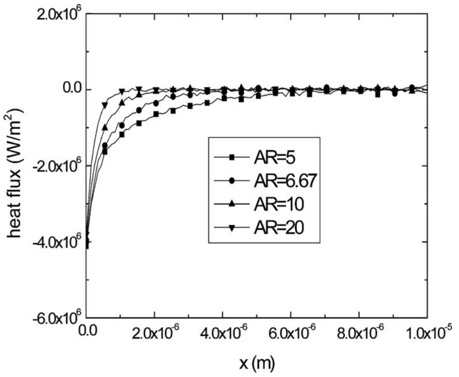

Fig. 9 Wall heat flux distributions along the microchannel at different AR

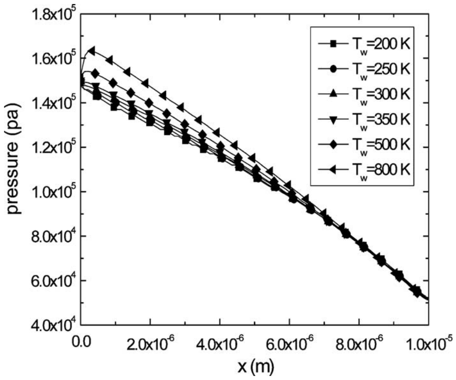

Fig. 10 Effect of T_w on pressure distributions along the channel

For case 4 with AR=20 with a smaller characteristic length, the rarefaction of the flow thus becomes more notable. Consequently, the rarefaction increases the collisions between the simulated molecules and the channel walls, causing the flow temperature to rapidly reach the wall temperature and become almost isothermal thereafter. The temperature drop in case 4 near the exit is also much lower than that in case 1. According to the molecular kinetic theory, the molecules move arbitrarily with their thermal velocities in every direction and thus molecules at the exit can either enter or escape from the channel. However, the energy of molecules entering the channel outlet is always different from that of the molecules escaping from the channel outlet, causing energy exchange between the wall and the bulk flow. Namely, the escaping molecules with high energy cause the temperature drop at the exit. On the other hand, the temperature drop is also relevant to the kinetic energy near the exit. Therefore, the velocity at the exit is directly related to the temperature drop at the exit. For example, the velocity of case 4 is much lower than that of case 1, so the temperature drop in case 4 is also much lower than that of case 1. As mentioned earlier in Fig. 6(*b*), when AR increases, the velocity in the microchannel decreases, which in turn leads to less energy loss. Similar temperature drop is also investigated at $T_w=500$ K (not shown here). These observations indicate that in microheating devices, AR of the microchannel should not be too high to avoid sharp drop of flow temperature at the exit.

Variations in local heat flux at different AR (case 1 to case 4) are shown in Fig. 9. The negative heat flux implies that heat is transferred from the wall to the gas flow. In case 4 (AR=20), heat flux mainly occurs at the entrance region while there is almost no heat transfer in the middle region of the microchannel. Conversely, in case 1 (AR=5), heat transfer occurs throughout the whole channel. This can be attributed to the fact that when AR =20, because of the smaller characteristic length, molecules have more chances to collide with the surface than when AR=5, and the temperature of the gas flow reaches the wall temperature in a very short distance from the inlet (shown in Fig. 8). This causes the thermal equilibrium position of the channel with high AR (in case 4) to move closer to the inlet than for the channel with small AR (in case 1). For case 1 (AR=5), molecules do not have enough time to collide with the wall before exiting; therefore the flow temperature is always lower than the wall temperature (shown in Fig. 8) and heat transfer occurs throughout the whole channel.

From the analysis above, it can be concluded that in microchannels with small AR, heat transfer takes places throughout the whole channel. As AR increases, heat transfer in the middle region gradually approaches thermal equilibrium and the gas flow better approximates isothermal condition, confining heat transfer only near the inlet of the channel.

5.3 Effect of Wall Temperatures (T_w) on Heat and Mass Transfer in Microchannels. In order to investigate the effect of the wall temperature on the flow and heat transfer characteristics, the wall temperature T_w is independently varied from 200 K to 800 K while the temperature of the incoming gas flow T_{in} is set constant at 300 K, as shown in Table 2. Figure 10 is the pressure distributions along the channel centerline in different wall temperature cases. It shows that as the wall temperature increases, the pressure in the microchannel also increases. Furthermore, when $T_w > T_{\text{in}}$, the pressure increases initially and peaks near the inlet and then drops along the flow direction. For the case with T_w $=500$ K, the pressure increases to 1.56×10^5 Pa at about x/L $=0.03$. When $T_w=800$ K, the value of the centerline pressure peak is the highest: the maximum pressure is 1.63×10^5 Pa. The increase in pressure at the entrance when $T_w > T_{\text{in}}$ is simply due to the fact that the hot wall can quickly heat up the gas once the flow enters the microchannel, as predicted by the equation of state P $=nkT$.

Figure 11 shows the effect of the wall temperature on the molecular number density in the microchannel. It shows that when $T_w=200$ K ($T_w < T_{\text{in}}$), the molecular number density increases near the inlet of the microchannel and reaches its peak of 4.4 $\times10^{25}$ at $x/L=0.2$. However, when $T_w=800$ K ($T_w > T_{\text{in}}$), the molecular number density drops sharply before $x/L=0.1$. In the $T_w < T_{\text{in}}$ condition, the incoming gas flow enters the channel between two cold walls. Under the restrictions of continuity of pressure in a pressure-driven flow, the molecular number density of the flow has to decrease along the flow direction after a short increase at the inlet. In the $T_w > T_{\text{in}}$ condition, the hot channel wall quickly heats up the incoming flow and causes the density of the gas flow to drop sharply. In addition, it can be observed that the

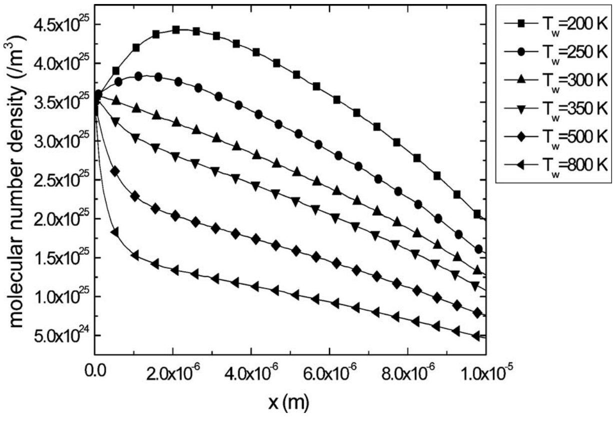

Fig. 11 Molecular number density distributions at different T_w

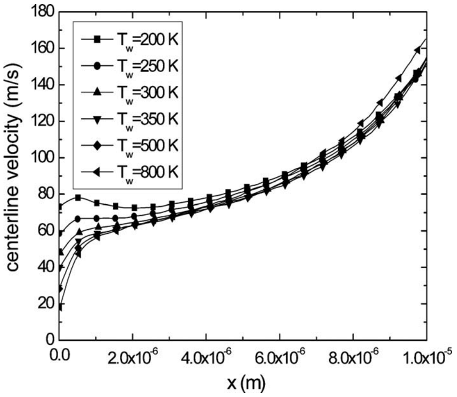

Fig. 12 Distributions of the centerline velocity at different T_w

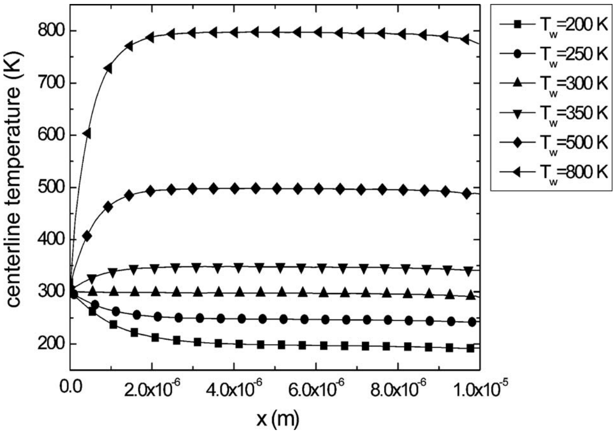

Fig. 14 Distributions of centerline temperature at different T_w

molecular number density of the flow decreases more rapidly in a higher T_w case than in a lower T_w case, especially near the inlet region of the channel.

The effect of the wall temperature on the flow velocity is shown in Fig. 12. The flow velocity increases along the channel in all cases. Before the region $x/L=0.1$, higher inlet velocity is observed with a lower T_w. When $T_w=200$ K, the inlet velocity is about 70 m/s. When $T_w=800$ K, the inlet velocity decreases to 20 m/s. It shows the inlet velocity is sensitive to the wall temperature while T_w has no effect on the velocity in the remaining part of the channel. As mentioned above, when $T_w < T_{\text{in}}$, the flow is cooled by the wall, further driving the flow to satisfy pressure continuity. When $T_w > T_{\text{in}}$, the flow is heated up by the wall at the entrance region; but the expansion will encounter the resistance from the inlet pressure. Based on these reasons, the inlet velocity of the low T_w case is higher than that of the high T_w case. In the second half of the channel, the entrance effect disappears and the velocity distributions of all cases converge.

Figure 13 shows the effect of the wall temperature on the mass transfer characteristics. At $T_w=200$ K, the mass flowrate is 1.1×10^{-5} kg/s; at $T_w=300$ K, the mass flowrate drops 34%; and at $T_w=800$ K, because of the heat expansion effect, the mass flowrate decreases to only 3.11×10^{-6} kg/s. The flow in microchannel is sensitive to the wall temperature and becomes more rarefied as the wall temperature increases, which leads to a decrease in mass flowrate. The distributions of the centerline temperature are shown in Fig. 14. In case 5 when $T_w=200$ K, the centerline temperature is cooled from 300 K to 200 K at $x/L=0.2$. In case 9 when $T_w=500$ K, the centerline temperature is heated from 300 K to 500 K at $x/L=0.2$. Similar phenomena can be observed in the other cases. It can be noted that the flow is sensitive to the wall temperature and tends to develop into the wall temperature at the entrance region.

Figure 15 shows the temperature jump, the difference between the wall temperature and the gas temperature near the wall, defined as

$$T_j = T_g - T_w \tag{14}$$

where T_g represents the gas temperature near the wall and T_w is the wall temperature. At the entrance region, the temperature jump in case 5 decreases very quickly. As the difference between the wall temperature and the incoming gas temperature increases, the temperature jump increases even faster at the entrance region, which is consistent with the analysis discussed above. When $T_w > T_{\text{in}}$, there is also a temperature jump near the channel exit, which becomes more remarkable as the T_w increases. As discussed above, the temperature drop is mainly attributed to the escaping molecules with high energy, which causes increases in kinetic energy near the exit. Although the velocities at the exit are almost the same in cases 5–10, the wall temperature in these cases are different. For case 10, the wall temperature is 800 K, which is much higher than other cases, so there is a large amount of energy exchange at the exit and the temperature jump is the most remarkable, which is about 30 K.

Figure 16 is the wall heat flux at different wall temperature. It shows that most of the wall heat flux occurs at the entrance region. In case 8 where $T_w=350$ K, the heat flux at the inlet reaches 6×10^6 W/m^2 and increases to 2.15×10^7 W/m^2 as $T_w=500$ K. For case 10 at $T_w=800$ K, the value of the heat flux at the inlet reaches as high as 5.1×10^7 W/m^2. At the midway of the channel, as the flow becomes entirely heated or cooled by the wall, the temperature of the flow is almost the same as that of the channel wall, resulting in very little heat transfer. Heat transfer is depen-

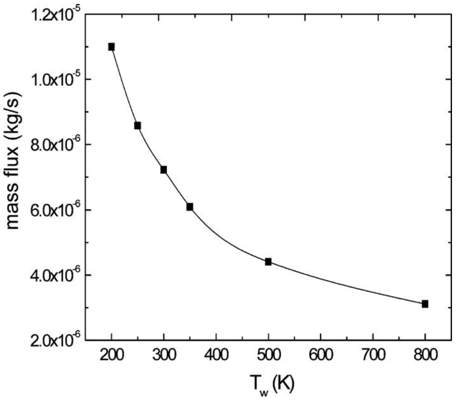

Fig. 13 Effect of the T_w on the mass flowrate

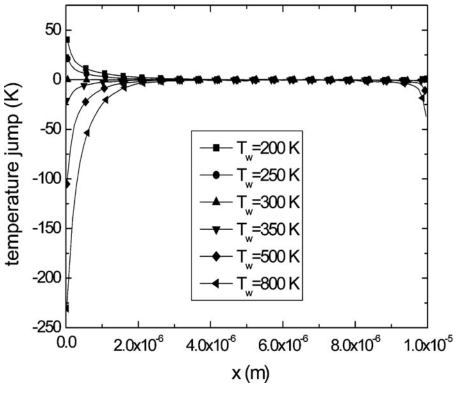

Fig. 15 Distributions of temperature jump at different T_w

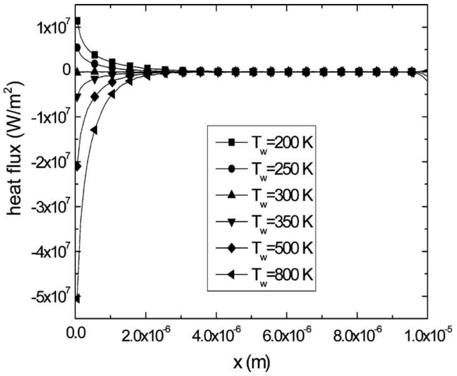

Fig. 16 Wall heat flux distributions at different T_w

dent on the molecule-surface collision. At the entrance region and the exit region, the energy of the incoming molecules is different from that of the walls, ensuing heat transfer between them. The number of the incoming molecules at entrance is much greater than that at the exit region, so the heat flux of the entrance region is much greater than that of the exit region. In the middle region of the channel, there are still a large number of molecules colliding with the wall surface; however, because the flow temperature develops to the same as the wall temperature, the molecule-surface interaction exchanges very little energy, and therefore the heat flux is nearly zero.

6 Conclusions

The DSMC method with improved pressure-driven boundary condition is applied in simulation to investigate the heat and mass transfer behaviors of gas flow in microchannels. Results show that as AR increases, both the velocity and the mass flowrate decrease. In a small AR channel, heat transfer occurs throughout the whole channel; as AR increases, the region of thermal equilibrium expands. More interesting results can be found by varying wall temperature of the microchannel. Increasing T_w leads to slight increase in pressure but a rapid drop of the molecular number density near the inlet. Moreover, as T_w increases, the mass flowrate decreases and the gas temperature increases more rapidly near the inlet, meaning more heat is exchanged between the gas and the channel wall. As T_w transits from $T_w < T_{\text{in}}$ to $T_w > T_{\text{in}}$, a growing flow resistance can be found at the entrance region; while there is no effect on the flow velocity downstream. Regarding the heat transfer characteristics, most of the wall heat flux and temperature jump occur at the entrance region. The magnitudes of the wall heat flux in the higher T_w cases are greater than that of the lower T_w cases. Far from the entrance region where the flow is completely heated or cooled by the channel, there is little heat transfer between the channel wall and the flow. Furthermore, when $T_w > T_{\text{in}}$, heat transfer is observed at the exit region of the microchannel. The results and explanation showed that the heat transfer characteristics between cooling and heating were different even under the same temperature difference in the microchannel. Further study on the detailed physics for heat and mass transfer in microchannels is worthwhile.

Acknowledgment

This project is supported by the Natural Science Foundation of China under Grant No. 50475100, Australia-China Fund of National Science Fund of China under Grant No. 50611120055, Chinese Universities Scientific Fund under Grant No. 2009QNA4031, and the high-technology research and development program of China (Project 863, Number 2009AA05Z118). The research was performed in the Center for Engineering and Scientific Computation, Zhejiang University.

Nomenclature

a = local sound speed (m/s)
c = velocity of a molecule (m/s)
c_0 = mean velocity of simulated molecules (m/s)
c_w = cell length (m)
F_{n_p} = number of gaseous molecules associated with a simulated molecule
H = channel height (m)
k = Boltzmann constant (J/K)
Kn = Kundsen number
L = channel length (m)
m_d = molecule mass (kg)
n = molecular number density (m^{-3})
n_p = total number of simulated molecules
p = pressure (Pa)
q = wall heat flux (W/m^2)
T = gas temperature (K)
T_{in} = temperature of the incoming gas flow (K)
T_j = temperature jump (K)
T_{tr} = translational temperature (K)
T_{rot} = rotational temperature (K)
u,v,w = molecular velocity components in x, y, and z directions (m/s)
Δt = time step (s)
Δt_s = time period of the sampling (s)
ζ_r = number of rotational degrees of freedom
ρ = density (kg/m^3)
λ = mean free path (m)

Subscripts

m = cell m
in = inlet
e = outlet
w = wall
inc = incident molecules
ref = reflected molecules

References

[1] Womac, D. J., Incropera, F. P., and Ramadhyani, S., 1994, "Correlating Equations for Impingement Cooling of Small Heat Sources With Multiple Circular Liquid Jets," ASME J. Heat Transfer, **116**, pp. 482–486.
[2] Darabi, J., and Ekula, K., 2003, "Development of A Chip-Integrated Micro Cooling Device," Microelectron. J., **34**, pp. 1067–1074.
[3] Amon, C. H., Murthyj, Y., and Yao, S. C., 2001, "MEMS Enabled Thermal Management of High Heat Flux Devices EDIFICE: Embedded Droplet Impingement for Integrated Cooling of Electronics," Exp. Therm. Fluid Sci., **25**, pp. 231–242.
[4] Roy, S., Raju, R., and Chuang, H. F., 2003, "Modeling Gas Flow Through Microchannels and Nanopores," J. Appl. Phys., **93**(8), pp. 4870–4879.
[5] Yang, J. M., Ho, C. M., Yang, X., and Tai, Y. C., 2001, "Micromachined Particle Filter With Low Power Dissipation," ASME J. Fluids Eng., **123**, pp. 899–908.
[6] Pfahler, J., Harley, J., Bau, H., and Zemel, J., 1991, "Gas and Liquid Flow in Small Channel," *Winter Annual Meeting of the American Society of Mechanical Engineers*, ASME, New York, Vol. 32, pp. 49–60.
[7] Liu, J., Tai, Y., and Ho, C. M., 1995, "MEMS for Pressure Distribution Studies of Gaseous Flows in Microchannels," *Proceedings of IEEE Micro Electro Mechanical Systems (MEMS)*, IEEE, New York, pp. 209–215.
[8] Chen, C. S., Lee, S. M., and Sheu, J. D., 1998, "Numerical Analysis of Gas Flow in Microchannels," Numer. Heat Transfer, Part A, **33**(7), pp. 749–762.
[9] Xue, H., Fan, Q., and Shu, C., 2000, "Prediction of Microchannel Flows Using Direct Simulation Monte Carlo," Probab. Eng. Mech., **15**, pp. 213–219.
[10] Arkilic, E. B., Breuer, K. S., and Schmidt, M. A., 1994, "Gaseous Flow in Microchannels," *International Mechanical Engineering Congress and Exposition*, FED-Vol. 197, ASME, New York, pp. 57–65.
[11] Arkilic, E. B., Schmidt, M. A., and Breuer, K. S., 1997, "Gaseous Slip Flow in Long Microchannels," J. Microelectromech. Syst., **6**, pp. 167–178.
[12] Pong, K., Ho, C., Liu, J., and Tai, Y., 1994, "Non-Linear Pressure Distribution in Uniform Microchannels," *Application of Microfabrication to Fluid Mechanics*, FED-Vol. 197, ASME, New York, pp. 51–56.
[13] Bird, G. A., 1994, *Molecular Gas Dynamics and the Direct Simulation of Gas Flows*, Clarendon, Oxford.
[14] Bird, G. A., 1998, "Recent Advances and Current Challenges for DSMC," Comput. Math. Appl., **35**, pp. 1–14.
[15] Oh, C. K., Oran, E. S., and Sinkovits, R. S., 1997, "Computations of High-

Speed, High Knudsen Number Microchannel Flows," J. Thermophys. Heat Transfer, **11**, pp. 497–505.

[16] Chung, C. H., Kim, S. C., and De, K. J., 1995, "Numerical Analysis of Hypersonic Low-Density Scramjet Inlet Flow," J. Spacecr. Rockets, **32**, pp. 60–66.

[17] Fan, J., and Shen, C., 2001, "Statistical Simulation of Low-Speed Rarefied Gas Flows," J. Comput. Phys., **167**, pp. 393–412.

[18] Sun, Q. H., and Boyd, I. D., 2002, "A Direct Simulation Method for Subsonic, Microscale Gas Flows," J. Comput. Phys., **179**, pp. 400–425.

[19] Mavriplis, C., Ahn, J. C., and Goulard, R., 1997, "Heat Transfer and Flow fields in Short Micro-Channels Using Direct Simulation Monte Carlo," J. Thermophys. Heat Transfer, **11**, pp. 489–496.

[20] Liou, W. W., and Fang, Y. C., 2001, "Heat Transfer in Microchannel Devices Using DSMC," J. Microelectromech. Syst., **10**, pp. 274–279.

[21] Le, M., Hassan, I., and Esmail, N., 2006, "DSMC Simulation of Subsonic Flows in Parallel and Series Microchannels," ASME J. Fluids Eng., **128**, pp. 1153–1163.

[22] Kursun, U., and Kapat, J. S., 2007, "Modeling of Microscale Mass Flows in Transition Regime Part I: Flow Over Backward Facing Steps," Nanoscale Microscale Thermophys. Eng., **11**, pp. 15–30.

[23] Kaplan, C. R., and Oran, E. S., 2002, "Nonlinear Filtering for Low-Velocity Gaseous Microflows," AIAA J., **40**, pp. 82–90.

[24] Piekos, E. S., and Breuer, K. S., 1996, "Numerical Modeling of Micromechanical Devices Using the Direct Simulation Monte Carlo Method," ASME J. Fluids Eng., **118**, pp. 464–469.

[25] Nance, R. P., Hash, D. B., and Hassan, H. A., 1998, "Role of Boundary Conditions in Monte Carlo Simulation of MEMS Devices," J. Thermophys. Heat Transfer, **12**, pp. 447–449.

[26] Wu, J. S., Lee, F., and Wong, S. C., 2001, "Pressure Boundary Treatment in Micromechanical Devices Using the Direct Simulation Monte Carlo Method," JSME Int. J., Ser. B, **44**, pp. 439–450.

[27] Liou, W. W., and Fang, Y. C., 2000, "Implicit Boundary Conditions for Direct Simulation Monte Carlo Method in MEMS Flow Predictions," Comput. Model. Eng. Sci., **4**, pp. 119–128.

[28] Wang, M. R., and Li, Z. X., 2004, "Simulation for Gas Flows in Microgeometries Using the Direct Simulation Monte Carlo Method," Int. J. Heat Fluid Flow, **25**, pp. 975–985.

[29] Ye, J. J., Yang, J., and Zheng, J. Y., 2007, "New Treatment of Pressure Boundary Conditions for DSMC Method in Micro-Channel Flow Simulation," *Proceedings of FEDSM2007 Fifth Joint ASME/JSME Fluids Engineering Conference*, San Diego.

[30] Cheng, K. B., Wong, M., and Zohar, Y., 2003, "Parallel and Series Multiple Microchannel Systems," *Proceedings of IEEE Micro Electro Mechanical Systems (MEMS)*, IEEE, New York, pp. 291–294.

[31] Zhen, C. E., Hong, Z. C., Lin, Y. J., and Hong, N. T., 2007, "Comparison of 3-D and 2-D DSMC Heat Transfer Calculations of Low-Speed Short Microchannel Flows," Numer. Heat Transfer, Part A, **52**, pp. 239–250.

Thermal Characterization of Interlayer Microfluidic Cooling of Three-Dimensional Integrated Circuits With Nonuniform Heat Flux

Yoon Jo Kim
e-mail: yoonjo.kim@me.gatech.edu

Yogendra K. Joshi

Andrei G. Fedorov

G.W. Woodruff School of Mechanical Engineering,
Georgia Institute of Technology,
Atlanta, GA 30332

Young-Joon Lee

Sung-Kyu Lim

School of Electrical and Computer Engineering,
Georgia Institute of Technology,
Atlanta, GA 30332

It is now widely recognized that the three-dimensional (3D) system integration is a key enabling technology to achieve the performance needs of future microprocessor integrated circuits (ICs). To provide modular thermal management in 3D-stacked ICs, the interlayer microfluidic cooling scheme is adopted and analyzed in this study focusing on a single cooling layer performance. The effects of cooling mode (single-phase versus phase-change) and stack/layer geometry on thermal management performance are quantitatively analyzed, and implications on the through-silicon-via scaling and electrical interconnect congestion are discussed. Also, the thermal and hydraulic performance of several two-phase refrigerants is discussed in comparison with single-phase cooling. The results show that the large internal pressure and the pumping pressure drop are significant limiting factors, along with significant mass flow rate maldistribution due to the presence of hot-spots. Nevertheless, two-phase cooling using R123 and R245ca refrigerants yields superior performance to single-phase cooling for the hot-spot fluxes approaching $\sim 300\ \mathrm{W/cm^2}$. *In general, a hybrid cooling scheme with a dedicated approach to the hot-spot thermal management should greatly improve the two-phase cooling system performance and reliability by enabling a cooling-load-matched thermal design and by suppressing the mass flow rate maldistribution within the cooling layer.*

[DOI: 10.1115/1.4000885]

Keywords: microchannel, microfluidic cooling, three-dimensional IC, nonuniform heat flux, single-phase, two-phase, pressure drop

1 Introduction

As the complementary metal-oxide semiconductor (CMOS) technology advanced to sub-100 nm to fulfill the demands of high-performance computing and information technology, the challenges of on-chip wiring or interconnect density, and matching the interconnect performance with that of transistors have become increasingly critical [1]. In the future gigascale integrated systems, the signaling interconnections or wiring need to be driven at ever-higher clock speed, even with the increased number and length of global wires [2]. Consequently, a substantial fraction of power consumption in the high-power chips is attributed to the increasing interconnect loading, such as wiring networks used for clock distribution [3]. Geometric flexibility in the stacked chip design and chip-to-chip routing within a stack, which can be enabled by three-dimensional (3D) stacking, have been proposed to address the interconnect delay and power consumption issues [4]. The employment of the third dimension provides higher device density and smaller chip area in 3D ICs [5]. Also, 3D integration may be used either to partition a single chip into multiple strata to reduce on-chip global interconnects length and/or to stack chips that are homogeneous or heterogeneous [6].

To practically implement and fully exploit the 3D integration of electronic systems, the accompanying thermal issues need to be addressed. By stacking active device layers, the heat dissipation rates per unit volume and per unit horizontal footprint area are proportionally increased. Also, the interior layers of the 3D structure are thermally removed from the heat sink [7]. Heat transfer is further restricted by the low thermal conductivity bonding interfaces and thermal obstacles in multiple IC layers. Moreover, the inherent spatial nonuniformity of the power/heat flux distribution/dissipation within each active layer generates hot-spots of localized intense power dissipation, which yields a spot temperature increase, degrading the functionality of circuits and creating thermal stress issues due to nonuniform thermal expansion. In particular, high temperatures brought by local hot-spots and/or excessive power consumption cause degradation of carrier mobility and escalated leakage power [8].

Thus, thermal design in sub-100 nm IC technologies has been one of the major challenges to the IC computer-aided design (CAD) community [9]. Also, the thermal management solutions cost 1–3 USD or more per watt of heat dissipated for high-performance processors [10,11]. Consequently, power—as well as temperature—aware microprocessor design, modeling and implementation, which include spatially nonuniform power distribution, have been substantially explored for planar (2D) ICs [8,9,12–15]. Among pioneering efforts, Kleiner et al. [16] performed the thermal analysis on the vertically integrated circuits (VICs) and showed that the silicon thickness of the upper chip layers is a crucial parameter in determining the thermal performance of VICs. Rahman and Reif [17] conducted the 3D system-level modeling of power dissipation, and analytical and numerical modeling of device-level and package-level heat removal. Loi et al. [18] studied the benefits of 3D technology under the influence of ther-

---

Contributed by the Heat Transfer Division of ASME for publication in the JOURNAL OF HEAT TRANSFER. Manuscript received February 2, 2009; final manuscript received September 25, 2009; published online February 19, 2010. Editor: Satish G. Kandlikar.

mal constraints using a processor-cache-memory system, and the performance of 3D architecture was compared with a conventional planar (2D) design.

Several kinds of advanced cooling technologies also have been presented such as microjet impingement [19,20], compact thermosyphon [21], loop heat pipe [22], electro-osmotically pumped loop [23], stacked microchannel heat sink [24], thermoelectric microcooler [25], miniature vapor compression heat pump [26], and miniature absorption heat pump [27]. However, such cooling solutions for 2D planar circuits do not translate readily to 3D stack, with the limited surface area available for thermal management, and the large vertical thermal resistance between the bottom layer and the heat sink of 3D integrated circuits. Koo et al. [28] conducted thermal analysis for integrated interlayer microchannel cooling for a 3D electronic circuit architecture and indicated that a layer of integrated microchannel cooling can remove heat densities up to $135\ \text{W/cm}^2$ within a 3D architecture with a maximum circuit temperature of 85°C. This study considered the vertical (i.e., for different device layers) nonuniformity of power distribution and resulting thermal couplings, but assumed a uniform power distribution within each layer. However, in-plane nonuniformity of power distribution and hot-spots will bring much higher local surface temperatures than predicted by the above mentioned calculations. Brunschwiler et al. [29] experimentally characterized the capability of area-interconnect-compatible interlayer cooling in vertically integrated high-performance chip stacks, in which several types of heat transfer structures have been explored. A maximum heat removal capability of $537\ \text{W/cm}^2$ with 60 kPa of pressure drop was measured with de-ionized water as a single-phase working fluid. Sekar et al. [30] and Bakir et al. [31] proposed a cooling solution for 3D ICs, which features the use of microchannel heat sink in each stratum of the 3D stack and the use of wafer-level batch fabricated electrical and fluidic chip input/output (I/O) interconnects. Lee et al. [6] considered the routing with multifunctional interconnects, including through-silicon-vias (TSVs) for signal, thermal, and power distribution networks in 3D ICs and demonstrated the methodology to account for various physical (space), electrical, and thermomechanical requirements.

In summary, thermal management in 3D has emerged as one of the key enabling technologies for the practical implementation of 3D integration of ICs. Thermal performance of the 3D circuit architectures remains a critical bottleneck, and further investigation of different cooling schemes and associated performance improvement is needed. In this work, the integrated interlayer microfluidic cooling scheme is adopted and numerically investigated. Using the model, the effects of the cooling mode (i.e., single-phase versus two-phase convective cooling) and geometry variation on the cooling performance are quantitatively analyzed, yielding an insight and guidance on the TSV scaling and electrical interconnect congestion. The heat transfer and pressure drop performance of the two modes are evaluated and compared. Lastly, the significance of planar nonuniformity of power distribution resulting in a presence of spatially distributed hot-spots is discussed.

2 3D-Stacked IC and Nonuniform Power Map

Figure 1 shows the spatial heat flux distribution, or power map, of the 45 nm Intel Core 2 Duo processor code-named Penryn [32], in which the two cores are mirror images of each other right below the L2 cache. To create this map, a publicly released die photo of the Penryn was examined and the floor plan was generated [33]. The total power of each core and L2 cache are 43.1 W and 4.32 W, respectively. The power density of L2 cache region is $11.3\ \text{W/cm}^2$, which is negligibly small compared with the maximum power density value $305\ \text{W/cm}^2$.

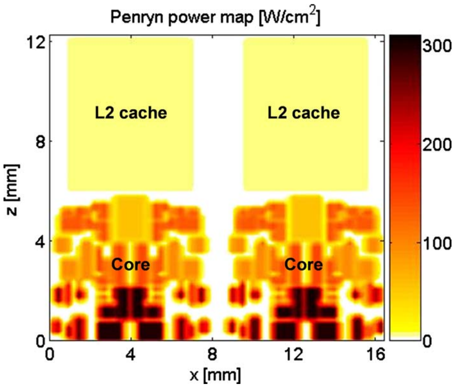

Fig. 1 Power map: Intel Core 2 Duo processor—Penryn

Each active layer in Fig. 2 consists of a single Penryn core on which a single L2 cache is stacked. The four-tier IC structure was designed to simulate a hypothetical 3D quad-core processor by stacking the four active layers integrated with intermediate metal-oxide isolation layers. Microfluidic channel layer capped with polymer Avatrel cover, as illustrated in Fig. 2, are integrated for thermal management of each high-power processor tier. While the active layers are the main power consuming layers, heat is also generated in the metal-oxide layers due to Joule heating. The microfluidic channels are capped with thin polymer (Avatrel 2000 P) coatings ($\sim 30\ \mu\text{m}$) [34]. The thicknesses of the Avatrel cover and the metal-oxide layers are set to be $10\ \mu\text{m}$ and $6\ \mu\text{m}$, respectively. The dimensions of $100\ \mu\text{m}$, $200\ \mu\text{m}$, $50\ \mu\text{m}$, and $50\ \mu\text{m}$ are taken for the baseline channel depth, width, side-wall thickness, and base thickness. Unless specifically noted, all of the calculations reported have been conducted for the baseline geometry described above. Only for the performance comparison in Sec. 4.4 and Table 3, the physical dimensions of the microfluidic channels are parametrically varied within the ranges listed in Table 1. The numbers in the parenthesize are the corresponding numbers of microfluidic channels.

3 Model Description

The thermal model of Koo et al. [28] is enhanced to deal with the three-dimensional thermal transport including the lateral temperature and fluid flow rate distribution due to nonuniform power/heat flux distribution. Figure 3 shows the cross-sectional view of the 3D-stacked IC with embedded microfluidic channels. It is assumed that the temperatures of the fluid and the solid domains (including the side-wall, base, Avatrel cover, and the oxide layer) are different but uniform at each cross section within each control volume. In reality, the temperature of the Avatrel cover and the oxide-metal layer will be slightly different from that of the silicon structure. However, these layers are very thin ($<10\ \mu\text{m}$) so that the temperature differences across these layers are insignificant even with the low thermal conductivity ($\sim 10\ \text{W/m K}$). Thus, the

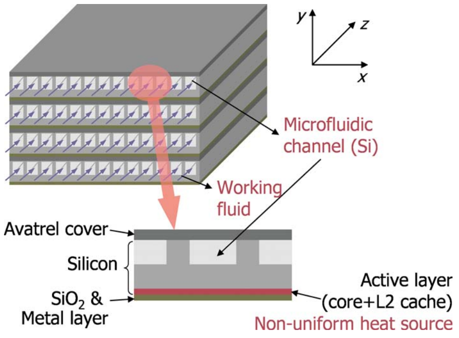

Fig. 2 3D-stacked ICs integrated with microfluidic channels for thermal management

Table 1 Physical dimensions of 3D-stacked IC and microfluidic channel. (The numbers in the parenthesize are the corresponding numbers of microfluidic channels with a single-pass channel configuration. For dual-pass, the number of channels is doubled.)

Description	Values (*: baseline)
Channel depth (μm)	50, 100*, 150, 200
Channel width (μm)	150 (40), 200*(32), 300 (22), 400 (17)
Channel side-wall thickness (μm)	25 (35), 50*(32), 100 (26), 150 (22)
Channel base thickness (μm)	25, 50*, 75, 100
Avatrel cover (μm)	0, 10*
Oxide layer (μm)	6
Channel length (mm)	6
Channel total width (mm)	8

silicon structure temperature (T_w) can be reasonably considered as the representative temperature of the control volume without any destructive influences on the thermal behaviors of the silicon structures. Also, the horizontal thermal resistances of these layers are usually more than 100 times higher compared with those of silicon structures due to the low thermal conductivity and the thin layer; the horizontal direction heat transfers through these layers are negligibly small. Thermal and fluid flow in microfluidic channels are described by the following energy and momentum conservation equations:

$$\dot{m}\frac{di}{dz} = \eta_o h_{\text{conv}}\tilde{P}(T_{w,j} - T_{f,j}) + h_{\text{conv}} w(T_{w,j+1} - T_{f,j}) \tag{1}$$

$$-\left.\frac{dP}{dz}\right|_{\text{sp}} = \frac{2fG^2}{d_h\rho} \quad \text{(for single-phase flow)} \tag{2a}$$

$$-\left.\frac{dP}{dz}\right|_{\text{tp}} = \left(\frac{2f_l G(1-x_v)}{d_h\rho_l}\right)\phi_l^2 + G\frac{d}{dz}\left(\frac{x_v^2}{\varepsilon\rho_v} + \frac{(1-x_v)^2}{(1-\varepsilon)\rho_l}\right) \quad \text{(for two-phase flow)} \tag{2b}$$

$$\frac{\partial}{\partial x}\left(k_w\frac{\partial T_w}{\partial x}\right) + \frac{\partial}{\partial y}\left(k_w\frac{\partial T_w}{\partial y}\right) + \frac{\partial}{\partial z}\left(k_w\frac{\partial T_w}{\partial z}\right) + \dot{q}_g + \dot{q}_{\text{conv}} = 0 \tag{3}$$

where T_w and T_f represent the temperatures of solid and fluid, respectively, and $\dot{m}$, i, and h_{conv} are mass flow rate, enthalpy, and convective heat transfer coefficient, respectively. For each microfluidic channel, heat is supplied only to the channel base, and the channel side-wall is analyzed as a fin attached to the base (η_o is the overall surface efficiency, including an array of fins and the base surface). The microchannel geometry is described by the channel perimeter $\tilde{P}$ and width w. Equation (3) is the three-dimensional thermal transport equation for the solid, consisting of Si. It has two source/sink terms owing to heat generated from the active and metal-oxide layers and convective heat transfer to the fluid.

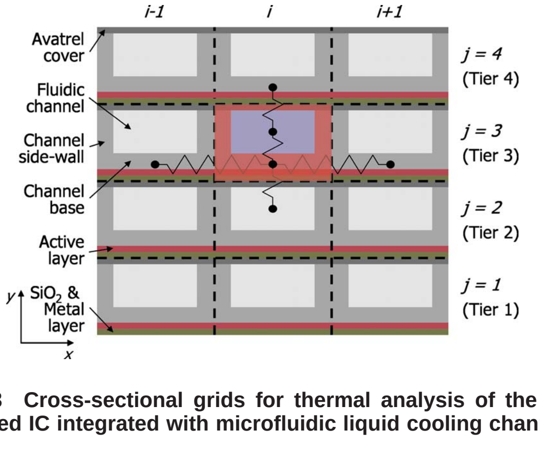

Fig. 3 Cross-sectional grids for thermal analysis of the 3D-stacked IC integrated with microfluidic liquid cooling channels

Equation (1) represents the fluid enthalpy change due to the convective heat transfer owing to the temperature difference between the solid and fluid. The two terms on the right-hand-side of Eq. (1) does account for the vertical (across the stack) thermal coupling between the layers, which in essence specify the thermal resistances between each fluid-filled channel in a given chip layer and the walls above and below it. Since these interlayer walls are shared between the different layers in the stack, it provides thermal coupling between the layers and is equivalent to an interface condition between the layers that would be used in a more general 3D formulation of the problem. A general correlation of Garimella et al. [35] is adopted in this study for evaluating single-phase convective heat transfer coefficients for fully developed as well as simultaneously thermally-hydraulically developing flow regions in the rectangular channel. The correlation covers laminar and turbulent flow having Reynolds numbers ranging from 118 to 10,671, Prandtl numbers from 6.48 to 16.20, and bulk-to-wall property variations (μ_b/μ_w) from 0.243 to 0.630.

Several correlations for two-phase heat transfer coefficients have been proposed for small channels and/or microchannels [36–41]. The boiling number Bo$=q''/G\lambda$ allows one to determine the quality at which the transition from nucleate-boiling-dominated to convective-boiling-dominated heat transfer occurs [36]. Lazarek and Black [36] suggested that the occurrence of nucleate-boiling-dominated heat transfer all the way up to CHF could be attributed to the high (above 5×10^{-4}) Boiling numbers of their data. Lin et al. [42] observed that for heat fluxes greater than ~60 kW/m^2, the heat transfer coefficient decreases as vapor quality increases, which suggests that nucleate boiling is the dominant heat transfer mechanism, regardless of vapor quality at these heat fluxes. For these conditions, the heat transfer coefficient is almost constant or slightly decreases, as the vapor quality increases. Since the Boiling number in this study ranges from 4×10^{-4} to 2×10^{-3}, nucleate boiling is the dominant heat transfer mechanism. Therefore, an enhancement of heat transfer in two-phase flow due to convection, which increases with increasing vapor quality, is largely suppressed so that the heat transfer coefficient is fairly independent of vapor quality change. The model of Tran et al. [37] suggests that nucleate boiling is a dominant two-phase heat transfer mechanism. The present study adopts the model of Yu et al. [40], who modified the model of Tran et al. [37].

The single-phase pressure drop along the microfluidic channel is obtained from the fluid momentum balance Eq. (2a), wherein P, G, and ρ are pressure, mass flux, and density of the fluid, respectively. A fanning friction factor for laminar flow in a rectangular channel and Blasius equation [43]. for turbulent flow were adopted according to the following equations:

$$f_{\text{lam}}\ \text{Re} = 24(1 - 1.3553\beta + 1.9467\beta^2 - 1.7012\beta^3 + 0.9564\beta^4 - 0.2537\beta^5) \tag{4a}$$

$$f_{\text{tub}} = 0.079\frac{1}{\text{Re}^{0.25}} \tag{4b}$$

For two-phase pressure drop, a separate model with a two-phase multiplier is used in Eq. (2b). Lee and Mudawar [44] proposed a correlation for the C value, which appeared in the classical two-phase multiplier correlation of Lockhart and Martinelli [45]. The void fraction ε can be calculated using the model of Zivi [46].

De-ionized water is considered as a working fluid for single-phase cooling. For two-phase cooling, several refrigerants have been explored as listed in Table 2, with their critical pressures and saturation pressure ranges corresponding to the temperatures

Table 2 Tested refrigerants with their critical pressures and saturation pressures

Refrigerants	P_{crit} (kPa)	P_{sat} (T_{sat}:30–70°C) (kPa)
Water	22,059	4–31
R134a	4059	771–2117
R113	3392	54–201
R236ea	3502	244–784
R227ea	2929	527–1486
R245ca	3925	122–436
R123	3662	110–377

range of 10–70°C. Equations (1), (2*a*), (2*b*), and (3) are numerically integrated over a control volume and then discretized using the upwind scheme [47]. The resulting system of linear algebraic equations is iteratively solved using the successive under relaxation (SUR) method. The thermophysical properties of water and the refrigerants are determined using REFPROP 6.0 software [48]. The inlet fluid temperature for the single-phase cooling was set at 30°C at atmospheric pressure. For two-phase cooling, all the working fluids enter the microfluidic channels at saturated liquid state ($x_{v,\mathrm{in}}=0$). The corresponding saturation temperatures are set as 50°C for the refrigerants R134a, R236ea, R227ea, R245ca, and R123 whereas for water and R113 saturation temperature of 70°C is required due to their small hydraulic budgets as listed in Table 2. Due to single inlet and exit ports for all microfluidic channels in the layer, the pressure drop from the inlet to the outlet of each microfluidic channel is fixed at 30 kPa and 50 kPa, for single-phase and two-phase cooling, respectively. Note that for two-phase cooling with water as working fluid, fixed pressure drop of 20 kPa was imposed considering the saturation pressure of 31.2 kPa at 70°C. It is assumed that the inlet and outlet pressure headers do not affect the mass flow rate maldistribution.

4 Results and Discussion

4.1 Model Validation. Zhang et al. [49] conducted an experimental study on the single-phase and two-phase convective flow with single-channel and multichannel microstructures. The multichannel design consists of 2 cm-long 40 microfluidic channels, 20 μm-wide and 70 μm-deep ($d_h=31$ μm). Due to the lateral heat loss, as well as the size mismatch between the attached heater and the microfluidic channel, the heat flux is nonuniformly distributed. In Figs. 4(*a*)–4(*c*) the measured pressure drops (Fig. 4(*a*)), wall temperature distributions (Fig. 4(*b*)), and local wall temperatures (Fig. 4(*c*)) captured from Zhang et al. [49] are compared with the calculated data using the present model. Both the pressure drop changes with respect to power dissipation in Fig. 4(*a*), and the wall temperature distributions in Fig. 4(*b*) are in very good agreement except the last data point (power dissipation 2.35 W), for which the measured pressure drop was unexpectedly higher. The middle point and the outlet local wall temperatures in Fig. 4(*c*) were also well predicted, whereas the inlet local wall temperatures were slightly underpredicted. Zhang et al. [49] reported that their microstructures had significant heat loss up to 39% of applied heat power with 20% lost to preheating of inlet water. Since the inlet heat loss information was not available in detail, the inlet heat loss seems to be overestimated in this study.

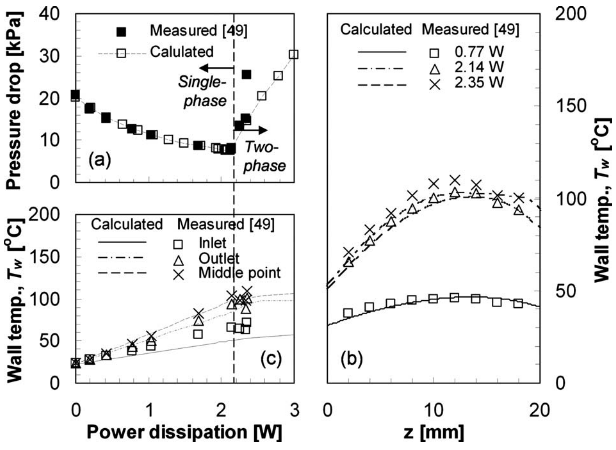

Fig. 4 Comparisons of calculated (*a*) pressure drop, (*b*) wall temperature distribution, and (*c*) local wall temperatures with the experimental data of Zhang et al. [49] for a microfluidic channel heat sink

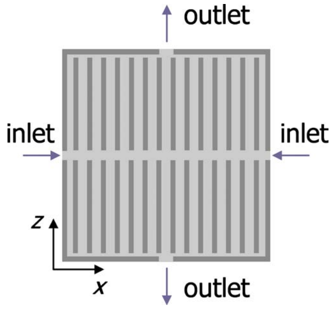

Fig. 5 Dual-pass microfluidic channel heat sink

4.2 Dual-Pass Microfluidic Channel Heat Exchanger. Kandlikar and Upadhye [50] presented a novel microchannel heat exchanger for single-phase flow, which has a split-flow arrangement (dual-pass), as depicted in Fig. 5. By providing dual-pass for refrigerant flow inside microchannels, both the flow length and the mass flux of each microchannel are reduced by half so that the pressure drop can be significantly (roughly by one-fourth) reduced. However, the thermal performance of dual-pass microfluidic channel, with single-phase flow, seems to be slightly inferior to that of single-pass microfluidic channel, as observed in Figs. 6(*a*) and 6(*b*). As aforementioned, in the comparison in Figs. 6(*a*) and 6(*b*), the total pressure drop through the channel was fixed at 30 kPa. The wall temperature at the strongest hot-spot was slightly increased from 60.07°C to 60.97°C by adopting the dual-pass configuration. It should be, however, noted that most of the hot-spots are located in the lower part of the power map so that most of the dissipated heat (90% of total power) from the Penryn core was imposed on the bottom set of channels, whereas the top channels have been largely unutilized. As expected, the mass flow rate for the tier 1 was augmented from 2.1 g/s to 7.1 g/s due to the aforementioned feature of dual-pass configuration, which made the thermal performance of the half length microfluidic channel comparable to that of full length microfluidic channel. For two-phase flow, the dual-pass configuration featured slight improvement in hot-spot temperatures as observed in Figs. 7(*a*) and 7(*b*).

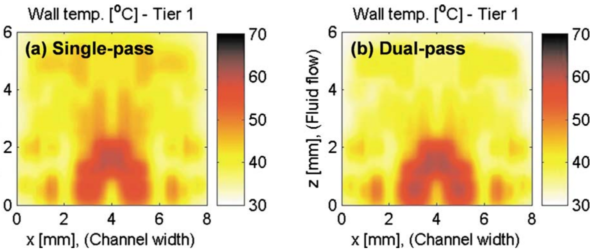

Fig. 6 Wall temperature distributions of the tier 1 with single-phase (*a*) single-pass microfluidic channel cooling and (*b*) dual-pass microfluidic channel cooling

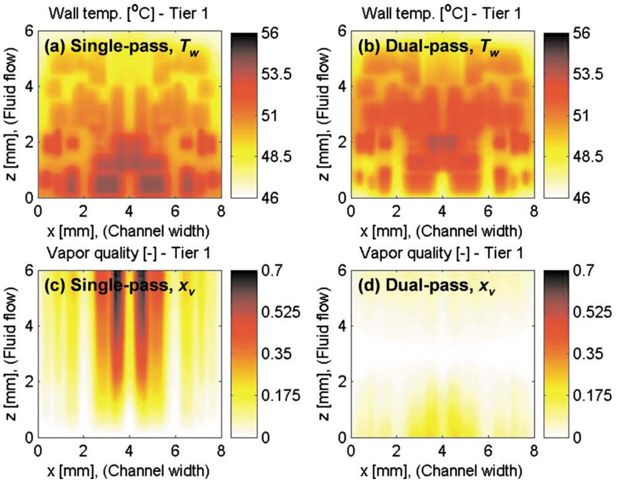

Fig. 7 Wall temperature and vapor quality distributions of the tier 1 with two-phase (*a* and *c*) single-pass microfluidic channel cooling and (*b* and *d*) dual-pass microfluidic channel cooling using R236ea as a working fluid

The highest hot-spot temperature was 54.29°C and 53.78°C for single-pass and dual-pass configurations, respectively. It should be noted that due to the pressure drop, microfluidic channel has the lowest fluid temperature at the outlet as long as the fluid flow is in two-phase throughout the microfluidic channels. Therefore, the strength of the hot-spot located in the lowest part ($0\ \text{mm}<z<1\ \text{mm}$) in Fig. 7(*a*) is suppressed in Fig. 7(*b*). Under the uniform pressure drop of 50 kPa with R236ea coolant, dual-pass microfluidic microchannel heat exchanger offered increased mass flow rate of 7.3 g/s for tier 1, which is about four times the single-pass configuration mass flow rate, 2.0 g/s. Consequently, vapor quality distribution in Figs. 7(*c*) and 7(*d*) indicate that the dual-pass configuration allowed more refrigerant to flow through microfluidic channels so that the outlet vapor qualities were much lower than those in single-pass configuration. The vapor quality is a very important parameter to determine the reliability of the thermal management system. Since at sufficiently high vapor quality, dry-out (or partial dry-out) can occur, and the channel will suffer from a lack of liquid-phase to cool the chip. The chip temperature will be drastically increased due to the poor heat transfer coefficient of refrigerant vapor. Thus, Figs. 7(*c*) and 7(*d*) suggest that the dual-pass configuration offers significantly enhanced reliability.

The drawback of the dual-pass configuration is the larger pumping power consumption. The total pumping power with the dual-pass configuration was 1.23 W, whereas with the conventional single-pass configuration it was only 0.36 W. However, the pumping powers are negligibly small compared with the total power (189.68 W) generated by the stacked chips. The comparison of pumping power between the configurations is thus not very meaningful; the pumping power budget is still abundant. If the thermal performance could be enhanced, higher pumping power would be needed to pump the coolant at sufficiently high flow rates.

4.3 Nonuniform Heat Flux.

The total power generated from the nonuniform power map of all four tiers is ~190 W. Assuming a uniform power dissipation map, with the same total power, yields the power density (heat flux) of ~100 W/cm^2 that would result in the highest wall temperature of ~43°C. Meanwhile, the highest temperature observed in Fig. 8 is ~61°C. This means that the about 20°C of the wall temperature difference between the two simulated cases should be attributed to the in-plane nonuniformity of the power density, known as the hot spots. The fluid temperature difference was around 5°C, which brought about a variation in the fluid properties, such as density and viscosity and, in turn, channel-by-channel maldistribution of the mass flow rate. Figure 9(*a*) shows that the microfluidic channels in the hot-spot region have higher mass flow rates, which is consistent with the results of Zhang et al. [49] plotted in Fig. 4(*a*). Given that G is constant, from Eqs. (2*a*) and (4), the single-phase pressure drop scales as $\Delta P_{\text{sp}} \sim \mu^a \rho^{-1}$ ($a=1$ for laminar flow, $a=0.25$ for turbulent flow). When the water temperature changes from 29°C to 34°C, both the viscosity and density decrease, but the density change is negligibly small. Thus, the reduced viscosity at the elevated fluid temperature should result in a smaller pressure drop. Under the fixed pressure drop condition, the viscosity reduction will reciprocally induce a higher flow rate through the microfluidic channels in the hot-spot region. This improves thermal performance of the single-phase microfluidic channel, and facilitates hot-spot temperature suppression because higher flow rate usually provides higher heat transfer coefficient.

Although the same power density and floor plan are imposed on each tier, vertical wall temperature differences and distribution are observed in Fig. 8. This is because the first tier thermal management only depends on the microfluidic channel above it, while the other tiers have double-sided cooling, as shown in Fig. 3. Also, tier 4 does not share the cooling power of microfluidic channel heat exchanger above it with other tiers. Therefore, tier 4 has the lowest maximum wall temperature, which is reduced by 5°C rela-

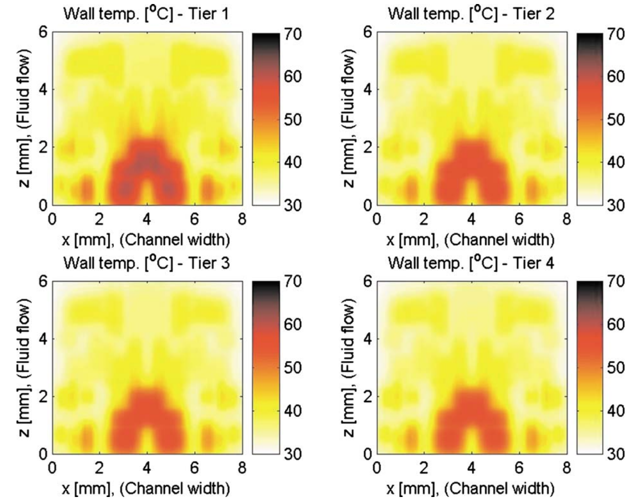

Fig. 8 Wall temperature distributions with single-phase dual-pass microfluidic channel cooling

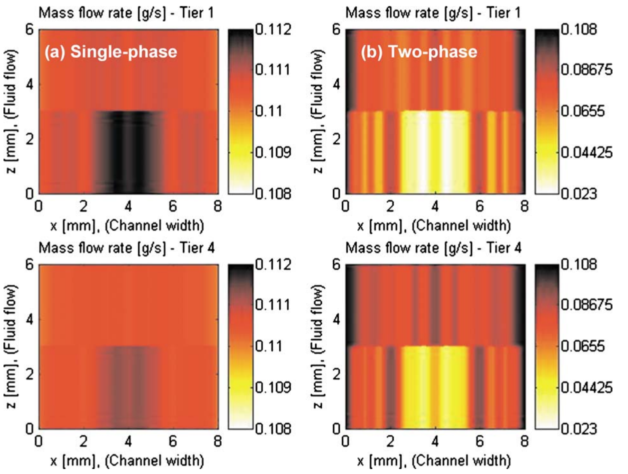

Fig. 9 Mass flow rate distributions for (*a*) single-phase and (*b*) two-phase (R123) dual-pass microfluidic channel cooling

Table 3 Single-phase dual-pass microfluidic channel cooling performance with respect to channel geometry variations

Description	$T_{w,\max}$ (°C)	$T_{f,\max}$ (°C)	$\dot{m}$ (g/s)	W_p (W)
$d=50\ \mu$m	77.92	45.67	6.03	0.19
$d=100\ \mu$m	60.97	33.66	28.36	0.91
$d=150\ \mu$m	54.14	31.77	59.07	1.89
$d=200\ \mu$m	51.32	31.11	94.81	3.03
$w=150\ \mu$m	60.85	34.28	23.92	0.76
$w=200\ \mu$m	60.97	33.64	28.36	0.91
$w=300\ \mu$m	62.01	33.09	32.96	1.08
$w=400\ \mu$m	63.35	32.80	36.45	1.23
$s=25\ \mu$m	59.37	33.38	30.99	0.99
$s=50\ \mu$m	60.97	33.64	28.36	0.91
$s=100\ \mu$m	65.29	34.24	23.07	0.75
$s=150\ \mu$m	69.07	34.75	19.55	0.64
$b=25\ \mu$m	63.01	33.81	28.36	0.91
$b=50\ \mu$m	60.97	33.64	28.36	0.91
$b=75\ \mu$m	59.56	33.53	28.36	0.91
$b=100\ \mu$m	58.47	33.44	28.36	0.91

tive to the maximum wall temperature of tier 1. This suggests placing higher power chip close to tier 4 for improved thermal performance. When tiers 3 and 4 are inactive and only tiers 1 and 2 are active, the observed highest wall temperature was 53.4°C. With the reversed operation (i.e., tiers 3 and 4 are active, while tiers 1 and 2 are inactive), the highest wall temperature rose to 58.0°C. This implies an existence of between the layer flow maldistribution. Indeed, the mass flow rate distribution in different layers of a 3D stack is shown in Fig. 9(*a*) with significant nonuniformity between the cooling layers. The maximum mass flow rates in tier 1 and tier 4 are 0.1119 g/s and 0.1113 g/s (per channel), respectively, which are passing thought the hot-spot region. However, the effects on the total mass flow rates were insignificant; total mass flow rates through tier 1 and tier 4 are 7.10 g/s and 7.08 g/s, respectively.

4.4 Microfluidic Channel Geometry. The on-chip thermofluidic network is composed of fluidic TSVs and microfluidic channels. It is assumed that all the fluidic TSVs are located outside the region where all the gates and metal wiring are distributed. Thus, only microfluidic channels are considered for routing requirement analysis. Since microfluidic channels are fabricated on the back side of a silicon die, they do not affect routing capability on metal layers. However, these channels obstruct TSV connections. Due to their large size, the microfluidic channels decrease the routing capacity of TSVs quite considerably. In fact, the scarcest resource is usually the signal TSV capacity. Due to the microfluidic channels placement, many routing tiles have no capacity left for signal TSVs [6]. Therefore, the microfluidic cooling channels compete with wire routability for space.

The effect of channel geometry variation on cooling system parameters and performance is summarized in Table 3. As the channel depth increases, the microfluidic channel gains more mass flow rate (under fixed pressure drop), which augments the heat transfer capability of the fluid. Also, since the fluid temperature rise is reduced by the increased mass flow rate, the wall and fluid temperatures can be further lowered. An increase in the channel depth from 50 μm to 200 μm reduced the hot-spot temperature by 26.6°C. However, in terms of TSV performance, shorter channel depth as well as TSV length are preferred. Lee et al. [6] reported that the reduced TSV signal length brought by the channel depth decrease from 100 μm to 50 μm increased the *y*-direction routing capacity, so that the *y*-direction routing tile usage has been 17.7%. An increase in the channel width also leads to the mass flow rate augmentation, but the number of microfluidic channels is, at the same time, reduced. Consequently, the total mass flow rate increment induced by the channel width increment is less than that by the channel depth increment. Also, the available surface area (per unit volume) for heat transfer between the fluid and the channel wall is reduced by 15%, as channel width increases from 150 μm to 400 μm. Hence, as shown in Table 3, the channel width increment has negative effect on the thermal performance, increasing the hot-spot temperature by 2.5°C.

Two heat transfer modes, convection and conduction, are incorporated by microfluidic channel cooling. Convective heat transfer occurs between the solid and the fluid dissipating the IC power to the fluid. Meanwhile, conductive heat spreading moderates hotspots. Increases in the channel side-wall and/or base thickness improve the conductive heat transfer. However, Table 3 shows that the increment of the channel base thickness reduced the hot-spot temperature by 4.54°C, while the increment of the channel side-wall thickness leads to the increase in hot-spot temperature by 9.7°C. This is because the increment of the channel side-wall thickness diminishes the convective heat transfer capability by eliminating a total number of available microfluidic channels, while incrementing the channel base thickness effectively augments the conductive heat transfer, without any adverse effect on convection. However, for TSV routing capacity, a wider channel side-wall is preferred and the channel base thickness is limited by the allowable TSV length.

4.5 Two-Phase Cooling. For the baseline channel geometry, the calculated heat transfer coefficients for single-phase cooling were quite uniform at $\sim 5.0\times 10^4\ \mathrm{W/m^2\,K}$, while two-phase heat transfer coefficients ranged from $\sim 5.0\times 10^4$ to $\sim 7.0\times 10^5\ \mathrm{W/m^2\,K}$, with the average value of $3.5\times 10^5\ \mathrm{W/m^2\,K}$ using R134a as a working fluid. If 10°C of driving temperature difference is taken, the two-phase cooling can, roughly, deal with the power density of $350\ \mathrm{W/cm^2}$, whereas a single-phase cooling capability is limited to $50\ \mathrm{W/cm^2}$. Moreover, single-phase flow has an additional penalty due to coolant temperature increase along the channel caused by the sensible heat transfer. The inlet fluid temperature, therefore, should be much lower in a single-phase flow, which requires larger cooling load at the air-side heat exchanger (or condenser) in the system. Thus, the higher heat transfer coefficient and a relatively constant fluid temperature indicate a better thermal performance of a two-phase cooling system.

The two-phase cooling results are summarized in Table 4. Most

Table 4 Two-phase dual-pass microfluidic channel cooling performance

Refrigerants	$T_{w,\max}$ (°C)	$\dot{m}$ (g/s)	W_p (W)	$x_{v,\max}$	$h_{\mathrm{conv,max}}$ $(\mathrm{W/m^2\,K})$
Water	135.50	2.11	0.048	0.999	28,316
R134a	52.92	45.32	2.215	0.109	726,630
R113	74.69	16.56	0.626	0.874	382,470
R236ea	53.78	30.39	1.229	0.234	499,420
R227ea	52.26	39.58	1.685	0.227	921,210
R245ca	55.38	19.60	0.807	0.329	328,970
R123	55.03	18.26	0.715	0.519	354,000

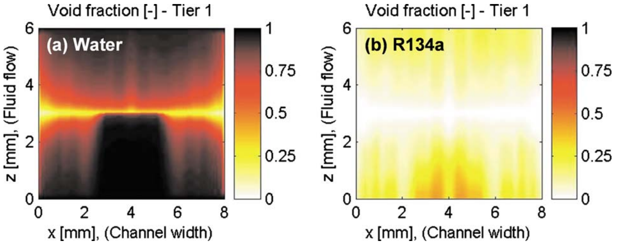

Fig. 10 Void fraction distributions of the coolant in the tier 1 with two-phase dual-pass microfluidic channel cooling using (*a*) water and (*b*) R134a as working fluids

of the refrigerants successfully kept the wall temperatures well below 85°C with the difference between maximum wall and inlet fluid temperatures only 2–5°C, which is significantly smaller than that for single-phase cooling. Considering that pumping power is comparable and inlet fluid temperatures are much higher, two-phase cooling seems to be very promising, as compared with single-phase. However, the channel interior pressures of R134a and R227ea yielding the best performance among the refrigerants are around 1300 kPa and 900 kPa, respectively, which are too high to be safely maintained in the thin silicon structure. On the other hand, the saturation pressure of water is sufficiently low to be allowable. However, the thermal performance of water shown in Table 4 was poor, due to its hydraulic properties providing exceptionally small mass flow rate through the channels. The saturation pressure of water at 70°C is only 31.2 kPa, which is very close to its triple point. The augmentation of flow rate for the increment of cooling capability could make the water easily reach its triple point and thus cause blockage of channel with ice; thus, the two-phase water cooling suffers from the lack of "hydraulic budget." Besides, the proximity of the water saturation pressure to its triple point further degrades its thermal capability by considerably amplifying the two-phase flow pressure drop. As shown in void fraction model by Zivi $\varepsilon = [1+(1/x_v - 1)(\rho_v/\rho_l)^{2/3}]^{-1}$ [46], void fraction is determined by vapor quality and vapor-phase and liquid-phase density ratio ρ_v/ρ_l. At the saturation pressures near the triple point $\rho_v/\rho_l \sim 0$, which makes $\varepsilon \sim 1$ even with low vapor quality. In fact, the two-phase multiplier is strongly related to void fraction. For annular flow, the two-phase multiplier can be approximated by $\phi_l^2 \simeq (1-\varepsilon)^{-2}$ [51], which implies low void fraction of water due to the proximity to its triple point, leading to a large two-phase multiplier. The additional pressure drop due to the liquid-vapor interaction during two-phase flow is, therefore, larger for water as a working fluid.

Figures 10(*a*) and 10(*b*) compare the void fraction distributions of water and R134a. At the vapor quality of ~0.11, the void fraction approaches 0.97, which means most of the channels were already filled with water vapor. The corresponding void fraction for R134a was only 0.44. These result in the two-phase pressure drop multipliers of $\phi_l^2 = 18.5$ and 2.35 for water and R134a, respectively. Also, the accelerational pressure drop, the second term of the right-hand side of Eq. (2*b*), strongly depends on the vapor-phase and liquid-phase densities and increases with increasing density difference between the phases, which is one of the indications of proximity to its triple point. Thus, poor thermohydraulic characteristics, such as the low hydraulic budget and a severe pressure drop in two-phase flow, which were mainly attributed to its proximity to triple point, considerably reduced the cooling capability of water and resulted in the maximum wall temperature of 135.5°C, well beyond an allowable limit of 85°C for the ICs.

The proximity of the saturation pressure to its critical point can be represented by reduced pressure $P_r = P_{\text{in}}/P_{\text{crit}}$, which is a "distance" of the saturation pressure from its critical point where the property differences between liquid and vapor phases vanish. In Fig. 11, the dependences of mass flow rates and maximum heat transfer coefficients of refrigerants on the reduced pressure of the fluid in the microfluidic channel inlet are depicted. It is clear that the mass flow rate strongly depends on the reduced pressure, regardless of refrigerant. Interestingly, the maximum heat transfer coefficients clearly follow the curve fitting the mass flow rate data, which indicates that the thermal performance is also dominantly determined by the reduced pressure. Considering that the reduced pressure generally dictates the hydraulic budget as well as the pressure drop potential, Fig. 11 shows that the pressure drop in channels is a significant limiting factor, which mainly results from the small channel hydraulic diameter. Also, it is obvious that the reduced pressure can be used as a valuable indicator to determine a refrigerant compatibility to two-phase microfluidic channel cooling. Based on these results, R245ca and R123 can be considered as viable working fluids for two-phase microfluidic cooling system. Although R113 shows similar thermal performance, its use has been prohibited by the Kyoto protocol.

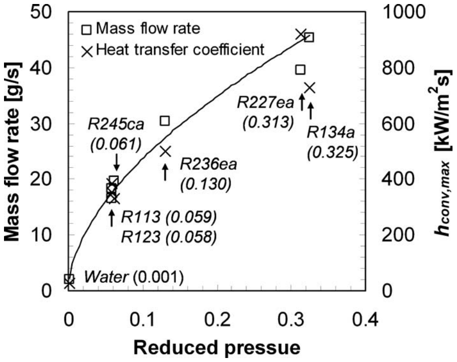

Fig. 11 Dependences of mass flow rates and maximum heat transfer coefficients on the reduced pressure. (The numbers in the parenthesis are the corresponding reduced pressures of each working fluid.)

Mass flow rate maldistribution can be observed in Fig. 9(*b*) for R123 refrigerant. Compared with the single-phase case in Fig. 9(*a*), the maldistribution was more severe in two-phase flow. Moreover, fluid flow rate was significantly reduced in the hot-spot region. In tier 1, the maximum mass flow rate was 0.104 g/s (per channel), which was reduced to 0.024 g/s in the channel passing through the hot-spot region. The vertical flow rate distribution was also observed. The total mass flow rate supplied to tier 1 and tier 4 were 4.3 g/s and 4.9 g/s, respectively, and the maximum and minimum mass flow rates (per channel) in tier 4 were 0.105 g/s and 0.038 g/s, respectively. As previously mentioned, the two-phase multiplier and the accelerational pressure drop increase with increasing vapor quality. The fluid passing through the channels above the hot-spot region absorbs more heat from the chip and thus more vapor is generated. Consequently, the mass flow rate decreases under the fixed pressure drop condition due to an increased flow resistance by the generated vapor. This is a positive feedback loop, in which the reduction in mass flow rate and increase in vapor quality enhance each other, ultimately leading to the failure of the cooling system. Therefore, the negative effect of the mass flow rate maldistribution is much more amplified than may be intuitively expected. Indeed, as shown in Fig. 12, only 50% reduction in the power dissipation resulted in around 90% of vapor quality reduction. Thus, although some of the two-phase refrigerant, namely R123 and R245ca, performed satisfactorily with the hot-spot fluxes of ~300 W/cm^2, all liquid coolants may potentially suffer from a lack of coolant delivery to the hot-spots up to 1 kW/cm^2 as expected in the future 3D ICs. Further studies on the hot-spot management technique and cooling integration schemes [52–54] should greatly improve performance of conventional two-phase thermal management systems.

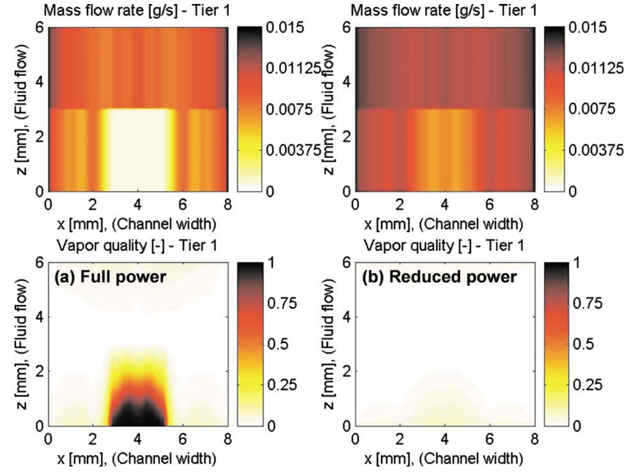

Fig. 12 Mass flow rate and vapor quality distributions for two-phase, dual-pass microfluidic channel cooling using water as a working fluid: (*a*) full power map and (*b*) 50% reduced power map

5 Conclusion

In the present study, we have numerically investigated the performance of interlayer microfluidic channel cooling for 3D-stacked ICs. Both in-plane, as well as, vertical nonuniformity in heat flux for both single-phase and two-phase flow are examined. It is verified that the dual-pass heat exchanger greatly helps in augmenting the mass flow rate through microfluidic channels so that the outlet vapor quality can be reduced, and the reliability of the cooling system can be considerably enhanced in two-phase cooling. Parametric investigation showed that increases of channel depth and channel base thickness are useful in reducing the wall temperature. However, this is limited by the maximum length scale of TSVs. The effect of channel width change was found not to be significant. For improved thermal performance, it is better to keep the channel side-wall thickness small; however, wider spacing between channels offers more vertical direction routing capacity.

A two-phase cooling scheme provided enhanced thermal performance as compared with single-phase cooling due to the higher heat transfer coefficient and relatively constant fluid temperature. However, R134a and R227ea were not suitable for the chip cooling application, due to the resulting high interior pressures. Thermal performance of the two-phase water cooling was significantly degraded because of its poor hydraulic properties. In two-phase microfluidic channel cooling, pressure drop acted as the significant limiting factor. The reduced pressure can be a good indicator of refrigerant compatibility to two-phase microfluidic channel cooling. Mass flow rate maldistribution has been also observed. Due to the positive feedback between the mass flow rate reduction and a vapor quality increase, fluid flow avoids the channels passing through the hot-spot regions. In summary, R245ca and R123 were shown to be viable working fluids for two-phase cooling system, which performed satisfactorily in terms of reliability and showed superior performance to the single-phase cooling system. In general, however, dedicated hot-spot thermal management and the hybrid cooling schemes combining different cooling methods based on their power dissipation capability are expected to be the major drivers to improve the 3D IC cooling system performance by suppressing the mass flow rate maldistribution, maintaining temperature uniformity within the stack, and enhancing the reliability.

Acknowledgment

The authors acknowledge the support of the Interconnect Focus Center, one of the five research centers funded under the Focus Center Research Program, a Semiconductor Research Corporation and DARPA program, and are grateful to Michael Healy for the Penryn power map and helpful discussion.

Nomenclature

Bo = boiling number, $q''/G\lambda$
b = channel base thickness (m)
c_p = specific heat (J/kg K)
d = channel depth (m)
d_h = channel hydraulic diameter (m)
f = fanning friction factor
G = mass flux (kg/m^2 s)
h_{conv} = convective heat transfer coefficient (W/m^2 K)
i = enthalpy (J/kg)
k = thermal conductivity (W/m K)
L = channel length (m)
$\dot{m}$ = mass flow rate (kg/s)
Nu = Nusselt number, hd_h/k_f
P = pressure (Pa)
$\widetilde{P}$ = perimeter (m)
Pr = Prandtl number, $\mu c_p/k$
P_r = reduced pressure
$\dot{q}_{\text{conv}}$ = volumetric convective heat transfer rate (W/m^3)
$\dot{q}_g$ = volumetric heat generation rate (W/m^3)
q'' = heat flux (W/m^2)
Re = Reynolds number, Gd_h/μ
s = channel side-wall thickness (m)
T = temperature (°C)
We = Weber number, $G^2d_h/\rho\sigma$
W_p = pumping power (W)
w = channel width (m)
X = Martinelli parameter
x, y, z = Cartesian coordinates (m)
x_v = vapor quality

Greek Symbols

β = channel aspect ratio
ε = void fraction
ϕ = two-phase multiplier
η_o = overall heat transfer efficiency
λ = latent heat (J/kg)
μ = dynamic viscosity (kg/m s)
ρ = density (m^3/kg)
σ = surface tension (N/m)

Subscripts

b = bulk
crit = critical
f = fluid
fd = fully developed
i,j,k = index corresponding to Cartesian coordinates x, y, and z, respectively
in = inlet
l = liquid-phase
lam = laminar flow
lo = liquid only in channel
max = maximum
sat = saturation
sp = single-phase
tp = two-phase
tub = turbulent flow
v = vapor-phase
w = channel wall

References

[1] Bohr, M. T., 1995, "Interconnect Scaling—The Real Limiter to High Perfor-

mance ULSI," Tech. Dig. - Int. Electron Devices Meet., **1995**, pp. 241–244.

[2] Yamashita, K., and Odanaka, S., 1997, "Interconnect Scaling Scenario Using a Chip Level Interconnect Model," VLSI Technology Symposium, pp. 53–54.

[3] Banerjee, K., Souri, S. J., Kapur, P., and Saraswat, K. C., 2001, "3-D ICs: A Novel Chip Design for Improving Deep-Submicrometer Interconnect Performance and Systems-on-Chip Integration," Proc. IEEE, **89**(5), pp. 602–633.

[4] Semiconductor Industry Association, 2006, "The International Technology Roadmap for Semiconductors (ITRS)."

[5] Rahman, A., and Reif, R., 2000, "System-Level Performance Evaluation of Three-Dimensional Integrated Circuits," IEEE Trans. Very Large Scale Integr. (VLSI) Syst., **8**(6), pp. 671–678.

[6] Lee, Y.-J., Kim, Y. J., Huang, G., Bakir, M., Joshi, Y., Fedorov, A., and Lim, S. K., 2009, "Co-Design of Signal, Power, and Thermal Distribution Networks for 3D ICs," *Proceedings Design, Automation and Test in Europe*, Nice, France, pp. 610–615.

[7] Im, S., and Banerjee, K., 2000, "Full Chip Thermal Analysis of Planar (2-D) and Vertically Integrated (3-D) High Performance ICs," Tech. Dig. - Int. Electron Devices Meet., **2000**, pp. 727–730.

[8] Huang, W., Ghosh, S., Velusamy, S., Sankaranarayanan, K., Skadron, K., and Stan, M. R., 2006, "HotSpot: A Compact Thermal Modeling Methodology for Early-Stage VLSI Design," IEEE Trans. Very Large Scale Integr. (VLSI) Syst., **14**(5), pp. 501–513.

[9] Huang, W., Stan, M. R., Skadron, K., Sankaranarayanan, K., Ghosh, S., and Velusamy, S., 2004, "Compact Thermal Modelling for Temperature-Aware Design," Design Automation Conference, San Diego, CA, pp. 878–883.

[10] Borkar, S., 1999, "Design Challenges of Technology Scaling," IEEE MICRO, **19**(4), pp. 23–29.

[11] Gunther, S., Binns, F., Carmean, D. M., and Hall, J. C., 2001, "Managing the Impact of Increasing Microprocessor Power Consumption," Intel Technol. J., **5**(1), pp. 1–9.

[12] Stan, M. R., Skadron, K., Barcella, M., Huang, W., Sankaranarayanan, K., and Velusamy, S., 2003, "HotSpot: A Dynamic Compact Thermal Model at the Processor-Architecture Level," Microelectron. J., **34**(12), pp. 1153–1165.

[13] Skadron, K., Stan, M. R., Sankaranarayanan, K., Huang, W., Velusamy, S., and Tarjan, D., 2004, "Temperature-Aware Microarchitecture: Modeling and Implementation," ACM Trans., Architecture and Code Optimization, **1**(1), pp. 94–125.

[14] Skadron, K., Stan, M. R., Huang, W., Velusamy, S., Sankaranarayanan, K., and Tarjan, D., 2003, "Temperature-Aware Computer Systems: Opportunities and Challenges," IEEE MICRO, **23**(6), pp. 52–61.

[15] Skadron, K., Stan, M. R., Huang, W., Velusamy, S., Sankaranarayanan, K., and Tarjan, D., 2003, "Temperature-Aware Microarchitecture," *Proceedings of the 30th Annual International Symposium on Computer Architecture*, pp. 2–13.

[16] Kleiner, M. B., Kühn, S. A., Ramm, P., and Weber, W., 1995, "Thermal Analysis of Vertically Integrated Circuits," Tech. Dig. - Int. Electron Devices Meet., **1995**, pp. 487–490.

[17] Rahman, A., and Reif, R., 2001, "Thermal Analysis of Three-Dimensional (3-D) Integrated Circuits (ICs)," *Proceedings of the IITC*, pp. 157–159.

[18] Loi, G. L., Agrawal, B., Srivastava, N., Lin, S.-C., Sherwood, T., and Banerjee, K., 2006, "A Thermally-Aware Performance Analysis of Vertically Integrated (3-D) Processor-Memory Hierarchy," *Proceedings of the Design Automation Conference*, San Francisco, CA, pp. 991–996.

[19] Bintoro, J. S., Akbarzadeh, A., and Mochizuki, M., 2005, "A Closed-Loop Electronics Cooling by Implementing Single Phase Impinging Jet and Mini Channels Heat Exchanger," Appl. Therm. Eng., **25**, pp. 2740–2753.

[20] Leland, J. E., Ponnappan, R., and Klasing, K. S., 2002, "Experimental Investigation of an Air Microjet Array Impingement Cooling Devices," J. Thermophys. Heat Transfer, **16**(2), pp. 187–192.

[21] Pal, A., Joshi, Y. K., Beitelmal, M. H., Patel, C. D., and Wenger, T. M., 2002, "Design and Performance Evaluation of a Compact Thermosyphon," IEEE Trans. Compon. Packag. Technol., **25**(4), pp. 601–607.

[22] Maydanik, Y. F., Vershinin, S. V., Korukov, M. A., and Ochterbeck, J. M., 2005, "Miniature Loop Heat Pipes-A Promising Means For Electronics Cooling," IEEE Trans. Compon. Packag. Technol., **28**(2), pp. 290–296.

[23] Jiang, L., Mikkelsen, J., Koo, J. M., Huber, D., Yao, S., Zhang, L., Zhou, P., Maveety, J. G., Prasher, R., Santiago, J. G., Kenny, T. W., and Goodson, K. E., 2002, "Closed-Loop Electroosmotic Microchannel Cooling System for VLSI Circuits," IEEE Trans. Compon. Packag. Technol., **25**(3), pp. 347–355.

[24] Wei, Y., and Joshi, Y., 2004, "Stacked Microchannel Heat Sinks for Liquid Cooling of Microelectronic Components," ASME J. Electron. Packag., **126**, pp. 60–66.

[25] Fan, X., Zeng, G., LaBounty, C., Bowers, J. E., Croke, E., Ahn, C. C., Huxtable, S., Majumdar, A., and Shakouri, A., 2001, "SiGeC/Si Superlattice Microcoolers," Appl. Phys. Lett., **78**(11), pp. 1580–1582.

[26] Mongia, R., Masahiro, K., DiStefano, E., Barry, J., Chen, W., Izenson, M., Possamai, F., Zimmermann, A., and Mochizuki, M., 2006, "Small Scale Refrigeration System for Electronics Cooling Within a Notebook Computer," *Proceedings of the ITHERM*, San Diego, CA, pp. 751–758.

[27] Kim, Y. J., Joshi, Y. K., and Fedorov, A. G., 2008, "An Absorption Based Miniature Heat Pump System for Electronics Cooling," Int. J. Refrig., **31**, pp. 23–33.

[28] Koo, J.-M., Im, S., Jiang, L., and Goodson, K. E., 2005, "Integrated Microchannel Cooling for Three-Dimensional Electronic Circuit Architectures," ASME J. Heat Transfer, **127**, pp. 49–58.

[29] Brunschwiler, T., Michel, B., Rothuizen, H., Kloter, U., Wunderle, B., Oppermann, H., and Reichl, H., 2008, "Forced Convective Interlayer Cooling in Vertically Integrated Packages," *Proceedings of the ITHERM*, Las Vegas, NV, pp. 1114–1125.

[30] Sekar, D., King, C., Dang, B., Spencer, T., Thacker, H., Joseph, P., Bakir, M. S., and Meindl, J. D., 2008, "A 3D-IC Technology With Integrated Microchannel Cooling," International Interconnect Technology Conference, Burlingame, CA, pp. 13–15.

[31] Bakir, M. S., King, C., Sekar, D., Thacker, H., Dang, B., Huang, B., Naeemi, A., and Meindle, J. D., 2008, "3D Heterogeneous Integrated Systems: Liquid Cooling, Power Delivery, and Implementation," Custom Integrated Circuits Conference, San Jose, CA, pp. 663–670.

[32] George, V., Jahagirdar, S., Tong, C., Smits, K., Damaraju, S., Siers, S., Naydenov, V., Khondker, T., Sakar, S., and Singh, P., 2007, "Penryn: 45-nm Next Generation Intel Core™ 2 Processor," IEEE Asian Solid-State Circuits Conference, Jeju, Korea, pp. 14–17.

[33] Healy, M., and Lim, S. K., 2009, "A Study of Stacking Limit and Scaling in 3D ICs: An Interconnect Perspective," IEEE Electronic Components and Technology Conference, pp. 1213–1220.

[34] Dang, B., Bakir, M. S., and Meindl, J. D., 2006, "Integrated Thermal-Fluidic I/O Interconnect for an On-Chip Microchannel Heat Sink," IEEE Electron Device Lett., **27**(2), pp. 117–119.

[35] Garimella, S., Dowling, W. J., Van der Veen, M., and Killion, J. D., 2001, "The Effect of Simultaneously Developing Flow on Heat Transfer in Rectangular Tubes," Heat Transfer Eng., **22**, pp. 12–25.

[36] Lazarek, G. M., and Black, S. H., 1982, "Evaporative Heat Transfer, Pressure Drop and Critical Heat Flux in a Small Vertical Tube With R-113," Int. J. Heat Mass Transfer, **25**(7), pp. 945–960.

[37] Tran, T. N., Wambsganss, M. W., Chyu, M. C., and France, D. M., 1997, "A Correlation for Nucleate Flow Boiling in Small Channels," *Compact Heat Exchangers for the Process Industries*, R. K. Shah, ed., Begel House, New York, pp. 353–363.

[38] Lee, H. J., and Lee, Y. L., 2001, "Heat Transfer Correlation for Boiling Flows in Small Rectangular Horizontal Channels With Low Aspect Ratios," Int. J. Multiphase Flow, **27**, pp. 2043–2062.

[39] Warrier, G. R., Dhir, V. K., and Momoda, L. A., 2002, "Heat Transfer and Pressure Drop in Narrow Rectangular Channels," Exp. Therm. Fluid Sci., **26**, pp. 53–64.

[40] Yu, W., France, D. M., Wambsganss, M. W., and Hull, J. R., 2002, "Two-Phase Pressure Drop, Boiling Heat Transfer, and Critical Heat Flux to Water in a Small-Diameter Horizontal Tube," Int. J. Multiphase Flow, **28**, pp. 927–941.

[41] Lee, J., and Mudawar, I., 2005, "Two-Phase Flow in High-Heat-Flux Micro-Channel Heat Sink for Refrigeration Cooling Applications: Part II-Heat Transfer Characteristics," Int. J. Heat Mass Transfer, **48**, pp. 941–955.

[42] Lin, S., Kew, P. A., and Cornwell, K., 2001, "Two-Phase Heat Transfer to a Refrigerant in a 1 mm Diameter Tube," Int. J. Refrig., **24**, pp. 51–56.

[43] Blasius, H., 1913, "Das Ahnlichkeitsgesetz bei Reibungsvorgangen in Flussigkeiten," Forschungsarbeiten des Ver, Deutsh. Ing., Paper No. 131.

[44] Lee, J., and Mudawar, I., 2005, "Two-Phase Flow in High-Heat-Flux Micro-Channel Heat Sink for Refrigeration Cooling Applications: Part I-Pressure Drop Characteristics," Int. J. Heat Mass Transfer, **48**, pp. 928–940.

[45] Lockhart, R. W., and Martinelli, R. C., 1949, "Proposed Correlation of Data for Isothermal Two-Phase Two-Component Flow in Pipes," Chem. Eng. Prog., **45**, pp. 39–48.

[46] Zivi, S. M., 1964, "Estimation of Steady State Steam Void Fraction by Means of the Principle of Minimum Entropy Production," ASME J. Heat Transfer, **86**, pp. 247–252.

[47] Patankar, S. V., 1980, *Numerical Heat Transfer and Fluid Flow*, Hemisphere, Washington, DC.

[48] McLinden, M. O., Klein, S., Lemmon, E., and Peskin, A., 1998, *NIST Thermodynamic and Transport Properties of Refrigerants and Refrigerant Mixtures Database (REFPROP), Version 6.0*, National Institute of Standards and Technology, Gaithersburg, MD.

[49] Zhang, L., Koo, J.-M., Jiang, L., Ashegi, M., Goodson, K. E., Santiago, J. G., and Kenny, T. W., 2002, "Measurements and Modeling of Two-Phase Flow in Microchannels With Nearly Constant Heat Flux Boundary Conditions," J. Microelectromech. Syst., **11**(1), pp. 12–19.

[50] Kandlikar, S. G., and Upadhye, H. R., 2005, "Extending the Heat Flux Limit With Enhanced Microchannels in Direct Single Phase Cooling of Computer Chips," *Proceedings of the 21st IEEE Semi-Therm Symposium*, San Jose, CA, pp. 8–15.

[51] Collier, J. G., 1981, *Convective Boiling and Condensation*, 2nd ed., McGraw-Hill, New York, p. 37.

[52] Sahu, V., Joshi, Y., and Fedorov, A., 2008, "Hybrid Solid State/Fluidic Cooling for Hotspot Removal," Intersociety Conference on Thermal and Thermomechanical Phenomena in Electronic Systems, Orlando, FL, pp. 626–631.

[53] Narayanan, S., Fedorov, A. G., and Joshi, Y. K., 2009, "Gas-assisted Thin-Film Evaporation From Confined Spaces for Dissipation of High Heat Fluxes," Nanoscale Microscale Thermophys. Eng., **13**(1), pp. 30–53.

[54] Green, C., Fedorov, A. G., and Joshi, Y. K., 2009, "Fluid-to-Fluid Spot-to-Spreader (F2/S2) Hybrid Heat Sink for Integrated Chip-Level and Hotspot-Level Thermal Management," ASME J. Electron. Packag., **131**(2), p. 025002.

Representative Results for Condensation Measurements at Hydraulic Diameters $\sim$100 Microns

Akhil Agarwal
Shell Global Solutions, Inc.,
Houston, TX 77210

Srinivas Garimella[1]
George W. Woodruff School of Mechanical Engineering,
Georgia Institute of Technology,
Atlanta, GA 30332-0405
e-mail: srinivas.garimella@me.gatech.edu

Condensation pressure drops and heat transfer coefficients for refrigerant R134a flowing through rectangular microchannels with hydraulic diameters ranging from 100 μm to 200 μm are measured in small quality increments. The channels are fabricated on a copper substrate by electroforming copper onto a mask patterned by X-ray lithography and sealed by diffusion bonding. Subcooled liquid is electrically heated to the desired quality, followed by condensation in the test section. Downstream of the test section, another electric heater is used to heat the refrigerant to a superheated state. Energy balances on the preheaters and postheaters establish the refrigerant inlet and outlet states at the test section. Water at a high flow rate serves as the test-section coolant to ensure that the condensation side presents the governing thermal resistance. Heat transfer coefficients are measured for mass fluxes ranging from 200 $\mathrm{kg/m^2\,s}$ to 800 $\mathrm{kg/m^2\,s}$ for $0<$ quality <1 at several different saturation temperatures. Conjugate heat transfer analyses are conducted in conjunction with local pressure drop profiles to obtain accurate driving temperature differences and heat transfer coefficients. The effects of quality, mass flux, and saturation temperature on condensation pressure drops and heat transfer coefficients are illustrated through these experiments. [DOI: 10.1115/1.4000879]

Keywords: condensation, microchannels, measurement, heat transfer, pressure drop, refrigerants

1 Introduction

Two-phase flow, evaporation, and boiling in microchannels have received considerable attention in the recent past due to the growing interest in the high heat fluxes made possible by these channels. Condensation in such channels has been studied by fewer investigators, although heat removal and rejection applications can also benefit from high heat flux condensation. Researchers have until now attempted to understand condensation by extrapolating from studies on adiabatic flows of air-water mixtures, and only recently has some understanding of the flow regimes and pressure drops during phase-change in these channels begun to emerge. While compact condensers with rectangular tubes containing multiple parallel channels of 0.4 mm$<D_h<$0.7 mm have been used for some years by the automotive industry, the measurement of condensation heat transfer coefficients has thus far proved somewhat elusive. Unlike in the case of evaporation and boiling, where heat transfer rates can be accurately measured based on the direct measurement of electrical heat input, condensation heat transfer rates have to be determined indirectly. The small flow rates in microchannels result in small heat transfer rates, particularly if the measurements are to be conducted across small quality increments across the vapor-liquid dome. Furthermore, the small heat transfer rates, coupled with the high heat transfer coefficients in these microchannels, require the deduction of heat transfer coefficients based on extremely small temperature differences.

Two-phase flow mechanisms and flow regime transitions in microchannels are considerably different from those found in the more conventional larger diameter tubes because of the significant differences between large round tubes and the smaller noncircular tubes in the relative magnitudes of gravity, shear, and surface-tension forces, which determine the flow regime established at a given combination of liquid-phase and vapor-phase velocities. Neither the same measurement techniques nor the same modeling approaches used for the larger scale channels are adequate for addressing these phenomena that are specific to microchannels. In addition, pressure drop and heat transfer are strong functions of local vapor quality; thus, the variation in pressure drop and heat transfer coefficients as the refrigerant changes from vapor to liquid through varying flow mechanism must be understood.

The authors' research group has previously reported results of a comprehensive experimental research program on condensation flow mechanisms and the development of flow regime based models for pressure drop and heat transfer in channels with 0.4 mm $<D_h<$5 mm. Coleman and Garimella [1–3] demonstrated and interpreted the significant differences in the flow regime transitions between large round tubes and microchannels on the basis of the differences in the relative magnitudes of gravity, shear, surface-tension forces, and transitions for air-water flows [1] as well as for the condensation of refrigerants [2–4]. Having established the pertinent flow mechanisms and transition criteria for the condensation of refrigerants in microchannels, Garimella and coworkers [4–8] developed experimentally validated models for pressure drops during intermittent condensing flows in circular [5] and noncircular [6] microchannels. In addition, they developed a model for condensation pressure drop in annular flow [7], and further extended it to comprehensive multiregime pressure drop models for circular [4] and noncircular [8] microchannels. Heat transfer coefficients were also measured in these same channels using a novel thermal amplification technique [9], followed by the development of heat transfer models for circular [10] and noncircular [11] channels.

---

[1] Corresponding author.

Contributed by the Heat Transfer Division of ASME for publication in the JOURNAL OF HEAT TRANSFER. Manuscript received December 1, 2008; final manuscript received April 28, 2009; published online February 22, 2010. Assoc. Editor: Satish G. Kandlikar.

2 Prior Work

A comprehensive review of the literature on condensation in minichannels and microchannels appears in Ref. [12]. A brief overview is presented here. In annular flow models, the technique of relating the interfacial shear (through a boundary layer analysis that usually uses the von Karman velocity profile) to the heat transfer across the liquid film has been used widely, starting with the work of Carpenter and Colburn [13], with refinements and improvements to the contribution of various forces to the interfacial shear, for example, by Soliman et al. [14], Traviss et al. [15], and others. There have also been some attempts such as the work of Chen et al. [16] to develop general purpose annular flow correlations starting with asymptotic limits, and blending them through some simple combination of the terms at the respective limits. Another approach has been to directly apply a multiplication factor to a single-phase liquid or vapor-phase heat transfer correlation, with the multiplier determined using adaptations of the pressure drop multipliers by Lockhart and Martinelli [17] and by Friedel [18].

One correlation that continues to be used frequently is the purely empirical Shah [19] correlation, because of its simplicity, the wide range of data that were utilized in its development, and its comparatively good predictions for annular flows. In recent years, large experimental efforts, or analyses of data from multiple researchers, have been undertaken to develop models that address a wide range of mass fluxes, diameters, and fluids. Representative models include those by Dobson and Chato [20], Cavallini et al. [21], and Thome et al. [22]. While these studies have yielded smoother, and in general, more accurate, predictions over a wide range of conditions, they still address primarily stratified/wavy and annular flows. The quasi-homogeneous model of Soliman [23] is one of the few examples of a model dedicated to mist flow.

The availability of reliable local condensation heat transfer measurements and models in microchannels of $D<3$ mm is especially limited. A group of researchers led by Webb [24–28] has made some progress in measuring heat transfer coefficients in extruded aluminum tubes with multiple parallel ports of $D_h<3$ mm. In these papers, they have attempted several different approaches to modeling the heat transfer coefficients including shear stress models and equivalent mass flux models. A reliable model that predicts and explains the variety of trends seen in these results has however yet to be developed. Yang and Webb [27] explicitly accounted for surface-tension forces in microchannels (with microfins) by computing the drainage of the liquid film from the microfin tips and the associated heat transfer enhancement when the fin tips are not flooded. Wang and co-workers [29–31] have proposed analytical treatments that account for the combined influence of surface tension, shear, and gravity during the condensation process in horizontal square and equilateral triangular section minichannels or microchannels. They demonstrate this model for channel sizes (side of square or triangle) in the range of 0.5–5 mm for condensation of refrigerants R134a, R22, and R410A. In another recent study, Cavallini et al. [32] measured heat transfer coefficients during condensation of R134a and R410A inside multiple parallel 1.4 mm D_h channels. They found that the models in the literature [21,28,33–36] underestimated their results, particularly at high values of mass flux. They attributed these differences to the much higher gas velocities in their experiments where mist flow might prevail, whereas the available correlations are primarily for annular flow in larger diameter tubes.

It is clear from the above discussion that heat transfer coefficients for condensation in microchannels with $D_h<200$ μm have not been reported in the literature, and there are no models for the prediction of condensation heat transfer at such microscales. The prior work on condensation heat transfer by the present authors is also limited to $D_h>400$ μm. The present study, therefore, reports the development of techniques for the measurement of condensation heat transfer and pressure drop in rectangular microchannels with 100 μm$<D_h<$160 μm. Results for one such set of channels of dimensions 100×200 μm are reported here.

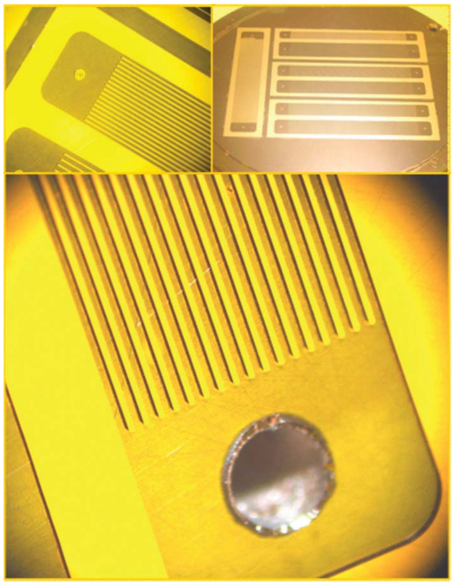

Fig. 1 Microchannel layout

3 Experimental Approach

Tests were conducted on the microchannels under investigation for $30°\text{C}<T_{\text{sat}}<60°\text{C}$ and $300\ \text{kg/m}^2\ \text{s}<G<800\ \text{kg/m}^2$ s. The primary challenge posed by these test conditions was the measurement of low condensation heat duties. Thus, the small heat transfer rate in the test section (due to the small flow rates in microchannels, coupled with the small quality change) must be measured within an acceptable degree of uncertainty. For example, for $D_h=100$ μm with aspect ratio $\alpha=1$, a mass flux of 200 kg/m^2 s implies a flow rate of 2×10^{-6} kg/s. The heat of condensation of R134a ranges from 173.1 kJ/kg at a saturation temperature of 30°C to 124.3 kJ/kg at 70°C. If local heat transfer coefficients are desired, with a resolution of at least $\Delta x=0.25$, the corresponding heat transfer rate is 0.06 W. Clearly, these flow rates and heat transfer rates present considerable challenges. If the fluid flows through 20 channels in parallel, the heat transfer rates range from a minimum of 1.24 W at 70°C and $G=200$ kg/m^2 s to 6.92 W at 30°C and $G=800$ kg/m^2-s. The approach described below was specifically developed to address this challenge and yield accurate heat transfer coefficients as a function of quality for the different mass fluxes, saturation temperatures, and geometries under consideration.

Refrigerant flows through multiple parallel rectangular channels as shown in Fig. 1. The channels are fabricated (by HT Micro, Inc., Albuquerque, NM) on a copper substrate by electroforming copper onto a mask patterned by X-ray lithography. Figure 2 shows the layout of the mask used for X-ray lithography. Seven different devices (each set of channels, for example twenty 0.1×0.1 mm^2 channels, is referred to as one device) are obtained from each wafer. All devices have a constant depth of 100 μm, but the varying number of channels and widths yield different channel aspect ratios. The overall lengths of the channels with and without headers are 48 mm and 40 mm, respectively. The corners of the headers and channel wall ends are rounded to radii of curvature of 1 mm and 100 μm, respectively, to reduce the mechanical stress under high pressure operation. An open header area and the location of the inlet and exit ports allow for the distribution of refrigerant into the various parallel channels. The channels are then sealed using diffusion bonding with another copper wafer on top of the refrigerant channels, which provides for leak proof

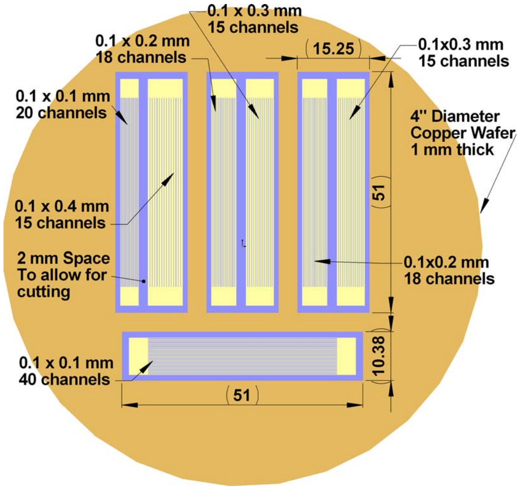

Fig. 2 Wafer layout for electroforming

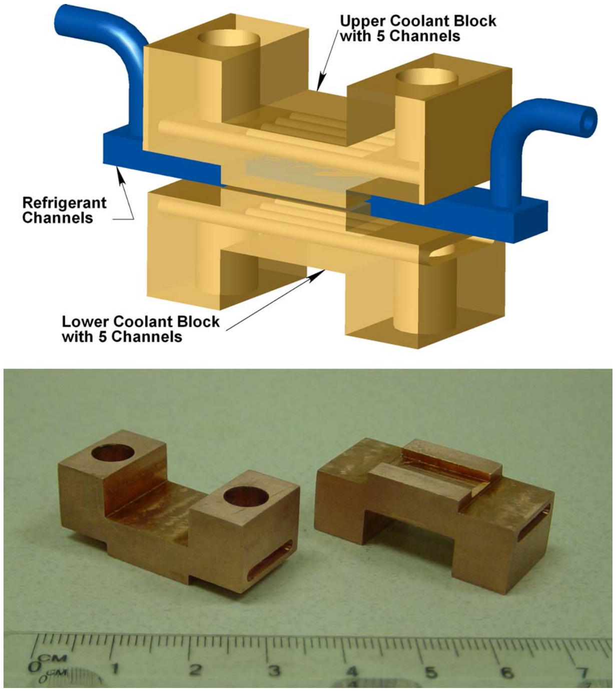

Fig. 4 Coolant channels, test-section subassembly

flows at saturation pressures as high as 10 MPa. After the bonding process, the copper wafers on either side are thinned to the desired thickness of 1 mm from the initial thickness of 6 mm and the individual devices are diced to yield separate refrigerant channels. The dimensional uncertainty of the channels is ±0.5 μm, with a surface roughness of ∼10–15 nm and a taper in the vertical walls of less than 1 deg, as validated by scanning electron microscope (SEM) images of the channels. Sections of the refrigerant channels taken after the diffusion bonding process validated joint integrity. Figure 3 shows a picture of the assembled device. Inlet and outlet tubes (3.175-mm outside diameter) are soldered to mating holes drilled in the channels for the supply of refrigerant. Coolant flows through a set of multiple (five) parallel 0.794-mm diameter circular channels with a heat transfer length of 15 mm, drilled into copper blocks, in counterflow to the refrigerant flow path. Two such blocks are soldered to the refrigerant channels, thus forming the test-section assembly shown in Fig. 4.

The test section described above is installed in the test facility shown schematically in Fig. 5. Subcooled liquid is supplied to an 80 W, 6.35-mm diameter, 50.8-mm long cartridge heater, with the refrigerant flowing in an annulus formed by a 10.16-mm i.d. tube surrounding the heater, which preconditions it to the desired test-section inlet quality (by varying the heat input). The two-phase mixture flows to the test section, where it is condensed using cooling water flowing through the channels described above. High cooling water flow rates are maintained to ensure that the condensation side presents the governing thermal resistance. The temperature and flow rate of the cooling water are controlled to achieve the desired condensation rate and test-section exit quality. Heat rejected to the cooling water in the test section is ultimately rejected using a 12.7 cm long counterflow tube-in-tube heat exchanger formed by 6.35-mm and 12.7-mm o.d. tubes, with water flowing on the tube-side and water/glycol coolant from the lab chiller in the annulus. An 80 W cartridge heater is also placed in line with this coolant heat exchanger to allow finer control of the temperature of the cooling water supplied to the test section.

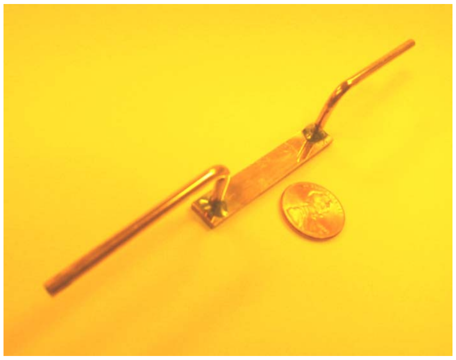

Fig. 3 Assembled refrigerant channels

At the exit of the test section, another heater (similar to the preheater) is used to heat the refrigerant back to a superheated state. Energy balances on the preheaters and postheaters establish the refrigerant inlet and outlet states at the test section. Refrigerant exiting the postheater is condensed and subcooled in an 8.9 cm long counterflow tube-in-tube heat exchanger with refrigerant flowing through a 3.175-mm o.d. tube, and chilled glycol/water coolant flowing in the annulus. Upon exiting this subcooler, the refrigerant is pumped back to the preheater using a Micropump GA 180 gear pump with a 500–4000 rpm dc drive over a $\Delta P_{\max}$ of 262 kPa. A bypass loop is used to enable the pump to run at high rpm while providing lower flow rates to the test section. A sight glass ensures that the refrigerant flowing to the pump is subcooled. An accumulator connected to a nitrogen tank provides independent control of the refrigerant pressure and holds refrigerant charge. The cooling water for the test section is circulated in a closed loop using a Micropump GB 200 gear pump controlled by a 500–9000 rpm ac drive. A photograph of the facility is shown in Fig. 6. Additional details of the test facility are available in [37].

Refrigerant mass flow rate is measured using a DEA Microflowmeters (FMTD4) flowmeter. This nutator flow meter is coupled to a photo emitter/detector device for signal detection, which results in accuracies of ±0.5% (repeatability of ±0.1%) for the range of flow rates 0.9–252 ml/min. Rosemount absolute pressure transducers with uncertainties of ±0.25% of the span (0–2758 kPa) are used to measure pressures of the refrigerant at the inlet and outlet of the preheater and postheater. Similarly, a Rosemount differential pressure transducer is used for measuring the test-section pressure drop with an accuracy of 0.075% of the span (0–248 kPa). The power input to the preheater and postheaters is measured using an Ohio Semitronics Inc. GW5-103E watt transducer with an accuracy of 0.2% while the power input to each of the heaters was controlled using separate inline variable transformers. Microprobes (ThermoWorks, Inc.) with NIST traceable

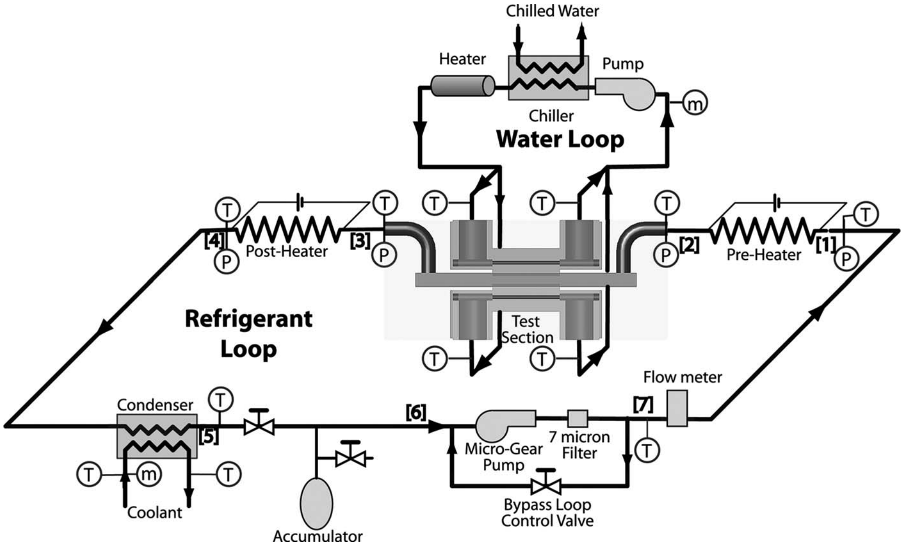

Fig. 5 Test facility schematic

calibration for an accuracy of $\pm 0.1°C$ ($0°C < T < 50°C$) and $<0.3°C$ ($T < 90°C$) are used for temperature measurement at the preheater and postheater inlet and exits, and also at the inlets and exits of both the lower and upper water channels blocks. A standard T type thermocouple (Omega Inc., TMQSS-062(G)-6) with $\pm 0.5°C$ uncertainty was used at the flow meter inlet (for density calculation). The water loop flow rate was measured using a rotameter with a range of 4.2×10^{-6}–4.2×10^{-5} m^3/s and an accuracy of $\pm 4\%$. This water flow rate was used to determine the water flow velocities in the test-section heat exchanger, which in turn were used to determine the water-side h using correlations available in literature. A 25% uncertainty was assumed in the determined water-side h, irrespective of the flow measurement uncertainties; therefore, higher accuracies in this measurement are unnecessary.

4 Data Analysis

4.1 Test-Section Quality and Duty. A representative data point for the 200×100 μm channel (18 channels in parallel) with $G = 606$ kg/m^2 s ($\dot{m} = 2.18 \times 10^{-4}$ kg/s, $A = 3.6 \times 10^{-7}$ m^2), $T_{sat} = 60.5°C$, and $x_{ave} = 0.39$ is used to illustrate the analysis of the data. With the refrigerant entering the preheater at 1727 kPa and a nominal subcooled temperature of 29.3°C ($T_{sat} = 61.1°C$, $\Delta T_{subcooling} = 31.8°C$), a power input of 31.02 W is supplied to the preheater to heat the refrigerant to the desired saturation temperature and quality. With a heater insulation outside diameter of 40.64 mm and an ambient temperature of 23°C, the combined natural convection and radiation heat transfer coefficient is 8.6 W/m^2 K, which yields an insulation surface temperature of 30.6°C. Over an effective heater length of 95 mm, the heat loss is ~0.80 W. Similarly, the heat loss in the tubing (outside diameter 3.18 mm, inside diameter 1.55 mm, and length 67 mm) from the preheater to the test section is 0.27 W. This results in an overall heat loss of 1.07 W for the preheater and tubing assembly, and a net 29.95 W supplied to the refrigerant. A 50% uncertainty is assumed in these calculated heat losses. With a test-section channel inlet pressure of 1724 kPa and this heat input into the refrigerant, the test-section inlet enthalpy is determined to be 0.64 kJ/kg. The energy balance for the postheater is conducted in a similar manner, and from the post heater exit state ($h = f(p = 1679$ kPa, $T = 65.7°C$)) and a heater input into the refrigerant of 27.83 W, yields a test-section exit quality of 0.14, and an average test-section quality $x_{ave} = 0.39$. The corresponding test-section condensation heat duty is 15.54 W. (Considering an uncertainty of ± 6.9 kPa in the absolute pressure measurement as compared with only a ± 0.19 kPa uncertainty in the differential pressure measurement, the test-section exit pressure is derived based on a combination of absolute pressure measurements and the measured ΔP as explained below.) This analysis established the test-section inlet and exit conditions for the refrigerant. The following discussion explains the test-section pressure drop and heat transfer analysis.

4.2 Pressure Drop. Figure 7 illustrates the flow path of the refrigerant and indicates the various expansion and contraction pressure losses, frictional losses and acceleration/deceleration losses taken into account before determining the frictional pressure drop in the 40-mm long refrigerant channels. (Preliminary single-phase validation tests were used to ensure that all the relevant minor losses in the fluid flow path were accounted for.) Contraction ΔPs encountered at sections AA (fitting to tubing: 51 Pa), CC (inlet header to channels: 923 Pa), and EE (header to tubing: 22 Pa) are estimated using the homogenous model recommended by Hewitt et al. [38]. The expansion ΔPs encountered at sections BB (tubing to header: 6 Pa), DD (channels to header: 118 Pa), and FF (tubing to fitting: 5 Pa) are estimated using the separated flow model [38]. The pressure drop in the tubing between the heater and the refrigerant channels consists of frictional ΔPs in the horizontal/vertical sections of the tubing and the bends. The frictional ΔP in the tubing is estimated using the multiple flow regime model of Garimella et al. [4]. The respective ΔPs in the inlet and outlet tubing sections are 108 Pa and 45 Pa. The pressure

Fig. 6 Test facility photograph

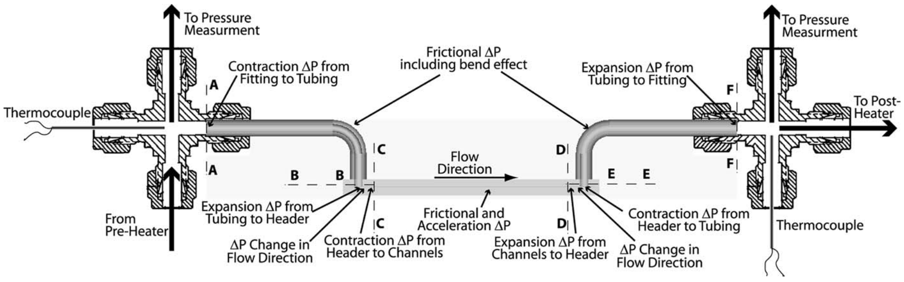

Fig. 7 Refrigerant flow path schematic for pressure drop analysis

drops in the tube bends and also due to change in flow direction at the channel headers are estimated using the homogenous flow model [38], with the loss coefficient for the sharp bend at the header obtained from [39]. The resulting tube bend ΔPs are 8 Pa and 2 Pa at the inlet and exit, respectively, while the ΔPs in the sharp turns at channel inlet and exit headers are 452 Pa and 146 Pa, respectively. Summing these pressure drops and gains (due to expansion, as appropriate) on the inlet- and exit-sides, the net ΔPs on the inlet- and exit-sides are 1.5 kPa and 89 Pa, respectively. The variations in these different minor loss items are due to the changing local mass fluxes along the flow path, with the inlet losses being typically higher than those at the exit due to the higher refrigerant quality at the inlet. In addition to the above minor pressure losses/gains, the refrigerant also undergoes a deceleration, and therefore, a pressure rise of 1610 Pa, due to the decrease in quality from the channel inlet to the outlet estimated using the approach described in Ref. [40]. A 50% uncertainty is assumed in all minor losses described above for uncertainty estimation. Finally, the frictional component of the ΔP in the test section is calculated as follows:

$$\begin{aligned}\Delta P_{\text{fric,TS}} &= \Delta P_{\text{measured}} - \Delta P_{\text{others,in}} - \Delta P_{\text{others,out}} + \Delta P_{\text{deceleration}} \\ &= 47.2 - 1.5 - 0.1 + 1.6 = 47.2 \text{ kPa} \qquad (1)\end{aligned}$$

From the above analysis, it can be seen that the frictional pressure drop for this case is approximately 100% of the measured pressure drop because the deceleration pressure gain essentially compensates for the inlet/exit minor losses. The deceleration, inlet and outlet pressure drops/gains are 3.4%, 3.2%, and 0.2% of $\Delta P_{\text{measured}}$, respectively, for this data point. Figure 8 depicts the contributions of each of the pressure change elements in the refrigerant flow path between the ΔP measurement locations indicated in Fig. 7.

It should be noted that the results discussed above and the heat transfer analyses and results to be discussed in Sec. 4.3 depend on the refrigerant *channel* inlet and exit pressures, which are determined after subtracting the inlet and exit losses from the measured absolute pressures at the *test-section* inlet and exit. The uncertainties in the measurement of absolute pressures at the heater inlet and exit are ±6.89 kPa, compared with an uncertainty of only ±0.19 kPa in the ΔP measurement. Thus, to minimize the effect of the uncertainty in the absolute pressure measurements, the refrigerant channel inlet/exit pressures are estimated by offsetting the minor loss terms from the average of the measured inlet and outlet pressures rather than any one of the measured pressures. Thus, for the representative case, channel inlet and exit pressures are determined to be 1724±4.9 kPa and 1679±4.9 kPa, respectively. It should be noted that the pressure losses/gains calculated here are dependent on the inlet/exit qualities calculated from an energy balance, which in turn are dependent on the channel inlet and exit pressures estimated here. Therefore, calculations are conducted iteratively to obtain the pertinent pressures and qualities. In addition to obtaining the channel ΔP, the channel inlet and outlet pressures reported here are required for the calculation of heat transfer coefficients, as described in Sec. 4.3.

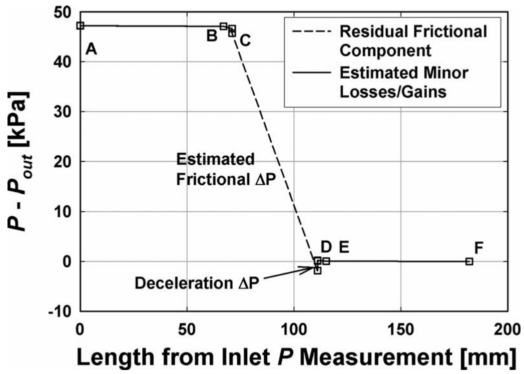

Fig. 8 Pressure drop along the length of the test section for the representative case

4.3 Heat Transfer Coefficient.

In establishing the methodology for the heat transfer calculations, two important factors should be considered. First, since the refrigerant channels are fabricated from a copper wafer, which has a very high thermal conductivity, there is a strong potential for axial conduction through the walls of the refrigerant channels. The total length of the refrigerant channels is 40 mm, out of which the central 15-mm length is in direct contact with the water channel blocks to form the heat exchanger. The remaining 12.5-mm lengths on either end act as extended surfaces. Second, due to high pressure drops through the test section in some cases, refrigerant saturation temperatures vary from the inlet to the exit of the channels. Due to the simultaneous coupled conduction and convection within the channels and the channel walls, conjugate effects must be addressed. Therefore, the heat transfer analysis is conducted by dividing the test section into segments. There are five main steps in the segmental heat transfer analysis: (1) definition of the segments and nodes, (2) definition of the boundary conditions (i.e., refrigerant-side and water-side temperatures), (3) definition of the thermal resistance for each potential heat flow path, (4) an energy balance computation for each node, and (5) calculation of additional parameters such as average refrigerant and wall temperatures and resistance ratios.

Figure 9 shows a sample coarse grid structure for the segmental heat transfer analysis. There are three main sections of the complete geometry under consideration, the inlet-side extended section of 12.5 mm, the central heat exchanger section of 15 mm and the exit-side extended section of 12.5 mm. For illustration of the technique, the inlet and exit sections are subdivided into three segments each ($N_{\text{seg,fin}}$), while the central heat exchanger section is divided into four segments ($N_{\text{seg,HE}}$). The number of segments for the refrigerant-side and water-side are the same in the central heat exchanger section. In the actual calculations, a much larger number of segments (10 segments in each of the three sections) is used. The effect of the number of the segments on the resulting heat transfer coefficient is discussed later in this section.

The next step in the analysis is to determine the refrigerant and

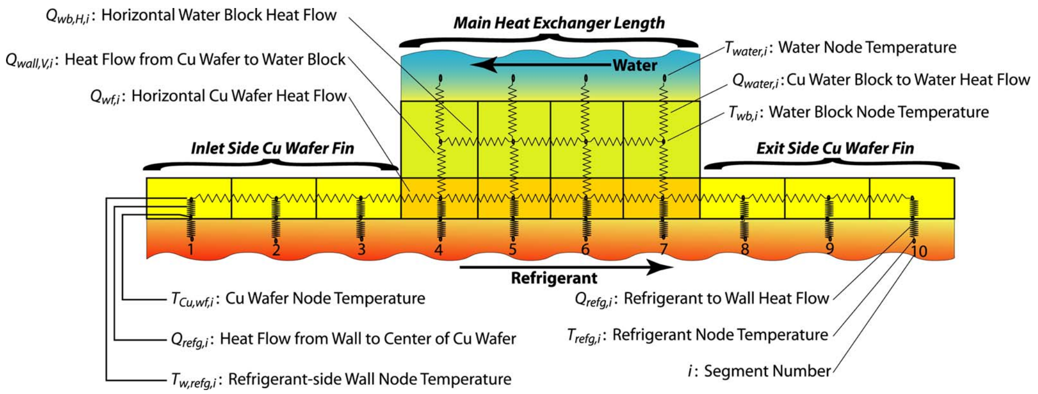

Fig. 9 Segmental conjugate heat transfer analysis

water-side temperatures. The water-side flow rates are kept as high as possible to minimize the coolant-side thermal resistance. Thus, for all the data points taken in this study, $\Delta T_{\mathrm{coolant}} < 0.1^{\circ}\mathrm{C}$. The water inlet and exit temperatures (56.3°C and 56.4°C, respectively, for this case) are averages of the measured water temperatures in the upper and lower coolant blocks, and the water temperature at each of the nodes is determined through interpolation between these temperatures.

Refrigerant-side temperatures are determined based on the refrigerant saturation pressures at each of the nodes in the channel, which are dependent on pressure drop in the channel. The pressure gradient is a strong function of quality and increases with increasing qualities, yielding higher ΔP in the segments close to the channel entrance, making linear interpolation between inlet and outlet pressures to obtain the interior pressures within the channels invalid. Thus, empirical expressions were developed from each data set (each G, T_{sat}, and geometry) to determine the variation in pressure gradient with quality. The refrigerant saturation pressure along the length of the channels was then calculated using these pressure gradient expressions and the deceleration pressure gain. It should be noted that the qualities required for the above pressure calculations are determined based on the specific refrigerant condensation heat duty in each of the segments. Therefore, this procedure was conducted iteratively between the pressure drop calculations, saturation properties, and nodal heat transfer rates.

Figure 9 also shows the thermal resistance network for the segmental heat transfer analysis. The heat transfer from the refrigerant to the water flowing in the counter current direction is considered, along with the axial heat flow along the length of the copper wafer. The refrigerant-side condensation heat duty $Q_{\mathrm{refg},i}$ was defined based on the refrigerant-side convective thermal resistance, taking into account the additional extended surface area provided by the walls separating adjacent channels. (It should be noted that for each data point, the refrigerant-side heat transfer coefficient is assumed to be the same for all the segments. Even though the heat transfer coefficient also depends on quality, the measurements were not taken in enough detail to enable a segment-wise evaluation of the refrigerant heat transfer coefficient. Instead, the effect of quality on heat transfer coefficient was of course addressed by taking different data points with different entering and exiting test-section qualities at each mass flux, saturation temperature and geometry.) This same heat flow from the refrigerant to the copper wafer surface is also transferred from the surface to the center of the wafer across the conduction resistance and the corresponding ΔT. The path for the axial heat flow in the copper wafer was also included in the analysis using the conductive resistance in this direction. The next thermal resistance in the heat flow path is the conduction thermal resistance for heat flow from the copper wafer nodes to the water channel copper block nodes, which is comprised of the conduction resistance from the center of the copper wafer to the interface, and the resistance from the interface to the center of the water channel blocks. In addition, the axial heat flow between the adjacent water block nodes is defined based on the corresponding conduction thermal resistance in the horizontal orientation. The remaining thermal resistance is for heat flow from the water channel block to the water flowing at high velocity through the 10 channels (total in both the upper and lower blocks), which in turn again consists of the water block conduction thermal resistance and the water-side convective thermal resistance in series. The conduction thermal resistance from the center of the water channel block to the surface is determined in the same way as that from the interface to the center of the water channel block. For the convective resistance, at a water flow velocity of 7.65 m/s and $\mathrm{Re}=12.1\times10^{3}$, the Dittus–Boelter equation yields a water-side h of 54.6 $\mathrm{kW/m^{2}\,K}$. The walls separating adjacent water channels provide additional surface area for heat transfer, at an average “fin efficiency” of 97%, and were therefore treated simply as additional prime surface area for the convective thermal resistance calculation.

Based on the thermal resistances described above, a system of energy balance equations in each coordinate direction as applicable is solved iteratively to obtain all the unknown temperatures, heat flow rates and the refrigerant-side heat transfer coefficient. Closure for these nodal equations is, of course, prescribed by setting the summation of the net heat loads in each node equal to the experimentally determined test-section heat load described above. Figure 10 shows the temperature variation in each of the segments based on the heat transfer analysis discussed above. The temperature of the water is the lowest while the entering refrigerant temperature is the highest. The temperature of the water does not change much due to the high flow rates, while as the refrigerant flows through the refrigerant channels, its saturation temperature decreases more significantly due to the decrease in pressure. The temperature of the Cu wafer nodes first decreases in the inlet fin as we move toward the center and then again increases in the exit fin,

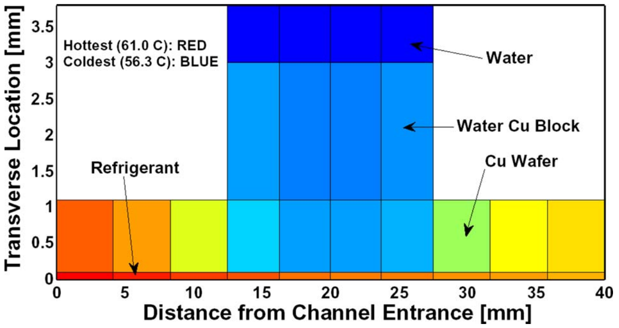

Fig. 10 Temperature distribution for the representative case

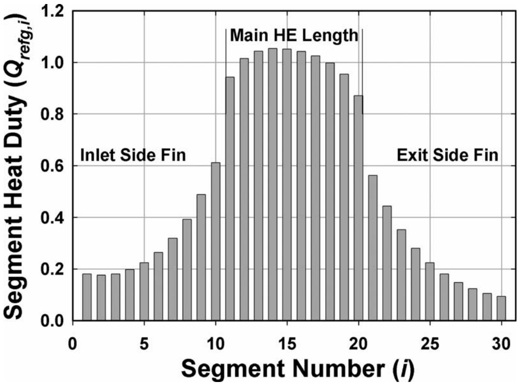

Fig. 11 Variation in segment heat duty along channel length

indicating that in both the fins heat is flowing toward the central heat exchange section. Also, in all the segments, the Cu wafer temperature is lower than the corresponding segment refrigerant temperature, indicating that heat flows from the refrigerant to the Cu wafer. The difference between the Cu wafer temperature and the refrigerant temperature is the highest in the central HE section, indicating that most of the heat is transferred from the refrigerant to the wall in the central HE section. The temperature variation for the copper wafer nodes is larger on the inlet-side fin compared with that in the exit-side fin, indicating that more heat is transferred from the refrigerant to the Cu wafer in the inlet-side fin as compared with the exit-side fin.

To determine the sensitivity of the results to the grid size, the analysis was repeated using progressively finer grids. For a total number of segments greater than 20, the change in the estimated refrigerant-side heat transfer coefficient is less than 1%. Based on this analysis, a total of 30 segments (10 segments in each of the two extended surfaces and 10 segments in the central heat exchange section) were chosen for analyzing the data from this study. The heat transfer coefficient for the representative case based on this analysis is 21.7 $\mathrm{kW/m^2\,K}$.

Figure 11 shows the variation in the segmental refrigerant condensation heat duty along the length of the channel. Since the temperature gradient in the central HE section is the highest, most of the heat is transferred in this section as indicated by the high segmental heat duties. The heat duties in the fin segments decrease as we go further away from the central HE section. The heat duties in the inlet-side fin are higher than the exit-side fin due to higher refrigerant temperatures. Of the total heat transferred in the test section (15.54 W), 9.99 W, i.e., 64% of the condensation heat duty is extracted out of the refrigerant in the central heat exchange segments and the remaining heat duty is transferred in the inlet (3.03 W) and exit (2.52 W) fin sections. The refrigerant temperature (59.9°C to 61.03°C) and the wall temperature (57.33°C to 60.39°C) vary along the length of the test section. Due to these variations in heat duty and temperatures along the length of the channel, a simple average of refrigerant or refrigerant-side wall temperature would not be a good representation of the effective refrigerant or refrigerant-side wall temperatures required for the estimation of uncertainties in the results. Thus, the average refrigerant (60.4°C) or refrigerant-side wall temperatures (58.1°C) were determined from a weighted average based on segmental heat duties. Similarly, in calculating the refrigerant-side effective heat transfer area (needed to calculate resistance ratios) the difference in the fin effect on the inlet- and exit-sides was taken into account. Based on the above refrigerant temperature, and the average water temperature of 56.3°C determined earlier, the total effective resistance of the whole test-section heat exchanger (approximated on a 1D basis) is estimated to be 0.259 K/W. For determining the effective refrigerant-side area for each of the fin sections, they are treated as simple one-dimensional fins, wherein the base temperature is the temperature of the adjacent central HE section corner node. The resulting areas for the inlet and exit fin sections are $4.77\times10^{-5}\ \mathrm{m^2}$ and $4.78\times10^{-5}\ \mathrm{m^2}$, yielding a total refrigerant-side effective area of $2.574\times10^{-4}\ \mathrm{m^2}$. The average refrigerant temperatures for the inlet- and exit-side fin sections are determined to be 60.7°C and 60.1°C, respectively. The total effective refrigerant-side heat transfer area and heat transfer coefficient yield an effective convective resistance of 0.179 K/W. Thus, the resistance ratio $(R_{\mathrm{refg}}/(R_{\mathrm{total}}-R_{\mathrm{refg}}))$ for the representative case is determined to be 2.3. The resistance ratio of 2.3 clearly indicates that the refrigerant-side convective resistance is the dominant resistance. Such high resistance ratios are important to maintain low uncertainties in the determination of the refrigerant heat transfer coefficients.

4.4 Uncertainty Analysis. An analysis of the uncertainties in the results discussed above was conducted using a propagation of errors approach [41]. The uncertainty in the differential pressure measurement between the test-section inlet and exit is ±0.19 kPa. A 50% uncertainty is assumed in the calculation of the inlet/exit pressure losses and the deceleration pressure gain. Thus, the uncertainty in frictional pressure drop is determined to be 47.2±1.1 kPa, i.e., a 2.3% uncertainty. The refrigerant mass flow rate of $2.18\times10^{-4}\pm1.1\times10^{-6}$ kg/s ($\approx\pm0.52\%$ uncertainty) and the ±0.5 μm dimensional uncertainty in the channels yields a refrigerant mass flux of $606\pm4.6\ \mathrm{kg/m^2\,s}$ ($\approx\pm0.8\%$ uncertainty) for the representative case under consideration. With the uncertainties in temperature and pressure measurement at the preheater inlet, the refrigerant inlet enthalpy is estimated as 93±0.14 kJ/kg. The electrical input in the heater is 31.02 W (±0.2%), while the losses are 1.07 W (where a 50% uncertainty is assumed for the estimation of heat losses). This yields a heat input to the refrigerant of 29.95±0.54 W ($\approx\pm1.8\%$). Combining the measurement uncertainty in mass flow rate and the uncertainty in the refrigerant heat input, the test-section inlet enthalpy is calculated to be 230±2.6 kJ/kg, which yields a test-section inlet quality of 0.64±0.02. Similar calculations on the postheater yield a test-section outlet quality of 0.14±0.02. These test-section inlet and outlet conditions yield a heat duty of 15.54±0.78 W, i.e., an uncertainty of 5%.

Uncertainties in the channel inlet and exit pressures are determined by combining the uncertainty in the measurement of absolute (±6.89 kPa) and differential (±0.19 kPa) pressures at test-section inlet/exit, resulting in channel inlet and exit pressures of 1724±4.9 kPa and 1679±4.9 kPa, respectively. This channel inlet/exit pressure uncertainty corresponds to an approximately 0.13°C uncertainty in refrigerant inlet and exit temperatures. The uncertainty in the water inlet and exit temperatures is 0.1°C. An uncertainty of ±25% is assumed for the calculation of the water-side heat transfer coefficient. With these uncertainties and a 5% uncertainty in the test-section condensation heat duty, the heat transfer coefficient is estimated to be $21.7\pm2.98\ \mathrm{kW/m^2\,K}$, i.e., an uncertainty of 14%.

5 Results and Discussion

Tests were conducted on the 200×100 μm channels at saturation temperatures of 30°C, 40°C, 50°C, and 60°C and mass fluxes of 300 $\mathrm{kg/m^2\,s}$, 400 $\mathrm{kg/m^2\,s}$, 600 $\mathrm{kg/m^2\,s}$, and 800 $\mathrm{kg/m^2\,s}$. Results from these tests and trends in heat transfer and pressure drop are discussed here.

5.1 Pressure Drop. Figure 12 shows representative pressure drop results for the 200×100 μm channels for the different saturation temperatures.

The average uncertainty in the pressure drop results for all the data for this geometry was 2.8%. The average minor losses are 3.7%, while the average deceleration pressure gains are 3.9% of the $\Delta P_{\mathrm{measured}}$. The uncertainty in the frictional ΔP data is proportional to the inlet/exit minor losses and the deceleration pressure

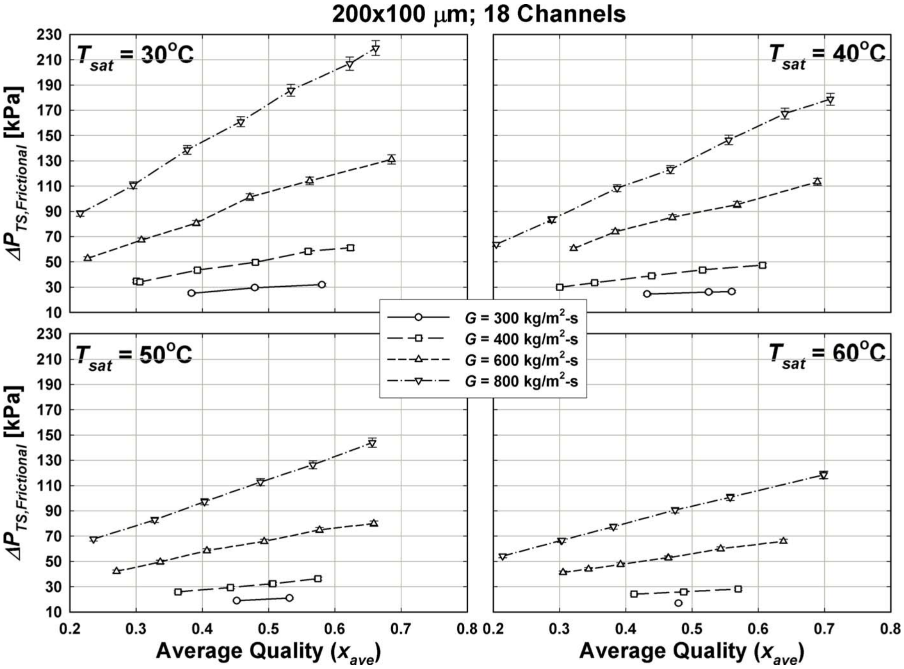

Fig. 12 Frictional pressure drop for 200×100 μm channels

gain, which in turn are proportional to the square of the flow velocities. Hence, the minor losses for the lower mass flux cases are lower than those for the higher mass flux cases. Deceleration pressure gain is dependent on the Δx across the test-section. As x increases, the frictional ΔP at a particular G increases, and as the G increases, the frictional ΔP increases for the same x. As the T_{sat} decreases, the ΔP increases for the same G and average x due to a decrease in the vapor-to-liquid density ratio ($\rho_v/\rho_l=0.083$ at 60°C and $\rho_v/\rho_l=0.032$ at 30°C). This decrease in density ratio leads to higher void fractions, yielding higher flow velocities. This increase in flow velocities leads to an increase in ΔP. At low ρ_v/ρ_l values, the shear between the vapor-phase and liquid-phase is larger, which also leads to higher ΔP.

5.2 Heat Transfer. Figure 13 shows representative heat transfer results for these 200×100 μm channels for different T_{sat}. Many of the trends seen in the pressure drop results are also followed in the heat transfer results. For the same G and T_{sat}, h_{refg} increases as x increases, and similarly, for the same x and T_{sat}, h_{refg} increases as the mass flux increases. Based on the existing

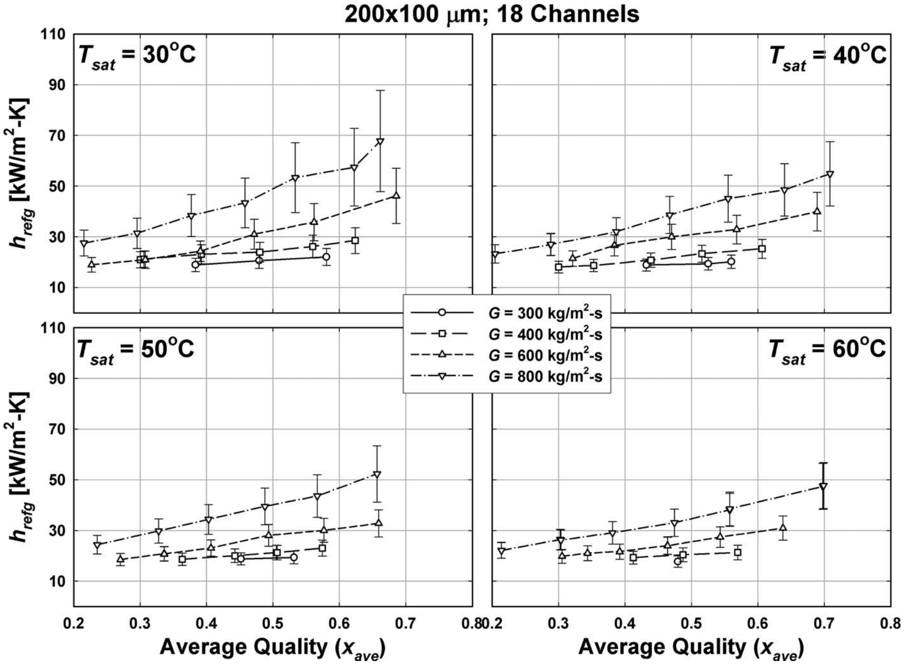

Fig. 13 Heat transfer results for 200×100 μm channels

flow transition criteria in the literature, for the channels under consideration, the flow will be either intermittent or annular. The probability of occurrence of annular flow is higher at higher G and x. Heat transfer coefficients are expected to be higher for annular flow, compared with those in intermittent flow, due to the formation of the thin liquid film around the wall. Thus, as G and x increase, the flow tends more to annular flow, leading to higher h_{refg}. Most of the differences in the data for the different T_{sat} at the same G and x are within the respective uncertainty bands; thus, it is not possible to derive definitive conclusions. However, it does appear that in most cases, as the T_{sat} decreases, the h_{refg} increases, which is similar to the trend observed in the ΔP results. As the T_{sat} decreases, the vapor-to-liquid density ratio decreases, leading to an increase in the flow velocities and interfacial shear, and therefore, the increase in h_{refg}. Also, as the T_{sat} decreases from $60^{\circ}\mathrm{C}$ to $30^{\circ}\mathrm{C}$, h_{fg} increases from 139 kJ/kg to 173 kJ/kg. This change in h_{fg} also leads to higher h_{refg} at lower T_{sat}. Due to the coupled effect of the above factors, h_{refg} values for the lowest T_{sat} $(30^{\circ}\mathrm{C})$ and the highest G $(800\ \mathrm{kg/m^2\,s})$ case are extremely high.

The average uncertainty in h_{refg} for all the data for this geometry is 16%. The most important contributor to the uncertainty in h_{refg} is the assumed 25% uncertainty in the water-side h, particularly when the ratio of the refrigerant resistance to remaining resistances is low. The water-side flow rate was almost the same for all cases and therefore the variation in water-side thermal resistance is insignificant. Thus, as G increases, leading to higher h_{refg} and low resistance ratios, the uncertainty in h_{refg} increases. Similarly, for the same mass flux, as x increases, h_{refg} increase and the resistance ratios decrease, leading to higher uncertainties in h_{refg}. As T_{sat} decreases, h_{refg} increases, leading to lower resistance ratios, thus yielding higher uncertainties in h_{refg}.

5.3 Comparison of Pressure Drop Results With the Literature. This section compares the data from the present study with some of the commonly cited correlations in the literature. Surprisingly, the correlation by Lockhart and Martinelli [17] with $C=12$ (laminar film and turbulent vapor core) for all the data yielded the least average deviation (-1%) among the available correlations from the present data for this geometry, although the absolute deviations for the individual data were higher. (In this paper, the deviations are reported as percentages of the measured values from this study.) The correlations by Chisholm [42] and by Friedel [18] exhibit overall average deviations of −39% and −18%, respectively. The underprediction of pressure drop by these three classical correlations is perhaps due to the small D_h with rectangular shape of aspect ratio of 2 for the present channels, whereas these correlations were developed for large, round tubes.

Examples of modifications to classical correlations include the work on air-water flows through 1–4-mm tubes of Mishima and Hibiki [43], who developed an expression in terms D_h for the C parameter by Chisholm [44] in the correlation by Lockhart and Martinelli [17]. But since their curve fit was based only on 1–4-mm tubes, it significantly underpredicts (by an average deviation of −78%) the data from the present study. Lee and Lee [45] noted that in surface-tension dominated air-water flows through 20-mm wide rectangular channels with gaps of 0.4–4 mm, the effects of slug Reynolds number, the ratio of viscous and surface-tension effects were significant and the correlated parameter by Chisholm [44] in the correlation by Lockhart and Martinelli [17] to account for the gap size as well as the phase flow rates. They state that the flow tends more to plug and slug flow as the gap size decreases, and the effect of surface tension increases due to the curved gas/liquid interface at the edge of the bubble. Even though their correlation incorporates the effect of surface tension, the dependence is not captured for the present data set because the constants and exponents in their expression for this range of phase Re values essentially make this dependence vanish. This correlation also significantly underpredicts the data with an average deviation of −44%, which is worse than the prediction of the correlation by Lockhart and Martinelli [17] with the parameter by Chisholm [44], but better than the correlation by Mishima and Hibiki [43]. The Chen et al. [46] correlation for air-water (in 1.02-mm, 3.17-mm, 5.05-mm, and 7.02-mm tubes) and R410A (in 3.17-mm, 5.05-mm, 7.02-mm, and 9.0-mm tubes) modifies the correlation by Friedel [18] because they believed that this correlation does not emphasize surface tension (We) enough, and may emphasize gravity (Fr) too much when used for small tubes, For the present study, however, all the data exhibit $\mathrm{Bo}<2.5$; hence, the effect of surface tension (We) is still not accounted for, and the correlation predicts the data with an average deviation of −85%, which is far worse than the predictions of the original correlation by Friedel [18]. Wilson et al. [47] studied the effect of progressively flattening a smooth round tube of 8.91-mm diameter and tubes with microfins, and found that the pressure drop at a given G and x increased as the tube approached a rectangular shape. They recommended the circular tube liquid-only two-phase multiplier correlation of Jung and Radermacher [48]. Unlike other correlations discussed previously, this correlation significantly overpredicts the frictional ΔP from the present study with an average deviation of +83%.

Since the flow visualization studies of Coleman and Garimella [1,3] indicated that the intermittent and annular flow regimes are both important at these small scales, the predictions of the annular flow models of Garimella et al. [4] and Agarwal and Garimella [8], and the intermittent flow models of Refs. [5,6] are compared with the data from the present study. In the annular flow model [8], the interfacial friction factor is computed from the corresponding liquid-phase Re, friction factor, the Martinelli parameter, and a surface-tension-related parameter. This correlation predicted the data from the present study with an average deviation of −25%. For modeling pressured drop in intermittent flow, Garimella and co-workers [5,6] included contributions from the liquid slug, shear at the vapor bubble/liquid film interface, and the flow of liquid between the film and slug. A slug frequency correlation based on slug Re and D_h was developed for closure. This correlation predicted the data from the present study with an average deviation of 1%, which is excellent overall agreement; however, it should be pointed out that the trends in pressure drop seen in the data were different (exhibited different slopes) than those seen in the predicted values.

The modified version of the correlation by Friedel [18] proposed by Cavallini et al. [21] based on data from several researchers for 3-mm to 21-mm tubes predicts the data with an average deviation of 22%.

It appears from this discussion that the available correlations are unable to predict the data from the present study accurately. Empirical correlations for large databases in general yield reasonable predictions. But subsequent modifications [43,45] for smaller diameter tubes sometimes yield larger disagreements, probably because the original correlation was modified just to fit the data of the specific researchers.

5.4 Comparison With Heat Transfer Correlations. The correlation by Shah [19] is one of the most widely used general purpose condensation correlations, due to the large database from 21 investigators used for its development, and also its ease of use. The data from the current study are clearly out of the range of applicability of this model, and it was found that this correlation predicted the heat transfer data with an average deviation of −59%. The poor predictions are most probably because this correlation was based on data for tubes with diameter greater than 7 mm. The correlation by Soliman et al. [14] for annular flow evaluates the wall shear stress as a combination of friction, momentum, and gravity contributions based on data for tube diameters $7.44\ \mathrm{mm}<D<11.66\ \mathrm{mm}$. Extrapolation of this correlation to the much lower diameter of interest in the present study leads to significant underprediction of heat transfer coefficients, with an average deviation of −73%.

The heat-momentum analogy correlation by Traviss et al. [15] for annular flow in terms of the turbulent film thickness predicts the data from the present study with an average deviation of −54%. One reason that this model and other models based on the annular flow assumption underpredict the data may be that they are based on shear stresses for large diameter tubes. Dobson and Chato [20] reasoned that the boundary layer analyses used by several investigators such as Traviss et al. [15] are similar in basis to the two-phase multiplier approach used by others. They distinguished annular and wavy flows based on G and a modified Soliman–Froude number $\mathrm{Fr}_{\mathrm{so}}$. For all data points in the current study $\mathrm{Fr}_{\mathrm{so}} > 20$, hence only the annular flow correlation was used for comparison. This correlation predicts the heat transfer coefficients with an average deviation of −56%. One reason for this poor prediction may be that for the smallest diameter (3.14 mm) tube tested by Dobson and Chato [20], the data had large uncertainties due to difficulties in measuring small Q accurately, which led to relatively larger deviations from their own correlations. The Moser et al. [33] correlation relates friction in the vapor-phase and liquid-phase through the two-phase multiplier concept by using an equivalent Re ($\mathrm{Re}_{\mathrm{eq}} = \phi_{\mathrm{lo}}^{8/7}\,\mathrm{Re}_{\mathrm{lo}}$), with ϕ_{lo}^2 obtained from the correlation by Friedel [18]. This correlation predicts heat transfer coefficients from this study with an average deviation of −65%, which is only slightly less than the deviations of the correlation by Traviss et al. [15].

The correlations by Cavallini et al. [21] for annular and stratified flow determine the applicable regime based on the criteria similar to those of Breber et al. [49]. The annular flow prediction uses the model by Kosky and Staub [50] with a modified correlation by Friedel [18] for shear stress. This model predicts the heat transfer coefficients from the present study with an average deviation of −33%, which is better than the deviations of the other models discussed in this section. However, Cavallini et al. [32] conducted condensation experiments for R134a and R-410A in multiple parallel 1.4-mm channels and indicated that this correlation underpredicts their data. The correlation by Thome et al. [22] handles the flow as fully annular forced convective, or as consisting of varying combinations of upper gravity driven, and lower forced convective terms. In addition, they state that intermittent flow is very complex, and assume that it can be predicted by annular flow equations. Their annular flow correlation based on the film thickness from the void fraction model by El Hajal et al. [51] predicts heat transfer coefficients from the present study with an average deviation of −69%. The main reason for this disagreement is the extrapolation of the correlation to diameters much below the range of applicability of this correlation. Also, this correlation was developed for circular tubes, while the channels under consideration here are rectangular.

The annular flow model of Bandhauer et al. [10] for circular tubes with $0.4\ \mathrm{mm} < D_h < 4.9\ \mathrm{mm}$ is based on boundary layer analyses analogous to Traviss et al. [15], but with the shear stress computed from the ΔP models of Garimella et al. [4] developed specifically for microchannels. This model predicts the heat transfer coefficients with an average deviation of −46%. One possible reason for this underprediction may be the underpredictions of their annular flow pressure drop model (−25%), which leads to underprediction of the shear stresses. These heat transfer predictions are still better than those of most of the other heat transfer models discussed here.

It is clear that all the above models underpredict the heat transfer coefficients, further emphasizing the need for a new heat transfer model for microchannels. Unlike the pressure drop models, even the empirical models using large experimental databases are not able to predict the heat transfer coefficients for the small diameter tubes accurately due to a lack of accurate heat transfer data for small diameter channels. Predictions of the shear flow models based on boundary layer analyses seem to provide better predictions, but the results are strongly dependent on the flow models used to determine the film thickness and the applicable shear stress. Improved shear stress predictions would also improve heat transfer predictions. Furthermore, most of the models assume annular flow and do not account for the existence of intermittent flow in the channels. The film thickness determined by using an annular flow assumption could be larger than the actual film thickness in the bubble section of intermittent flow with correspondingly lower heat transfer coefficients.

6 Conclusions

An innovative technique to accurately measure heat transfer coefficients and pressure drops in microchannels ($D_h = 133\ \mu\mathrm{m}$) was developed. Refrigerant microchannels were fabricated using X-ray lithography and electroforming processes, which provide excellent dimensional accuracy and minimal surface roughness. Heat transfer and pressure drop experiments were conducted on 40-mm long rectangular channels of $200 \times 100\ \mu\mathrm{m}$ for the condensation of refrigerant R134a over a range of mass fluxes $300\ \mathrm{kg/m^2\,s} < G < 800\ \mathrm{kg/m^2\,s}$, qualities $0 < x < 1$, and saturation temperatures 30°C, 40°C, 50°C, and 60°C. Frictional pressure drops were obtained from the measured pressure drops by accounting for expansion and contraction terms, and acceleration or deceleration pressure changes, as applicable. Heat transfer in the channels was analyzed using a detailed segmental analysis of the conjugate conduction and convection processes in the test section. Careful attention was paid to the effect of pressure drop within the channels on saturation temperatures and the resulting driving temperature differences between the refrigerant and coolant. Uncertainties in pressure drops and heat transfer coefficients were conducted using a rigorous propagation of errors approach.

It was found that both pressure drop and heat transfer increased with increasing vapor quality, increasing mass flux and decreasing saturation temperature. Comparisons with commonly cited pressure drop models revealed that most correlations did not adequately predict the data from the present study, primarily because these models in the literature were developed for adiabatic flows of air-water mixtures through larger tubes of circular cross sections, or only for channels with aspect ratios close to one. It was also found that most of the models from the literature significantly underpredicted the heat transfer data from the present study. Therefore, an integrated pressure drop and heat transfer model based on these data that accounts for the coexistence of the annular and intermittent flow regimes in microchannels is currently being developed by the authors. The resulting fundamental understanding of condensation at the microscales will yield far reaching benefits not only for electronics cooling, refrigeration and air-conditioning industries, but also for other as-yet untapped applications such as portable personal cooling devices, hazardous duty and high ambient air-conditioning, and medical devices, to name a few.

Nomenclature

A = area, m^2
Bo = Bond number
D_h = hydraulic diameter, mm
Fr = Froude number
G = mass flux, $\mathrm{kg/m^2\,s}$
h = heat transfer coefficient, $\mathrm{W/m^2\,K}$
H = channel height, μm
HE = heat exchange
$\dot{m}$ = mass flow rate, kg/s
N = number of channels
p = pressure, kPa
Q = heat transfer rate, W
R = thermal resistance, K/W
Re = Reynolds number
T = temperature, °C
W = channel width, μm
We = Weber number

x = refrigerant quality
α = channel aspect ratio (W/H)
ΔP = pressure drop, kPa
ΔT = temperature difference, K
ϕ = square root of two-phase multiplier
ρ = density, $\mathrm{kg/m^3}$

Subscripts and Superscripts

ave = average
eq = equivalent
fg = liquid to vapor phase-change
h = hydraulic
l = liquid
lo = liquid only
max = maximum
refg = refrigerant
sat = saturated
seg = segment
so = Soliman
v = vapor

References

[1] Coleman, J. W., and Garimella, S., 1999, "Characterization of Two-Phase Flow Patterns in Small Diameter Round and Rectangular Tubes," Int. J. Heat Mass Transfer, **42**(15), pp. 2869–2881.
[2] Coleman, J. W., and Garimella, S., 2000, "Two-Phase Flow Regime Transitions in Microchannel Tubes: The Effect of Hydraulic Diameter," ASME Paper No. HTD-366.
[3] Coleman, J. W., and Garimella, S., 2003, "Two-Phase Flow Regimes in Round, Square and Rectangular Tubes During Condensation of Refrigerant R134a," Int. J. Refrig., **26**(1), pp. 117–128.
[4] Garimella, S., Agarwal, A., and Killion, J. D., 2005, "Condensation Pressure Drop in Circular Microchannels," Heat Transfer Eng., **26**(3), pp. 28–35.
[5] Garimella, S., Killion, J. D., and Coleman, J. W., 2002, "An Experimentally Validated Model for Two-Phase Pressure Drop in the Intermittent Flow Regime for Circular Microchannels," ASME J. Fluids Eng., **124**(1), pp. 205–214.
[6] Garimella, S., Killion, J. D., and Coleman, J. W., 2003, "An Experimentally Validated Model for Two-Phase Pressure Drop in the Intermittent Flow Regime for Noncircular Microchannels," ASME J. Fluids Eng., **125**(5), pp. 887–894.
[7] Garimella, S., Agarwal, A., and Coleman, J. W., 2003, "Two-Phase Pressure Drops in the Annular Flow Regime in Circular Microchannels," *Proceedings of the 21st IIR International Congress of Refrigeration*, Washington, DC, Paper No. ICR0360.
[8] Agarwal, A., and Garimella, S., 2006, "Modeling of Pressure Drop During Condensation in Circular and Non-Circular Microchannels," ASME Paper No. IMECE2006-14672.
[9] Garimella, S., and Bandhauer, T. M., 2001, "Measurement of Condensation Heat Transfer Coefficients in Microchannel Tubes," *Proceedings of the 2001 ASME International Mechanical Engineering Congress and Exposition*, Vol. 369, ASME, New York, pp. 243–249.
[10] Bandhauer, T. M., Agarwal, A., and Garimella, S., 2006, "Measurement and Modeling of Condensation Heat Transfer Coefficients in Circular Microchannels," ASME J. Heat Transfer, **128**(10), pp. 1050–1059.
[11] Agarwal, A., Bandhauer, T. M., and Garimella, S., 2007, "Heat Transfer Model for Condensation in Non-Circular Microchannels," ASME Paper No. ICNMM2007–30223.
[12] Kandlikar, S., Garimella, S., Li, D., Colin, S., and King, M. R., 2005, *Heat Transfer and Fluid Flow in Minichannels and Microchannels*, Elsevier, New York.
[13] Carpenter, F. G., and Colburn, A. P., 1951, "The Effect of Vapor Velocity on Condensation Inside Tubes," *General Discussion of Heat Transfer*, Institute of Mechanical Engineers and ASME, pp. 20–26.
[14] Soliman, H. M., Schuster, J. R., and Berenson, P. J., 1968, "A General Heat Transfer Correlation for Annular Flow Condensation," ASME J. Heat Transfer, **90**(2), pp. 267–276.
[15] Traviss, D. P., Rohsenow, W. M., and Baron, A. B., 1973, "Forced-Convection Condensation inside Tubes: A Heat Transfer Equation for Condenser Design," ASHRAE Trans., **79**(1), pp. 157–165.
[16] Chen, S. L., Gerner, F. M., and Tien, C. L., 1987, "General Film Condensation Correlations," Exp. Heat Transfer, **1**(2), pp. 93–107.
[17] Lockhart, R. W., and Martinelli, R. C., 1949, "Proposed Correlation of Data for Isothermal Two-Phase, Two-Component Flow in Pipes," Chem. Eng. Prog., **45**(1), pp. 39–45.
[18] Friedel, L., 1979, "Improved Friction Pressure Drop Correlations for Horizontal and Vertical Two Phase Pipe Flow," *Proceedings of the European Two Phase Flow Group Meeting*, Ispra, Italy, Paper No. E2.
[19] Shah, M. M., 1979, "A General Correlation for Heat Transfer During Film Condensation inside Pipes," Int. J. Heat Mass Transfer, **22**(4), pp. 547–556.
[20] Dobson, M. K., and Chato, J. C., 1998, "Condensation in Smooth Horizontal Tubes," ASME J. Heat Transfer, **120**(1), pp. 193–213.
[21] Cavallini, A., Censi, G., Del Col, D., Doretti, L., Longo, G. A., and Rossetto, L., 2002, "Condensation of Halogenated Refrigerants Inside Smooth Tubes," HVAC&R Res., **8**(4), pp. 429–451.
[22] Thome, J. R., El Hajal, J., and Cavallini, A., 2003, "Condensation in Horizontal Tubes, Part 2: New Heat Transfer Model Based on Flow Regimes," Int. J. Heat Mass Transfer, **46**(18), pp. 3365–3387.
[23] Soliman, H. M., 1986, "Mist-Annular Transition During Condensation and Its Influence on the Heat Transfer Mechanism," Int. J. Multiphase Flow, **12**(2), pp. 277–288.
[24] Webb, R. L., and Ermis, K., 2001, "Effect of Hydraulic Diameter on Condensation of R-134a in Flat, Extruded Aluminum Tubes," J. Enhanced Heat Transfer, **8**(2), pp. 77–90.
[25] Yang, C.-Y., and Webb, R. L., 1996, "Friction Pressure Drop of R-12 in Small Hydraulic Diameter Extruded Aluminum Tubes With and Without Micro-Fins," Int. J. Heat Mass Transfer, **39**(4), pp. 801–809.
[26] Yang, C.-Y., and Webb, R. L., 1996, "Condensation of R-12 in Small Hydraulic Diameter Extruded Aluminum Tubes With and Without Micro-Fins," Int. J. Heat Mass Transfer, **39**(4), pp. 791–800.
[27] Yang, C.-Y., and Webb, R. L., 1997, "Predictive Model for Condensation in Small Hydraulic Diameter Tubes Having Axial Micro-Fins," ASME J. Heat Transfer, **119**(4), pp. 776–782.
[28] Zhang, M., and Webb, R. L., 2001, "Correlation of Two-Phase Friction for Refrigerants in Small-Diameter Tubes," Exp. Therm. Fluid Sci., **25**(3–4), pp. 131–139.
[29] Wang, H. S., and Rose, J. W., 2004, "Film Condensation in Horizontal Triangular Section Microchannels: A Theoretical Model," *Proceedings of the Second International Conference on Microchannels and Minichannels (ICMM2004)*, Rochester, NY, Jun. 17–19, pp. 661–666.
[30] Wang, H. S., Rose, J. W., and Honda, H., 2004, "A Theoretical Model of Film Condensation in Square Section Horizontal Microchannels," Chem. Eng. Res. Des., **82**(4), pp. 430–434.
[31] Wang, H. S., and Rose, J. W., 2005, "A Theory of Film Condensation in Horizontal Noncircular Section Microchannels," ASME J. Heat Transfer, **127**(10), pp. 1096–1105.
[32] Cavallini, A., Del Col, D., Doretti, L., Matkovic, M., Rossetto, L., and Zilio, C., 2005, "Condensation Heat Transfer and Pressure Gradient Inside Multiport Minichannels," Heat Transfer Eng., **26**(3), pp. 45–55.
[33] Moser, K. W., Webb, R. L., and Na, B., 1998, "A New Equivalent Reynolds Number Model for Condensation in Smooth Tubes," ASME J. Heat Transfer, **120**(2), pp. 410–417.
[34] Akers, W. W., Deans, H. A., and Crosser, O. K., 1959, "Condensation Heat Transfer Within Horizontal Tubes," Chem. Eng. Prog., Symp. Ser., **55**(29), pp. 171–176.
[35] Koyama, S., Kuwahara, K., and Nakashita, K., 2003, "Condensation of Refrigerant in a Multi-Port Channel," *Proceedings of the First International Conference on Microchannels and Minichannels*, Vol. 1, Rochester, NY, Apr. 24–25, pp. 193–205.
[36] Wang, W.-W. W., Radcliff, T. D., and Christensen, R. N., 2002, "A Condensation Heat Transfer Correlation for Millimeter-Scale Tubing With Flow Regime Transition," Exp. Therm. Fluid Sci., **26**(5), pp. 473–485.
[37] Agarwal, A., 2006, "Heat Transfer and Pressure Drop During Condensation of Refrigerants in Microchannels," Ph.D. thesis, Georgia Institute of Technology, Atlanta, GA.
[38] Hewitt, G. F., Shires, G. L., and Bott, T. R., 1994, *Process Heat Transfer*, CRC/Begell House, Boca Raton, FL.
[39] Hewitt, G. F., 1984, "Two-Phase Flow Through Orifices, Valves, Bends and Other Singularities," *Proceedings of the Ninth Lecture Series on Two-Phase Flow*, Norwegian Institute of Technology, Trondheim, p. 163.
[40] Carey, V. P., 1992, *Liquid-Vapor Phase-Change Phenomena: An Introduction to the Thermophysics of Vaporization and Condensation Processes in Heat Transfer Equipment* (Taylor & Francis Series), Hemisphere, Washington, DC.
[41] Taylor, B. N., and Kuyatt, C. E., 1994, *Guidelines for Evaluating and Expressing the Uncertainty of NIST Measurement Results*, National Institute of Standards and Technology, Gaithersburg, MD.
[42] Chisholm, D., 1973, "Pressure Gradients Due to Friction During the Flow of Evaporating Two-Phase Mixtures in Smooth Tubes and Channels," Int. J. Heat Mass Transfer, **16**(2), pp. 347–358.
[43] Mishima, K., and Hibiki, T., 1996, "Some Characteristics of Air-Water Two-Phase Flow in Small Diameter Vertical Tubes," Int. J. Multiphase Flow, **22**(4), pp. 703–712.
[44] Chisholm, D., 1967, "A Theoretical Basis for the Lockhart-Martinelli Correlation for Two-Phase Flow," Int. J. Heat Mass Transfer, **10**(12), pp. 1767–1778.
[45] Lee, H. J., and Lee, S. Y., 2001, "Pressure Drop Correlations for Two-Phase Flow within Horizontal Rectangular Channels with Small Heights," Int. J. Multiphase Flow, **27**(5), pp. 783–796.
[46] Chen, I. Y., Yang, K.-S., Chang, Y.-J., and Wang, C.-C., 2001, "Two-Phase Pressure Drop of Air-Water and R-410a in Small Horizontal Tubes," Int. J. Multiphase Flow, **27**(7), pp. 1293–1299.

[47] Wilson, M. J., Newell, T. A., Chato, J. C., and Infante Ferreira, C. A., 2003, "Refrigerant Charge, Pressure Drop, and Condensation Heat Transfer in Flattened Tubes," Int. J. Refrig., **26**(4), pp. 442–451.
[48] Jung, D. S., and Radermacher, R., 1989, "Prediction of Pressure Drop During Horizontal Annular Flow Boiling of Pure and Mixed Refrigerants," Int. J. Heat Mass Transfer, **32**(12), pp. 2435–2446.
[49] Breber, G., Palen, J. W., and Taborek, J., 1980, "Prediction of Horizontal Tubeside Condensation of Pure Components Using Flow Regime Criteria," ASME J. Heat Transfer, **102**(3), pp. 471–476.
[50] Kosky, P. G., and Staub, F. W., 1971, "Local Condensing Heat Transfer Coefficients in the Annular Flow Regime," AIChE J., **17**(5), pp. 1037–1043.
[51] El Hajal, J., Thome, J. R., and Cavallini, A., 2003, "Condensation in Horizontal Tubes, Part 1: Two-Phase Flow Pattern Map," Int. J. Heat Mass Transfer, **46**(18), pp. 3349–3363.

Investigation Into the Similarity Solution for Boundary Layer Flows in Microsystems

Suhil Kiwan[1]
e-mail: kiwan@just.edu.jo

M. A. Al-Nimr

Department of Mechanical Engineering,
Jordan University of Science and Technology,
P.O. Box 3030,
Irbid 22110, Jordan

An investigation toward the existence of a complete similarity solution for boundary layer flows under the velocity slip and temperature jump conditions is carried out. The study is limited to the boundary layer flows resulting from an arbitrary freestream velocity $U(x)=U_o x^m$ *and wall temperature given by* $T_w-T_\infty=Cx^n$*. It is found that a similar solution exists only for* $m=1$ *and* $n=0$*, which represents stagnation flow on isothermal surface. This case has been thoroughly investigated. The analysis showed that three parameters control the flow and heat transfer characteristics of the problem. These parameters are the velocity slip parameter* K_1*, the temperature jump parameter* K_2*, and Prandtl number. The effect of these parameters on the flow and heat transfer of the problem has been studied and presented. It is found that the slip velocity parameter affects both the flow and heat transfer characteristics of the problem. It is found that the skin friction coefficient decreases with increasing* K_1 *and most of changes in the skin friction takes place in the range* $0<K_1<1$*. The skin friction coefficient is found to be related to* K_1 *and* Re_x *according to the relation:* $C_f=3.38Re_x^{-0.5}(K_1+1.279)^{-0.8}$ *for* $0<K_1<5$ *with an error of ±4%. On the other hand, the correlation between Nu,* K_1*,* K_2*, and Pr has been found by the equation* $Nu=[(0.449+1.142K_1^{1.06})/(0.515+K_1^{1.06})](K_2+1.489Pr^{-0.44})^{-1}$*, for* $0<K_1$*,* $K_2<5$*,* $0.7\leq Pr\leq 5$ *within a maximum error of ±3%.* [DOI: 10.1115/1.4000886]

Keywords: similarity solution, stagnation surface, rarefied gas, velocity slip parameter, temperature jump parameter

1 Introduction

The rapid growth of novel techniques applied in micro-electro-mechanical systems (MEMS) that found applications in many industrial and biomedical fields has attracted many researchers. An excellent review for the fundamentals, theory, and applications of these microscale systems may be found in Refs. [1–3]. As a result of this revolutionary raised interest in these microscale systems, researchers revisited many macroscale mechanical components and focused on investigating and predicting the change in their thermal and hydrodynamics behavior if they fabricated at microscale sizes. Many MEMS have been fabricated and are in use. These include electrostatic, magnetic, electromagnetic, pneumatic and thermal actuators, motors, valves, gears, cantilevers, diaphragms, and tweezers less than 100 μm in size. These have been used as sensors for pressure, temperature, mass flow, velocity, sound, and chemical composition; as actuators for linear and angular motions; and as simple components for complex systems such as robots, microheat engines, and microheat pumps [1–3].

The flow characteristics in microsystems differ from those in macroscopic systems and cannot always be predicted from the classical flow and energy models such as the Navier–Stokes and energy equations with no-slip and no-jump boundary conditions at a fluid-solid interface. Moreover, the presence of velocity slip and temperature jump is not strictly associated with microscale applications. On a macroscale level, if the pressure of the gas is reduced sufficiently, the velocity slip and temperature jump conditions exists. This motivated many researchers to revisit classical problems in macrosystems and resolve under the slip and jump boundary conditions. For example, Barron et al. [4] solved the Gratez problem in slip flow. Guo and Li [5] and Chakraborty et al. [6] have studied flows in microchannels; Aydin and Avci [7] studied flows in micropipes, Poiseuille flow [8], in a micro-annulus between two concentric cylinders [9]; and Kiwan and Al Nimr [10] studied the flow and heat transfer induced by stretched microsurface. Martin and Boyd [11] have studied the effect of slip boundary conditions of a flow over a flat plate. The flow was not self similar.

In the present paper, the well-known Falkner–Skan families of solutions in classical fluid mechanics case is reconsidered under the velocity slip and temperature jump conditions. The main objective is to find the case(s) where complete similarity exist under constant thermophysical properties conditions. The problem under consideration, to the best of the author's knowledge, has not been reported in the literature.

2 Problem Formulation

Consider the steady, incompressible, two-dimensional laminar forced convection flow resulting from an arbitrary freestream velocity $U(x)$. On the basis of the boundary layer approximations with constant thermophysical properties, the conservation of mass and the balance of momentum are given by

$$\frac{\partial u}{\partial x}+\frac{\partial v}{\partial y}=0 \tag{1}$$

$$u\frac{\partial u}{\partial x}+v\frac{\partial u}{\partial y}=U\frac{dU}{dx}+\nu\frac{\partial^2 u}{\partial y^2} \tag{2a}$$

It should be noted that Eq. (2a) is valid for any value of m. From the y-momentum of the boundary layer approximation, it is clear that pressure does not vary in the transverse direction of the boundary layer. As a result, the pressure distribution in the

---

[1] Corresponding author.

Manuscript received March 28, 2009; final manuscript received September 6, 2009; published online February 22, 2010. Assoc. Editor: Satish G. Kandlikar.

x-direction inside the boundary layer is similar to that outside the boundary layer. Now, apply the x-momentum outside the boundary layer where $v=0$, one can obtain

$$U\frac{dU}{dx} - \frac{\mu}{\rho}\frac{d^2U}{dx^2} = -\frac{1}{\rho}\frac{dp}{dx} \tag{2b}$$

Since $U=U_o x^m$, it is possible to neglect the second term on the LHS of this equation for $m=0$ and 1. However, it is possible to neglect the second term as compared with the first one and for any value of m based on a simple order of magnitude analysis. The ratio of the second term (axial momentum diffusion) to the first one (convective axial momentum) is proportional to 1/Re. But since the boundary layer approximation is valid for $\mathrm{Re} \gg 1$, then neglecting the second term as compared with the first one is well justified. As a result, $UdU/dx=(1/\rho)dP/dx$ and this has been inserted in Eq. (2b).

Neglecting the dissipation term in the energy equation, the balance of energy is given by

$$\rho c_p\left(u\frac{\partial T}{\partial x} + v\frac{\partial T}{\partial y}\right) = k\left(\frac{\partial^2 T}{\partial y^2}\right) \tag{3}$$

For flow at microscales and rarefied length scales, the flow and temperature fields are subjected to the following boundary conditions: velocity jump at the wall [8]

$$u_s = u - u_w = \frac{(2-\sigma_v)}{\sigma_v}\lambda\left.\frac{\partial u}{\partial y}\right|_w + \frac{3}{4}\frac{\mu}{\rho T_{wg}}\left.\frac{\partial T}{\partial x}\right|_w \tag{4a}$$

where T_{wg} is the temperature of the gas at the wall. Temperature jump at the wall

$$T_s = T - T_w = 2\frac{(2-\sigma_T)}{\sigma_T}\lambda\left.\frac{\partial T}{\partial y}\right|_w \tag{4b}$$

Impermeable wall

$$v = 0 \quad @\, y = 0 \tag{4c}$$

Away from the wall, as $y \to \infty$

$$u = U(x), \quad T \to T_\infty \tag{4d}$$

Assume that the flow outside the boundary layer is in the form $U(x)=U_o x^m$ and the wall temperature is given by $T_w - T_\infty = Cx^n$. The following similarity transformations are defined [3]:

$$u = U_o x^m f'(\eta), \quad T - T_\infty = Cx^n\theta(\eta) \tag{5}$$

$$\eta = y\sqrt{\frac{m+1}{2}}\sqrt{\frac{U_o x^m}{\nu x}} = \frac{y}{x}\sqrt{\frac{m+1}{2}}\sqrt{\mathrm{Re}_x} \tag{6}$$

$$v = -x^{(m-1)/2}\sqrt{\frac{2\nu U_o}{m+1}}\left(\frac{m+1}{2}f + \frac{m-1}{2}f'\eta\right) \tag{7}$$

Substituting the above parameters into the governing equations yields

$$f''' + ff'' - \frac{2m}{m+1}f'^2 + \frac{2m}{m+1} = 0 \tag{8}$$

$$\theta' + \mathrm{Pr}\left(f\theta' - \frac{2n}{m+1}f'\theta\right) = 0 \tag{9}$$

The transformed boundary conditions are

$$f(0) = 0, \quad f'(\infty) = 1, \quad \theta(\infty) = 0 \tag{10}$$

The slip velocity condition becomes

$$f'(0) = K_1 f''(0)x^{(m-1)/2}\sqrt{\frac{m+1}{2}} + \frac{3}{4}\frac{\mu}{\rho}\frac{n}{U_o x^{m+1}\theta(0)} \tag{11}$$

and the temperature jump becomes

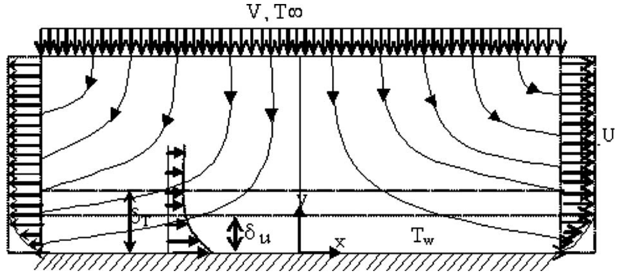

Fig. 1 Stagnation on plane flow for the case when $m=1$, $n=0$

$$\theta(0) = 1 + K_2\theta'(0)x^{(m-1)/2}\sqrt{\frac{m+1}{2}} \tag{12}$$

Equations (8)–(12) indicate that the similarity solution exists only when $m=1$ and $n=0$. That is flow toward a stagnation point at a rigid isothermal boundary (Hiemenz flow in macroscales), as shown schematically in Fig. 1. For this case, Eqs. (5)–(7) reduce to

$$u = U_o x f'(\eta), \quad \frac{(T-T_\infty)}{(T_w - T_\infty)} = \theta(\eta) \tag{13}$$

$$\eta = y\sqrt{\frac{U_o}{\nu}} = \frac{y}{x}\sqrt{\mathrm{Re}_x} \tag{14}$$

$$v = -f\sqrt{\nu U_o} \tag{15}$$

and the governing equations become

$$f''' + ff'' - f'^2 = -1 \tag{16}$$

$$\theta'' + \mathrm{Pr} f\theta' = 0 \tag{17}$$

and the velocity slip and temperature jump boundary conditions reduce to

$$f'(0) = K_1 f''(0) \tag{18}$$

$$\theta(0) = 1 + K_2\theta'(0) \tag{19}$$

where

$$K_1 = \frac{(2-\sigma_v)}{\sigma_v}\lambda\sqrt{\frac{U_o}{\nu}} = \frac{(2-\sigma_v)}{\sigma_v}\mathrm{Kn}\mathrm{Re}_L^{1/2} \tag{20}$$

$$\mathrm{Kn} = \lambda/L \tag{21}$$

and

$$K_2 = 2\frac{(2-\sigma_T)}{\sigma_T}\lambda\sqrt{\frac{U_o}{\nu}} = 2\frac{(2-\sigma_T)}{\sigma_T}\mathrm{Kn}\mathrm{Re}_L^{1/2} \tag{22}$$

The expression for the shear stress can be developed from the similarity solution for $m=1$ in the form

$$C_f = \frac{2\tau_w}{\rho u^2(x)} = \frac{2f''(0)}{\sqrt{\mathrm{Re}_x}} \tag{23}$$

At the stationary surface, $f''(0)=0.5C_f\sqrt{\mathrm{Re}_x}$. The local heat transfer coefficient h can be expressed as

$$h = \frac{-\left.k\frac{\partial T}{\partial y}\right|_{y=0}}{(T_w - T_\infty)} \tag{24}$$

and in dimensionless form the Nusselt number is

Table 1 Values of functions for a no-slip case with Pr=1

η	$f(0)$	$f'(0)$	$f''(0)$	$\theta(0)$	$\theta'(0)$
0.00	0.00000	0.00000	1.23259	1.00000	−0.57047
0.10	0.00600	0.11826	1.13283	0.94296	−0.57035
0.20	0.02332	0.22661	1.03445	0.88595	−0.56957
0.30	0.05099	0.32524	0.93863	0.82909	−0.56750
0.40	0.08806	0.41446	0.84633	0.77251	−0.56361
0.50	0.13359	0.49465	0.75831	0.71644	−0.55744
0.60	0.18670	0.56628	0.67517	0.66111	−0.54861
0.80	0.31242	0.68594	0.52513	0.55384	−0.52211
1.00	0.45923	0.77787	0.39801	0.45308	−0.48349
1.25	0.66472	0.86079	0.27115	0.33981	−0.42030
1.50	0.88733	0.91617	0.17696	0.24384	−0.34628
1.75	1.12114	0.95158	0.11045	0.16690	−0.26945
2.00	1.36197	0.97322	0.06583	0.10870	−0.19757
2.25	1.60700	0.98584	0.03740	0.06723	−0.13632
2.50	1.85443	0.99285	0.02023	0.03942	−0.08845
2.75	2.10316	0.99656	0.01040	0.02188	−0.05393
3.00	2.35256	0.99842	0.00508	0.01149	−0.03090
3.25	2.60229	0.99931	0.00235	0.00570	−0.01663
3.50	2.85217	0.99972	0.00103	0.00267	−0.00841
4.00	3.35211	0.99996	0.00017	0.00049	−0.00178
4.50	3.85210	1.00000	0.00002	0.00007	−0.00029
5.00	4.35210	1.00000	0.00000	0.00001	−0.00004
6.00	5.35210	1.00000	0.00000	0.00000	0.00000

$$\mathrm{Nu} = \frac{h\sqrt{\nu/U_o}}{k} = -\,\theta'(0) \tag{25}$$

It should be noted that the constant U_o for $m=1$ has the dimensions of $L^{1-m}t^{-1}$. Finally, the hydrodynamic and the thermal boundary layer thicknesses are defined, respectively, as

$$\eta_H = (\eta\,@\,f'(\eta) = 0.99) \tag{26}$$

$$\eta_T = (\eta\,@\,\theta(\eta) = 0.01) \tag{27}$$

3 Numerical Solution Procedure

The nonlinear coupled system of differential equations given by Eqs. (16) and (17) along with the boundary conditions at two points given by Eqs. (10), (18), and (19) are solved using a variable order, variable step size finite difference method with deferred corrections. The solution method is based on the subprogram of Pereyra [12]. The first step in the solution is to reduce the governing equations to a system of first order differential equations. The basic discretization of the first order differential equations is the trapezoidal rule over a nonuniform mesh. This mesh is chosen adaptively, to make the local error approximately the same size everywhere. Higher-order discretizations are obtained by deferred corrections. Global error estimates are produced to control the computation. The resulting nonlinear algebraic system is solved by Newton's method with step control. The linearized system of equations is solved by Gauss elimination.

The solution of $f'(\eta)$ and $\theta(\eta)$ is obtained iteratively on η. The solution is first obtained by assuming a certain value of η, then η increased until the values of $f'(\eta)$ and $\theta(\eta)$ at infinity decay exponentially to one and zero, respectively (at least of order 10^{-4}). The maximum possible value of η is taken. A typical run is presented in Table 1. It is clear that the values of $f'(\eta)$ and $\theta(\eta)$ decay exponentially to 1 and 0, respectively. Several validation cases are presented by the current authors in [10]. In addition to that, Table 1 shows the values of the functions calculated for no-slip conditions while Table 2 shows the values for slip conditions. The hydrodynamic values in Table 1 are exactly the same values presented by Schlichting [13]

4 Results and Discussion

The governing equations and the boundary conditions of the problem indicate that there are three parameters control the flow and heat transfer characteristics of the problem. The slip parameter K_1, the temperature jump parameter K_2, and the Prandtl number Pr. The effect of each parameter is studied and presented next.

Figure 2 represents the variation in the dimensionless transverse velocity component $f(\eta)$ with the similarity independent variable η. As predicted, v increases as η increases since large values of η apply for locations far from the plate (large y) where the flow approaches the horizontal plate with transverse component v. The same figure shows that $f(\eta)$ increases as K_1 increases. As K_1 increases, the slip at the plate surfaces increases and less flow is escaping the boundary layer in the positive transverse direction η. As a result, the net difference between the negative transverse velocity component of the approaching flow, in the negative direction of η, and the positive transverse component of the escaping flow, in the positive direction of η, increases. Note that the effect of K_1 becomes less significant at large values of K_1 because at very large values of K_1 the flow profile becomes almost plug with uniform axial velocity distribution and there will be no flow escaping the boundary layer in the transverse direction any more. As a result, the net difference in the transverse velocity component approaches fixed values at very large K_1.

Figure 3 shows the variation in the dimensionless axial velocity component $f'(\eta)$ with the similarity independent variable η. The velocity component u increases as η increases to reach one far away from the plate when the penetration effect of the stationary surface diminishes. Note that the fluid dimensionless velocity at the wall is 0 when $K_1=0$ that represents the no-slip case. As the hydrodynamics slipping parameter K_1 increases, the slip velocity at the wall increases. Again, it is clear that as slipping parameter increases, the penetration of the stagnant surface through the fluid domain decreases leading to a reduction in the hydrodynamics boundary layer measured by the displacement thickness. Increasing slipping factor may be looked at as a miscommunication between the stationary plate and the moving fluid. Note that hydrodynamics behavior of the problem under consideration is more sensitive to the variations in small values of K_1 as compared with the variations in large values of it. Figure 3 shows that increasing

Table 2 Values of functions for a slip case with Pr=1, $K_1=0.1$, and $K_2=0.1$

η	$f(0)$	$f'(0)$	$f''(0)$	$\theta(0)$	$\theta'(0)$
0.00	0.0000	0.1134	1.1343	0.9434	−0.5659
0.10	0.0169	0.2219	1.0364	0.8868	−0.5654
0.20	0.0441	0.3208	0.9410	0.8304	−0.5638
0.30	0.0807	0.4103	0.8490	0.7741	−0.5603
0.40	0.1258	0.4907	0.7612	0.7184	−0.5546
0.50	0.1786	0.5627	0.6782	0.6633	−0.5462
0.60	0.2381	0.6265	0.6004	0.6092	−0.5350
0.80	0.3744	0.7324	0.4616	0.5052	−0.5034
1.00	0.5293	0.8127	0.3458	0.4087	−0.4600
1.25	0.7421	0.8843	0.3018	0.2320	−0.3926
1.50	0.9694	0.9313	0.1491	0.2130	−0.3170
1.75	1.2063	0.9609	0.0915	0.1433	−0.2416
2.00	1.4489	0.9787	0.0536	0.0916	−0.1734
2.25	1.6950	0.9889	0.0300	0.0556	−0.1170
2.50	1.9430	0.9945	0.0159	0.0320	−0.0743
2.75	2.1920	0.9974	0.0080	0.0174	−0.0443
3.00	2.4416	0.9988	0.0038	0.0090	−0.0248
3.25	2.6914	0.9995	0.0017	0.0044	−0.0131
3.50	2.9413	0.9998	0.0008	0.0020	−0.0065
4.00	3.4413	1.0000	0.0001	0.0004	−0.0013
4.50	3.9413	1.0000	0.0000	0.0000	−0.0002
5.00	4.4413	1.0000	0.0000	0.0000	0.0000
5.50	4.9413	1.0000	0.0000	0.0000	0.0000
6.00	5.4413	1.0000	0.0000	0.0000	0.0000

K_1 leads to an increase in the axial velocity u. The axial velocity component becomes so close to the freestream velocity U_∞ at large values of K_1. Large slip parameters make the flow approaching the plug (uniform) distribution even at small values of η.

Figure 4 shows the variation in the shear parameter f'' with the independent similarity parameter η. As predicted, the shear parameter f'' decreases as η increases since the penetration effects of the stationary surface decreases as one marches into the fluid domain. Also, f'' decreases as K_1 increases due to the increase in the slip conditions at the stationary surface since as slip conditions increase the flow will be less aware to the existence of the stationary plate. The slope of the axial velocity distribution at the wall decreases as K_1 increases and in the limiting case, when the flow becomes uniform at large values of K_1, the slope approaches 0.

Figure 5 shows the variation in the dimensionless temperature θ with η at different values of the hydrodynamics slip parameter K_1 and for the temperature jump parameter $K_2=1$. As the velocity slip parameter K_1 increases, more flow will penetrate through the boundary layer due to the slipping effect. As a result, the hot plate heats more amounts of fluid and this causes the decrease in the fluid temperature. It will be shown later that the problem thermal behavior is much more sensitive to the variations in K_2 as compared with the variations in K_1. The parameter K_2 has direct effects on the fluid thermal behavior because K_2 is a measure for the temperature jump at the wall. On the other hand, K_1 affects the fluid hydrodynamics behavior directly and this hydrodynamics behavior affects the problem thermal behavior indirectly through the enthalpy flow in the energy equation. Also, note that the temperature profile becomes almost linear for small η and K_1. Less fluid flows within the boundary layer for small values of K_1 and the heat conduction mode will have significant effect in this case,

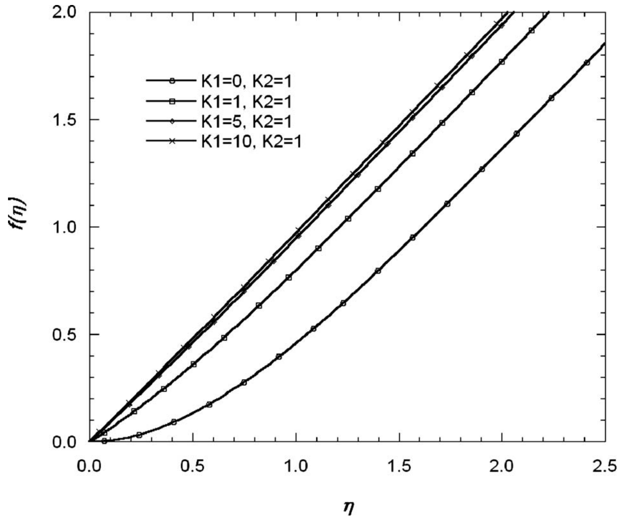

Fig. 2 Variation in the dimensionless transverse velocity distribution with the similarity parameter η at different slip parameters, K_1 and Pr=1

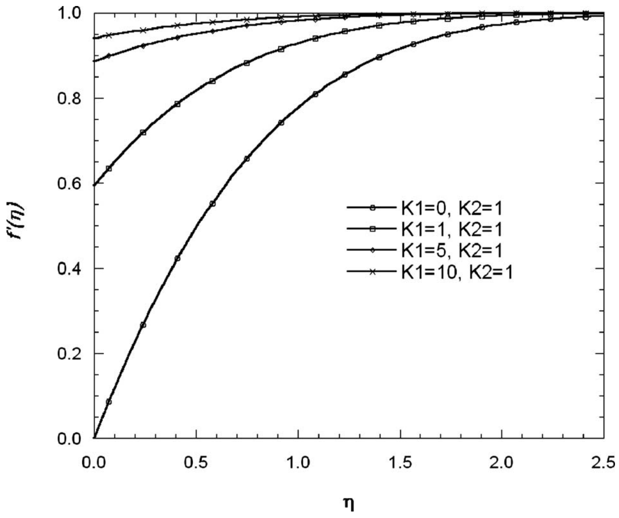

Fig. 3 Variation in the dimensionless axial velocity distribution with the similarity parameter η at different slip parameters, K_1, and Pr=1

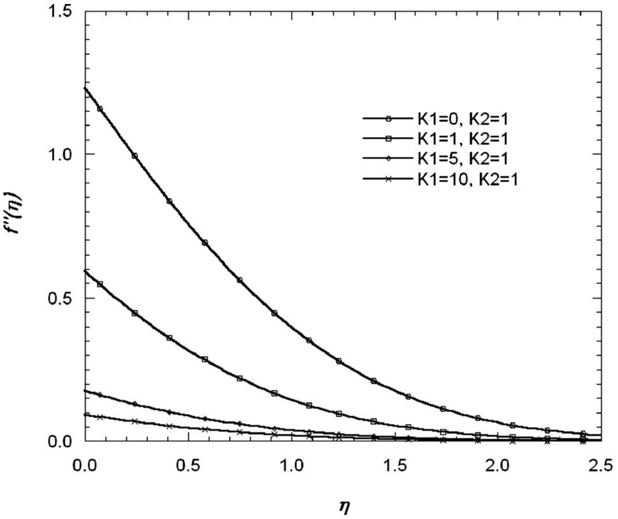

Fig. 4 Variation in the dimensionless shear parameter distribution with the similarity parameter η at different slip parameters, K_1 and Pr=1

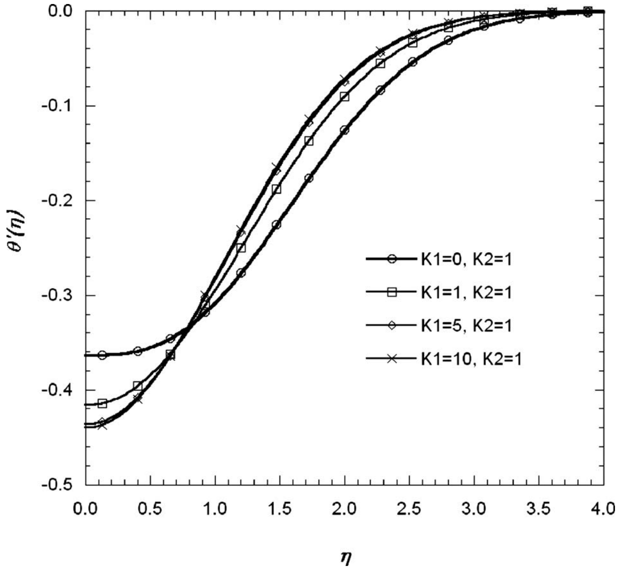

Fig. 6 Variation in the dimensionless temperature gradient distribution with the similarity parameter η at different slip parameters, K_1 and Pr=1

yielding the linear looking profile for the temperature. Again, the effect of K_1 is insignificant at high values of it as explained previously.

Figure 6 shows the variation in θ' with η and for different values of K_1 at $K_2=1$. The parameter θ' is a measure for the heat transfer within the domain and the absolute positive value of this parameter decreases as η increases because the penetration of the hot plate heating effect decreases as η increases. Also, note that negative values for θ' imply positive heat transfer rates in the positive η direction because the heat transfer is proportional to $-\theta'(0)$. Also, increasing K_1 leads to an increase in the amount of heat transfer near the plate surface, since more flow is penetrating through the boundary layer and carrying more enthalpy with it.

Figure 7 shows the variation in the dimensionless temperature θ with the similarity parameter η and at $K_1=1$ and at different values of K_2. As predicted, increasing the temperature jump parameter K_2 leads to a reduction in the fluid temperature. As the temperature jump parameter K_2 increases, the fluid will not sense the heating effects of the plate and less amount of heat will be extracted from the hot plate to the fluid. Also, the thermal behavior of the problem is more sensitive to K_2 variations in its lower range as compared with that in its higher ranges. As an example, increasing K_2 from 0 to 1 yields to an increase in the wall temperature jump from 0 to 0.425 while increasing K_2 from 1 to 5 raises the temperature jump at the wall from 0.425 to 0.775.

Figure 8 shows the effect of the temperature jump parameter K_2 on the distribution of θ'. As predicted, less amount of heat transfer generates within the fluid domain as K_2 increases. This is due to the thermal miscommunication between the hot wall and the fluid as the temperature jump parameter increases. The fluid will not be aware of the wall thermal conditions due to the increase in the temperature jump parameter. Table 3 shows of functions evaluated at the wall for several values of velocity slip parameter, temperature slip parameter, and Prandtl numbers. It also shows the values of boundary layer thicknesses at different parameters.

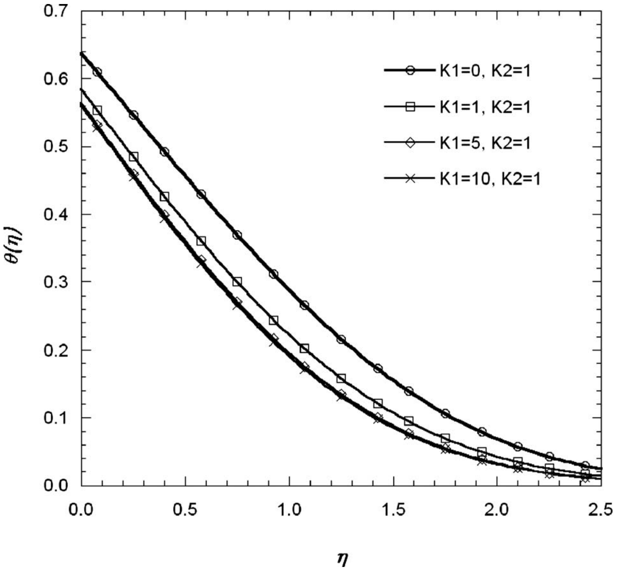

Fig. 5 Variation in the dimensionless temperature distribution with the similarity parameter η at different slip parameters, K_1 and Pr=1

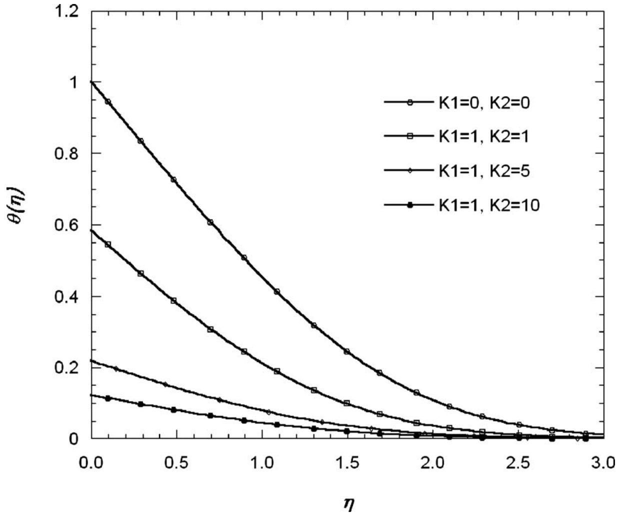

Fig. 7 Variation in the dimensionless temperature distribution with the similarity parameter η at different jump parameters, K_2 and Pr=1

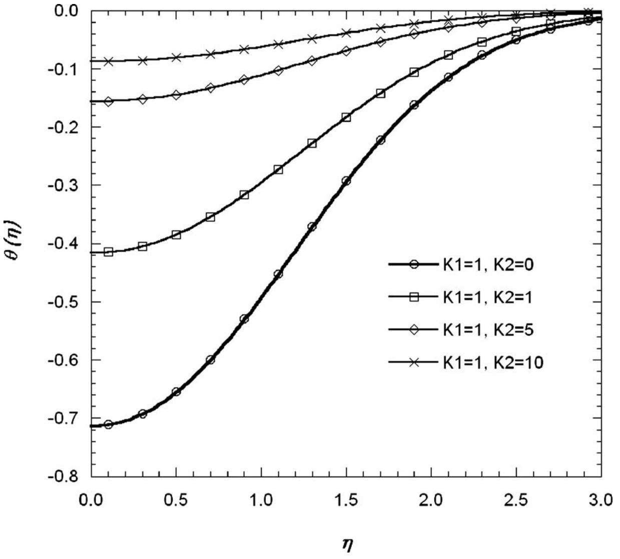

Fig. 8 Variation in the dimensionless temperature gradient distribution with the similarity parameter η at different jump parameters, K_2 and Pr=1

Figure 9 shows the effect of Pr on the temperature distribution for $K_1=0.5$ and $K_2=0.5$. As predicted lower Pr leads to higher temperatures. Lower Pr implies fluids having higher thermal diffusivity α and lower viscosities μ. The heating effect of the hot wall is able to penetrate deeper and deeper through the fluid as α increases and this yields higher fluid temperatures. Also, more fluid penetrates through the boundary layer as μ decreases and the hot plate is supposed to heat less amount of fluid. This in turns yields higher temperatures for the plate at lower values of Pr.

Figure 10 shows the effect of Pr on θ' distribution. The parameter θ' is proportional to the heat transfer through the fluid domain and this convicted heat is proportional to Pr as explained previously. It is known that all heat transfer correlations predict that q is proportional to Pr.

Figure 11 shows the variation in the hydrodynamics boundary thickness with the velocity slip parameter K_1. The boundary layer thickness decreases as K_1 increases because the fluid is not able to sense the presence of the stationary plate as the slip parameter increases. As a result, the retardation effect of the stationary plate does not penetrate deeply through the fluid due to this hydrodynamics miscommunication. Note that there is an asymptotic lower limit for the effect of K_1 on the hydrodynamics boundary layer thickness and this has been explained previously.

Table 3 Numerical result of the momentum and the thermal problem of stagnation flow for a microsystem

Pr	K_1	K_2	$f'(0)$	$-f''(0)$	$\theta(0)$	$-\theta'(0)$	η_H	η_T
0.7	0	0	0.0000	1.2326	1.0000	0.4959	3.5806	2.4036
	0.01	0.1	0.0122	1.2226	0.9525	0.4746	3.5518	2.3938
	0.5		0.4107	0.8215	0.9459	0.5413	3.3281	2.0534
	1		0.5935	0.5935	0.9431	0.5690	3.2419	1.8596
	10		0.9404	0.0940	0.9382	0.6178	3.0985	0.9845
	0.2	0.01	0.2085	1.0426	0.9947	0.5331	3.4547	2.2326
		0.1	0.2085	1.0426	0.9491	0.5087	3.4346	2.2326
		1	0.2085	1.0426	0.6511	0.3489	3.2684	2.2326
		5	0.2085	1.0426	0.2718	0.1456	2.8489	2.2326
		10	0.2085	1.0426	0.1572	0.0843	2.5551	2.2326
1	0	0	0.0000	1.2326	1.0000	0.5705	3.0756	2.4036
	0.01	0.1	0.0122	1.2226	0.9457	0.5426	3.0473	2.3938
	0.5		0.4107	0.8215	0.9371	0.6294	2.8228	2.0534
	1		0.5935	0.5935	0.9335	0.6654	2.7371	1.8596
	10		0.9404	0.0940	0.9271	0.7286	2.5954	0.9845
	0.2	0.01	0.2085	1.0426	0.9938	0.6197	2.9490	2.2326
		0.1	0.2085	1.0426	0.9413	0.5869	2.9293	2.2326
		1	0.2085	1.0426	0.6159	0.3841	2.7707	2.2326
		5	0.2085	1.0426	0.2429	0.1514	2.3883	2.2326
		10	0.2085	1.0426	0.1382	0.0862	2.1263	2.2326
2	0	0	0.0000	1.2326	1.0000	0.7437	2.3113	2.4036
	0.01	0.1	0.0122	1.2226	0.9303	0.6970	2.2842	2.3938
	0.5	0.1	0.4107	0.8215	0.9161	0.8388	2.0598	2.0534
	1		0.5935	0.5935	0.9103	0.8968	1.9757	1.8596
	10		0.9404	0.0940	0.9002	0.9977	1.8361	0.9804
	0.2	0.01	0.2085	1.0426	0.9917	0.8270	2.1802	2.2285
		0.1	0.2085	1.0426	0.9230	0.7697	2.1613	2.2285
		1	0.2085	1.0426	0.5453	0.4547	2.0175	2.2285
		5	0.2085	1.0426	0.1934	0.1613	1.6990	2.2285
		10	0.2085	1.0426	0.1071	0.0893	1.4879	2.2285
5	0	0	0.0000	1.2326	1.0000	1.0434	1.6077	2.3950
	0.01	0.1	0.0122	1.2226	0.9046	0.9537	1.5819	2.3852
	0.5		0.4107	0.8215	0.8788	1.2117	1.3608	2.0452
	1		0.5935	0.5935	0.8686	1.3139	1.2814	1.8506
	10		0.9404	0.0940	0.8513	1.4867	1.1597	0.9756
	0.2	0.01	0.2085	1.0426	0.9879	1.2055	1.4800	2.2231
		0.1	0.2085	1.0426	0.8912	1.0875	1.4621	2.2231
		1	0.2085	1.0426	0.4504	0.5496	1.3360	2.2231
		5	0.2085	1.0426	0.1408	0.1718	1.0854	2.2231
		10	0.2085	1.0426	0.0757	0.0924	0.9242	2.2231

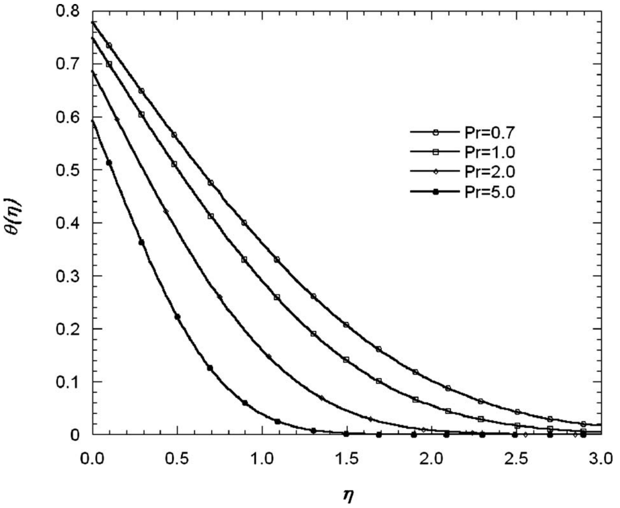

Fig. 9 Variation in the dimensionless temperature distribution with the similarity parameter η at different Prandtl numbers for $K_1=0.5$ and $K_2=0.5$

Figure 12 shows the effect of K_1 on the thermal boundary layer thickness and at different values of Pr. As predicted decreasing Pr increases the thermal boundary layer thickness because Pr decreases as the fluid thermal diffusivity increases and this enable the heating effects of the hot wall to penetrate deeper into the fluid. This in turns causes the thickening the thermal boundary layer. Also, increasing K_1 leads to a decrease in the thermal boundary layer. This has been explained previously because as K_1 increases more fluid flow penetrates through the boundary layer due to the slipping effect. As a result, the hot wall heating effect will not be able to penetrate deeper into the fluid because it has to heat more amount of fluid.

Figure 13 shows the effect of temperature jump parameter K_2 on the thermal boundary layer thickness and for different values of Pr. The increase in the thermal boundary layer thickness with decreasing Pr has been justified and discussed before. The reduction in the thermal boundary layer thickness with K_2 is obvious because K_2 represents the temperature jump at the wall. The fluid will not sense the heating effect of the hot wall as K_2 increases and this causes less thermal penetration through the fluid domain.

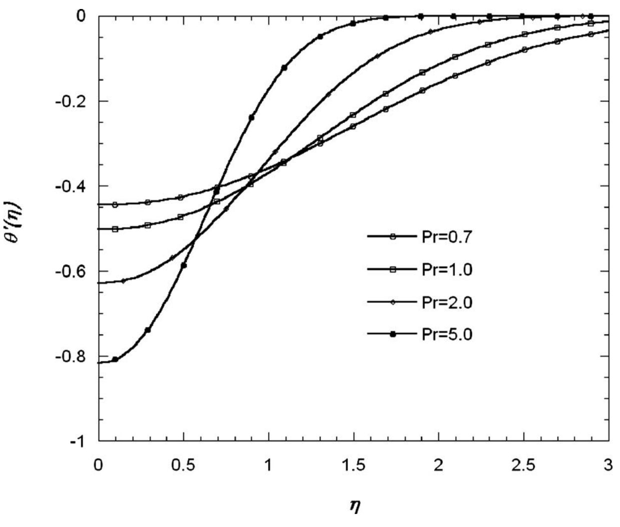

Fig. 10 Variation in the dimensionless temperature gradient with the similarity parameter η at different Prandtl numbers for $K_1=0.5$ and $K_2=0.5$

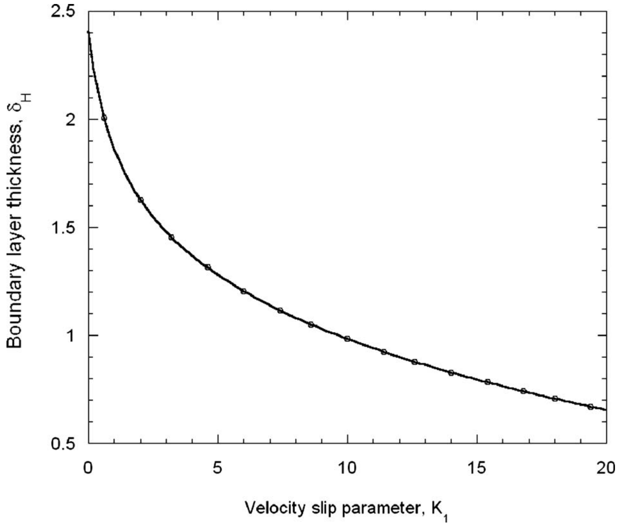

Fig. 11 Variation in the hydrodynamic boundary layer thickness with the variation in the slip parameter K_1 for all values of K_2 and Pr

Figure 14 shows the effect of K_1 on the skin friction dimensionless parameter $0.5C_f\mathrm{Re}_x^{0.5}$. As predicted, the increase in the velocity slip parameter yields a reduction in the skin friction parameter because velocity gradients near the wall decreases. In the limiting case as $K_1 \rightarrow \infty$, the fluid is not aware of the retardation effect of the stationary wall and this implies that shear stress at the wall is almost zero. The variation in the skin friction coefficient has been correlated with the variation in K_1 and it is found that: $C_f = 3.38\mathrm{Re}_x^{-0.5}(K_1+1.279)^{-0.8}$ for $0 \leq K_1 < 5$ with maximum error of $\pm 4\%$.

Figure 15 shows the effect of K_1 on Nu for different values of Pr. It has been mentioned previously that heat transfer increases as Pr increases. This trend has already been described and justified. However, Nu increases as K_1 increases because increasing K_1 causes more amount of fluid to flow through the boundary layer due to the slipping effect. More fluid flow within the boundary layer means better convective heat transfer due to the more carried enthalpy.

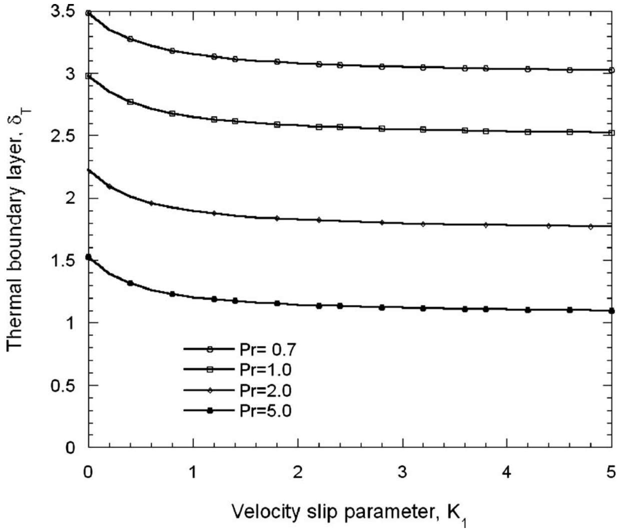

Fig. 12 Variation in the thermal boundary layer thickness with the variation in slip parameter K_1 for different Prandtl numbers and $K_2=0.5$

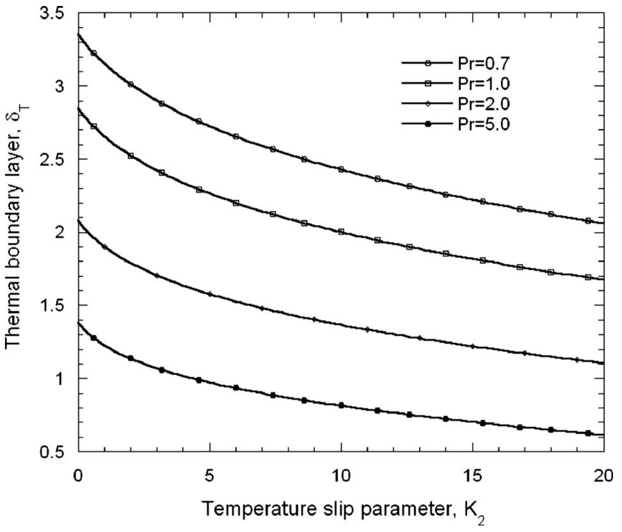

Fig. 13 Variation in the thermal boundary layer thickness with the variation in jump parameter K_2 for different Prandtl numbers and $K_1=0.5$

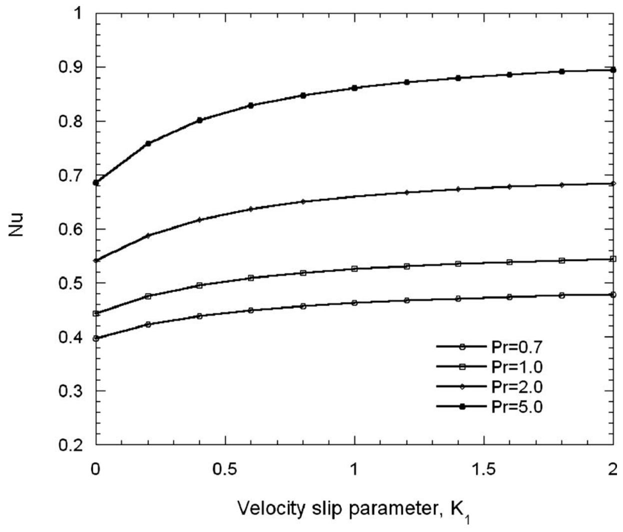

Fig. 15 Variation in Nusselt number with the variation in slip parameter K_1 for different values of Pr and $K_2=0.5$

Figure 16 shows the effect of K_2 on Nu and at different values of Pr. The increase in Nu with increasing Pr has been described and explained before. On the other hand, increasing K_2 enhances the thermal miscommunication between the hot wall and the fluid and this justifies the reduction in Nu. The variation in Nu with the variation in K_1, K_2, and Pr has been correlated. It is found that

$$\mathrm{Nu}=\frac{0.449+1.142K_1^{1.06}}{0.515+K_1^{1.06}}(K_2+1.489\mathrm{Pr}^{-0.44})^{-1},\quad \text{for}\quad 0\le K_1,\ K_2 < 5\quad \text{and}\quad 0.7\le \mathrm{Pr}\le 5$$

within maximum error of ±3%.

5 Conclusions

The existence of complete similarity solution for boundary layer flows resulting from an arbitrary freestream velocity $U(x)=U_o x^m$ and wall temperature given by $T_w-T_\infty=Cx^n$ under slip and jump conditions is carried out. It is found that the self similar solution exist only for the case of flow toward stagnation point over isothermal surface (i.e., when $m=1$ and $n=0$). The case has been investigated and it is found that three parameters control the flow and heat transfer characteristics of the problem; K_1, K_2, and Pr. The effect of these parameters have been studied and presented. The variation in skin friction and Nusselt number are presented for different values of K_1, K_2, and Pr. Correlations for skin friction parameter and Nusselt numbers are found and presented.

Nomenclature

c_f = skin friction coefficient
c_p = specific heat at constant pressure (J kg^{-1} K^{-1})
f = transformed variable
h_x = local heat transfer coefficient (W m^{-2} K^{-1})
k = thermal conductivity (W m^{-1} K^{-1})
K_1 = slip velocity parameter, Eq. (20)
K_2 = temperature jump parameter, Eq. (22)
Kn = Knudsen number, Eq. (21)
Nu = Nusselt number for $m=1$, $n=0$, $(h\sqrt{\nu/U_o}/k)$
Pr = Prandtl number (ν/α)
Re_x = local Reynolds number for $m=1$, $(U_o x^2/\nu)$

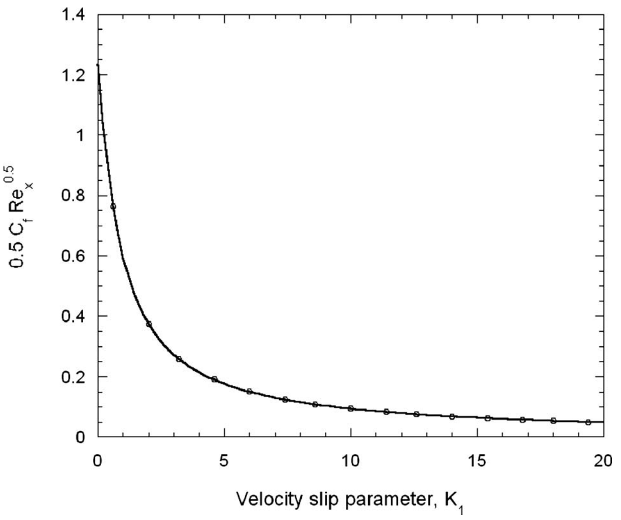

Fig. 14 Variation in skin friction parameter with the variation in slip parameter K_1 for all values of Pr and K_2

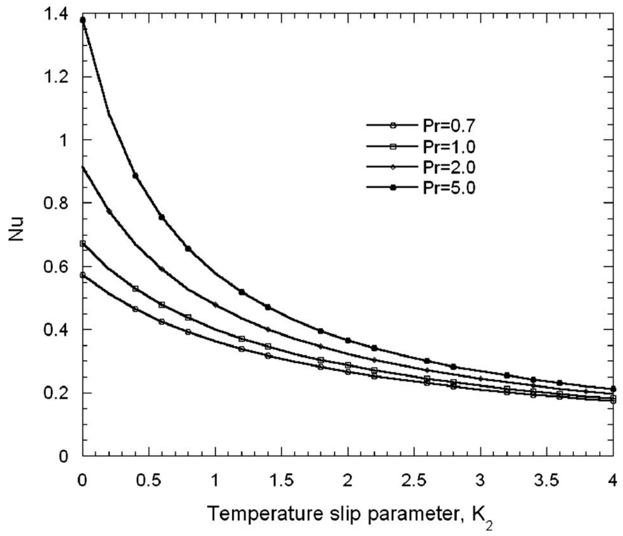

Fig. 16 Variation in Nusselt number with the variation in jump parameter K_2 for different values of Pr and $K_1=0.5$

T = temperature (K)
U_o = constant, $L^{1-m}\ s^{-1}$
u = velocity component along the moving plate (m s^{-1})
v = velocity component normal to the plate (m s^{-1})
x, y = coordinate along and normal to the plate (m)
α = thermal diffusivity (m^2 s^{-1})
η = transformed variable
θ = dimensionless temperature
ν = kinematic viscosity (m^2 s^{-1})

Subscripts

w = conditions at wall
∞ = ambient conditions
$(\ )'$ = derivative with respect to η

References

[1] Duncan, G. P., and Peterson, G. P., 1994, "Review of Microscale Heat Transfer," Appl. Mech. Rev., **47**(9), pp. 397–428.
[2] Gad-el-Hak, M., 1999, "The Fluid Mechanics of Microdevices—The Freeman Scholar Lecture," ASME J. Fluids Eng., **121**, pp. 5–33.
[3] Gad-el-Hak, M., 2002, "Flow Physics in Microdevices," *The Handbook of MEMS*, CRC, Boca Raton, FL.
[4] Barron, R. F., Wang, X., Ameel, T. A., and Warrington, R. O., 1997, "The Graetz Problem Extended to Slip-Flow," Int. J. Heat Mass Transfer, **40**(8), pp. 1817–1823.
[5] Guo, Z. Y., and Li, Z. X., 2003, "Size Effect on Single-Phase Channel Flow and Heat Transfer at Microscale," Int. J. Heat Fluid Flow, **24**(3), pp. 284–298.
[6] Chakraborty, S., Som, S. K., and Rahul, 2008, "A Boundary Layer Analysis for Entrance Region Heat Transfer in Vertical Microchannels With the Slip Flow Regime," Int. J. Heat Mass Transfer, **51**, pp. 3245–3250.
[7] Aydın, O., and Avcı, M., 2006, "Heat and Flow Characteristics of Gases in Micropipes," Int. J. Heat Mass Transfer, **49**, pp. 1723–1730.
[8] Aydın, O., and Avcı, M., 2007, "Analysis of Laminar Heat Transfer in Micro-Poiseuille Flow," Int. J. Therm. Sci., **46**, pp. 30–37.
[9] Avcı, M., and Aydın, O., 2008, "Laminar Forced Convection Slip-Flow in a Micro-Annulus Between Two Concentric Cylinders," Int. J. Heat Mass Transfer, **51**, pp. 3460–3467.
[10] Kiwan, S., and Al-Nimr, M. A., 2009, "Flow and Heat Transfer Over a Stretched Micro-Surface," ASME Trans. J. Heat Transfer, **131**(6), p.061703.
[11] Martin, M. J., and Boyd, I. D., 2006, "Momentum Heat Transfer in a Laminar Boundary Layer With Slip Flow," J. Thermophys. Heat Transfer, **20**(4), pp. 710–719.
[12] Pereyra, V., 1978, "PASVA3: An Adaptive Finite-Difference FORTRAN Program for First Order Nonlinear Boundary Value Problems," *Lecture Notes in Computer Science*, Springer-Verlag, Berlin, p. 76.
[13] Schlichting, H., 1987, *Boundary Layer Theory*, 7th ed., McGraw-Hill, New York.

Analytical Modeling of Annular Flow Boiling Heat Transfer in Mini- and Microchannel Heat Sinks

A. Megahed

I. Hassan[1]
e-mail: ibrahimh@alcor.concordia.ca

Department of Mechanical and Industrial
Engineering,
Concordia University,
Montreal, QC, H3G 1M8, Canada

An analytical model is proposed to predict the flow boiling heat transfer coefficient in the annular flow regime in mini- and microchannel heat sinks based on the separated model. The modeling procedure includes a formulation for determining the heat transfer coefficient based on the wall shear stress and the local thermophysical characteristics of the fluid based on the Reynolds' analogy. The frictional and acceleration pressure gradients within the channel are incorporated into the present model to provide a better representation of the flow conditions. The model is validated against collected data sets from the literature produced by different authors under different experimental conditions, different fluids, and with mini- and microchannels of hydraulic diameters falling within the range of 92–1440 μm. The accuracy between the experimental and predicted results is achieved with a mean absolute error of 10%. The present analytical model can correctly predict the different trends of the heat transfer coefficient reported in the literature as a function of the exit quality. The predicted two-phase heat transfer coefficient is found to be very sensitive to changes in mass flux and saturation temperature. However, it is found to be mildly sensitive to the change in heat flux. [DOI: 10.1115/1.4000887]

Keywords: annular flow, two-phase flow, two-phase heat transfer coefficient, mini- and microchannel heat sinks

1 Introduction

The need for reliable thermal management of electronic devices illustrates the critical role of heat transfer for certain areas of the electronic industry. In recent years, enormous progress has been made in developing new thermal fluid microelectromechanical system (MEMS) devices. A review of recent progress in the development of thermal fluid MEMS devices can be found in Ref. [1].

A review of recent literature [2–7] clearly indicates that many experimental studies have been conducted to investigate the heat transfer characteristics of flow boiling in mini- and microchannels. There remains, however, a lack of information about the two-phase forced convection heat transfer coefficients. With respect to trends, the presented studies in the literature can be divided into two groups. In the first group of studies [2–4], the heat transfer coefficient increases with increasing exit quality. The second group of studies [5–7] shows that as the exit quality increases, a significant decrease in the heat transfer coefficient is observed.

Recently, Bertsch et al. [8] provided a critical review of experimental works relating to flow boiling in mini- and microchanels including heat transfer, pressure drop, critical heat flux, flow patterns, and flow instabilities. Twenty-five published correlations have been tested against a large number of experimental data collected from the open literature, covering channels of hydraulic diameters ranging from 160 µm to 2000 µm. Their assessment of the reported correlations for small channels showed that none of the tested correlations appear to provide good predictions over the conventional size tubes correlations. This is mainly due to the fact that those correlations rely heavily on the regression analysis of the tested data rather than on analytical modeling. In addition, the database of each correlation does not cover a wide range of fluid properties and channels sizes. More work on theoretically based models was recommended.

Three analytical models have been presented in the literature to model heat transfer during annular flow boiling. Fossa [9] developed an analytical model using 1D steady flow analysis of air-water mixtures. The model accounts for variable flow cross sections such as nozzles and diffusers. It allows the calculation of different flow parameters such as the mean film thickness, pressure drop, temperature, and velocity distributions in each phase. To check for the existence of annular flow, the constraint of Turner et al. [10] was defined as follows:

$$\frac{u_g\rho_g^{1/2}}{[\sigma g(\rho_L-\rho_g)]^{1/4}} \geq 3.1 \tag{1}$$

However, to obtain a solution for this model requires solving 16 ordinary differential equations. In addition, this model depends on many correlations to calculate the closure relationships such as interfacial friction factor, mean droplet diameter, and the evaporation rate. The model presented reasonable predictions with the isothermal experimental data.

Fu and Klausner [11] developed an analytical model using the Reynolds' analogy involving energy balance at the liquid-vapor interface for evaporative heat transfer in a vertical annular flow. Although their model can be applied for microgravity flow conditions, it requires the knowledge of the interfacial friction factor, liquid film eddy viscosity, turbulent Prandtl number, and entrainment rate. They used a data bank consisting of 1618 data points for annular flow boiling using water, n-Butanol, and many refrigerants. Their model was developed based on a turbulent flow assumption. The model's applicability to laminar flow is therefore questionable. Moreover, extending the model beyond the flow and

---

[1] Corresponding author.

Contributed by the Heat Transfer Division of ASME for publication in the JOURNAL OF HEAT TRANSFER. Manuscript received April 6, 2009; final manuscript received November 11, 2009; published online February 22, 2010. Editor: Satish G. Kandlikar.

thermal conditions for which it has been tested is also questionable, since the empirical closure relations were calibrated against the collected experimental database.

Qu and Mudawar [12] developed an analytical model to predict the flow boiling heat transfer coefficient in microchannel heat sinks. Their model differs from the previous models in certain aspects. Their model included several unique features of microchannels, such as a very small hydraulic diameter and rectangular channel geometry. They developed the model to suit a variety of conditions including laminar-liquid laminar-vapor flow, smooth interface, droplet entrainment, and deposition effects. The onset of annular flow was determined by using the model of Taitel and Duckler [13], given as

$$X_{vv} = 1.6 \tag{2}$$

The model results in a complicated system of equations that is difficult to solve analytically. Furthermore, a grid system has to be established containing a large number of nodes. Hence, an iteration procedure is required to solve the system of equations, and therefore, a numerical code must be developed. The verification of the model was done only with their experimental data and showed a good agreement.

A key element in flow boiling in mini- and microchannels—the heat transfer coefficient—is far from properly predicted. Though numerous correlations have been developed to predict the heat transfer coefficient during flow boiling in mini- and microchannel heat sinks, very little is known about the validity of these correlations. The available heat transfer correlations for flow boiling in mini- and microchannels satisfy only limited experimental data and there is little unanimity over a single correlation. Furthermore, these correlations were empirically derived and none were derived based on analytical modeling. Therefore, it is essential to have an analytical model to describe the flow boiling heat transfer in mini- and microchannel heat sinks. The drawbacks of the previous models are that they depend on empirical closure relations or iterations to find a numerical solution. The present model does not need any such initial guesses, iterations, or numerical codes, and hence, is advantageous to use.

The objective of the present study is to develop an analytical model for determining the heat transfer coefficient for annular flow boiling inside rectangular mini- and microchannels. The solution for the heat transfer coefficient is dependent on the Reynolds' analogy. In relating the wall shear stress to the heat transfer coefficient, the heat transfer coefficient has been expressed in terms of liquid-phase friction and acceleration induced pressure drops. The model considers the characteristics of mini- and microchannels during laminar/transition liquid annular flow. The predicted heat transfer coefficients are evaluated and compared with the experimental results using seven data sets over wide ranges of exit quality, channel aspect ratios, and heat and mass fluxes.

2 Analytical Model

2.1 Assumptions. The physical model of the problem is shown schematically in Fig. 1. The following assumptions are made in the analysis:

(1) Annular flow configuration is assumed for the analysis. Annular flow implies that the vapor occupies the central or core region of the channel, while the liquid remains in a thin layer adjacent to the microchannel wall.
(2) The thickness of the liquid film is assumed to be nonuniform all around the circumference of the channel, with a continuous central vapor core.
(3) Rectangular mini- or microchannel is considered with a depth H and width W.
(4) The temperature and velocity gradients are linear across the liquid film.

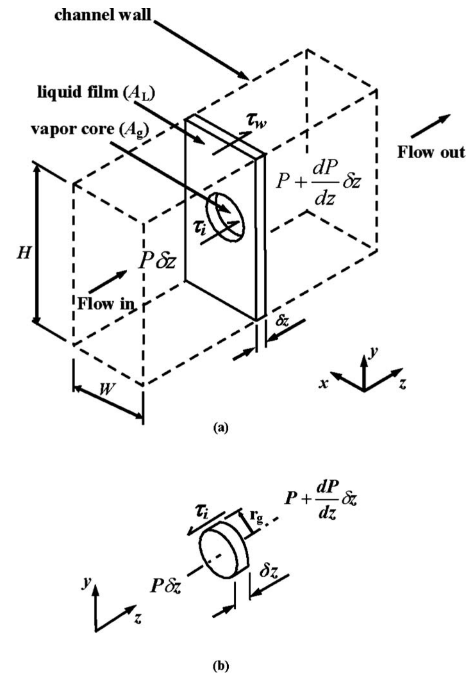

Fig. 1 (*a*) Parameters in the annular flow for force balance on the liquid film; (*b*) control volume analysis of the vapor differential element in the annular flow

(5) The liquid-vapor interface is assumed to be smooth. Hence, the liquid entrainment in the vapor core region can be neglected.
(6) One dimensional, steady, and laminar flows are assumed in the liquid film. The flow in the vapor core may proceed from laminar to turbulent.
(7) The liquid and vapor properties are assumed to be constant at the saturation temperature.
(8) The two phases flow separately in the channel.

2.2 Two-Phase Heat Transfer Coefficient. The governing differential equations for momentum and heat transfer across the liquid film during laminar flow may be expressed as follows:

$$\tau_w = \mu_L \frac{\partial u}{\partial x} \tag{3}$$

and

$$q_w = -k_L \frac{\partial T}{\partial x} \tag{4}$$

The above equations (Eqs. (3) and (4)) are the basic definitions of the wall shear stress and the wall heat flux, respectively, during laminar flow in the liquid film. Following Reynolds' analysis and assuming that the shear stress and heat flux profiles are similar

$$\frac{\tau(x)}{\tau_w} = \frac{q(x)}{q_w} = \mathrm{fun}(x) \tag{5}$$

Substituting Eqs. (3) and (4) into Eq. (5) results in

$$\frac{q_w}{\tau_w} = -\frac{k_L}{\mu_L}\frac{\partial T}{\partial u} = \frac{c_p}{\mathrm{Pr}}\frac{\partial T}{\partial u} \tag{6}$$

where Pr is the Prandlt number. The temperature distribution in the liquid film can be obtained by separating the differentials of variables T and u in Eq. (6) above, and integrating the velocity from 0 to u_L, and the temperature from T_s to T_{sat}

$$\int_0^{u_L} \frac{q_w}{k_L}\,\partial u = -\int_{T_s}^{T_{\text{sat}}} \frac{\tau_w}{\mu_L}\,\partial T \tag{7}$$

Hence the temperature drop across the liquid film may be obtained from Eq. (7) by performing the integration. The result is

$$\frac{q_w u_L}{k_L} = \frac{\tau_w}{\mu_L}(T_s - T_{\text{sat}}) \tag{8}$$

Using the definition of h_{tp}

$$q_w = h_{\text{tp}}(T_s - T_{\text{sat}}) \tag{9}$$

the two-phase heat transfer coefficient can be expressed in an alternative form as follows:

$$h_{\text{tp}} = \frac{q_w}{(T_s - T_{\text{sat}})} = \frac{\tau_w k_L}{u_L \mu_L} = \frac{\tau_w c_p}{u_L\ \text{Pr}} \tag{10}$$

Equation (10) expresses the two-phase heat transfer coefficient in terms of the wall shear stress, liquid velocity, viscosity, and thermal conductivity.

2.3 Mass Conservation.

The equation expressing the mass conservation in the vapor core is

$$A_{\text{ch}} G_g = A_{\text{ch}} G x_e = \rho_g u_g A_g = \rho_g u_g \alpha A_{\text{ch}} \tag{11}$$

where A_g is the vapor core area defined as

$$A_g = \pi r_g^2 \tag{12}$$

and α is the void fraction defined as

$$\alpha = \frac{A_g}{A_{\text{ch}}} = \frac{\pi r_g^2}{WH} \tag{13}$$

The conservation equation for the liquid film is given by

$$A_{\text{ch}} G_L = A_{\text{ch}} G(1 - x_e) = \rho_L u_L A_L = \rho_L u_L (1 - \alpha) A_{\text{ch}} \tag{14}$$

and A_L is the liquid film area defined as

$$A_L = A_{\text{ch}} - A_g \tag{15}$$

2.4 Momentum Conservation

2.4.1 Wall Shear Stress. Applying the principle of conservation of momentum to the differential liquid element δz, as illustrated schematically in Fig. 1(*a*), gives

$$\int_{S_{\text{ch}}} \tau_w \delta z\, dS = \int_{S_i} \tau_i \delta z\, dS_i + \int_{A_L} \left[P - \left(P + \frac{dP}{dz}\delta z \right) \right] dA_L \tag{16}$$

where S_{ch} and S_i are the channel and vapor core peripheries, respectively. The term on the left-hand side represents the wall shear stress. The terms on the right-hand side of the equation correspond to, in order, the interfacial shear stress and pressure gradient in the liquid film. Rearrangement of Eq. (16) yields

$$\tau_w = \left(\frac{S_i}{S_{\text{ch}}}\right)\tau_i - \left(\frac{A_L}{S_{\text{ch}}}\right) \left.\frac{dP}{dz}\right|_L \tag{17}$$

By neglecting the gravitational pressure drop component, the pressure gradient in the liquid film can be expressed in terms of the friction and acceleration-related terms as follows:

$$-\left.\frac{dP}{dz}\right|_L = -\left.\frac{dP}{dz}F\right|_L - \left.\frac{dP}{dz}a\right|_L \tag{18}$$

Substituting Eq. (18) into Eq. (17) yields

$$\tau_w = \left(\frac{S_i}{S_{\text{ch}}}\right)\tau_i - \left(\frac{A_L}{S_{\text{ch}}}\right) \left.\frac{dP}{dz}F\right|_L - \left(\frac{A_L}{S_{\text{ch}}}\right) \left.\frac{dP}{dz}a\right|_L \tag{19}$$

Equation (19) involves the shear stress at the interface, as well as the friction and acceleration induced liquid-phase pressure gradients.

2.4.2 Interfacial Shear Stress. The interfacial shear stress can be obtained by making a force balance on a disk of radius r_g and length δz in the vapor core, as shown in Fig. 1(*b*). This differential element is bounded by the interface and not by the channel wall. Balancing forces gives

$$2\pi r_g \delta z \tau_i = \pi r_g^2 \left[P - \left(P + \left.\frac{dP}{dz}\right|_g \delta z \right) \right] \tag{20}$$

The term on the left-hand side represents the interfacial shear stress, while the term on the right-hand side is the pressure gradient in the vapor core. Ignoring the gravitational and acceleration components, the pressure gradient in the vapor core is represented by the frictional term only. The acceleration term is ignored in the vapor core since the interfacial shear stress often has a value approximately equal to its value in adiabatic flow under the same flow conditions [14]. Equation (20) can be reduced to the following form:

$$\tau_i = -\left(\frac{r_g}{2}\right) \left.\frac{dP}{dz}F\right|_g \tag{21}$$

Substituting Eq. (21) into Eq. (19) gives

$$\tau_w = \left(\frac{-S_i r_g}{2S_{\text{ch}}}\right) \left.\frac{dP}{dz}F\right|_g - \left(\frac{A_L}{S_{\text{ch}}}\right) \left.\frac{dP}{dz}F\right|_L - \left(\frac{A_L}{S}\right) \left.\frac{dP}{dz}a\right|_L \tag{22}$$

Based on the assumption of separated flow, the liquid and gas phase pressure drops are considered equal. When the acceleration and gravitational terms are negligible compared with the frictional term, the frictional pressure drop in the liquid phase must equal the frictional drop in the vapor phase

$$\left.\frac{dP}{dz}F\right|_L = \left.\frac{dP}{dz}F\right|_g \tag{23}$$

Combining Eqs. (23) and (22) gives the following result relating the shear stress to the frictional and acceleration pressure gradients in the liquid film

$$\tau_w = -\left(\frac{S_i r_g + 2A_L}{2S_{\text{ch}}}\right) \left.\frac{dP}{dz}F\right|_L - \left(\frac{A_L}{S_{\text{ch}}}\right) \left.\frac{dP}{dz}a\right|_L \tag{24}$$

2.4.3 Frictional Pressure Gradient. The frictional pressure gradient for the liquid phase can be expressed in terms of the single-phase pressure gradient for the liquid phase considered to flow alone in the channel as follows:

$$-\left.\frac{dP}{dz}F\right|_L = -\left(\frac{dP}{dz}F\right)_f \phi_f^2 \tag{25}$$

where the two-phase frictional multiplier (ϕ_f^2) is then defined as

$$\phi_f^2 = 1 + \frac{C}{X} + \frac{1}{X^2} \tag{26}$$

where C is the two-phase multiplier parameter and X is the Martinelli parameter. The single-phase friction pressure gradient is calculated from the standard equation

$$-\left(\frac{dP}{dz}F\right)_f = \frac{2 f_f G^2 (1 - x_e)^2}{D_h \rho_L} \tag{27}$$

where f_f is friction factor defined as follows:

$$f_f = \frac{f\,\text{Re}_f}{\text{Re}_L} \tag{28}$$

and $f\,\text{Re}_f$ is defined as

$$f\,\mathrm{Re}_f = 24(1 - 1.355\gamma + 1.947\gamma^2 - 1.701\gamma^3 + 0.956\gamma^4 - 0.254\gamma^5) \tag{29}$$

and the superficial Reynolds number of the liquid-phase in the two-phase flow Re_L is defined as

$$\mathrm{Re}_L = \frac{G x_e D_h}{\mu_L} \tag{30}$$

2.4.4 Acceleration Pressure Gradient. The acceleration pressure drop of the separated model is given by [15]

$$\Delta P_a = G^2 \upsilon_L \left[\frac{x_{e,o}^2}{\alpha} \frac{\upsilon_L}{\upsilon_L} + \frac{(1 - x_{e,o})^2}{1 - \alpha} - 1 \right] \tag{31}$$

where α is the void fraction for conventional size tubes defined as [16]

$$\alpha = \frac{1}{1 + \left(\frac{1 - x_{e,o}}{x_{e,o}} \right) \left(\frac{\upsilon_L}{\upsilon_g} \right)^{2/3}} \tag{32}$$

All mini- and microchannel void fraction correlations were developed based on the homogeneous two-phase flow void fraction (volumetric quality). Therefore, all mini- and microchannel void fraction correlations cannot be used to predict the acceleration pressure drop, since they have been developed based on the homogenous model and not the separated model. Based on these considerations, the void fraction model presented by Eq. (32) has been selected to predict *only* the acceleration pressure drop based on the separated model due to the following reasons: (1) Equation (32) is a void fraction model developed specifically for annular flow, which matches with the present model. (2) This annular flow void fraction model, presented in Eq. (32), was also developed assuming no liquid entrainment in the vapor core. Assuming no liquid entrainment is one of the basic assumptions in the present model. Therefore, Eq. (32) has been used to estimate the acceleration pressure drop. The acceleration pressure gradient can be derived by applying the chain rule as follows:

$$\left. \frac{dP}{dz} a \right|_L = \frac{dP}{dx_e} \frac{dx_e}{dz} \tag{33}$$

dP/dx_e may be obtained by differentiating Eq. (31) with respect to x_e, which leads to the following equation:

$$\frac{dP}{dx_e} = G^2 \upsilon_L \left[2x_{e,o} \left(\frac{\upsilon_g}{\upsilon_L} - \left(\frac{\upsilon_g}{\upsilon_L} \right)^{2/3} - \left(\frac{\upsilon_g}{\upsilon_L} \right)^{1/3} + 1 \right) + \left(\left(\frac{\upsilon_g}{\upsilon_L} \right)^{2/3} + \left(\frac{\upsilon_g}{\upsilon_L} \right)^{1/3} - 2 \right) \right] \tag{34}$$

Alternatively, by applying a heat balance on the channel, it may be shown that

$$qA = \dot{m} x_e h_{fg} \tag{35}$$

In mini- and microchannel heat sinks, the heat flux is supplied through three walls only, since the adiabatic fourth wall is used to conduct flow visualization. Hence, the heat transfer area is introduced as

$$A = (2H + W)L \tag{36}$$

Hence, for a linear change in x_e over a length L, dx_e/dz could be given by

$$\frac{dx_e}{dz} = \frac{q(2H + W)}{\dot{m} h_{fg}} \tag{37}$$

and remembering that

$$\dot{m} = GWH \tag{38}$$

dx_e/dz for three-sided heating is expressed as

$$\frac{dx_e}{dz} = \frac{q(2H + W)}{HWGh_{fg}} \tag{39}$$

Similarly, for four-sided heating, dx_e/dz can be defined as

$$\frac{dx_e}{dz} = \frac{2q(H + W)}{G h_{fg} HW} \tag{40}$$

Substituting Eqs. (34) and (39) into Eq. (33) and rearranging, gives

$$\left. \frac{dP}{dz} a \right|_L = \frac{q(2H + W) G \upsilon_L}{HW h_{fg}} \left[2x_{e,o} \left(\frac{\upsilon_g}{\upsilon_L} - \left(\frac{\upsilon_g}{\upsilon_L} \right)^{2/3} - \left(\frac{\upsilon_g}{\upsilon_L} \right)^{1/3} + 1 \right) + \left(\left(\frac{\upsilon_g}{\upsilon_L} \right)^{2/3} + \left(\frac{\upsilon_g}{\upsilon_L} \right)^{1/3} - 2 \right) \right] \tag{41}$$

Substituting Eqs. (25) and (41) into Eq. (24) and rearranging, the resultant equation will give an equation for calculating τ_w, expressed as follows:

$$\tau_w = -\left(\frac{A_{\mathrm{ch}}}{S_{\mathrm{ch}}} \right) \left(\frac{dP}{dz} F \right)_f \phi_f^2 - (1 - \alpha) \left(\frac{A_{\mathrm{ch}}}{S_{\mathrm{ch}}} \right) \left. \frac{dP}{dz} a \right|_L \tag{42}$$

Combining Eq. (42) into Eq. (10), the analytical solution of the two-phase heat transfer coefficient for three-sided heating can be expressed as follows:

$$h_{\mathrm{tp}} = \frac{k_L (1 - \alpha) A_{\mathrm{ch}}}{\mu_L (1 - x_{e,o}) S_{\mathrm{ch}}} \left[\frac{2\phi_f^2 f_f G (1 - x_{e,o})^2}{D_h} - \frac{(1 - \alpha) q (2/\gamma + 1)}{H h_{fg}} \left(-2x_{e,o} \left(-\frac{\upsilon_g}{\upsilon_L} + 1 + \varepsilon \right) + \varepsilon \right) \right] \tag{43}$$

A similar equation may be derived for four-sided heating; the result is

$$h_{\mathrm{tp}} = \frac{k_L (1 - \alpha)}{\mu_L (1 - x_{e,o})} \left[\frac{2A_{\mathrm{ch}} \phi_f^2 f_f G (1 - x_{e,o})^2}{S_{\mathrm{ch}} D_h} - \frac{(1 - \alpha) q}{h_{fg}} \left(-2x_{e,o} \left(-\frac{\upsilon_g}{\upsilon_L} + 1 + \varepsilon \right) + \varepsilon \right) \right] \tag{44}$$

where ε is defined as

$$\varepsilon = \left(\frac{\upsilon_g}{\upsilon_L} \right)^{2/3} + \left(\frac{\upsilon_g}{\upsilon_L} \right)^{1/3} - 2 \tag{45}$$

3 Results and Discussion

3.1 Data Analysis. The presented model has been validated using experimental data sets published in the literature of seven different refrigerants from different researchers with a total of 292 data points suitable for the scope of this study. Table 1 describes the range of the experimental conditions for all the data sets used to validate the proposed model. Experiments for the selected data are carried out in rectangular mini- and microchannels with heat fluxes ranging from 5 $\mathrm{kW/m^2}$ to 461 $\mathrm{kW/m^2}$, mass fluxes ranging from 208 $\mathrm{kg/m^2\,s}$ to 988 $\mathrm{kg/m^2\,s}$, vapor quality ranging from 0.1 to 0.85, and hydraulic diameters in the range of 92–1440 μm. It should be noted that the experimental data exhibiting the characteristics of partial dryout are omitted from the comparisons as they are unrepresentative of annular flow. The refrigerant's thermophysical properties were taken from the NIST refrigerant database [17].

A flow regime map should be consulted to ensure that annular flow has been achieved for a given set of operating parameters. While many researchers have reported microchannel flow regime maps, most are adiabatically based. One notable exception is the work of Revellin and Thome [18]. Their map is developed by measuring flow pattern data and bubble frequency of diabatic R134a and R245fa flows in 0.509 mm and 0.79 mm diameter glass channels using two laser beams. The flow pattern map indi-

Table 1 Description of data obtained for annular flow boiling heat transfer in mini- and microchannels and comparison of the model with each data set

Reference	Fluid	D_h (μm)	G (kg/m^2 s)	$x_{e,o}$	No. of data points	MAE (%)	AE (%)
Megahed et al. [6]	FC-72	248	334–531	0.23–0.39	14	14	8.5
Yun et al. [3]	R410A	1360–1440	300–400	0.29–0.69	15	11	3.5
Dong et al. [5]	R141b	92	500–900	0.15–0.77	55	7.0	3.6
Yen et al. [7]	R123	214	400–800	0.16–0.68	16	11.9	0.45
Lee and Lee [2]	R113	783	208	0.21–0.68	25	5.7	−5.1
Bertsch et al. [26]	R134a	540	250	0.39–0.85	9	26.2	−26.2
Agostini et al. [25]	R236fa	336	413–988	0.1–0.57	159	10	−2
Total	Seven different refrigerants	92–1440	208–988	0.1–0.85	292	10	−1

cated that flow regimes observed at low mass flux are primarily annular and include slug and bubbly-slug regimes. The Revellin and Thome map is shown in Fig. 2. The solid line indicates the transition line of the experimental data from slug to annular flow. The dotted lines indicate model prediction's uncertainty (±20%). All the data within the annular regime in addition to the data within +20% transition regimes are selected to test the analytical model. The experimental data of Lee and Lee [2] have been tested on the flow map of Revellin and Thome. The flow map demonstrates that most of these data are identified to be in the bubbly coalescing regime, as presented in Fig. 2. This is because the aspect ratios of the test sections of Lee and Lee were low enough, with $\gamma=0.02$, to suppress the annular flow. However, Lee and Lee reported that the predominant flow pattern observed in all their tests was annular for a quality range of 0.15–0.75; thus, their experimental data set may be appropriate for this study. Ali et al. [19] reported the same type of flow regime for their specific test conducted through a narrow passage.

Figures 3(*a*) and 3(*b*) show the superficial liquid and vapor Reynolds range of available data as a function of the exit quality, respectively. The liquid-phase Reynolds number varies from 28 to 2640 and decreases as the exit quality increases. The superficial vapor core Reynolds number spans the laminar, transition, and turbulent ranges, and increases with increasing exit quality, as shown in Fig. 3(*b*).

The transition criteria where the liquid phase is characterized as being in the laminar or turbulent flow regime have to be indicated in the present study. Lockhart and Martinelli [15] proposed that the transition from laminar to turbulent flows occurs at a superficial Reynolds number of about 1000–2000. However, Kandlikar and Campbell [20] stated that the transition from laminar to turbulent flow begins at Reynolds numbers of approximately 1900 for the total flow, assumed to flow as liquid. In their work, the laminar-to-turbulent flow transition was reported to occur over a range of Reynolds numbers between 1900 and 3500. Analyses of the present data, over a range of $122 < \mathrm{Re}_{\mathrm{Lo}} < 3700$, are presented using the laminar and transition characterizations for the liquid-phase Reynolds number based on the criteria defined by Kandlikar and Campbell.

Void fraction and two-phase frictional multiplier correlations are needed for the current model. Three different void fraction correlations are presented in Table 2. These are the only correlations that have been found in the literature that could be used in mini- and microchannels. The correlation of Xiong and Chung [21] was developed from nitrogen and water data inside rectangular channels in addition to the data of Kawahara et al. [22] from ethanol-water/nitrogen gas mixtures inside a microtube. The aforementioned void fraction correlations for small channels are

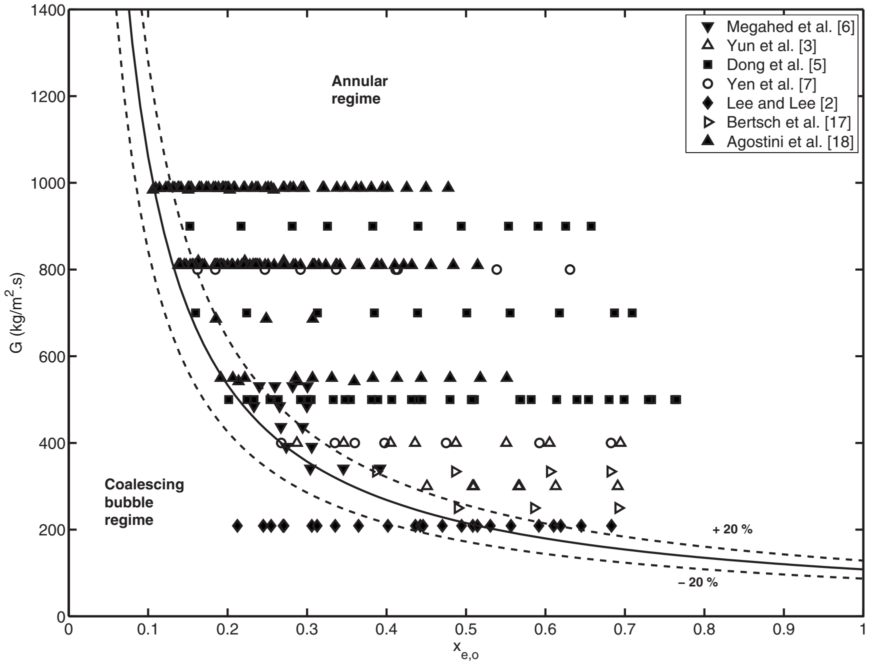

Fig. 2 Revellin and Thome [20] flow regime map for diabatic two-phase flow in microchannels

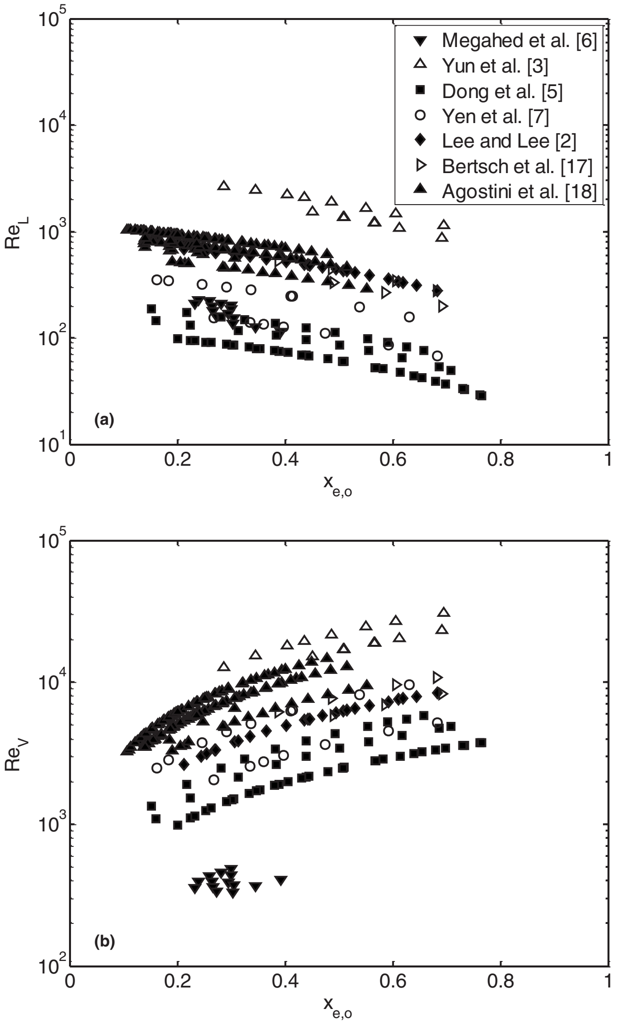

Fig. 3 (*a*) **Liquid-phase Reynolds number as a function of the exit quality** (*b*) **vapor-phase Reynolds number as a function of the exit quality**

based on channel's diameter and flow volumetric quality only. Caution should therefore be exercised before applying them to a different fluid. Table 2 lists these correlations along with their applicability to the tested refrigerants. The two-phase frictional multiplier is influenced by the choice of the two-phase multiplier parameter (C). The value of the two-phase multiplier parameter, depending on whether each phase is in turbulent or laminar flow conditions, has to be estimated for various flow combinations. Lee and Mudawar [23] and Lee and Garimella [24] provided correlations for the two-phase multiplier parameter in mini- and microchannels. In the laminar-liquid turbulent-vapor flow regime, the correlation of Lee and Mudawar is recommended. The correlation of Lee and Garimella can be used over a range covering laminar-liquid laminar-vapor regime and also the transition from laminar to turbulent-vapor regime. Uncertainties in the two-phase heat transfer coefficient predictions from the present model may have the following three sources: (1) the transition between the coalescing bubble and the annular flow regimes, (2) estimation of refrigerant physical and thermodynamic properties at the outlet of the test section, and (3) actual dimensions of the channel. The mean absolute error (MAE) and average error (AE) were set as the criterions to determine the effectiveness of the heat transfer model. MAE and AE were defined as:

$$MAE = \frac{1}{N}\sum_{1}^{N}\left|\frac{\text{experimental data} - \text{predicted data}}{\text{experimental data}}\right| \times 100 \tag{46}$$

and

$$AE = \frac{1}{N}\sum_{1}^{N}\frac{(\text{experimental data} - \text{predicted data})}{\text{experimental data}} \times 100 \tag{47}$$

where N is the total number of data points.

3.2 Model Validation. The validity of the analytical model was assessed by comparing the predicted data of the heat transfer coefficients versus experimental results obtained from the literature, as shown in Fig. 4. Very good agreement between the experimental results and the predicted values is observed. It is found that the experimental two-phase heat transfer coefficients could be predicted by the model with a MAE of 10%.

The model successfully predicts the experimental data set of Lee and Lee [2] and Dong et al. [5] and with a MAE of 5.7% and 7%, respectively. The heat transfer coefficient in the latter data set has a maximum uncertainty of 3.2%. The data of Agostini et al. [25] are also well predicted by this model, as shown in Fig. 6 with a MAE of 10%. The model overpredicts the FC-72 data sets from Megahed et al. [6] by 14%. The experimental data points of Bertsch et al. [26] have the maximum deviation and are underpredicted by the model by 26%. The detailed results of this comparison are summarized in Table 1.

The conditions of the test by Megahed et al. [6] obtained at q

Table 2 Void fraction correlations for mini- and microchannels

Authors	Channel size (μm)	Void fraction correlation	Refrigerants
Ali et al. [21]	Minichannels $D_h=1000$	$\alpha=0.8\beta$	R113, R410A
Xiong and Chung [23]	Microchannels $D_h=209$, 412, and 622	$\alpha=\frac{c\beta^{0.5}}{1-(1-C)\beta^{0.5}}$ $c=\frac{0.266}{1+13.8\times 10^{-6.88D_h}}$ where the unit of D_h is in mm	FC-72, R123, and R141b
Kawahara et al. [24]	Microchannels $D=100$	$\alpha=\frac{C_1\beta^{0.5}}{1-C_2\beta^{0.5}}$ $C_1=0.03$, and $C_2=0.97$	R123, R141b, R134, and R236fa

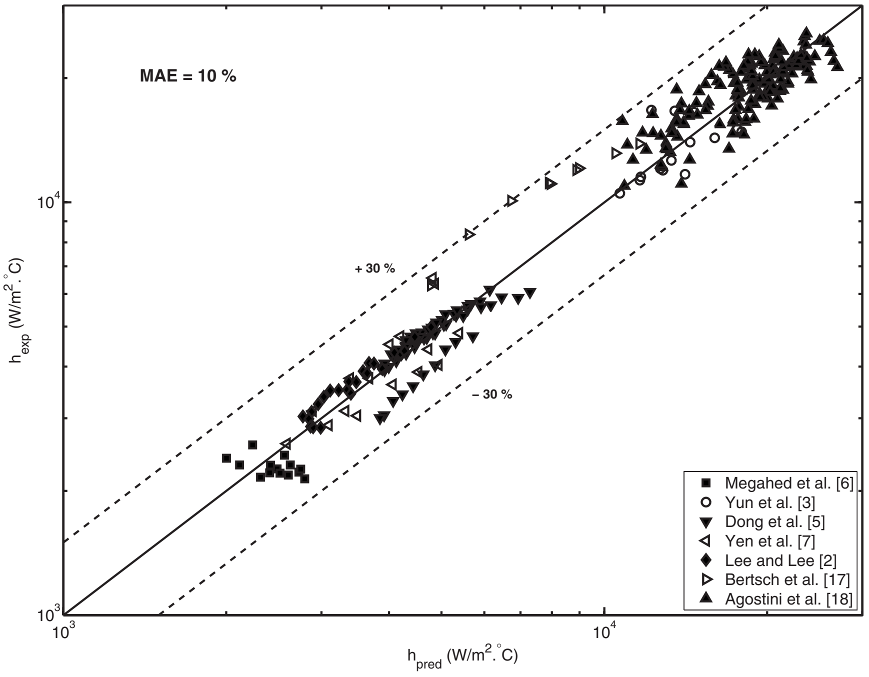

Fig. 4 Predicted and experimentally determined two-phase heat transfer coefficients

$=25\ \text{kW/m}^2$ and $G=391\ \text{kg/m}^2\ \text{s}$ using FC-72 are very similar to those of the test by Yen et al. [7] carried out at $q=25.3\ \text{kW/m}^2$ and $G=400\ \text{kg/m}^2\ \text{s}$ using R123. For higher values of exit quality ($x_{e,o}>0.2$), the experimental values of the two-phase heat transfer coefficient are almost equal. The agreement in heat transfer coefficients, for $x_{e,o}>0.2$, can be attributed to the difference in the vapor density and latent heat of vaporization. Comparing the thermophysical properties of FC-72 and R123 at atmospheric conditions, it is observed that the two refrigerants have almost the same parameter values for liquid density, viscosity, thermal conductivity, and vapor viscosity. However, FC-72 has a vapor density and liquid thermal conductivity about two times higher than that of R123 at the same saturation pressure. The two-phase heat transfer coefficient is inversely proportional to the vapor density and latent heat of vaporization, as shown in Eq. (43). It is also noted that R123 has a latent heat of vaporization about two orders of magnitudes higher than that of FC-72 at atmospheric conditions. These physical properties can explain the qualitative agreement in the experimental results.

The effectiveness of the presented analytical model to correctly predict the two-phase heat transfer coefficient trend in rectangular mini- and microchannels is assessed through comparison with the experimental results. Results obtained using the proposed model are compared with the experimental results obtained by Lee and Lee [2] and Yun et al. [3], as shown in Fig. 5. The tests conducted by Lee and Lee and Yun et al. were carried out in minichannels at a higher hydraulic diameter and relatively low heat and mass fluxes, as was presented in Table 1. The predicted results are well correlated with experimental values, and show that as the exit quality increases, the heat transfer coefficient increases. On the other hand, a completely different behavior for the heat transfer coefficient is observed in the data of Dong et al. [5] and Yen et al. [7], as shown in Fig. 6. These data present a smooth and constant decreasing heat transfer coefficient with increasing vapor quality. Nevertheless, the present model predicts the appropriate trend of the heat transfer coefficient with exit quality increase. Recently, Agostini et al. [25] reported that the two-phase heat transfer coefficients remain almost constant for the boiling region up to an exit quality of about 0.3. Figure 7 presents the two-phase heat transfer coefficient experimental data obtained by Agostini et al.

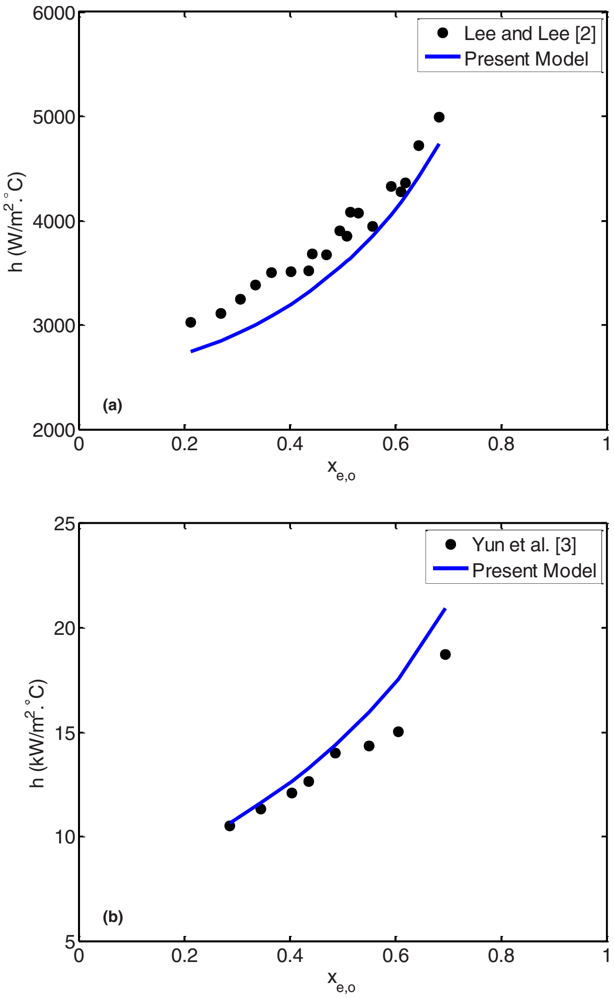

Fig. 5 Comparison of heat transfer coefficient at constant mass flux: (*a*) Lee and Lee [2] (R113, $G=208\ \text{kg/m}^2\ \text{s}$, and $q=5\ \text{kW/m}^2$); (*b*) Yun et al. [3] (R410A, $G=400\ \text{kg/m}^2\ \text{s}$, and $q=20\ \text{kW/m}^2$)

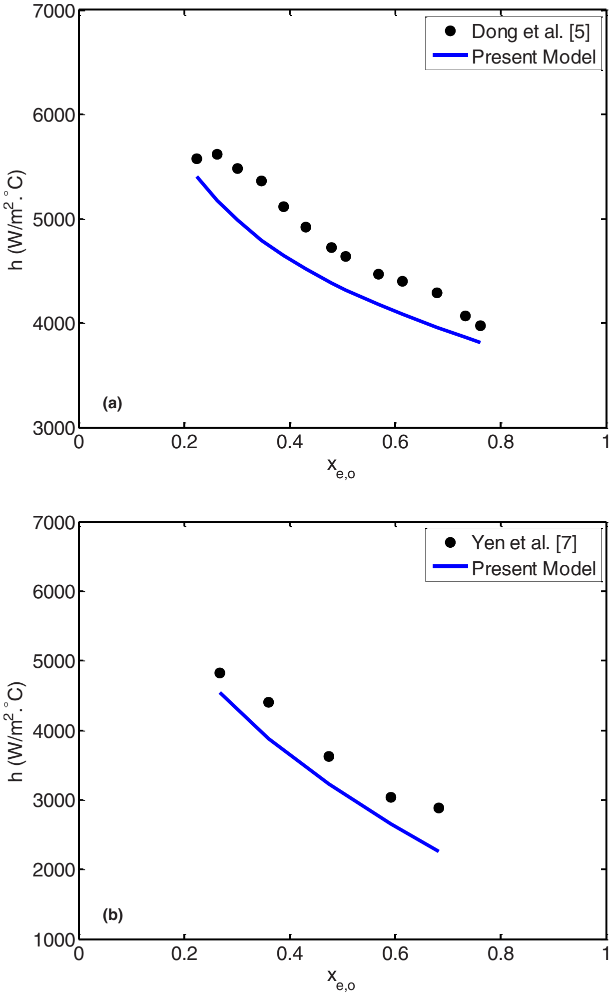

Fig. 6 Heat transfer coefficient predictions by the analytical model compared with (*a*) Dong et al. [5] (R141b, $G=500$ kg/m^2 s, and $q=100$ kW/m^2) and (*b*) Yen et al. [7] (R123, $G=400$ kg/m^2 s, and $q=25.32$ kW/m^2)

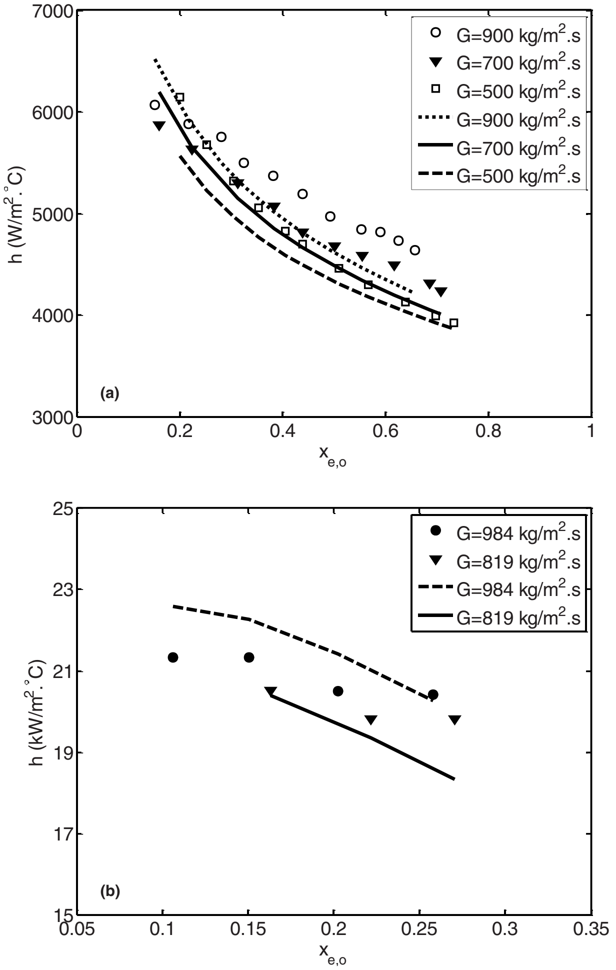

Fig. 8 The effect of mass flux on the experimental and predicted heat transfer coefficient: experimental data of (*a*) Dong et al. [5] ($q=100$ kW/m^2) and (*b*) Agostini et al. [18] ($q=236$ kW/m^2)

and those predicted by the proposed model. It is clear that the current model also follows the correct trend of the experimental data for the two-phase heat transfer coefficient.

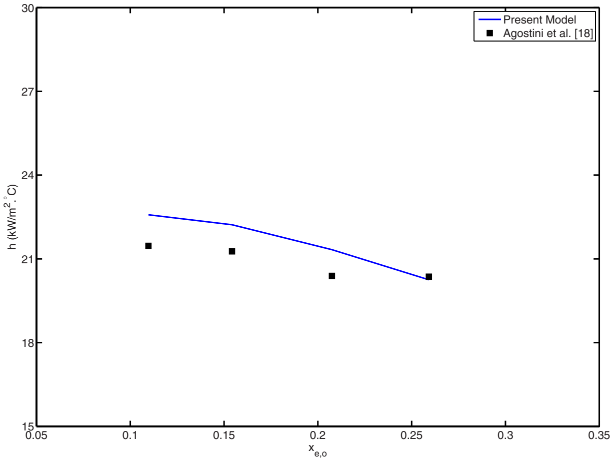

Fig. 7 Two-phase heat transfer coefficient as a function of the exit quality predicted by the analytical model compared with the data of Agostini et al. [18] (R236fa and $G=984$ kg/m^2 s)

In comparison with published experimental data sets, the model is shown to predict well the experimental data of Yun et al. [3] and Yen et al. [7] using refrigerants R410A and R123 in mini- and microchannels with hydraulic diameters of 1440 μm and 214 μm, respectively. Figures 5(*b*) and 6(*b*) show the heat transfer coefficient as a function of the exit quality for the same mass flux and comparable heat flux. In the R410A data of Yun et al. (Fig. 5(*b*)), the heat transfer coefficient is shown to increase with increasing exit quality. On the other hand, experimental results of Yen et al. show a contrary trend of heat transfer coefficient. It was found to decrease with increasing exit quality, as presented in Fig. 6(*b*). For the two data sets presented in Figs. 7(*b*) and 8(*b*), the mass flux was held constant at $G=400$ kg/m^2 s, and the heat flux was maintained at $q=20$ and 25.32 kW/m^2, respectively. Therefore, they have been selected to explain the different trends of flow boiling heat transfer coefficient in mini- and microchannels. Equation (43) can be simplified to provide a form that is suitable to carefully examine the contribution of each term to the estimated heat transfer coefficient as

$$h_{tp} = f_1(f_2 - f_3) \tag{48}$$

where

$$f_1 = \frac{k_L A_{ch}(1-\alpha)}{\mu_L S_{ch}(1-x_{e,o})} \tag{49}$$

and

$$\mathrm{f}_2 = \frac{2\phi_f^2 f_L G(1 - x_{e,o})^2}{D_h} \tag{50}$$

and

$$\mathrm{f}_3 = \frac{(1 - \alpha)q(2/\gamma + 1)}{h_{fg}}\left(- 2x_{e,o}\left(- \frac{v_g}{v_L} + 1 + \varepsilon\right) + \varepsilon\right) \tag{51}$$

The first term f_1 represents the effect of the void fraction. The second and third terms f_2 and f_3 account for the effect of the frictional and acceleration pressure gradients, respectively. For the test results of Yen et al. [7], the contribution of the f_2 term increases asymptotically with the exit quality. Meanwhile, the contribution of the f_3 term increases linearly with increasing of the exit quality. Based on the ratio of $\mathrm{f}_2/\mathrm{f}_3$, the acceleration component f_3 cannot be neglected as compared with the frictional component f_2. Another important aspect in explaining the experimental heat transfer coefficients in the data of Yen et al. is the change in the void fraction with respect to exit quality (f_1 term). The ratio of $(1-\alpha)/(1-x_{e,o})$ was found to decrease steeply with the increase in quality. Hence, the sum of the contributions of the abovementioned terms explains the decreasing trend of the experimental heat transfer coefficient. The frictional pressure gradient (f_2 term) is found to be relatively independent of the vapor quality in the experimental data of Yun et al. [3]. However, it dominates the pressure gradient where the effect of acceleration pressure gradient (f_3 term) could be ignored compared with f_2. However, contrary to microchannel behavior, the ratio of $(1-\alpha)/(1-x_{e,o})$ is shown to increase with increasing exit quality. As a result, the contribution of the void fraction term f_1 attributes to increase the estimated heat transfer coefficient with increasing of the exit quality.

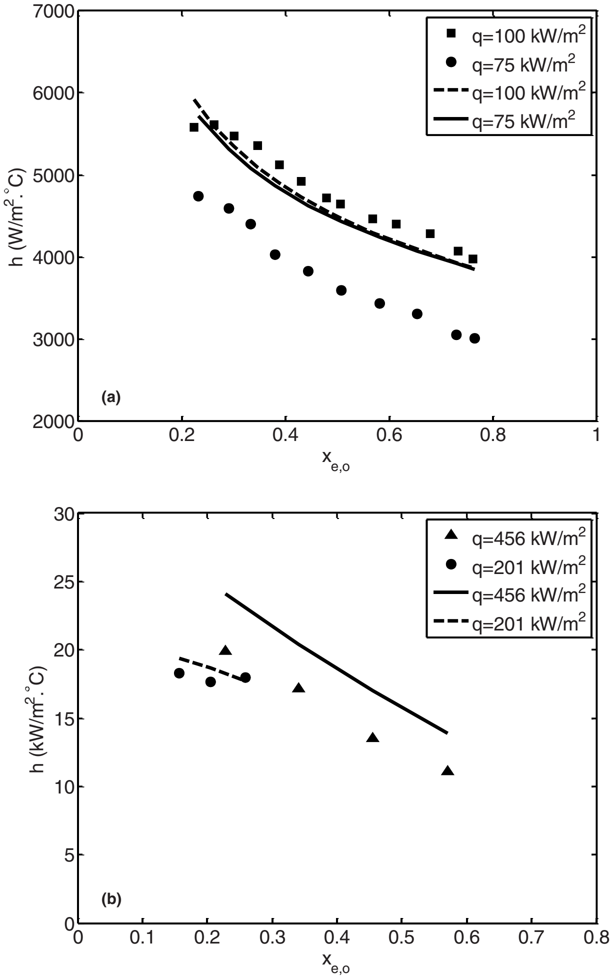

Fig. 9 Predicted influence of heat flux on two-phase heat transfer coefficient as a function of the exit quality, compared with experimental data of (*a*) Dong et al. [5] for the variation in the heat flux for *G*=500 kg/m^2 s, and (*b*) Agonstini et al. [18] (*G*=810 kg/m^2 s)

The effect of mass flux on the predicted results for the heat transfer coefficient is examined using the experimental results presented by Dong et al. [5]. Figure 8(*a*) presents the measured values along with the predicted values as a function of the exit quality at a constant heat flux of 100 kW/m^2 and a mass flux, which varies from 500 kg/m^2 s to 900 kg/m^2 s. The model is in excellent agreement with the experimental results and is sensitive to the change in mass flux. Another comparison with the model predictions for local heat transfer coefficient versus vapor quality for various mass fluxes is depicted in Fig. 8(*b*) for the data of Agostini et al. [25]. This figure is also included to demonstrate the effect of mass flux on the prediction. The model prediction is highly sensitive to the change in mass flux, as shown in the figure.

The predicted two-phase heat transfer coefficient as a function of the exit quality are compared with those obtained from the experiment of Dong et al. [5] at a constant mass flux of 900 kg/m^2 s and a heat flux which varies from 75 kW/m^2 to 100 kW/m^2, as shown in Fig. 9(*a*). While the data obtained by Dong et al. showed that the heat flux significantly influences the heat transfer coefficient over the range of exit quality investigated in their study, the predicted results do not correspond to the experimental results and are not well predicted by the model. The data are overpredicted at low heat flux and underpredicted as the heat flux increases. On the other hand, the model predictions show very good agreement with the experimental data presented by Agostini et al. [25] at a constant mass flux of 810 kg/m^2 s and different heat fluxes, varying from 201 kW/m^2 to 456 kW/m^2, as shown in Fig. 9(*b*). The heat transfer coefficient increases at first as the heat flux increases, and then decreases sharply as the exit quality increases for a constant heat and mass fluxes. The ability of the model to map the correct trends of the heat transfer coefficient with changing the heat flux can be clearly seen.

In order to demonstrate the dependence of the model predictions on the saturation temperature, the predicted results from the model are combined with the experimental results of Agostini et al. [25], as presented in Fig. 10. It should be noted that varying the saturation temperature over the range 14–19°C can result in changes in the heat transfer coefficient of 40%, as shown in the figure. Nonetheless, the model provides very good agreement for the experimental data over the examined range of saturation tem-

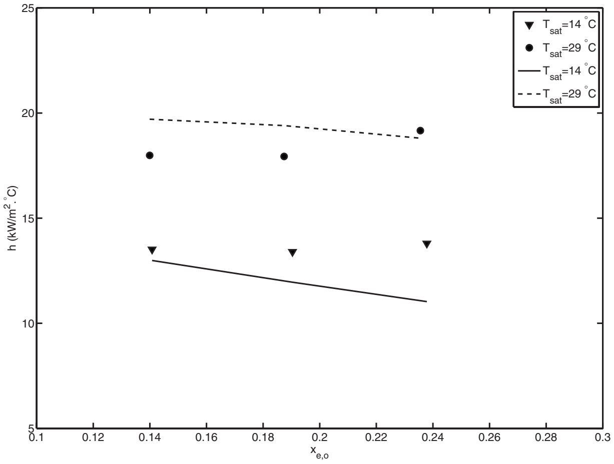

Fig. 10 Effect of the saturation temperature on the two-phase heat transfer coefficient: experimental data of Agostini et al. [18] (*G*=810 kg/m^2 s and *q*=18.6 kW/m^2)

peratures, and the influence of saturation temperature changes on the predicted heat transfer coefficient is found to be consistent with the experimental results.

3.3 Model Limitations. A comparison between the predictions of the model and experimental data for water and refrigerant R245 showed an underprediction of the heat transfer coefficient. The underprediction is due mainly to the fact that the void fraction correlations proposed by Xoing and Chung [20] and Kawahara et al. [21] significantly overpredict all the tested data for these two fluids. The overpredicted values of the void fraction mean that dry out took place in the channel and annular flow does not exist. At low liquid superficial velocities, if the gas superficial velocity is high enough, the annular flow pattern is formed. Consequently, a low liquid superficial velocity gives a higher volumetric quality that leads to a void fraction close to unity even at moderate values of exit quality. As a result, overpredicted values of void fraction result in highly underpredicted values of the heat transfer coefficient, as suggested by Eq. (43), which affects the model applicability. These results suggest the need for further development of void fraction correlations in microchannels and to consider refrigerant physical properties in future correlations, which would result in extending the applicability of the present model to include many refrigerants. In addition, the present model has been limited to annular laminar/transition liquid-phase flow in rectangular mini- and microchannels.

4 Conclusions

An analytical model has been developed to predict the flow boiling heat transfer coefficient in the annular flow regime in rectangular mini- and microchannels. The model provides a convenient and effective method for calculating the two-phase heat transfer coefficient based on the void fraction, frictional multiplier, two-phase flow thermophysical properties, and flow conditions. Predictions from the analytical model show excellent agreement with experimental data published in the open literature. For flow boiling in mini- and microchannels with uniform heat fluxes over the examined range of aspect ratios, and heat and mass fluxes, the agreement between the experimental and analytical results is within 10%. The model predicted the correct trends of the heat transfer coefficient variation with exit quality increases. This model proved to have a very good adaptability in predicting the flow boiling heat transfer coefficient during annular flow for different mass fluxes, heat fluxes, and saturation temperatures. It can be also used for predicting the heat transfer coefficient during annular flow boiling in narrow mini- and microchannels with very low aspect ratios.

Nomenclature

A = area (m^2)
C = two-phase multiplier parameter
c_p = specific heat (J/kg °C)
D_h = hydraulic diameter (m)
f = friction factor
fun = function
h_{fg} = latent heat of vaporization (J/kg)
G = mass flux (kg/m^2 s)
g = gravity constant (m/s^2)
H = channel height (m)
h = convective heat transfer coefficient (W/m^2 °C)
k = thermal conductivity (W/m °C)
L = channel length (m)
$\dot{m}$ = mass flow rate (kg/s)
N = total number of data points
P = pressure (Pa)
Pr = Prandlt number
q = heat flux (W/m^2)
Re = Reynolds number
r = radius (m)
S = periphery (m)
T = temperature (°C)
u = velocity (m/s)
W = channel width (m)
We = Weber number
X = Martinelli parameter
x = x-coordinate
x_e = vapor quality
y = y-coordinate
z = z-coordinate

Greek

α = void fraction for mini- and microchannels
β = volumetric quality
γ = channel aspect ratio
δ = thickness (m)
ε = parameter (Eq. (44))
μ = micro
μ = dynamic viscosity (N s/m^2)
v = specific volume (m^3/kg)
ρ = density (kg/m^3)
σ = surface tension (N/m)
τ = shear stress (N/m^2)
ϕ_f^2 = two-phase frictional multiplier

Gradients

dP/dz = pressure gradient (Pa/m)
$(dP/dz)F$ = frictional pressure gradient (Pa/m)
$(dP/dz)a$ = acceleration pressure gradient (Pa/m)

Subscripts

a = acceleration
ch = channel
g = vapor
i = interfacial
L = liquid
Lo = assuming total flow to be liquid
f = liquid alone flow
o = exit
s = surface
sat = saturation
tp = two-phase
vt = laminar-turbulent
vv = laminar-laminar
w = wall

Acronyms

NIST = National Institute of Standards and Technology

References

[1] Hassan, I., 2006, "Thermal-Fluid MEMS Devices: A Decade of Progress and Challenges Ahead," ASME J. Heat Transfer, **128**(11), pp. 1221–1233.
[2] Lee, H. J., and Lee, S. Y., 2001, "Heat Transfer Correlation for Boiling Flows in Small Rectangular Horizontal Channels With Low Aspect Ratios," Int. J. Multiphase Flow, **27**(12), pp. 2043–2062.
[3] Yun, R., Heo, J. H., and Kim, Y., 2006, "Evaporative Heat Transfer and Pressure Drop of R410A in Microchannels," Int. J. Refrig., **29**(1), pp. 92–100.
[4] Kuznetsov, V. V., and Shamirzaev, A. S., 2007, "Boiling Heat Transfer for Freon R21 in Rectangular Minichannel," Heat Transfer Eng., **28**(8–9), pp. 738–745.
[5] Dong, T., Yang, Z., Bi, Q., and Zhang, Y., 2008, "Freon R141b Flow Boiling in Silicon Microchannel Heat Sinks: Experimental Investigation," Heat Mass Transfer, **44**(3), pp. 315–324.
[6] Megahed, A., Hassan, I., and Ahmed, T., 2008, "Flow Boiling Heat Transfer in a Silicon Microchannel Heat Sink Using Liquid Crystal Thermography," *Proceedings of the Sixth International ASME Conference on Nanochannels, Microchannels and Minichannels (ICNMM2008)*, Darmstadt, Germany, Jun. 23–25.
[7] Yen, T.-H., Shoji, M., Takemura, F., Suzuki, Y., and Kasagi, N., 2006, "Visualization of Convective Boiling Heat Transfer in Single Microchannels With Different Shaped Cross-Sections," Int. J. Heat Mass Transfer, **49**(21–22), pp. 3884–3894.

[8] Bertsch, S. S., Groll, E. A., and Garimella, S. V., 2008, "Review and Comparative Analysis of Studies on Saturated Flow Boiling in Small Channels," Nanoscale Microscale Thermophys. Eng., **12**(3), pp. 187–227.

[9] Fossa, M., 1995, "A Simple Model to Evaluate Direct Contact Heat Transfer and Flow Characteristics in Annular Two-Phase Flow," Int. J. Heat Fluid Flow, **16**(4), pp. 272–279.

[10] Turner, R. G., Hubbard, M. G., and Dukler, A. E., 1969, "Analysis and Prediction of Minimum Flow Rate for the Continuous Removal of Liquid From Gas Wells," J. Pet. Technol., **21**(11), pp. 1475–1482.

[11] Fu, F., and Klausner, J., 1997, "Separated Flow Model for Predicting Two-Phase Pressure Drop and Evaporative Heat Transfer for Vertical Annular Flow," Int. J. Heat Fluid Flow, **18**(6), pp. 541–549.

[12] Qu, W., and Mudawar, I., 2003, "Flow Boiling Heat Transfer in Two-Phase Micro-Channel Heat Sinks—II. Annular Two-Phase Flow Model," Int. J. Heat Mass Transfer, **46**(15), pp. 2773–2784.

[13] Taitel, Y., and Dukler, A. E., 1976, "A Model for Predicting Flow Regime Transitions in Horizontal and Near Horizontal Gas-Liquid Flow," AIChE J., **22**, pp. 47–55.

[14] Hewitt, G. F., and Hall-Taylor, N. S., 1970, *Annular Two-Phase Flow*, Pergamon, New York.

[15] Lockhart, R. W., and Martinelli, R. C., 1949, "Proposed Correlation of Data for Isothermal Two-Phase, Two-Component Flow in Pipes," Chem. Eng. Prog., **45**, pp. 39–48.

[16] Zivi, S. M., 1964, "Estimation of Steady-State Stem Void-Fraction by Means of the Principle of Minimum Entropy Production," ASME J. Heat Transfer, **86**, pp. 247–252.

[17] The National Institute of Standards and Technology (NIST), website: http://webbook.nist.gov/

[18] Revellin, R., and Thome, J. R., 2007, "A New Type of Diabatic Flow Pattern Map for Boiling Heat Transfer in Microchannels," J. Micromech. Microeng., **17**(4), pp. 788–796.

[19] Ali, M. I., Sadatomi, M., and Kawaji, M., 1993, "Adiabatic Two-Phase Flow in Narrow Channels Between Two Flat Plates," Can. J. Chem. Eng., **71**(5), pp. 657–666.

[20] Kandlikar, S. G., and Campbell, L., 2004, "Effect of Entrance Condition on Frictional Losses and Transition to Turbulence," *Proceedings of the Second International Conference on Microchannels and Minichannels (ICMM2004)*, pp. 229–235.

[21] Xiong, R., and Chung, J. N., 2007, "An Experimental Study of the Size Effect on Adiabatic Gas-Liquid Two-Phase Flow Patterns and Void Fraction in Microchannels," Phys. Fluids, **19**(3), p. 033301.

[22] Kawahara, A., Sadatomi, M., Okayama, K., Kawaji, M., and Chung, P. M.-Y., 2005, "Effects of Channel Diameter and Liquid Properties on Void Fraction in Adiabatic Two-Phase Flow Through Microchannels," Heat Transfer Eng., **26**(3), pp. 13–19.

[23] Lee, J., and Mudawar, I., 2005, "Two-Phase Flow in High-Heat-Flux Micro-Channel Heat Sink for Refrigeration Cooling Applications: Part I—Pressure Drop Characteristics," Int. J. Heat Mass Transfer, **48**(5), pp. 928–940.

[24] Lee, P. S., and Garimella, S. V., 2008, "Saturated Flow Boiling Heat Transfer and Pressure Drop in Silicon Microchannel Arrays," Int. J. Heat Mass Transfer, **51**(3–4), pp. 789–806.

[25] Agostini, B., Thome, J. R., Fabbri, M., Michel, B., Calmi, D., and Kloter, U., 2008, "High Heat Flux Flow Boiling in Silicon Multi-Microchannels—Part I: Heat Transfer Characteristics of Refrigerant R236fa," Int. J. Heat Mass Transfer, **51**(21–22), pp. 5400–5414.

[26] Bertsch, S. S., Groll, E. A., and Garimella, S. V., 2008, "Refrigerant Flow Boiling Heat Transfer in Parallel Microchannels as a Function of Local Vapor Quality," Int. J. Heat Mass Transfer, **51**(19–20), pp. 4775–4787.

Experimental Investigation of Single-Phase Microjet Array Heat Transfer

Eric A. Browne

Gregory J. Michna

Michael K. Jensen

Yoav Peles

Department of Mechanical, Aerospace, and
Nuclear Engineering,
Rensselaer Polytechnic Institute,
Troy, NY 12180

The heat transfer performance of two microjet arrays was investigated using degassed deionized water and air. The inline jet arrays had diameters of 54 μm and 112 μm, a spacing of 250 μm, a standoff of 200 μm ($S/d=2.2$ and 4.6, $H/d=1.8$ and 3.7), and jet-to-heater area ratios from 0.036 to 0.16. Average heat transfer coefficients with deionized water were obtained for $150 \leq Re_d \leq 3300$ and ranged from 80,000 W/m^2 K to 414,000 W/m^2 K. A heat flux of 1110 W/cm^2 was attained with 23°C inlet water and an average surface temperature of 50°C. The Reynolds number range for the same arrays with air was $300 \leq Re_d \leq 4900$ with average heat transfer coefficients of 2500 W/m^2 K to 15,000 W/m^2 K. The effect of the Mach number on the area-averaged Nusselt number was found to be negligible. The data were compared with available correlations for submerged jet array heat transfer. [DOI: 10.1115/1.4000888]

Keywords: electronics cooling, microscale jet heat transfer, microjet, microjet array

1 Introduction

Heat dissipation in processors and power electronics is a major concern for reliability and may become a limiting factor as transistor densities rise. If heat dissipation rates in new devices continue to increase, air cooling of heat sinks and conventional forced convection with air will not be adequate. Higher heat transfer coefficients attainable using liquids will be necessary, as cooling approaches will be different from those currently used.

Fluid jet impingement has been used, for example, for quenching metals and drying paper or textiles and demonstrates good heat transfer performance. Reviews of jet array impingement heat transfer for a variety of conditions were conducted by Martin [1], Viskanta [2] and Webb and Ma [3]. Fluid jets can be arranged into patterns to form jet arrays. However, the term "jet array" is vague as arrays of jets vary greatly. Specificity is required when describing the conditions of jet array impingement. A dimensional analysis of the relevant parameters affecting heat transfer in jet arrays suggests

$$\overline{\mathrm{Nu}}_d = f(\mathrm{Re}_d, \mathrm{Pr}, A_r, H/d, L/S) \tag{1}$$

for a given jet impingement category, where $\overline{\mathrm{Nu}}_d$ is the area average Nusselt number based on jet diameter, Re_d is the Reynolds number also based on jet diameter, A_r is the ratio of jet area to heater area, H is the standoff between the jet exit and the heater, L is the heater length, and S is the spacing between jets. Therefore, jet type (i.e., slot or round nozzle) and condition (free or submerged), as well as geometric variables such as standoff, spacing, and array type (inline, staggered, or arbitrary) are all necessary to adequately describe jet array impingement conditions.

Jet array heat transfer data have generally been correlated using the form

$$\overline{\mathrm{Nu}}_d = C\,\mathrm{Re}_d^m\,\mathrm{Pr}^{0.4} \tag{2}$$

where m is calculated with a least-squares fit. Additional dependencies such as standoff or jet array spacing have been incorporated by adding variables or terms to Eq. (2). Martin [1] reported $m=2/3$ for a collection of data with a wide range of Reynolds number ($2000 < \mathrm{Re}_d < 100{,}000$). Garimella and Schroeder [4] studied confined air jet arrays in the range of $5000 < \mathrm{Re}_d < 20{,}000$ and reported a value of $m=0.693$. Another air jet study by Florschuetz et al. [5] was conducted for $2500 < \mathrm{Re}_d < 70{,}000$. The authors fit their data using a more complex format such that m was a function of several geometric parameters. However, a simplified form with the same Reynolds number dependence as Eq. (2) also gave a good fit and yielded a value of $m=0.727$. Kercher and Tabakoff [6] similarly found that m was a function of geometric parameters in their study of air jet arrays. The investigation included lower Reynolds numbers lower than the previously mentioned experiments with $300 < \mathrm{Re}_d < 30{,}000$. Kercher and Tabakoff concluded that a change in m occurs at $\mathrm{Re}_d \approx 3000-4000$ and reported values of m from 0.65 to 0.95. Robinson and Schnitzler [7] found $m=0.46$ for an array of submerged water jets in the range $600 < \mathrm{Re}_d < 6500$.

In addition to Reynolds number effects, geometric variables can have a significant effect on jet array heat transfer. To account for the spacing of arrays, a ratio of flow area to heated area A_r has been used. For a constant Reynolds number, increasing A_r generally has a positive effect on heat transfer [1–3,5–8]. Nondimensional standoff H/d has also been shown to be important. A recent review by Meola [8] concludes that increasing standoff has a negative effect on heat transfer as $\overline{\mathrm{Nu}}_d \propto (H/d)^{-0.3}$ for $1.6 < H/d \leq 20$. However, Robinson and Schnitzler [7] reported that the area-averaged Nusselt number is insensitive at nondimensional standoff distances of 2 to 3 diameters.

Goodro et al. [9] and Park et al. [10] studied the independent effects of the Mach and Reynolds numbers on air jet array impingement. The experiment used an infrared camera to measure the surface temperature of the heated impingement surface locally. The jet array was staggered with spacings of 8d and 12d; the standoff used was 3d. To hold the Reynolds number constant and vary the jet Mach number, the investigators used different orifice sizes, resulting in different jet velocities at a given Reynolds number. Goodro et al. varied the Mach number while holding $\mathrm{Re}_d = 60{,}000$, while Park et al. chose $\mathrm{Re}_d = 30{,}000$. Reported Mach numbers were as high is 0.74 and larger Mach numbers were reported to enhance heat transfer. The area-averaged Nusselt numbers were compared with the correlation of Florschuetz et al. [5]. At both Reynolds numbers, the low Mach number data were well predicted. However, higher Mach number data were significantly

---

Contributed by the Heat Transfer Division of ASME for publication in the JOURNAL OF HEAT TRANSFER. Manuscript received April 20, 2009; final manuscript received September 18, 2009; published online February 23, 2010. Editor: Jayathi Murthy.

underpredicted. To capture the Mach number effects, the authors used a correlation of the form $\overline{\mathrm{Nu}}/\overline{\mathrm{Nu}}_F=1+AMa^p$, where $\overline{\mathrm{Nu}}_F$ was calculated from Florschuetz et al. Goodro et al. reported $A=0.325$ and $p=1.55$ for $\mathrm{Re}_d=60{,}000$ and $0.21\leq \mathrm{Ma}\leq 0.74$. Park et al. reported $A=0.58$ and $p=1.35$ for $\mathrm{Re}_d=30{,}000$ and $0.2\leq \mathrm{Ma}\leq 0.6$.

Mach number effects were also investigated in a numerical study by Pence et al. [11] using a single air microjet $d=100$ μm, $H/d=2$ and 4, $419\leq \mathrm{Re}_d\leq 1782$, and $0.2\leq \mathrm{Ma}\leq 0.8$. The area-averaged Nusselt number was compared with the correlation of Martin [1] and was found to be underpredicted by as much as 22.4% at a Mach number of 0.6, Reynolds number of 1310, and $H/d=4$. The author also compared local Nusselt number profiles for compressible and incompressible fluids at $\mathrm{Ma}=0.2$, 0.4, 0.6, and 0.8. For the three highest Mach numbers, the compressible flows outperformed the incompressible flows by a margin that increased with Mach number.

Womac et al. [12] studied the effect of jet condition with arrays of submerged and free jets with FC-77 and water. Jet diameters of the 2×2 and 3×3 arrays were 0.513 mm and 1.02 mm. The array spacing was between 5*d* and 20*d*. Nusselt numbers were not explicitly reported, but it was concluded that submerged jets generally performed equal to or better than free jets.

A recent study by Geers et al. [13] used liquid crystal thermography to measure local temperatures of a thin film heater. Submerged air jets of 13 mm in diameter, with Reynolds numbers ranging from 5000 to 20,000, array spacing between 2*d* and 6*d*, and standoff between 3*d* and 10*d* were investigated. Nusselt numbers ranged from 40 to approximately 140. The maximum local heat transfer coefficient occurred at the primary jet stagnation points, and the heat transfer coefficients decreased with distance from the stagnation point. Increasing the standoff distance had the effect of reducing both the overall performance and peak-to-peak variations in the heat transfer coefficients.

Microjets and heat transfer at the microscale are of particular importance due to potentially positive length scale effects. Patil and Narayanan [14] performed an experimental study of a single, confined, submerged 125 μm circular air jet. Spatially resolved heat transfer data were obtained using an infrared radiometer to measure the temperature of the heated thin foil, onto which the jet impinged. Reynolds numbers were tested in the range of $700<\mathrm{Re}_d<1800$ with standoffs of 2*d*, 4*d*, and 6*d*. Heat transfer coefficients were determined to be insensitive to standoff in that range. The stagnation point Nusselt number varied from about $\mathrm{Nu}_d=15$ at $\mathrm{Re}_d=700$ to $\mathrm{Nu}_d=55$ at $\mathrm{Re}_d=1800$. These results were compared with the Nusselt numbers predicted by the correlation of Martin [1]. The observed Nusselt numbers were approximately 40% lower than that predicted at Reynolds numbers (based on orifice diameter) less than 1000, and approximately 25% higher than that predicted at Reynolds numbers greater than 1700.

Single submerged microjets are capable of producing high Nusselt numbers and heat transfer coefficients. However, to solve for the more practical problem of maintaining acceptable surface temperatures and thermal gradients in high-power electronics (i.e., larger surface areas), it will likely be advantageous to utilize arrays of microjets. In fact, Martin [1] stated that while there are three jet array variables to optimize (jet diameter, spacing, and standoff), "one will find that scaling down all three lengths simultaneously results in monotonically increasing transfer coefficients."

Microjet array literature is scarce, but at least four studies have been performed. Wang et al. [15] studied three different microjet arrays with varying jet diameters, spacings, and configurations using water. However, due to very low area ratios and flow rates, the authors concluded that the dominant heat transfer mechanism was pool boiling.

Fabbri and Dhir [16] studied single-phase heat transfer of impinging jet arrays with three different circular array patterns with circumferential and radial pitches of 1 mm, 2 mm, and 3 mm. Laser drilling was used to create ten arrays with these three spacings; jet diameters ranged from 69 μm to 250 μm at a standoff of 10 mm. Free jets of both water and FC-40 were studied; Reynolds number ranged from 73 to 3813. The heat transfer coefficients reported were $6000-60{,}000$ W/m^2 K. Although these values are numerically similar to those of Wang et al. [15], they are single-phase heat transfer coefficients and do not benefit from boiling. The authors show by comparison that a heat transfer coefficient of 40,000 W/m^2 K can be achieved with roughly one order of magnitude less volumetric flow (300 ml/min versus 3000 ml/min) than an array with a larger diameter.

Overholt et al. [17] used LIGA, an advanced MEMS technique, to create a manifolded microjet array, which removed spent fluid from the confined impingement area through exit holes accessing the center of a hollow orifice plate. This was done in an effort to create single jet impingement conditions over a larger area. Jet impingement diameters of 300 μm and 635 μm were used with water, and peak area averaged heat transfer coefficients of 280,000 W/m^2 K and 200,000 W/m^2 K were reported.

MEMS techniques were also employed by Leland et al. [18] to create a microjet array with an enhanced impingement surface etched in silicon. The enhanced surface consisted of straight parallel channels 45 μm wide, spaced 152 μm center to center and arranged from two opposite edges of the surface. The array consisted of 221,277 μm jets in an inline pattern with $S/d=4.5$ and $H/d\approx 1$. Air was used with $465\leq \mathrm{Re}_d\leq 1405$. Heat was provided by resistors soldered to a heat spreader that was instrumented with thermocouples. Heat fluxes were as high as 15 W/cm^2 with a temperature difference of approximately 50°C.

Because of the lack of data with microjet arrays, an investigation was performed to measure the area-averaged single-phase flow heat transfer coefficients for two micromachined submerged microjet arrays with both air and water. This study was built on a previous investigation of single microjet stagnation zone heat transfer performance [19]. The arrays had a standoff of 200 μm, an array spacing of 250 μm, and diameters of 54 μm and 112 μm. Area ratios were 0.036 and 0.16. The jet arrays impinged on a 1 mm × 1 mm thin-film heater. The effects of the Reynolds number and area ratio were investigated at the microscale. The diameters, standoff, and Reynolds numbers in this study were not solely chosen based on previous technical knowledge as publications on microjet arrays are scarce. The decisions were instead restricted by the manufacturing process used to create the devices.

2 Experimental Apparatus and Method

2.1 Apparatus. To obtain single-phase heat transfer coefficients from a submerged microjet array, a flow loop (Fig. 1) was constructed to supply fluid to a micromachined jet array heat transfer measurement device. For the water experiments, the upstream tank supplied degassed, deionized water pressurized with helium; the downstream tank recovered the water. Air experiments were conducted similarly with the exception of the fluid source; high pressure air was supplied by a compressor. The compressed air passed through a filter before entering the loop at the tank connection. A needle valve controlled the fluid flow rate through the loop. For the experiments conducted at a downstream chamber pressure of 2 bar, a needle valve downstream of the fixture and upstream of the rotameters was used to set the chamber pressure. Flow through the loop was measured using one of the two selectable rotameters.

The microdevices were seated in a custom-built fixture designed to receive them (Fig. 2). The fixture was precision machined from Delrin by a computer numerical controlled mill. Fluidic seals with the microdevices were achieved by small O-rings seated in the fixture. To make electrical contact with the microdevices, two spring-loaded contact pins were press fit into the fixture and protruded above the mating surface. The devices were held in

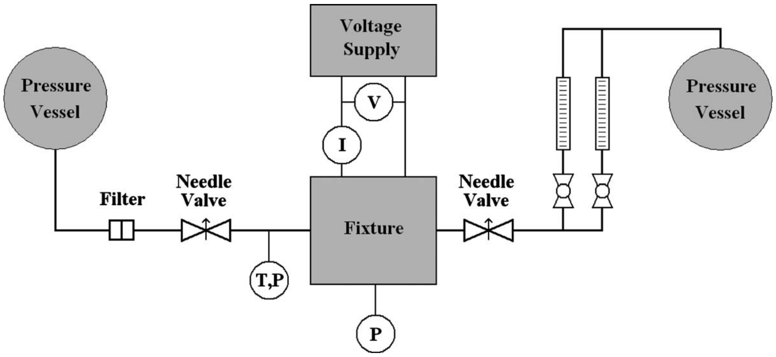

Fig. 1 Schematic of the flow loop

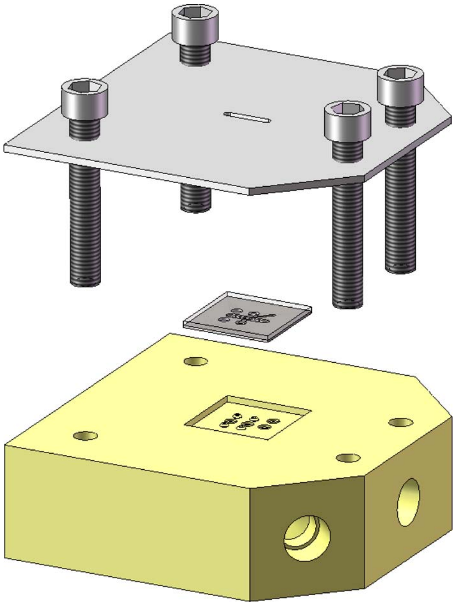

Fig. 2 Schematic of the assembly of the fixture, microdevice, and cover plate

the fixture by an aluminum cover plate.

Each microdevice (Fig. 3) contained a fluid channel, which served as a chamber for the jet arrays, which was 10 mm long, 2 mm wide, and 200 μm tall. A 1 mm × 1 mm thin-film heater, which was 100 nm thick, was centered on the top face of the channel. Fluid entered the channel through the orifice array located in the middle of the bottom face, centered on the heater. Fluid exited the channel at either end through round 1 mm diameter holes. The jet arrays had a spacing of 250 μm with diameters of 54 μm and 112 μm. This arrangement placed 16 orifices over the heater such that equal square unit cells centered on the orifices formed a 4×4 array on the heater. The geometry of the 112 μm array can be seen in the scanning electron microscope (SEM) image (Fig. 4).

Power was supplied to the heater by a dc power supply. The voltage across the heater and the current through the heater were measured simultaneously using two digital multimeters. Pressure transducers were used to measure upstream and chamber pressures. Upstream temperature was measured by a type-T thermocouple. LABVIEW and National Instruments data acquisition hardware were used with a PC to acquire and record the experimental measurements.

2.2 Microfabrication. The micromachined device was built using standard MEMS techniques in a clean room environment. A silicon wafer and a Pyrex wafer were both processed independently before being bonded together to close the fluid channel. A die-saw was used to separate the devices and cut them to their

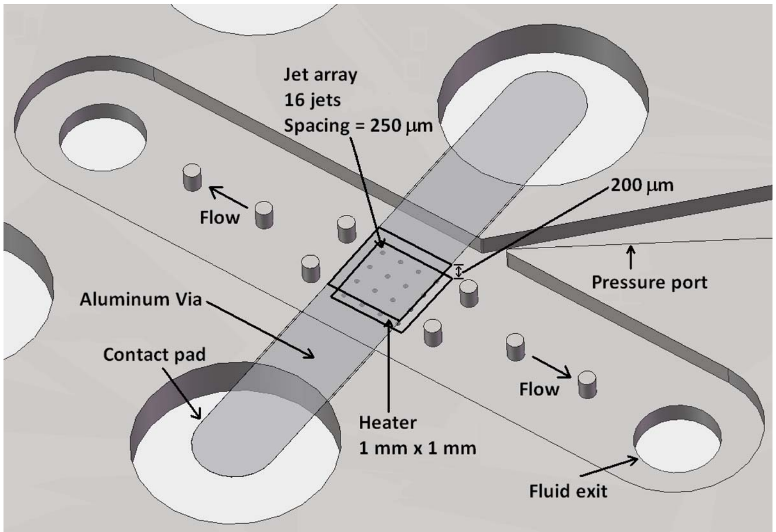

Fig. 3 Schematic of the microdevice. The heater is adhered to the bottom surface of the Pyrex wafer (not shown).

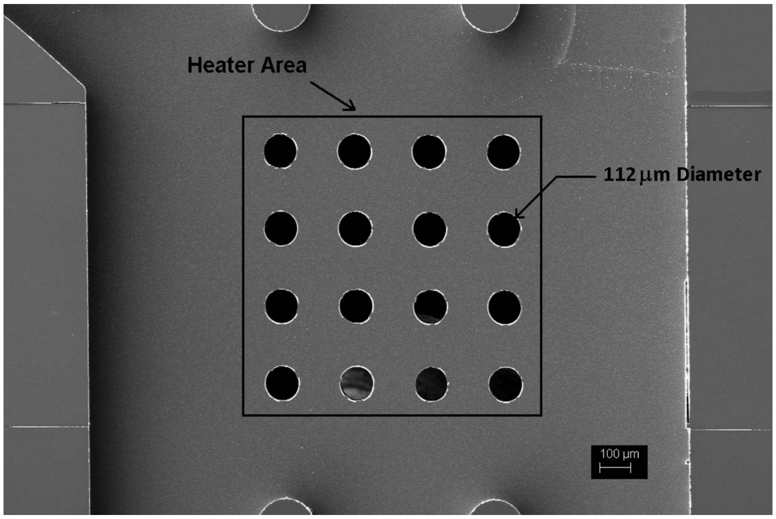

Fig. 4 SEM image of the 112 μm jet diameter array microdevice prior to bonding with the Pyrex wafer. The pictured heater area is 1 mm × 1 mm.

outer dimensions.

The silicon wafer was first etched 5 μm to create clearance for the heater and vias. Oxide was then deposited 2 μm thick on both sides. The wafer was then etched using deep reactive ion etching (DRIE), both to form a hard mask and to etch the features to depth. Oxide hardmasks were used due to the high etch rate selectivity and the protection of the bonding surface. Optical backside alignment was used to align the jet orifices to the channel. DRIE was again used with an oxide hardmask to etch the features on the backside.

Titanium and aluminum were deposited on the Pyrex wafer with a direct current sputturer in two consecutive steps to a thickness of 100 nm and 1 μm, respectively. The aluminum film was chemically etched to form the vias. The underlying titanium thin film was then etched such that it remained only under the aluminum vias and in the heater area. In this way, the titanium thin-film heater was electrically connected to the vias. A protective silicon oxide was deposited to a thickness of 1.15 μm on top of the heater and vias to electrically insulate them.

2.3 Experimental Procedures. Surface temperature measurements were made with the heater functioning as both a heater and a resistive temperature detector. Temperature calibration of the heater from 25°C to 100°C in 5°C steps was carried out in an oven with a thermocouple attached to the device. The resulting temperature and resistance data were fit with a third-order polynomial.

To measure heat losses, the device was installed in the fixture and evacuated. Power was then supplied to the heater. At steady state, the surface temperature and power were recorded to give an estimate of conductive heat losses.

The deionized water used in the experiments was degassed by evacuating the vapor space above the water in the upstream tank. The water was degassed over a span of at least two days to remove any soluble gasses that had diffused from the water. Degassing the working fluid prior to experiments was necessary to prevent degassing and cavitation in the orifice (high velocities/low pressure), which would break up the jet.

Prior to recording heat transfer data, an experiment was conducted to quantify the time required to reach steady state. The average heater temperature was within 0.1°C of its steady state value within 1 s of the application of electrical power.

During the water experiments, the upstream tank was pressurized with helium to produce the necessary flow; fine flow rate control was achieved with a needle valve. The flow rate was measured with one of two rotameters and recorded in LABVIEW along with heater voltage, heater current, upstream pressure, downstream pressure, and upstream temperature. The heater temperature was maintained at 60°C by varying the voltage across the heater, depending on flow conditions to provide an accurately measured temperature difference between the impingement surface and the incoming room temperature fluid. Room temperature during the experiments was 23 ± 1°C. The boundary condition created by the thin-film heater closely approaches constant heat flux conditions. The upstream pressure was limited to 500 kPa absolute to maintain the structural integrity of the device.

2.4 Data Reduction. The jet Reynolds number is defined as

$$\mathrm{Re}_d = \frac{\rho V d}{\mu} \tag{3}$$

where ρ is the density, V is the average velocity at the orifice exit, d is the orifice diameter, and μ is the dynamic viscosity. The thermophysical properties of the working fluid were evaluated at the film temperature, the average of the inlet and fluid temperatures, and surface temperature.

The total power dissipated in the heater was the product of heater current and heater voltage. The heater temperature was found from the heater's electrical resistance and the calibration discussed previously. The temperature of the impingement surface ($\overline{T_s}$) was calculated assuming a one-dimensional temperature drop across the oxide covering the heater with the heat through the oxide ($Q_{\mathrm{heater}} - Q_{\mathrm{loss}}$), its thickness ($t_{\mathrm{SiO_2}}$) its conductivity ($k_{\mathrm{SiO_2}}$), and the area of the heater (A_{heater})

$$\overline{T_s} = \overline{T_h} - \frac{(Q_{\mathrm{heater}} - Q_{\mathrm{loss}}) t_{\mathrm{SiO_2}}}{A_{\mathrm{heater}} k_{\mathrm{SiO_2}}} \tag{4}$$

A one-dimensional conduction model is appropriate since $L/t_{\mathrm{SiO_2}} \approx 1000$. Area-averaged heat transfer coefficients ($\overline{h}$) were calculated from the total power supplied to the heater (Q_{heater}), the heat loss estimate (Q_{loss}) discussed in Sec. 2.5, the heater area (A_{heater}), the average surface temperature ($\overline{T_s}$), and the inlet water temperature (T_{in}) using

$$Q_{\mathrm{heater}} - Q_{\mathrm{loss}} = \overline{h} A_{\mathrm{heater}} (\overline{T_s} - T_{\mathrm{in}}) \tag{5}$$

The use of inlet temperature in Eq. (5) is consistent with previous jet literature.

The area-averaged Nusselt numbers ($\overline{\mathrm{Nu}_d}$) were calculated from the average heat transfer coefficient, orifice diameter, and fluid conductivity (k) using the thermophysical properties at the film temperature

$$\overline{\mathrm{Nu}}_d = \frac{\bar{h}d}{k} \tag{6}$$

2.5 Heat Loss Estimation. Before the heat transfer experiments were performed, a calibration was performed to measure the heat lost from the heater by conduction through the Pyrex. The chamber was evacuated to a pressure of less than 1 kPa, and a voltage was applied to the heater. Once steady state was reached, both the voltage across and current supplied to the heater were measured. Since the relationship between the temperature and resistance of the heater had been determined by calibration, both the temperature of the heater and the power dissipated by it during this experiment could be calculated. However, due to the small size of the heater, the path of heat losses (heat dissipated by the heater that is not removed by convection from the surface of the heater) during the heat transfer experiments is different than the heat loss path during the vacuum loss experiments. Because no fluid is present, the heat loss measured in a vacuum neglects the heat transfer due to convection from the surface of the Pyrex and aluminum vias outside of the heater area. Because this heat loss is not captured, the heat loss determined from the vacuum heat loss experiments underestimates the heat losses that occur during the jet experiments.

Since a better understanding of the magnitude and path of the heat losses during the heat transfer experiments was desired, a finite element analysis of this conjugate problem was performed using COMSOL MULTIPHYSICS. The geometry simulated was a section of the Pryex measuring 2 mm × 2 mm ×1 mm, with the heater centered on one of the 2 mm × 2 mm faces. This included the entire thickness of the Pyrex and extended to the side walls of the channel. The aluminum vias and oxide layers on that face were included in the model. A constant temperature boundary condition was applied to the surfaces of the heater. Since all of the surfaces inside the chamber are in contact with the working fluid during the heat transfer experiments, a convection boundary condition was applied to the remainder of those surfaces. Because of the complexity of the flow and hardware limitations, the jet flow was not modeled at this time; a constant heat transfer coefficient was used. A constant temperature boundary condition (at ambient temperature) was applied to the remaining surfaces.

Because no jets impinge on the surface outside of the heater, it was expected that the heat transfer coefficient on the surface outside of the heater area would be less than that over the surface of the heater. In addition, the temperature on the other surfaces during the experiments must be some finite amount greater than the ambient temperature. Therefore, the boundary conditions applied during the finite element analysis ensured that the results would overestimate the heat losses.

The fraction of the heat dissipated by the heater, which was not removed by convection from the surface of the heater, depends on the heat transfer coefficient in the chamber (Fig. 5). This figure assumes that the temperature of the heater is 37°C higher than the ambient and inlet water temperatures, which is the approximate condition for the reported experiments.

Over the range of heat transfer coefficients reported in the water experiments, the heat losses estimated by the vacuum loss experiment were always less than 4% of the dissipated power. The heat losses estimated using the finite element analysis were less than 7% over the whole range of heat transfer coefficients measured in the water experiments. Since the air heat transfer coefficients were much lower, the estimated heat losses were much greater for the air experiments. The heat losses estimated by the vacuum loss experiment were between 18% and 58%, and the heat losses estimated by the finite element analysis were between 23% and 60%.

The boundary conditions used in the finite element analysis were chosen to give a worst-case estimate, so the results overstate the heat lost. The vacuum losses underestimate the heat lost. Therefore, in the reduction in the data, the heat loss Q_{loss} in Eq. (5) was taken to be the arithmetic mean of the two estimates, and the uncertainty in the heat loss was taken to be plus or minus one-half of the difference between those two heat loss estimates. Since the differences between the vacuum and simulation heat loss estimates were small relative to the total heat dissipated (less than 8% for all experiments), the uncertainties associated with the heat loss estimation are small.

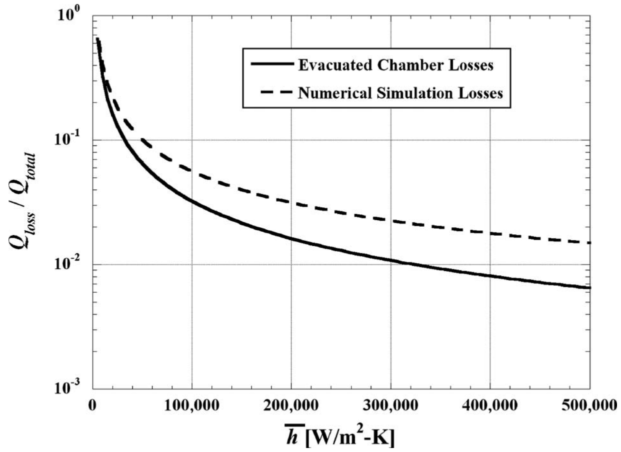

Fig. 5 Heat loss ratio as a function of the average heat transfer coefficient

The finite element analysis not only provided a worst-case estimate of the heat losses, it also provided insight into the path of heat losses. The finite element analysis showed that most of the heat losses in the water experiments (with very high heat transfer coefficients) were not by conduction to the outside boundaries of the Pyrex, but by conduction from the back side of the heater through the Pyrex and back to the surface of the Pyrex and aluminum vias inside the chamber.

2.6 Uncertainties. The propagation of uncertainties for the reduced data followed standard methods [20]. The uncertainty in the Reynolds numbers was less than ±10% for all experiments. The uncertainty in the pressure drop was ±4.2 kPa for all experiments. This results in a large percentage uncertainty at low pressure drops, but the majority of the data was collected in the range of $\Delta P > 100$ kPa, where the uncertainty is less than ±5%. The uncertainties in the area-averaged heat transfer coefficients and Nusselts numbers were less than ±6% for all experiments.

3 Results and Discussion

3.1 Water Data. Experiments were performed with water over a range of Reynolds numbers limited by the self-imposed upstream pressure limitation of 500 kPa absolute. The dimensional and nondimensional results are plotted in Figs. 6 and 7, respectively. Average jet velocities ranged from 0.9 m/s to 20 m/s. The measured average heat transfer coefficients reached as high as 414,000 $\mathrm{W/m^2\,K}$ at $\mathrm{Re}_d = 3290$, with a corresponding Nusselt number of 76. A heat flux of 1110 $\mathrm{W/cm^2}$ was obtained with an inlet water temperature of 23°C and a surface temperature of 50°C. Under these conditions, 11.1 W were dissipated from the 1 mm × 1 mm heater. This point represents the highest point recorded and benefits from a pressure drop of 360 kPa. However, with a pressure drop of only 10.9 kPa, the average heat transfer coefficient was 156,000 $\mathrm{W/m^2\,K}$ for the 112 μm device.

In Fig. 7, a change in the Reynolds number dependence appears to occur near $\mathrm{Re}_d = 1800$, which could indicate a change in the turbulence of the flow. In the region of the change, there appears

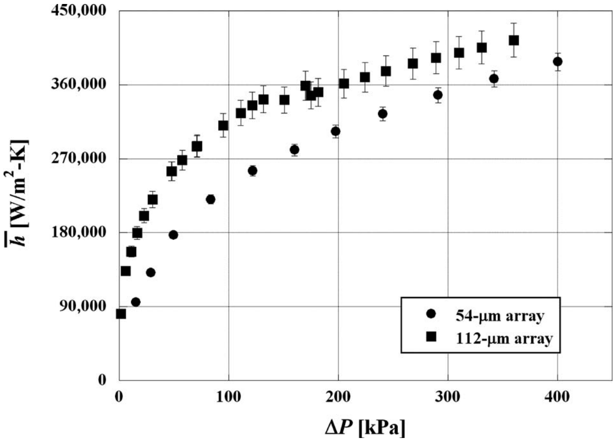

Fig. 6 Dimensional heat transfer performance of both jet arrays with water

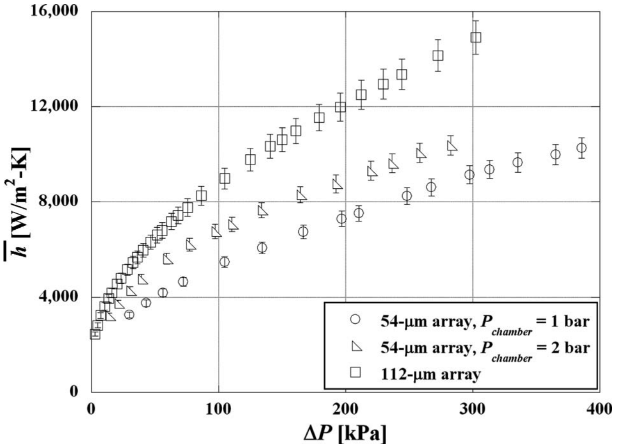

Fig. 8 Dimensional heat transfer performance of both jet arrays with air and the 54 μm jet array with a chamber pressure of 2 bar

to be increased scatter indicative of a transition region. Changes in the Reynolds number dependence have been observed by Kercher and Tabakoff [6] around $\mathrm{Re}_d=3000$. For a given pressure drop or Reynolds number, the 112 μm array outperformed the 54 μm array; this is likely due to the much higher area ratio of the 112 μm array (0.16 versus 0.036). Since the stagnation zone has characteristically high heat transfer rates, a higher area ratio creates a larger relative impingement area, enhancing the overall heat transfer.

3.2 Air Data. Air data were collected with the same upstream pressure limitation and are plotted dimensionally and nondimensionally in Figs. 8 and 9, respectively. The data taken with air have Mach numbers varying from incompressible $(\mathrm{Ma}<0.3)$ to choked $(\mathrm{Ma}=1)$. In Fig. 8, the data points above $\Delta P=100$ kPa (excluding the 54 μm array with a chamber pressure of 2 bars) are choked flow. The chamber pressure was within 10% of atmospheric pressure up to a $\mathrm{Re}_d=1600$ for the 112 μm array, after which it increased to a maximum of 150 kPa absolute. The 54 μm array chamber pressure varied by less than 5 kPa. Here, too, the larger area ratio array performed better. This is due to the higher performance of the impingement region.

The effect of chamber pressure was also investigated by maintaining a chamber pressure of 2 bar with the 54 μm array (Figs. 8 and 9). The higher chamber pressure has a positive effect on the heat transfer coefficient for a given pressure drop, but nondimensionally, the performance is effectively identical. This reinforces the validity of using the generally adopted nondimensional parameters used to quantify performance. In addition, the 1 bar and 2 bar data in Fig. 9 do not have the same Mach number for a given Reynolds number, but the performance was nearly identical. This shows that the effect of Mach number is relatively weak. A high Mach number jet flow should have local temperatures below the inlet temperature, possibly enhancing heat transfer by increasing the temperature difference between the fluid and the heater to beyond that of a low Mach number flow. However, the results do not support this scenario. If the fluid of high Mach number flows were cooler near the heater and the heat flux was the same, the surface temperature would be lower, thus increasing h.

3.3 Data Fit. The air and water data for each device were fit with a curve of the form from Eq. (2). The equations that best fit the data for the 54 μm and 112 μm arrays were

$$\frac{\overline{\mathrm{Nu}_d}}{\mathrm{Pr}^{0.51}} = 0.119\,\mathrm{Re}_d^{0.67} \qquad (7)$$

$$\frac{\overline{\mathrm{Nu}_d}}{\mathrm{Pr}^{0.29}} = 0.581\,\mathrm{Re}_d^{0.55} \qquad (8)$$

respectively; Figs. 10 and 11 plot these equations and the data for each array. The exponent on the Prandtl and Reynolds numbers are different in Eqs. (7) and (8), showing dependencies on geom-

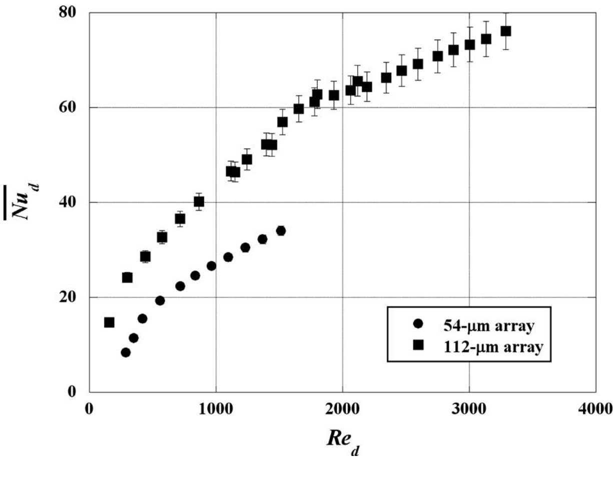

Fig. 7 Heat transfer performance of both jet arrays with water

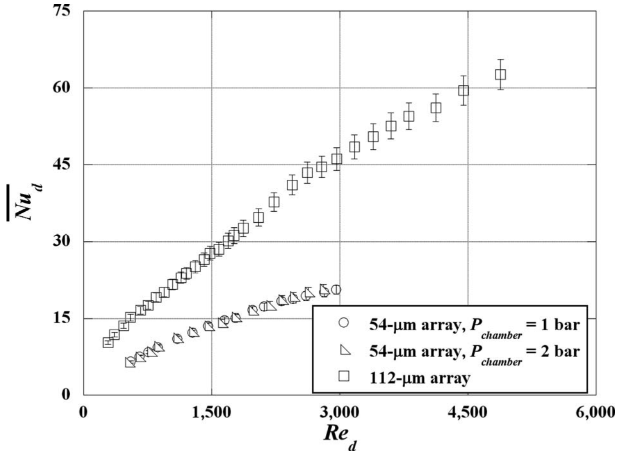

Fig. 9 Heat transfer performance of both jet arrays with air and the 54 μm jet array with a chamber pressure of 2 bar

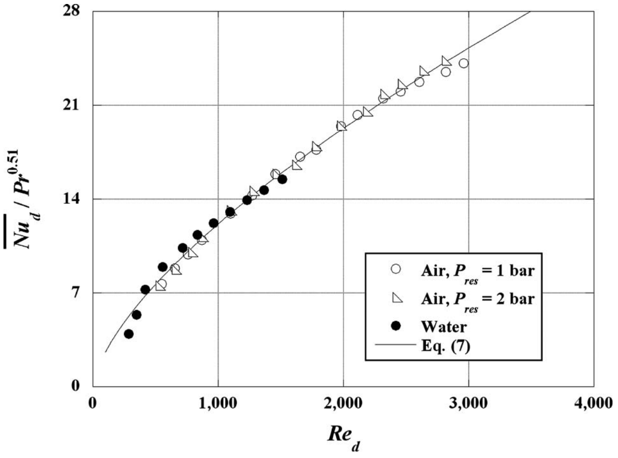

Fig. 10 Air and water data for 54 μm array with curve fit (Eq. (7))

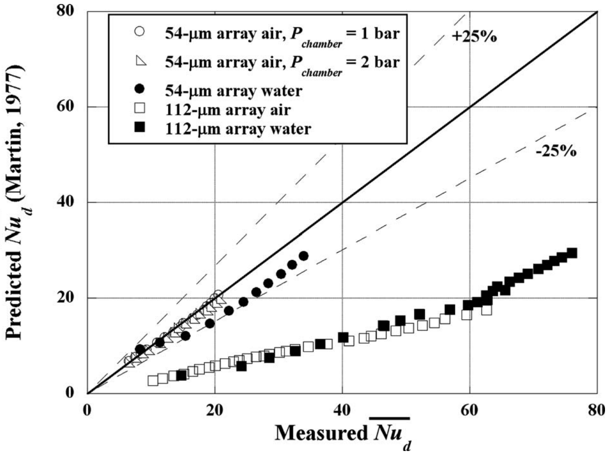

Fig. 12 Comparison of prediction by Martin [1] to the experimental data

etry. Womac et al. [12] reported a weaker Reynolds number dependence in the stagnation region, an area with a radius of 1.9d ($\mathrm{Re}_d^{0.5}$) than the wall jet region ($\mathrm{Re}_d^{0.8}$). Because the 112 μm array has an area ratio defined by Womac larger than 1, the heat transfer is dominated by the stagnation zone heat transfer. This is evident in the fact that the 112 μm array Reynolds number dependence is similar to that of the stagnation zone. The Reynolds number exponent in the 54 μm array is greater than half, but between the two values proposed by Womac et al. as the jet impingement zones did not cover as much of the heater. The Prandtl number dependence follows the same trend as the Reynolds number dependence.

Assuming that Mach number effects are indeed small, the Reynolds and Prandtl number effects are not effectively addressed by the power law fit as the data of the two fluids do not have the same shape. The change in the Reynolds number dependence for water with the 112 μm array seen in Fig. 7 at $\mathrm{Re}_d \approx 2000$ is also shown in Fig. 11. This shift in dependence may coincide with a transition to turbulence within the jet. If a transition to turbulence exists, the typical form may be satisfactory if made piecewise to cover the turbulent and laminar regimes independently. However, it is possible that the current power law fit does not accurately capture the trend of the physics.

3.4 Comparison With Correlation. Martin [1] created a correlation taking into account A_r, H/d, and Re_d using data at the macroscale; the correlation is shown in Eq. (9):

$$\frac{\overline{\mathrm{Nu}}_d}{\mathrm{Pr}^{0.42}} = \left[1+\left(\frac{(H/d)^6}{0.6/\sqrt{A_r}}\right)\right]^{-0.05}\sqrt{A_r}\,\frac{1-2.2\sqrt{A_r}}{1+0.2(H/d-6)\sqrt{A_r}}\,\mathrm{Re}_d^{2/3} \tag{9}$$

The stated range of the correlation is $0.004 < A_r < 0.04$, $2 < H/d < 12$, and $2000 < \mathrm{Re}_d < 100{,}000$. Although the range of diameters used to develop the correlation is not explicitly given, it is comprised entirely of jet arrays with diameters larger than those studied here. A comparison of the actual heat transfer performance and performance predicted by Eq. (9) is shown in Fig. 12. The area ratio of the 112 μm array (0.16) falls well outside the bounds of the Martin correlation. The 54 μm air and water data matched to some degree with predictions, while the 112 μm array's performance was significantly underpredicted. The Nusselt number predicted by Eq. (9) monotonically increases with A_r when holding all other variables constant through the range of 0.004–0.04. However, outside of this stated range, the calculated average Nusselt number from Eq. (9) drops precipitously. The high sensitivity to A_r at the correlation's stated bound represents an unphysical trend. This trend causes underestimation of the heat transfer coefficient in the 112 μm array. The relative agreement between the 54 μm array data and the prediction of Martin suggests that jet array behavior at the microscale is not significantly different from jet array behavior at the macroscale for this geometry. An observation discussed previously can again be seen in Fig. 12 as there is a change in the slope at measured $\overline{\mathrm{Nu}}_d = 60$ for the 112 μm array water data.

Womac et al. [12] divided the heat transfer domain into impingement and wall-jet regions for correlation. The impingement region was taken to be that part of the surface directly influenced by the potential core of the jets, which extends to a radius of 1.9d, while the wall-jet region was taken to be that part of the surface, which was primarily subjected to radial wall jet flow

$$\frac{\overline{\mathrm{Nu}}_d}{\mathrm{Pr}^{0.4}} = 0.509\,\mathrm{Re}_d^{0.5}\,A_{r,w} + 0.0363\,\mathrm{Re}_{L^*}^{0.8}(d/L^*)(1-A_{r,w}) \tag{10}$$

$$L^* = \frac{[\sqrt{2}L_e/2 - 1.9d] + [L_e/2 - 1.9d]}{2} \tag{11}$$

In Eq. (11), L_e is the side length of a unit cell. They stipulated that their area ratio, the ratio of stagnation zone area to total area ($A_{r,w} = \pi(1.9d)^2/L_e^2$) can, for some geometries, exceed unity, in which case it is set to unity and the second term of Eq. (10) is ignored. Different Reynolds number dependencies were used in each zone with an area-weighted average, providing the overall average heat transfer coefficient. Their impingement region Rey-

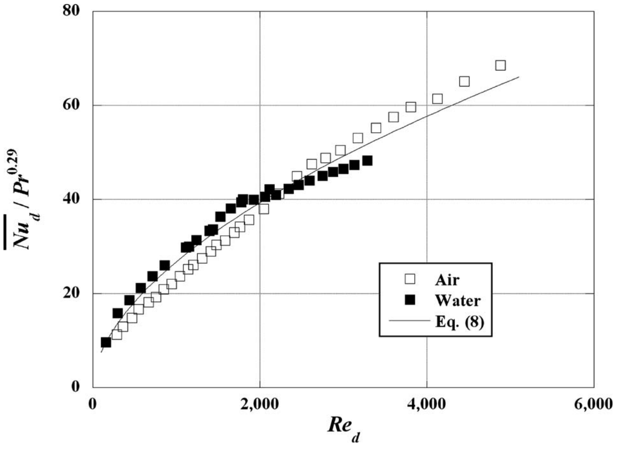

Fig. 11 Air and water data for the 112 μm array with curve fit (Eq. (8))

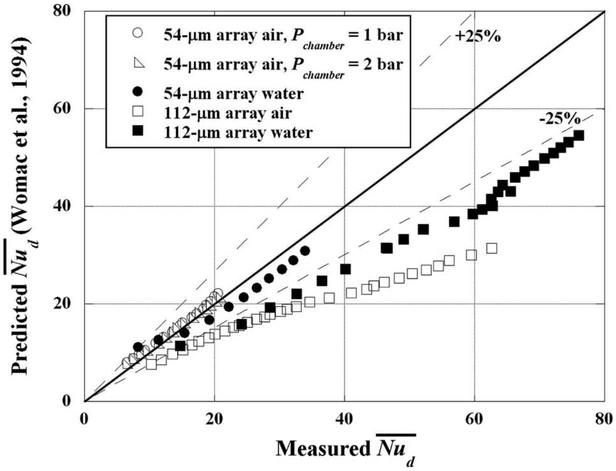

Fig. 13 Comparison of prediction by Womac et al. [12] to the experimental data

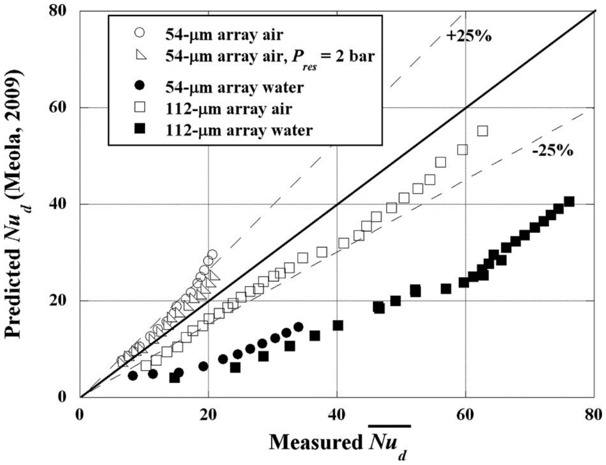

Fig. 14 Comparison of prediction by Meola [8] with the experimental data

nolds number dependence was weaker ($\overline{\mathrm{Nu}}_d \propto \mathrm{Re}_d^{0.5}$) than that of the wall-jet region ($\overline{\mathrm{Nu}}_d \propto \mathrm{Re}_d^{0.8}$). Comparison of the measured data with the prediction of Womac et al. is shown in Fig. 13. The correlation matches the data fairly well although the 112 μm array data are still underpredicted. The division of the heat transfer domain appears to be an effective method to try to capture the physics of the phenomenon; however, the size of the two regions or the regions' dependence on the Reynolds number could be improved to provide a better fit. Comparison of Eqs. (7) and (8) shows the change in the Reynolds number dependence with area ratio. Equation (8) is fit to data with $A_{r,w}=2.3$, placing the entire heater under the influence of stagnation flow. Therefore a Reynolds number dependence of $\overline{\mathrm{Nu}}_d \propto \mathrm{Re}_d^{0.55}$ agrees well with the model and its Reynolds dependence. The 54 μm array had $A_{r,w}=0.53$, indicating that both wall-jet and stagnation zone heat transfer mechanisms existed. The Reynolds number dependence (Eq. (7)) of $\overline{\mathrm{Nu}}_d \propto \mathrm{Re}_d^{0.67}$ falls between those of the stagnation zone and wall-jet region. It is interesting to note that the change in the slope of the 112 μm array brings the data closer to the prediction.

A more recent correlation is given by Meola [8]

$$\frac{\overline{\mathrm{Nu}}_d}{\mathrm{Pr}^{0.42}} = 0.3\ \mathrm{Re}_d^{0.68}\ C_F^{0.56} (H/d)^{-0.3} A_r^{0.15} \tag{12}$$

where C_F is the orifice flow coefficient. This correlation is valid in the range $200 < \mathrm{Re}_d < 100{,}000$, $1.6 < H/d \leq 20$, and $0.0008 \leq A_r < 0.2$. A correlation comparison plot is shown in Fig. 14. Unlike the correlations of Womac et al. and Martin, the 112 μm array is not consistently underpredicted; in fact, the air data of the 112 μm array are very well predicted. However, there is a systematic underprediction of water results when compared with air, regardless of the area ratio, and this may be caused by peculiarities in the use of the flow coefficient. Also, the data taken with the chamber at 2 bar do not fall on the data taken at 1 bar. This contradicts the observation from Fig. 9, where it was shown that the dominant nondimensional heat transfer variables (Reynolds and Nusselt numbers) characterized the heat transfer performance.

The general agreement between the data collected at the microscale with relatively low Reynolds numbers and correlations created with macroscale data indicates that there is no significant difference in the heat transfer. Turbulent jets common at the macroscale have exit profiles that are relatively flat as opposed to laminar jets, which have parabolic velocity profiles. At the standoffs studied here, it is expected that the potential core extends to the impingement surface and the velocity profiles, although viscous effects diffuse toward the jet centerline, are not substantially changed. Still, the difference in velocity profile in the impingement region does not appear to have a substantial effect on heat transfer. This trend is unexpected in a convective flow as flow regime typically affects heat transfer.

4 Conclusions

An experimental investigation of the area-averaged heat transfer coefficients of two submerged microjet arrays was conducted with both air and water. MEMS techniques were used to fabricate test devices with a constant heat flux boundary condition and the capability to measure average surface temperature. Area-averaged Nusselt numbers and area-averaged heat transfer coefficients of the two arrays were reported with both fluids. The data from each device were correlated by a best fit curve including Reynolds and Prandtl number dependencies. The effect of the Mach number was not isolated in this study but did not have a large impact on the average Nusselt numbers for the air data.

Comparison with the correlation of Martin [1] developed at the macroscale suggests that microjet array heat transfer follows trends similar to macroscale jet array heat transfer. A correlation form used by Womac et al. [12] predicted the performance of the two arrays with the most success. This form of correlation may provide a better correlation over a wider range of area ratios as it is derived from physical principals. High area ratio and small diameter arrays can be fabricated with MEMS techniques and may be desirable for their high heat transfer performance. However, currently available correlations cannot accurately predict the heat transfer coefficients of high area ratio, small diameter arrays. Therefore, additional study of high area ratio microjet arrays is necessary to quantify the performance available at the microscale.

Acknowledgment

This work is supported by the Office of Naval Research (ONR) under the Multidisciplinary University Research Initiative (MURI) Grant No. GG10919. The authors would like to acknowledge the staff of the Micro and Nano Fabrication Clean Room (MNCR) at Rensselaer Polytechnic Institute for their assistance in fabrication of the test devices.

Nomenclature

A_{heater} = surface area of the heater (m^2)
A_r = area ratio
$A_{r,w}$ = area ratio as defined by Womac et al.
C_F = flow coefficient
d = diameter of orifice (m)
H = standoff (distance from the orifice exit to the heater surface) (m)

$\overline{h}$ = area-averaged convective heat transfer coefficient (W/m^2 K)
k = thermal conductivity of the working fluid (W/m K)
k_{SiO_2} = thermal conductivity of the silicon oxide covering the heater (W/m K)
L = heater length (m)
L^* = estimated wall jet length (m)
Ma = Mach number
Nu_d = Nusselt number
$\overline{\mathrm{Nu}_d}$ = area-averaged Nusselt number
P_{chamber} = chamber pressure (kPa)
ΔP = pressure drop (Pa)
Q_{heater} = total power supplied to the heater (W)
Q_{loss} = heat loss from the heater other than convection directly to the fluid (W)
Re_d = jet Reynolds number
Re_{L^*} = Reynolds number based on L^*
t_{SiO_2} = thickness of the silicon oxide covering the heater (m)
$\overline{T_h}$ = average heater temperature (°C)
$\overline{T_s}$ = average surface temperature (°C)
T_{in} = fluid inlet temperature (°C)
V = average jet exit velocity (m/s)

Greek

μ = dynamic viscosity (kg/m s)
ρ = density (kg/m^3)

References

[1] Martin, H., 1977, "Heat and Mass Transfer Between Impinging Gas Jets and Solid Surfaces," Adv. Heat Transfer, **13**, pp. 1–60.
[2] Viskanta, R., 1993, "Heat Transfer to Impinging Isothermal Gas and Flame Jets," Exp. Therm. Fluid Sci., **6**(2), pp. 111–134.
[3] Webb, B. W., and Ma, C.-F., 1995, "Single-Phase Liquid Jet Impingement Heat Transfer," Adv. Heat Transfer, **26**, pp. 105–217.
[4] Garimella, S. V., and Schroeder, V. P., 2001, "Local Heat Transfer Distributions in Confined Multiple Air Jet Impingement," ASME J. Electron. Packag., **123**(3), pp. 165–172.
[5] Florschuetz, L. W., Truman, C. R., and Metzger, D. E., 1981, "Streamwise Flow and Heat Transfer Distributions for Jet Array Impingement With Crossflow," ASME J. Heat Transfer, **103**(2), pp. 337–342.
[6] Kercher, D. M., and Tabakoff, W., 1970, "Heat Transfer by a Square Array of Round Air Jets Impinging Perpendicular to a Flat Surface Including the Effect of Spent Air," ASME J. Eng. Power, **92**(1), pp. 73–82.
[7] Robinson, A. J., and Schnitzler, E., 2007, "An Experimental Investigation of Free and Submerged Miniature Liquid Jet Array Heat Transfer," Exp. Therm. Fluid Sci., **32**(1), pp. 1–13.
[8] Meola, C., 2009, "A New Correlation of Nusselt Number for Impinging Jets," Heat Transfer Eng., **30**(3), pp. 221–228.
[9] Goodro, M., Jongmyung, P., Ligrani, P., Fox, M., and Moon, H., 2007, "Effects of Mach Number and Reynolds Number on Jet Array Impingement Heat Transfer," Int. J. Heat Mass Transfer, **50**(1–2), pp. 367–380.
[10] Park, J., Goodro, M., Ligrani, P., Fox, M., and Moon, H., 2007, "Separate Effects of Mach Number and Reynolds Number on Jet Array Impingement Heat Transfer," ASME J. Turbomach., **129**(2), pp. 269–280.
[11] Pence, D. V., Boeschoten, P. A., and Liburdy, J. A., 2003, "Simulation of Compressible Micro-Scale Jet Impingement Heat Transfer," ASME J. Heat Transfer, **125**(3), pp. 447–453.
[12] Womac, D. J., Incropera, F. P., and Ramadhyani, S., 1994, "Correlating Equations for Impingement Cooling of Small Heat Sources With Multiple Circular Liquid Jets," ASME J. Heat Transfer, **116**(2), pp. 482–486.
[13] Geers, L. F. G., Tummers, M. J., Bueninck, T. J., and Hanjalic, K., 2008, "Heat Transfer Correlation for Hexagonal and In-Line Arrays of Impinging Jets," Int. J. Heat Mass Transfer, **51**(21–22), pp. 5389–5399.
[14] Patil, V. A., and Narayanan, V., 2005, "Spatially Resolved Heat Transfer Rates in an Impinging Circular Microscale Jet," Microscale Thermophys. Eng., **9**(2), pp. 183–197.
[15] Wang, E. N., Zhang, L., Jiang, L., Koo, J.-M., Maveety, J. G., Sanchez, E. A., Goodson, K. E., and Kenny, T. W., 2004, "Micromachined Jets for Liquid Impingement Cooling of VLSI Chips," J. Microelectromech. Syst., **13**(5), pp. 833–842.
[16] Fabbri, M., and Dhir, V. K., 2005, "Optimized Heat Transfer for High Power Electronic Cooling Using Arrays of Microjets," ASME J. Heat Transfer, **127**(7), pp. 760–769.
[17] Overholt, M. R., McCandless, A., Kelly, K. W., Becnel, C. J., and Motakef, S., 2005, "Micro-Jet Arrays for Cooling of Electronic Equipment," *Proceedings of the Third International Conference on Microchannels and Minichannels*, Toronto, ON, Canada, pp. 249–252.
[18] Leland, J. E., Ponnappan, R., and Klasing, K. S., 2002, "Experimental Investigation of an Air Microjet Array Impingement Cooling Device," J. Thermophys. Heat Transfer, **16**(2), pp. 187–192.
[19] Michna, G. J., Browne, E. A., Peles, Y., and Jensen, M. K., 2009, "Single-Phase Microscale Jet Stagnation Point Heat Transfer," ASME J. Heat Transfer, **131**(11), p. 111402.
[20] Kline, S. J., and McClintock, F. A., 1953, "Describing Uncertainties in Single-Sample Experiments," Mech. Eng. (Am. Soc. Mech. Eng.), **75**(1), pp. 3–8.